Fundamental Study of Filiform Corrosion on Novel Automotive Aluminium Alloys

Miss Sarah Jane Rowland BSc. Hons, P.G.C.E.

[redacted]@swansea.ac.uk

Sponsoring Company: BASF Coatings GmbH
Industrial Supervisor: Dr. P. Keil

Academic Supervisors (Swansea University):
Professor G. Williams
Professor H.N. McMurray
Professor D.J. Penney

Submitted to Swansea University in fulfilment of the requirements for the Degree of Doctor of Engineering.

Swansea University

2023

EU Funds: Investing in Wales

Summary

The aim of this work was to obtain an improved understanding of filiform corrosion (FFC) on 6000 series alloys. Chapter 3 describes kinetic and mechanistic studies on AA6014 and AA6022 identifying two types of attack, "surface active" (SA-FFC) and "successive pitting" (SP-FFC) FFC. SA-FFC is superficial with a depth c.a. 1-2 μm and occurs when a near-surface deformed layer (NSDL) is present at the alloy surface. SP-FFC is a form of intergranular attack which can penetrate to a greater depth of c.a. 10-50 μm. SP-FFC only occurs when the NSDL is absent or has already dissolved. In Chapter 4 the effect of relative humidity and presence of a NSDL on the type and rate of FFC on AA6014 and AA6022 was investigated. In all cases 80%RH was found to produce the largest rate of corrosion and showed most clearly the 2 types of FFC. At RH < 80% successive pitting is the more dominant FFC. At RH > 80% surface active FFC is more dominant. Although not measured, it was also visually clear that samples with a NSDL show the filament width increasing as %RH increases, up until 80% RH, after which the individual filaments are difficult to discern because they all merge into one unified feature. Chapter 5 investigated the effect of thermal treatment and presence of a NSDL on the type and rate of FFC on AA6014 and AA6022. It was concluded that thermal treatment has negligible effect on surfaces without a NSDL. The effect of thermal treatment is more clearly seen on surfaces with a NSDL with both AA6014 and AA6022 showing the greatest corrosion rates and greatest potential difference at 140°C. The thermal treatment temperatures of 210°C to 250°C showed the greatest corrosion resistance, with the slowest corrosion rates and smallest potential difference. Chapter 6 investigated the effect of inhibitors and presence of a NSDL on the type and rate of FFC on AA6014 and AA6022. Three inhibitors were investigated, at a range of pigment volume fractions (PVF): hydrotalcite (HT), diethyldithiocarbamate (HT-DEDTC) and cationic benzotriazole (CBP). The general efficiency ranking order of the pigments used could be described as CBP > HT > HT-DEDTC. Finally, chapter 7 shows the preliminary work investigating the effect of mechanical deformation on FFC on AA6014 and AA6022. The preliminary work identified the defects on the bent samples for AA6014 and AA6022 show that the corrosion observed mirrors the flat samples without a NSDL present. There was no evidence of a corrosion pattern on the apex of the bend that mirrored the corrosion pattern observed on the flat sample when a NSDL is present.

Declarations

This work has not previously been accepted in substance for any degree and is not being concurrently submitted in candidature for any degree.

Signed [redacted]

Date 24/04/2024

This thesis is the result of my own investigations, except where otherwise stated. Other sources are acknowledged by footnotes giving explicit references. A bibliography is appended.

Signed [redacted]

Date 24/04/2024

I hereby give consent for my thesis, if accepted, to be available for electronic sharing **after expiry of a bar on access approved by the Swansea University.**

Signed [redacted]

Date 24/04/2024

The University's ethical procedures have been followed and, where appropriate, that ethical approval has been granted.

Signed [redacted]

Date 24/04/2024

Acknowledgements

I would like to begin by thanking my academic supervisors, who have both taken the role as my primary supervisor over the duration of the EngD, Professor Neil McMurray and Professor Geraint Williams. I would like to thank them for their support and input of ideas. For their patience in passing on their depth and breadth of knowledge and experimental science skills. I would like to thank my industrial supervisor, Dr Patrick Keil, of BASF Coatings GmbH, for his additional support and encouragement throughout the EngD, and providing many interesting points of enquiry.

For providing the necessary funding for my project I would also like to take this opportunity to acknowledge BASF Coatings GmbH, the Engineering and Physical Sciences Research Council, Coated^2, the European Social Fund, EU Funds: Investing in Wales and Swansea University.

Thanks, must also go to former colleagues in the corrosion department for their support, training, and guidance throughout. There are too many to mention, but I would like to thank some by name: Dr. Christos Kousis, Dr Calvin Richards, Dr Christopher Griffiths, Dr Alexandra Reynolds, and Dr Christopher Batchelor. I would also like to thank Dr. Elinor Winrow and Dr Anna Toutountzi for their support, encouragement, kindness, and friendship, it would have been much harder without you.

Thank you to my mam Catherine and dad, David and the rest of my family and friends who have supported me, over the duration of the EngD, and for the love and patience you have shown. It has been challenging and difficult but having your support and encouragement has kept me going. Finally, the greatest of thank yous to Ed, I could not have done it without you. You have provided no-end of support and encouragement; you believed in me even when I did not. You are the most patient and most loving and I am grateful to have you.

Contents

Chapter 1 – Introduction and literature review

1.1 Project overview

Aluminium sheet alloys of the aluminium alloy 6000 (AA6000) series, Al–Mg–Si–(Cu), were being increasingly used for a variety of applications in the automotive industry. The main driving forces for its growing popularity is the demand to increase the fuel efficiency, public appeal, saleability, and to reduce the CO_2 emission, to meet current climate change targets. Aluminium alloys lower the weight of the automotive bodies, when compared to steel, hence providing the desired outcome. As a result, aluminium alloys have seen a surge in demand in the automotive industry and were used to produce body panel or the whole bodies.

Throughout its increased use in manufacturing a variety of the AA6000 series had been used effectively. Previously, AA6111 and AA6016 dominating the North American and European automotive industries, respectively. Presently, AA6022 and AA6014 were the alloys of choice in the North American and European automotive industries, respectively.

The popularity of the AA6000 series is due to the amalgamation of strength and formability in naturally aged T4 temper. However, for the AA6000 series to obtain the required strength for automotive applications it undergoes a paint-bake cycle. This process produces intermetallic, IM, phases which accounts for the increased strength. The microstructural changes that occur from this paint-bake process, unfortunately, create corrosion issues as the AA6000 series is more susceptible to serious cosmetic corrosion, filiform corrosion, FFC. This could limit the use of aluminium alloys applications in the automotive industry. However, by understanding the mechanisms of corrosion new methods can be developed to postpone corrosion attack. Therefore, the focus of this project is to develop a better understanding of the influence of the paint-bake and surface preparation processes.

Earlier investigations on the AA6000 series have shown the formation of under film corrosion, specifically FFC, due to microstructural changes and the presence of a NSDL. [1–6] NSDL is induced by surface metalwork, widely used in automotive refinish technologies, e.g., grinding processes. Cosmetic FFC creates a poor aesthetic

appearance in the Aluminium Alloys, which is undesirable for consumers and reduces saleability.

This project will investigate the kinetics and mechanism of filiform corrosion, FFC, on organically coated and uncoated aluminium alloys AA6022, AA6014 to determine the influence of the surface preparation and paint bake process on the surface chemistry and microstructure. During the surface preparation and paint bake process intermetallic, IM, phases were formed along with a near surface deformed layer, NSDL. Subsequently, to then determine the influence these changes have on the susceptibility of FFC and its impact on the kinetics of FFC. The method(s) will predominately follow earlier work producing comparable data.[1–6] However, it may be necessary to adapt and modify the following procedure depending on the behaviour of the materials.

1.2 Aluminium and its alloys

1.2.1 Why use Aluminium in the automotive industry?

Cast aluminium transmission housings and pistons have been commonly used in cars and trucks since the early 1900's. Aluminium and aluminium alloys appeared on the 1908 Bugatti, whose construction included extensive aluminium sand castings and formed aluminium body panels that were butt-welded and hand-worked to a polished condition. The bodies were of good appearance, durable and structurally sound. European car manufacturers made extensive use of aluminium and its alloy. During the 1920's and 1930's, it was used to make artistic automotive bodies due to its ductility and formability. Beautiful limited production custom and racing coachwork for automobiles of the 1930's exhibited extremely fine aluminium metal artwork that reached its pinnacle during this period. Today, cast products, primarily engine and other under-the-hood components make up more than half of the aluminium used in cars. In September 1993, the Audi Space Frame (ASF) concept was unveiled. The objective was to design and develop a car that would be substantially lighter than any other vehicles in its class and an all-aluminium monocoque was debuted, which helped to reduce weight and preserve structural rigidity.

Today, light-duty vehicles were responsible for approximately 12% - 15% of total EU emissions of carbon dioxide (CO_2).[7] Under conditions defined by EU law, the Worldwide Harmonised Light Vehicle Test Procedure (WLTP) laboratory test was used to measure fuel consumption and CO_2 emissions from passenger cars, as well as their pollutant emissions. EU[8,9] legislation had set mandatory emission reduction targets for new cars, by:

- 2015 Target - New Passenger cars sold must have an average emission of no more than 130g (CO_2)/km.
- 2020/2021 Target - New Passenger cars sold must have an average emission of no more than 95g (CO_2)/km.

Since monitoring started in 2010[10], emissions have decreased by 22 g CO_2/km (16%). Low-carbon emission, fuel-efficient, vehicles save drivers and businesses money through using less fuel. A target of 80g/km for cars in 2025 would save a new car buyer

c.a. £320 p.a. and pay back the costs of technology within three years. No vehicle technology strategy can cost-effectively achieve a 50+ MPG fuel economy target without significant weight reduction. Automotive manufacturers were replacing a vast quantity of heavy steel with the lighter aluminium alloys. By doing so a substitution of 1 kg of aluminium in a car reduces CO_2 emissions by 17 kg during its whole life cycle. Based on a yearly European production of 16 million cars, this corresponds to roughly 40 million tons of avoided CO_2 emissions during their lifespan. In summary, the benefits of increasing the volume of aluminium alloys in vehicles[11]:

- Efficiency - For every 10% weight reduction with aluminium with the use of smaller, more efficient engines and smaller fuel-efficient multi-speed transmissions, can save 5%-7% on fuel.
- Performance - Lighter vehicles accelerate faster, brake in shorter distances and handle better.
- Durability – Steel is approximately three times heavier than Aluminium, meaning parts can be made thicker and stronger while still reducing the weight of a vehicle.
- Safety - Aluminium can absorb twice as much crash energy as steel and increases the energy absorption capacity of a vehicle's crumple zones.
- Sustainability - Recycling aluminium saves more than 90% of the greenhouse gas, GHG, emissions associated with primary aluminium production, and requires only 8% of the energy.

However, aluminium and its alloys were susceptible to cosmetic corrosion due to surface metalwork used in automotive refinish technologies and post-sale damage to paintwork, e.g., scratches. The annual global cost of automotive corrosion during 2016 was £2trillion[12,13]. Implementing corrosion prevention best practices could result in global savings of £285-£685 billion[14]. This project will give a better understanding of the main alloys used in the automotive industries in both North America and the EU.

1.2.2 Physical and chemical properties of Aluminium

Aluminium is the most widely available metallic element and the third most abundant element comprising about 8% by mass of the Earth's crust[15] However, it always exists in a combined form, and very stable combinations with other materials, particularly as silicates and oxides, of which bauxite is the principal ore, containing approximately 25% Aluminium[16.] In 1886, wo scientists, Hall and Héroult[17], working independently, developed, and patented a new process for direct electrolytic decomposition of aluminium oxide (Al_2O_3) the process was later enhanced with the evolution of the Bayer process[18] Aluminium is 100 percent recyclable, with minimal downgrading of its qualities[19,20]. The re-melting of aluminium requires only about 5 percent of the energy, compared with the process above, hence, the proportion of aluminium produced from scrap (secondary aluminium) is rising rapidly.

Thermodynamically, metallic aluminium is highly active and seeks to return to its natural oxidized state through the process of corrosion. On contact with air the aluminium surface oxidises to form a thin, compact, and strongly adherent aluminium oxide film. This film produces a protective layer against further corrosive attack, however, any defects or scratches in the layer may lead to localised corrosion. It is this layer of aluminium oxide that gives aluminium its passive behaviour and elevated corrosion resistance.

In its pure state aluminium is a relatively soft metal and tends to lose strength over time. But this can be improved with alloying with varying quantities of heavy metals such as copper or zinc, but still maintaining their relative lightness but now include improved mechanical properties[16]. Consequently, by increasing the mechanical properties the corrosion resistance of the alloys can be adversely affected.

Aluminium and its alloys have many applications and were used in many areas such as: automotive, architectural, packaging electrical and electronic applications[21,22]. Aluminium is an important structural engineering material, its usage ranking only behind ferrous alloys because it retains its toughness at very low temperatures, without becoming brittle like carbon steels therefore, matching or exceeding the strength of common construction steel[23–25]. The technical demands made on aluminium alloys in the vast variety of applications were met by the extensive array of alloys available (BS

1470-75, 1490), The alloy designated for any application is based on the mechanical and physical properties required, as well as economic and environmental impact [16].

Property	Value
Atomic Number	13
Atomic Weight	26.9815 g/mol
Valency	3
Crystal Lattice	Face centred cubic
Melting Point	660.2 °C
Boiling Point	2480 °C
Mean Specific Heat (0-100°C)	0.219 cal/g. °C
Thermal Conductivity (0-100°C)	0.57 cal/cm °C
Co-Efficient of Linear Expansion (0-100°C)	23.5 x10-6/°C
Electrical Resistivity at 20°C	2.65 x 10-8Ωm
Density	2.6898 g/cm^3
Modulus of Elasticity	70 GPa
Poisons Ratio	0.34
Electrode Potential	-1.66V

Table 1: properties of aluminium

Pure aluminium is an excellent thermal and electrical conductor, it is magnetically neutral, and when highly polished it reflects well making it excellent for decorative applications e.g., alloy wheels[19]. Aluminium had a low poison ration, therefore is non-toxic and is used in contact with foodstuffs.

Aluminium and aluminium alloys were available in a wide range of strength values-from highly ductile low-strength commercially pure aluminium to very tough high-strength alloys with ultimate tensile strengths approaching 690MPa[19]. Aluminium can be formed and fabricated by all common metalworking and joining methods[27,30,33,40–71]. Aluminium alloys were divided into two major categories: wrought composition and cast compositions. The properties of aluminium alloys depend on a complex interaction of chemical composition and microstructural features developed during solidification, thermal treatment and, for wrought alloys, deformation processing[16,17]

1.2.3 Alloying and Tempering designations and the role of Intermetallics

The mechanical, physical, and chemical properties of aluminium alloys depend on composition and microstructure.[22] By adding selected elements, the properties were changed to suit the application it is required for. The major alloying additions used with aluminium were copper, manganese, silicon, magnesium, and zinc, as well as other trace elements for grain refinement and development of additional properties. Impurity elements were also present, but their total percentage is usually less than 0.15% in aluminium alloys[24,66–70]. Aluminium alloys for sheet products were identified by a four-digit numerical system used to classify the different types of alloys incorporating the product form which is administered by the Aluminium Association and were covered by the American National Standards Institute (ANSI)[19]. "The alloys were conveniently divided into eight groups based on their principal alloying element."

Wrought Alloy Families. A four-digit numerical designation system is used to identify wrought aluminium and aluminium alloys. The first digit of the four-digit designation indicates the group[61,66,71,72]. Other digits were used for the following reasons:

For the 1xxx series, the last two of the four digits correspond with the two digits after the decimal which indicate the minimum aluminium. For example, the aluminium content of 1040 is 99.40% minimum, 1475 is 99.75% minimum and so on. For the 2xxx through 8xxx series, the alloy group is determined by the alloying element present in the greatest mean percentage. The second digit, not including 0, in groups 2xxx through 8xxx, indicates a minor modification for one or more impurities and identifies an alloy modification when compared to that of the original alloy (indicated with 0). The last two digits identify the different alloys in the group. For instance, 4266 is the second modification of 4066 alloy. The last two digits of the other groups were sequential numbers issued by the Aluminium Association to ensure each alloy is uniquely identified.[19] Explicit rules have been established for determining whether a proposed composition is merely a modification of a previously registered alloy or if it is an entirely new alloy. The 6xxx series alloys, however, contains magnesium and silicon in approximately equal amounts, dependent on the alloys requirements, to form magnesium silicide precipitates (Mg_2Si).

Alloys were split into different designation categories based on the type of treatment that they can undergo, they include solution heat treatment, quenching, and precipitation (age) hardening, work hardening, and annealing. Aluminium alloys can be hardened and strengthened by an aging heat treatment designated by the letter T, as well as other techniques. The technique, in which the metal is heated to an elevated temperature followed by rapid cooling, followed by a precipitation hardening process (or "aging" process), had a range of temper designations based on the sequences of treatments used to produce the various tempers. The temper designation follows the alloy classification and is separated by a hyphen.[19] The designations were further separated by the type of heat treating and indicated by one or more digits following the letter T, e.g., AA2024 – T3[4,] AA6016 – T4[3]

Series	Primary alloying components	Content range (wt. %)	Typical Applications	Properties modified via
1000	None	Al>99%	Chemical and food processing industries	Cold worked
2000	Copper	2-6	Aircraft structural components	Solution heat treatment and age hardening
3000	Manganese	0.5-0.15	Architectural, cooking utensils, canning, chemical equipment	Cold worked
4000	Silicon	0.8-1.7	Architectural lighting, machined parts	Low Melting Point Alloys olution heat treatment and age hardening
5000	Magnesium	0.5-5	Automotive, storage tanks, boat hulls, marine applications, unprotected structural and architectural applications	Cold worked
6000	Magnesium and silicon	Mg: 0.2-1.5 Si: 0.2-1.5	Automotive applications, windows, common extrusion, building industry	Solution heat treatment and age hardening
7000	Zinc and Magnesium	Zn: 5-7 Mg: 1-2	High strength applications such as aerospace aircraft structures	Solution heat treatment and age hardening
8000	Silicon and Iron	Si: 0.3-1 Fe: 0.6-2	Not widely used at present	

Table 2: Summary of different aluminium alloys[19,73,74]

To increase the strength of the alloy further, fine particles were dispersed that impede dislocation motion[22]. The alloy mix then undergoes a heat treatment process produce the preferential distribution of the precipitate in the matrix. If hardening occurs from this structure, then the process is called precipitation hardening or age hardening. Heat treatment normally involves the following stages: Solution treatment at a relatively high temperature within the single-phase region; Rapid cooling or quenching, usually to room temperature, to obtain a supersaturated solid solution (SSSS) of these elements in aluminium; Controlled decomposition of the SSSS to form a finely dispersed precipitate, usually by aging for convenient times at one and sometimes two intermediate temperatures[19].

During heat treatment processes, surface treatment and mechanical processes the microstructure of the Alloys changes. When metal A is alloyed with enough element B to exceed the solid solubility of B in A, a new phase is formed. This may be the other terminal solid solution of A in B. Alternatively, an intermediate solid-solution phase, with a crystal structure different from that of either of the terminal solid solutions, may be formed over a range of compositions. In some alloys, intermediate phases were formed that were best regarded as compounds. [23]This change can lead to regions across the alloys surface to become more susceptible to corrosion and is more of a problem for heterogeneous alloys, 2xxx, 7xxx and heat-treatable 6xxx series. The most common features of a microstructure were the intermetallic particles which were classified into precipitates, constituent particles and dispersoids [75]. Each of these features consists of different electrochemical characteristics and act as the sites which dictate the severity of corrosion attack.[71,76–82] The knowledge of intermetallic chemistry and the electrochemistry allows a prediction of the mode of corrosion and the propensity of the attack [83].

The AA6xxx series alloys, containing magnesium and silicon were precipitation hardened, with Mg_2Si as the hardening precipitate [19,22,73]. Silicon lowers the melting point, increases the fluidity, and a moderately increases the alloy's strength. Magnesium provides substantial strengthening and improvement of the work-hardening characteristics of aluminium. If there is a low alloy concentration of magnesium and silicon, then all the Mg_2Si can be dissolved during solution heat treatment and used in the precipitation hardening reaction [84]. They have a relatively

good corrosion resistance, however, of the Al-Mg-Si alloys is slightly inferior to that of the Al-Mg alloys [24]

Term	Description
T1	Cooled from an elevated temperature shaping process, and naturally aged to a noticeably stable condition. This designation applies to products which the effect of cold work in shaping, flattening, or straightening does not influence mechanical properties.
T2	Cooled from an elevated temperature shaping process, cold worked, and naturally aged to a noticeably stable condition. This designation applies to products which were cold worked to improve strength, by shaping, flattening, or straightening does influence mechanical properties.
T3	Solution heat treated, cold worked, and naturally aged to a noticeably stable condition. This designation applies to products which were cold worked to improve strength after solution heat treatment, or in which the effect of flattening or straightening does influence mechanical properties.
T4	Solution heat treated and naturally aged to a noticeably stable condition. This designation applies to products which were not cold worked after solution heat treatment, or in which the effect of cold work in flattening or straightening does not influence mechanical properties. Where the product can age harden at room temperature following a solution treatment.
T5	This designation applies to products which were not cold worked after cooling from an elevated temperature shaping process, or in which the effect of cold work in flattening or straightening does not influence mechanical properties.
T6	Solution heat treated and then artificially aged. This designation applies to products which were not cold worked after solution heat treatment, or in which the effect of cold work in flattening or straightening does not influence mechanical properties. Applies to products that were reheated to a low temperature following a solution treatment. This allows the metal to achieve its highest heat-treated strength level.
T7	Solution heat treated and overaged/stabilised. This designation applies to products which were artificially aged after solution heat treatment to carry them beyond a point of maximum strength to provide control of some significant characteristic other than mechanical properties.

Table 3: Definition of heat treatment designations for aluminium and aluminium alloys[19,39,66,85,86]

Both wrought and cast aluminium have found widespread applications in automobile industry, e.g., cylinder heads, transmission housings, brake valves, wheels, monocoques, body panels.[19] As fuel emission and climate regulation come into force the percentage of aluminium used in automotive applications is expected to increase considerably[87]. Aluminium had one-third the density of steel, which means a component can be 1.5 times thicker than a steel version while remaining 50% lighter. It can absorb twice as much energy as steel at the same weight which can only lead to

improved vehicle acceleration and handling and reduce noise and vibration characteristics. Additionally, aluminium is corrosion resistant, unlike steel, which means continued high strength over a longer period.

Component Element	AA6014	AA6022	AA6016	AA6005A	AA6111	AA7075 T6	AA2024 T3
Aluminum, Al	≤ 97	96.7 - 98.7	96.4 - 98.8	96 - 99	95.6 - 98.3	87.1 - 91.4	90.7 - 94.7
Chromium, Cr	≤ 0.20	≤ 0.10	≤ 0.10	≤ 0.30	≤ 0.10	0.18 - 0.28	≤ 0.10
Copper, Cu	≤ 0.25	0.01 - 0.11	≤ 0.20	≤ 0.30	0.50 - 0.90	1.2 - 2.0	3.8 - 4.9
Iron, Fe	≤ 0.35	0.05 - 0.20	≤ 0.50	≤ 0.35	≤ 0.40	≤ 0.50	≤ 0.50
Magnesium, Mg	0.40 - 0.80	0.45 - 0.70	0.25 - 0.60	0.40 - 0.70	0.50 - 1.0	2.1 - 2.9	1.2 - 1.8
Manganese, Mn	0.05 - 0.20	0.02 - 0.10	≤ 0.20	≤ 0.50	0.10 - 0.45	≤ 0.30	0.30 - 0.90
Silicon, Si	0.30 - 0.60	0.80 - 1.5	1.0 - 1.5	0.50 - 0.90	0.60 - 1.1	≤ 0.40	≤ 0.50
Titanium, Ti	≤ 0.10	≤ 0.15	≤ 0.15	≤ 0.10	≤ 0.10	≤ 0.20	≤ 0.15
Zinc, Zn	≤ 0.10	≤ 0.25	≤ 0.20	≤ 0.20	≤ 0.15	5.1 - 6.1	≤ 0.25
Vanadium, V	0.05 - 0.20	-	-	-	-	-	-
Cr + Mn	-	-	-	0.12 - 0.50	-	-	-
Other, each	≤ 0.05	≤ 0.05	≤ 0.05	≤ 0.05	≤ 0.05	≤ 0.05	≤ 0.05
Other, total	≤ 0.15	≤ 0.15	≤ 0.15	≤ 0.15	≤ 0.15	≤ 0.15	≤ 0.15
Physical Properties	**AA6014**	**AA6022**	**AA6016**	**AA6005A**	**AA6111**	**AA7075 T6**	**AA2024 T3**
Density kg/m³	2700	2690	2700	2700	2710	2810	2780

Table 4: The compositions of earlier aluminium alloys investigated and AA6014 and AA6022 to be investigated: [88,89]

In North America, previously, the high strength alloy AA6111 is used, however this is currently being replaced in favour for AA6022. Whereas Europe previously used the lower copper alloy AA6016, due to its increased resistance to corrosion, and is currently increasing its use of AA6014. Both AA6022 and AA6014 were solution treated and naturally aged at T4 temper, and therefore, the alloys demonstrate a good combination of formability and strength. Subsequently, the alloys undergo a paint bake cycle to increase their strength by the formation of precipitates.

In addition to the precipitation, the surface of the aluminium sheet alloys develops a deformed, micrograined layer. This deformed layer is produced as a result of the abrasion of the surface caused by the rolling process. Consequently, the surface layer is left with different electrochemical properties, compared to that of the bulk of the alloy, due to these microstructural changes.[25,79,90–95] The formation of the deformed

surface layer results in the aluminium alloys being more susceptible to corrosion; filiform corrosion and intergranular corrosion.

When aluminium sheet alloys of the 6000 of the T4 temper undergo a paint bake process, the strength of the alloy by forming intermetallic precipitates.[44,96] The presence of intermetallic precipitates increases their susceptibility of intergranular corrosion, IGC (Intergranular corrosion).[97,98]

In 2010 Scamans et al[99]. published work regarding the ubiquitous Beilby layer on aluminium surfaces. A Beilby layer is first identified by Beilby in 1921 and other research followed in support of the original findings[100]. The Beilby layer a multicrystalline, surface layer that is generated as a result of plastic deformation due to mechanical working. Results suggested it is formed by local melting if a oxidised surface layer 1-100nm thick and a 1-100μm thick worked layer. Further work identified that the Beilbey layers were between 0.4 and 0.8 μm thick and composed of ultrafine grains.[47,101] Scamans found that the combination of high-shear surface processing of aluminium alloys by hot and cold rolling, resulted in ultrafine grained surface layers which altered the alloys surface appearance and corrosion resistance. They identified that grinding and other forms of mechanical work produced similar layers to the Beilby layer. Both layers, Beilby and Beilby-like, are noted to have a different electrochemical behaviour compared with un-worked alloys. This has been attributed to precipitations at grain boundaries within the layer.

The precipitation sequence[102–107] in Al-Mg-Si-Cu alloys has traditionally been assumed to be analogous to that of Al-Mg-Si without Cu [108,109]. Conversely, it has been identified that the precipitation sequence can depend on whether or not the alloy contains Cu. The presence and percentage of Cu affects the precipitation sequence [102,110] and the number of possible intermetallic phases formed. In addition to the main β-phase, Mg_2Si and Q-phases ($Al_5Mg_8Si_6Cu_2$ and $Al_4Cu_2Mg_8Si_7$), pure Si may precipitate if the Mg:Si ratio is low[111]. Chacrabarti et al [112] noted that the Q-phase, metallic Si and the β-phase are the expected precipitates when the Cu content is in the range 0.2–0.5%. Some of the other intermetallic phase formed include: binary θ-phase (Al_2Cu) as well as Al_5FeSi and α-Al(MnCrFe)Si phases[127,112].

1.3 Corrosion

1.3.1 Corrosion thermodynamics

Thermodynamics provides a means of predicting the equilibrium state of a system of specified components but provides no information on the detailed course of the reaction nor of the rate at which the system proceeds to equilibrium.[24]

Most metals were found in nature in the combined form as minerals, which were then reduced to the metal by the expenditure of sufficient energy (chemical, electrical or thermal) to reverse the natural spontaneous reaction. The extracted metal is in a higher energy state than when combined in its ore form and thus there is a thermodynamic tendency for the metal to return to a lower energy state signifying that most metals were thermodynamically unstable. The rate at which the reaction proceeds may be so slow that for all practical purposes the metal is stable.

Metals have different electrode potential, E^0, which expresses the measure of ease of extraction and likelihood of corrosion. To measure an electrical potential a reference system must be used. In measuring the electrode potentials for half-cells, a standard hydrogen half-cell is used. [24]

A standard electrolytic cell; metal is surrounded by an aqueous solution containing ions of the metal. Reactions will take place between the metal and ions until equilibrium between the two reactions is reached.

An electric double layer is formed at the interface and causes the metal to have a different potential than the solution. The potential is known as the Galvani Potential (Φ). The difference in the Galvani potential between the metal and the solution, when compared with the Galvani potential of a reference electrode, is known as the electrode potential (E). A relationship then exists between this electrode potential and the activity of the metal ion, and the effective metal ion concentration in the solution, and is represented by the Nernst equation [1],

$$E = E^{\circ} - \frac{RT}{zF} \ln \frac{[\text{products}]}{[\text{reactants}]} \qquad [1]$$

where E is the potential when the reaction has completed, E^o is the cell potential under standard conditions [reactants] and [products] were the molar concentrations of the oxidant and reductant respectively, R is the gas constant (8.31 J mol-1 K-1), T is

temperature (Kelvin), z the number of electrons involved in the redox reaction and F is Faraday's constant.

$Cl_2 + 2e^- \rightarrow 2Cl^-$	1.36	$PbSO_4 + 2e^- \rightarrow Pb + SO_4^{2-}$	−0.35
$Cr_2O_7^{2-} + 14H^+ + 6e^- \rightarrow 2Cr^{3+} + 7H_2O$	1.33	$Cd^{2+} + 2e^- \rightarrow Cd$	−0.40
$O_2 + 4H^+ + 4e^- \rightarrow 2H_2O$	1.23	$Fe^{2+} + 2e^- \rightarrow Fe$	−0.44
$MnO_2 + 4H^+ + 2e^- \rightarrow Mn^{2+} + 2H_2O$	1.21	$Cr^{3+} + e^- \rightarrow Cr^{2+}$	−0.50
$IO_3^- + 6H^+ + 5e^- \rightarrow \frac{1}{2}I_2 + 3H_2O$	1.20	$Cr^{3+} + 3e^- \rightarrow Cr$	−0.73
$Br_2 + 2e^- \rightarrow 2Br^-$	1.09	$Zn^{2+} + 2e^- \rightarrow Zn$	−0.76
$VO_2^+ + 2H^+ + e^- \rightarrow VO^{2+} + H_2O$	1.00	$2H_2O + 2e^- \rightarrow H_2 + 2OH^-$	−0.83
$AuCl_4^- + 3e^- \rightarrow Au + 4Cl^-$	0.99	$Mn^{2+} + 2e^- \rightarrow Mn$	−1.18
$NO_3^- + 4H^+ + 3e^- \rightarrow NO + 2H_2O$	0.96	$Al^{3+} + 3e^- \rightarrow Al$	−1.66
$ClO_2 + e^- \rightarrow ClO_2^-$	0.954	$H_2 + 2e^- \rightarrow 2H^-$	−2.23
$2Hg^{2+} + 2e^- \rightarrow Hg_2^{2+}$	0.91	$Mg^{2+} + 2e^- \rightarrow Mg$	−2.37
$Ag^+ + e^- \rightarrow Ag$	0.80	$La^{3+} + 3e^- \rightarrow La$	−2.37
$Hg_2^{2+} + 2e^- \rightarrow 2Hg$	0.80	$Na^+ + e^- \rightarrow Na$	−2.71
$Fe^{3+} + e^- \rightarrow Fe^{2+}$	0.77	$Ca^{2+} + 2e^- \rightarrow Ca$	−2.76
$O_2 + 2H^+ + 2e^- \rightarrow H_2O_2$	0.68	$Ba^{2+} + 2e^- \rightarrow Ba$	−2.90
$MnO_4^- + e^- \rightarrow MnO_4^{2-}$	0.56	$K^+ + e^- \rightarrow K$	−2.92
$I_2 + 2e^- \rightarrow 2I^-$	0.54	$Li^+ + e^- \rightarrow Li$	−3.05
$Cu^+ + e^- \rightarrow Cu$	0.52		

Table 5: Standard Reduction Potentials[113]

From Equation [1] the standard electrode potential, E, of all metals can be calculated and this is used to generate a table of standard reduction potentials, table 5. In general, when two metals were coupled together the metal with the more positive standard electrode potential (higher up in the table), is more likely to be reduced while the metal with the more negative electrode potential is more likely to be oxidised.

Due to the thermodynamically instability of metals, metals were likely to corrode. The likeliness of corrosion is related to the change in Gibbs free energy, ΔG. The difference in free energy between the metal and its corrosion product, figure 1.3.1a. The more negative ΔG, the higher the tendency for the reaction to occur. For most metals, the formation of an oxide is favourable and so corrosion is inevitable. Corrosion is inevitable for most metals, however, the activation energy barrier ΔG* can keep metals stable. For a metal to corrode the activation energy, ΔG*, must be overcome. The larger the ΔG*; the less likely the metal will corrode. However, ΔG only tells us that the metals tend to corrode and nothing about the rate at which this reaction will occur.

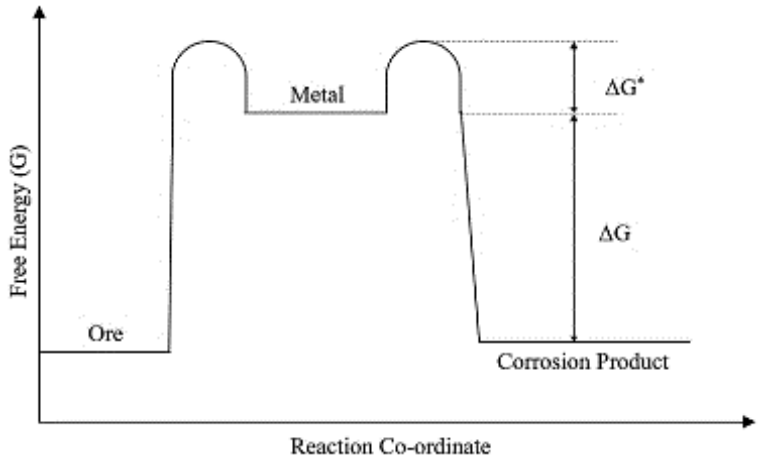

Figure 1.3.1a: Gibbs free energy diagram

During an electrochemical process, electrons flow from the anode to the cathode. The movement of charge sets up a potential difference that relates to Gibbs free energy ΔG:

$$\Delta G = - n F E \qquad [2]$$

Where E is the electrode potential of the metal, where: n = number of electrons transferred and F = Faraday's constant (96847 C mol^{-1})

Electrode potentials act as a guide to activity but were precise values measured under certain conditions for pure metals. The Galvanic series is a more realistic guide based in sea water and includes metal alloys. Standard reduction potentials are determined under standard conditions; cell must be at 298K, 1atm, and all solutions must be at 1M. Potentials shown have been measured against a standard calomel electrode (SCE). Metals with more negative potentials vs SCE most likely to be anodic, therefore, metals with more positive potentials vs SCE most likely to be cathodic. The greater the difference in potential; the worse the corrosion via a dissimilar metal mechanism will be. A more realistic picture of metals tendency to corrode is given by the galvanic series.

Measuring potentials alone will not provide sufficient information to determine whether a given metal or alloy will experience corrosion under a given set of environmental conditions. Therefore, even though a material may have a high susceptibility to corrosion, the rate of the corrosion maybe so slow that it is not an

issue. This means that for a more complete picture the rate of corrosion propagation must also be known.

The surface of a corroding metal/alloy surface can be described at a poly-electrode since both anodic and cathodic reactions are occurring simultaneously. Equation [3] is used when there is no net current, i.e. $i_{anodic} = i_{cathodic}$ [31,133]. Under these conditions the free corrosion current, i_{corr}, can be established experimentally by carrying out a Tafel extrapolation from a polarisation curve:

$$\sum i_{anodic} = -\sum i_{cathodic} = i_{corr} \qquad [3]$$

i_{anodic} is the partial current due to any anodic processes

$i_{cathodic}$ is the partial current due to any cathodic processes

i_{corr} is the rate of corrosion expressed in terms of current.

All corrosion currents are potential dependent. The free corrosion potential is measured through the potential difference between the immersed metal and the appropriate reference electrode. When no net electrical current flows to and from a metal's surface, the corroding metal potential is expressed as E_{corr}. At this potential, the material is described as being in a steady-state condition. The mathematical relationship between current density i, and potential E is defined by Tafel[24]:

$$i_{anodic} \propto exp(E) \qquad And \qquad -i_{cathodic} \propto exp(E) \qquad [4]$$

When E is plotted as a function of log i, a straight line is produced and this is identified as a Tafel plot, figure 1.3.1b:

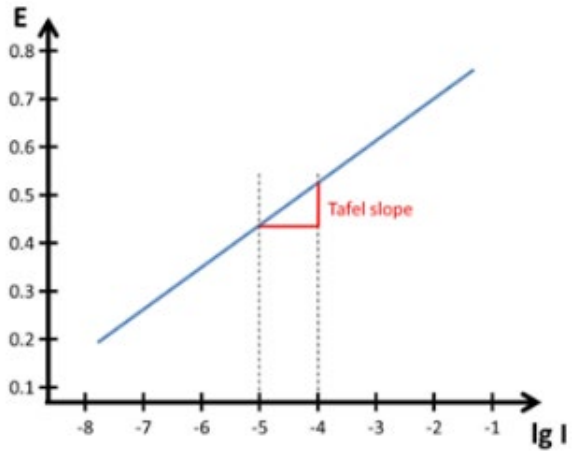

Figure 1.3.1b: Tafel plot with arbitrary scale and slope indicated.[116]

A combination of reduction and oxidation is required for corrosion to occur. If the Tafel plot of both side reactions is known then the theoretical corrosion current and corrosion potential can be identified since: an immersed conducting sample has one potential at any instant and thus all reactions must happen at that potential; the reactions have to happen at the same rate which implies the same current. This means that the corrosion current and the corrosion potential are determined by the point where the two Tafel plots meet. Plotting the two Tafel plots together is known as an Evans diagram, figure 1.3.1c.

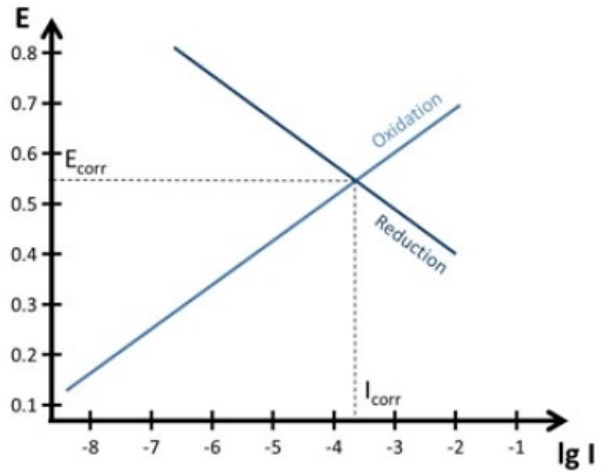

Figure 1.3.1c: An Evan's diagram depicting E_{corr}[116]

By combining both the anodic and cathodic processes for a corrosion reaction on one graph, a mixed potential plot, polarisation curve is produced, figure 1.3.1d. The goal of recording a polarisation curve is to extract the corrosion potential as well as the corrosion current.

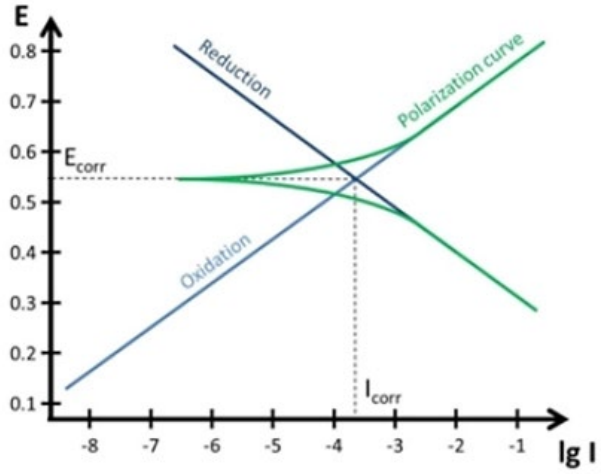

Figure 1.3.1d: Polarisation curve (green) with an Evan's Diagram (Blue)[116]

Corrosion rates are determined by applying a current to produce a polarisation curve (the degree of potential change as a function of the amount of current applied). When the potential of the metal surface is polarised by current in a positive direction, it is said to be anodically polarised; a negative direction signifies that it is cathodically polarised.

The variation of potential as a function of current identifies the effect of concentration and activation processes on the rate at which anodic or cathodic reactions can give up or accept electrons. Figure 1.3.1d can also be plotted with the opposite axis, as shown in figure 1.3.1e. Figure 1.3.1e shows the open circuit potential, OCP, or free corrosion potential, $E_{corr.}$ The free corrosion potential (OCP or Ecorr) is the potential where there is no net current. If you have a passive metal immersed in corrosive solution it will exist at its OCP in the absence of external polarisation. The metal is likely to corrode when the applied potential exceeds the breakdown potential as indicated in fig 1.3.1e.

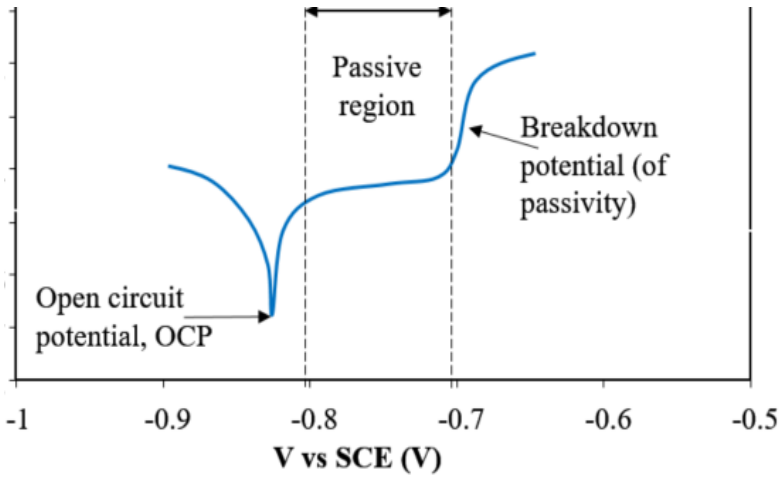

Figure 1.3.1e Schematic of a polarisation curve for aluminium.

1.3.2 Pourbaix Diagrams

Pourbaix diagrams display the regions over which metals will be immune, corrode, passive and trans-passive. It allows metals to be easily, and quickly, compared when uses in different chemical environments were needed. Pourbaix identified three states of corrosion;

1. A metal is corroding when the concentration of its ions is 10^{-6} Mol dm^{-3}

2. If the concentration is below 10^{-6} Mol dm^{-3}, this the metal is said to be immune,

3. If the metal is being protected by an insoluble layer, then it is said to be passive.

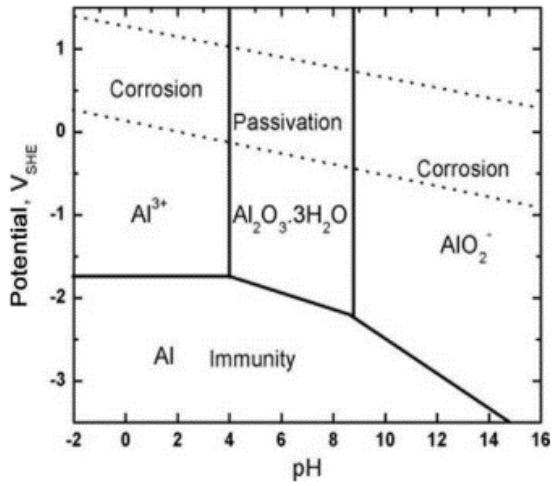

Figure 1.3.2a: Pourbaix diagram for Aluminium[117]

Figure 1.3.2a shows the Pourbaix diagram of Aluminium under different pH conditions, showing the amphoteric nature of aluminium; at low and high pHs aluminium is expected to corrode, however, for a small range, near neutral aluminium is passive, due to its oxide layer.[118,119]

The lines on the Pourbaix diagram were simply calculated using the electrode potentials and Nernst. Vertical lines divide the diagram into separate areas, and their corresponding species, that were in acid or alkali equilibrium. There were 2 types of non-vertical lines. They both indicate species at redox equilibrium. The horizontal lines separate redox equilibrium species not involving hydrogen or hydroxide ions. The diagonal lines separate redox equilibrium species involving hydrogen or hydroxide ions. The area between the dashed lines represents the conditions where the aqueous solvent to oxidation or reduction i.e., the region of interest in aqueous systems is thermodynamically stable under standard conditions.

1.3.3 General Corrosion

All materials or products, plants, constructions, and buildings made of such materials were subject to physical wear during use. While mechanical reactions lead to wear, chemical and electrochemical reactions cause corrosion. Such processes emanate from the materials' surfaces and lead to modifications of the material properties or to their destruction.

DIN EN ISO 8044[120] defines corrosion, or to corrode, as *'physicochemical interaction between a metal and its environment which results in changes in the properties of the metal, and which may often lead to impairment of the function of the metal, the environment or the technical system of which these form a part'*[24]

Additional terms were derived such as[66,121]:

- Corrosion system: A system consisting of one or several metals and such parts of the environment that affect corrosion.
- Corrosion resistance: Ability of a metal to maintain operational capability in each corrosion system.
- Electrochemical corrosion: Corrosion including at least one anodic and one cathodic reaction.

Corrosion can be described as the degradation of a metal to its metal oxide by an electrochemical reaction with its environment. The process arises because most metals do not exist as pure metals in nature but as oxides in metal ores. When the metal is extracted from its ore, the metal had absorbed energy and is thermodynamically unstable, due to its higher energy state, than the corrosion products. Therefore, by undergoing corrosion the energy of the material is reduced.

Corrosion can range from the highly uniform (chemical or electrochemical polishing) to the highly localised such as occurs during pitting. [24] Uniform, or near-uniform, corrosion accounts for the greater proportion of metal deterioration in terms of both mass of metal converted to corrosion products and cost. However, although detrimental it is at least predictable and somewhat avoidable. However, localised corrosion is far less predictable, and therefore more complex to understand and prevent.

The nature of the metal and its' environment will influence the type of corrosion. Uniform corrosion occurs when both the composition of the alloy and the environment were also uniform. Localised corrosion occurs when both the composition of the alloy and the environment were non-uniform. Finally, a third scenario exists where there exists a uniform environment, but the composition of the alloy is non-uniform, this type of corrosion is commonly found in galvanic and intergranular corrosion.

1.3.4 Aqueous Corrosion

There were many types of wet corrosion involving different conditions that will be the focus of this chapter.[122] There were four fundamental components in an electrochemical corrosion cell; anodic region, cathodic region, electrolyte to support, number 4, electron flow.

The basic electrochemical process that governs corrosion involves transfer of electrons between species to initiate chemical change; a REDOX process.[22,122]

The general anodic reaction of metal dissolution, with the formation of metal ions and the release of electrons, and is given by: $M_{(s)} \rightarrow M_{n(aq)}^{+} + ne^{-}$ [5]

Simultaneously, a reduction of H^{+} protons produced from dissociation of water molecules by consuming the electrons produced during metal dissolution. The cathodic site undergoes reactions which were dependent on the pH:

Very low pH (<<7); hydrogen evolution: $2H^{+}_{(aq)} + e^{-} \rightarrow H_{2(g)}$ [6]

The H_2 can diffuse into the metal which can cause hydrogen embrittlement. However, in aerated, acidic conditions: $O_{2(g)} + 4H^{+} + 4e^{-} \rightarrow 2H_2O_{(aq)}$ [7]

However, more commonly under aerobic conditions at near neutral pH, the reduction of dissolved oxygen occurs by the following reaction

$2H_2O_{(aq)} + O_{2(g)} + 4e^{-} \rightarrow 4OH^{-}_{(aq)}$; E0 = +0.4V [8]

The metal ions and hydroxide ions created then combine and chemically react to form the metal oxide corrosion product that characterises metal corrosion.

Metal ions may also react with other species, at the interface, to form insoluble solid corrosion products. These products were often deposited on the metal surface and block further metal dissolution, resulting in passivation of the surface.

To stop or prevent wet corrosion happening any one of the four components must be removed, e.g., remove water and oxygen from the surface and so eliminate the cathodic reaction or supply electrons to the cathodic reaction from another source to prevent the dissolution of the metal to release electrons. [19]

1.3.5 Localized Corrosion

Localized corrosion is caused by a difference in corrosion potential in a local cell formed by differences in or on the metal surface. The difference is usually in the surface layer because of the presence of cathodic micro-constituents that can be insoluble intermetallic compounds or single elements. Additionally, the difference can be on the surface of the metal due to localised environmental difference.[123]

Localised corrosion is usually initiated at weak spots in the oxide film and takes one of the following forms: crevice corrosion, pitting corrosion, filiform corrosion (FFC), intergranular corrosion (IGC), galvanic corrosion, exfoliation corrosion, and biological corrosion.

In almost all cases of localized corrosion, the process is a reaction with water, for aluminium: $2Al + 6H_2O \rightarrow Al_2O_3 \cdot 3H_2O + 3H_2$ [9]

The corrosion product is almost always aluminium oxide trihydroxide, bayerite.

Many types of localised attack occur in near-neutral solutions containing dissolved oxygen, and the pH changes that occur at the anodic and cathodic sites were of fundamental importance when the reaction products were prevented from mixing by the geometry of the system.

Alloys utilise combinations of metal atoms to produce superior performance materials. The combination of these different metals can be dangerous and give rise to Selective Attack Corrosion. Metallic structures were rarely uniform and can contain a wide variety of defects in their structure. Since defect sites were highly localised the corrosion that ensues is also localised and can be highly damaging and penetrating

The following factors play an important part in most forms of localised attack[24].

1. The cathode/anode area relationship.

2. Differential aeration.

3. pH changes at the cathodic and anodic sites.

4. Corrosion products (films) present initially on the metal surface and those formed during the corrosion reaction.

1.3.6 Differential Aeration Corrosion

Differential aeration refers to the different oxygen levels at various parts of the metal. Low levels of oxygen results in the domination of anodic metal dissolution and areas of high oxygen levels were dominated by cathodic reduction of oxygen reduction to hydroxide ions. For example, corrosion under a rain drop:

Initially anodic and cathodic reactions occur across the metal surface where the cathodic activity results in the consumption of oxygen that must be replenished from the atmosphere. The oxygen is easily replenished at the edge of the drop, due to a shorter oxygen diffusion path length, however it is more difficult for oxygen diffusion to the middle of the droplet, longer path length. Consequently, the centre of drop becomes focal anode and edge cathode resulting in metal ions diffusing out from the centre and hydroxide ions diffusing inwards towards the centre. Where they meet a ring of corrosion product develops. Additionally, the corrosion products can form a lid that covers the anodic pit forming a skin [24].

Therefore, to prevent differential aeration corrosion several precautions can be made, including avoiding debris traps (which will absorb or hold water), sharp edges, and water absorbent materials, and planning for good drainage and ventilation amongst others. Differential aeration can lead to, or extend the corrosion mechanisms, of crevice, pitting, and filiform corrosion.

1.3.7 Crevice and Pitting Corrosion

Crevice and pitting corrosion arise from the creation of a localized aggressive environment that breaks down the normally corrosion resistant passivated surface of the metal.[19] This localized environment normally contains halide anions (e.g., chlorides) and is generally created because of differential aeration, which creates corrosion potential drops between most of the surface and occluded regions (e.g., Pits or crevices) that concentrate the halide at discrete locations.

The initiation event is associated with the creation of a localized aggressive environment in a macroscopic crevice. As with pitting, however, the mechanism of this localization is associated with deaeration, low potential, inside the crevice, coupled with an aerated, high-potential, environment outside.

In pitting this localization can begin at microscopic heterogeneities such as scratches and inclusions. Above a given potential, negatively charged anions (e.g., Cl") accumulate on the metal surface and can cause breakdown of the protective oxide. Catastrophic localized breakdown occurs at a specific corrosion pitting potential, which is a function of the material, chloride concentration, pH, and temperature. Once this breakdown occurs, pit propagation can progress rapidly.

Crevice corrosion and pitting have many features in common, and it had been said that pitting may be regarded as crevice corrosion in which the pit forms its own crevice; however, while a macroscopic heterogeneity determines the site of attack in crevice corrosion, the sites of attack in pitting were determined by microscopic or sub-microscopic features in the passive film.[24]

Many of the factors that have been considered above in relation to crevice corrosion were equally applicable to pitting, e.g., the large cathode and small anode area relationship, differences in concentration of the cathode reactant, auto-catalytic formation of acid within the occluded cell, etc. but there were certain distinct differences that must be considered.

Crevice Corrosion

Crevice corrosion is a localised form of corrosive attack. It can be considered as a form of pitting. This form of corrosion is usually associated with a stagnant solution on the micro-environmental level[95,124]. Sand, dirt, corrosion products, and other solids could contribute to crevice formation as the deposits act as a barrier and creates a stagnant condition[125].

Crevice corrosion occurs at narrow openings or spaces between two metal surfaces or between metals and non-metal surfaces.[122] A concentration cell develops as the oxygen is being depleted from the crevice. The differential aeration between the crevice and the external surface gives the crevice an anodic character, producing a highly corrosive condition in the crevice. Crevice corrosion may lead to sudden devastating failure of the metal in service because it occurs in the areas that were not clearly visible.[126–130]

Typically, a crevice site is any area that is about 25-100μm wide; Crevice corrosion is often associated with the geometry of materials and/or structures, e.g., riveted plates, welds contact of metal and non-metal components.

The Fontana Greene Mechanism is a mechanism proposed for the crevice corrosion in stainless steels, but the corrosion mechanisms were similar in other metals[24,125]. Initially, crevice corrosion appears to be simply the formation of a differential aeration cell.[24,39,66] The exposed metal outside the crevice is predominantly cathodic, whilst the metal within the crevice is predominantly anodic. The large cathodic current is acts on the small anodic area thus resulting in intense attack. However, the formation of the high concentration of Cl^- ions within the crevice, leads to a different mechanism.

The obvious method of controlling crevice corrosion is to avoid crevices in the design of the structure and to avoid geometrical conditions that lead to the formation of deposits on the metal. If the geometry cannot be changed, sealing the joints, and covering the area in a barrier coating or applying cathodic protection. [24]

Pitting Corrosion

Pitting may occur in most metals with protective film, but it is particularly characteristic of aluminium and aluminium alloys.[27,156,161,168–181] It is a localised form of corrosion by which cavities, initiates on a metal surface where there is a defect in a protective barrier coating, dislocations, slip step, or a precipitate.[144] For aluminium alloys, pitting corrosion had been found to initiate at the intermetallic compounds.[143]. Therefore, depending on the composition of the alloys and the environment, the pitting corrosion might initiate preferentially on different intermetallic particle types, resulting in different electrochemical behaviour.[145] The presence of an aggressive anion is a necessary condition for pitting corrosion to occur. Many studies have shown that such aggressive anions for aluminium and its alloys include[132,137,146–152]; Cl^-, Br^-, I^-, ClO_4^-, IO_3^-, NO_3^-, SO_4^{2-}

Pitting is first noticeable as a white or grey powdery deposit, like dust, that blotches the surface. During pitting corrosion, the entry of the pit is built by with corrosion product, this enhances the differential aeration and supports the propagation of the pit. The pit must create its own environment to survive. The process of pit initiation can be divided into several steps: the induction period, pit initiation and propagation processes. Each step may be stifled and thus pit repassivation may occur.[153,154] Pitting can penetrate several millimetres during a brief period if the conditions were extremely unfavourable. It can be described in terms of four distinct and consecutive stages[143,155,156]:

- Processes occurring on the passive film, at the boundary of the passive film and the solution.

- Processes occurring within the passive film when no visible microscopic changes occur in a film.

- Formation of metastable pits which initiate and grow for a brief period below the critical pitting potential and then re-passivate (this is an intermediate step in pitting)

- Stable pit growth happens above a certain potential termed the critical pitting potential.

Consequently, pits have varying levels of success. Some initiate but were unable to set up the conditions needed. Some pits can survive the nucleation process and were

referred to as metastable pits since their continued survival is dependent on their maintaining the oxide layer. It is only when pits become stable that the corrosive attack becomes potentially damaging.

Pitting attack is almost inevitable with stainless steels and aluminium alloys due to inhomogeneities in the surface of the metal, if the metal surface can be prepared so that stable pitting can be prevented. Like crevice corrosion, pitting corrosion favours stagnant conditions, therefore if avoided pitting may not initiate or an active attack may stop.

The rapid anodic dissolution of aluminium when exposed to aggressive anions such as Cl- appears to be due to the ability of the chlorine ion to influence the nature of the passive oxide films formed on aluminium and its alloys.[157] It usually starts with the local breakdown of the passive film (from a weak point in the oxide), and after initiation, the reactions within the pit reduce the pH and increase the chloride concentration and, in this way, sustain the reaction.[122,158]

1.3.8 Intergranular Corrosion, IGC

Intergranular corrosion occurs when a grain boundary is attacked because of the presence of precipitates at, and around, the grain boundary. Precipitates can be: intermetallics (mixed metal species), Compounds (metal/non-metal species). Intergranular corrosion (IGC) is localised attack along, or immediately adjacent to, the grain boundaries.[124,159] During heat treatment, aluminium alloys were heated to a temperature that dissolves the alloying elements. As the metal cools, the alloying elements combine to form other compounds. If the cooling rate is slow, they form predominantly at the grain boundaries. The compounds formed differ electrochemically from the metal adjacent to the grain boundaries. These altered compounds can be either anodic or cathodic to the adjoining areas, depending on their composition. The presence of an electrolyte will only complete the cycle for corrosion to take place. This attack may be relatively rapid and can exist without visible evidence. Corrosion products building up along these grain boundaries exert pressure between the grains.[124] Precipitation can form cathodic or anodic sites that can lead to damaging localised corrosion. The composition of the precipitate formed at the grain boundary controls the severity and nature of the attack.

This type of attack can seriously weaken structural members before the volume of corrosion products accumulate on the surface and the damage becomes clear.

In aluminium alloys, intergranular attack usually results from the establishment of local cells along grain boundaries in which second phase, intermetallic precipitates concentrate.[124] Susceptibility to intergranular corrosion is mainly dependent upon alloy composition and heat-treatment.

1.3.9 Galvanic Corrosion

In this process, one metal directly connected to another, induced corrosion in it. The tendency of metals to corrode is given in the galvanic series, table 6. Metals that have a large separation in the galvanic series were worst in combination and should be avoided. For galvanic corrosion to occur, the following three conditions must exist: two electrochemically dissimilar metals present, an electrically conductive path between the two metals, and a conducive path for the metal ions to move from the more anodic metal to the more cathodic metal.

Dissimilar metal, galvanic, corrosion occurs when different metals were coupled together in direct electrical contact in the presence of an electrolyte.[122] Metals have different electrode potentials. The electrode potential, E_0, indicates the thermodynamic driving force for corrosion. The more negative electrode potential is; the more likely that the metal will corrode. Therefore, if in each system there were two metals of different potential were connected in the presence of the electrolyte, setting up an electrochemical cell, then corrosion is favourable. The metal with the more negative electrode potential, oxidises and therefore corrode and the other metal becomes the oxygen reduction cathode.

Anodes and cathodes can appear on the same surface in the corrosion of a single metal. Differences in potential at the metal surface can arise through differences in metals, phases of different compositions, differences in oxygen concentration, differences in pH, local inhibition, coating of an area with an inert layer etc.[124] Electrons will flow through the metal and ions through solution above the metal surface to balance the charges generated at each site.

The degree to which aluminium corrodes when coupled with a more cathodic metal depends on the degree to which it is polarised in the galvanic cell. [19] The metal or alloy possessing the more negative, active, potential tends to suffer accelerated corrosion i.e., anodic dissolution consumes the material, while the metal or alloy possessing the more positive, noble, potential tends to remain practically unaffected. [124]

To protect metals or alloys from an aqueous environment or the atmosphere, a variety of coatings have been applied to the surface of such metals or alloys. In the presence of an electrolyte, which could be a thin film of moisture, galvanic action between

coating and substrate is a crucial factor in determining the protection offered by most coatings. [160]

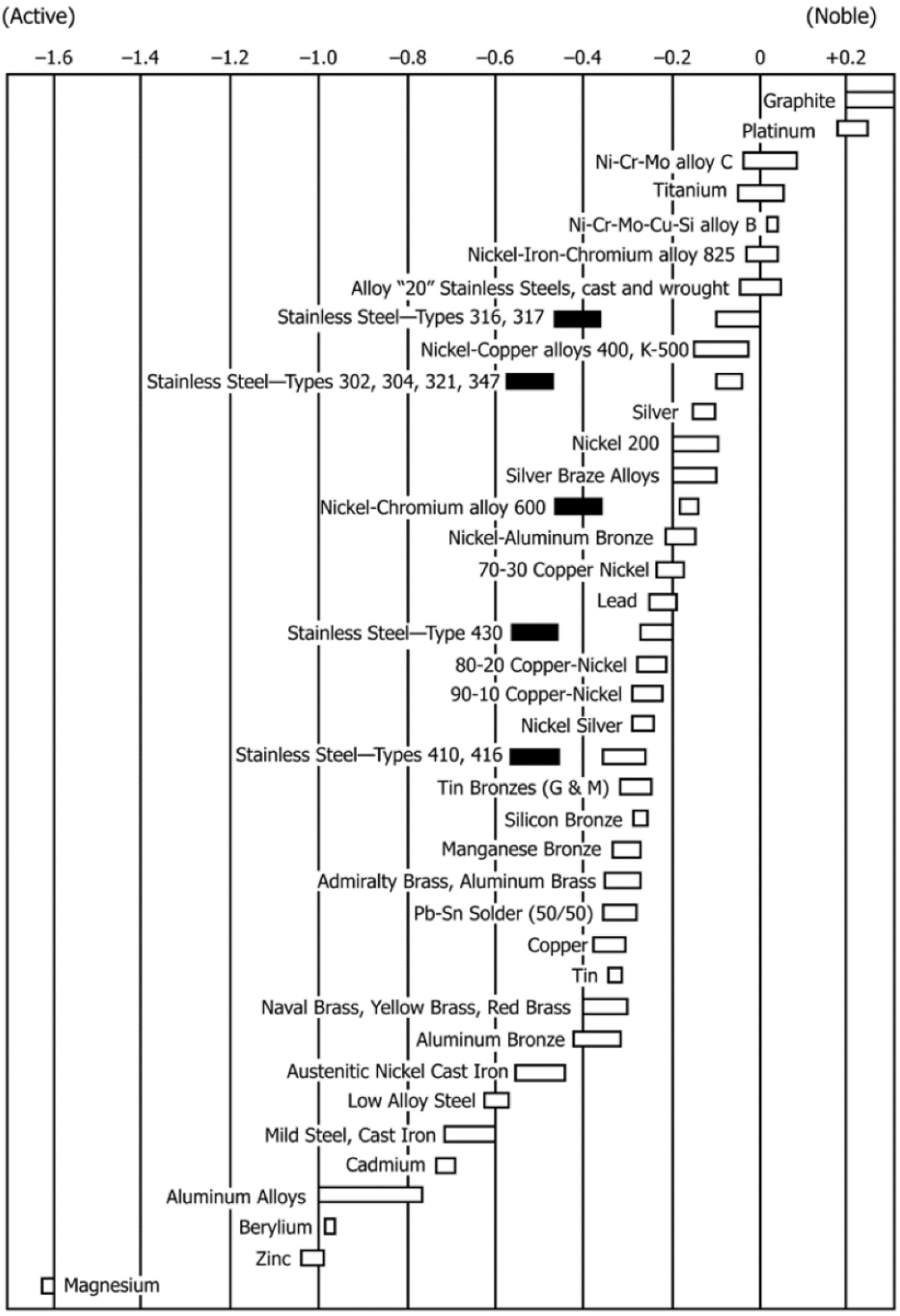

Table 6: A galvanic series of various metals and alloys in flowing seawater at 2.4 to 4.0 m s–1 for 5 to 15 days at 5 to 30 °C. Dark boxes indicate active behaviour of active-passive alloys. Values of top axis: volts versus SCE. Source: ASTM G82–98(2014)

1.3.10 Filiform corrosion, FFC

FFC is a type of localised, under-film, atmospheric corrosion that produces hair-like features, FFC filaments. FFC filaments consist of an active, electrolyte-filled head and a tail of dry, porous corrosion product.

Although FFC attack is largely considered to be superficial in nature, it is aesthetically unpleasant and hence undesirable which is why it is of importance in the automotive industry where extended warranties necessitate more corrosion resistant alloys. FFC only occurs in the presence of atmospheric oxygen and high humidity. Values of humidity dependent upon the metal studied, but typically FFC only occurs above 30% R.H. up to around 95% R.H. Above this relative humidity filaments coalesce, and blistering occurs a relative humidity of 60 - 95% must all be present. [121,161–165]

Filiform Initiation on Aluminium had been shown to start at defects in the coating – for example cut edges, scratches, rivet heads and other sites where the coating is discontinuous.[1,2,4,163–167] At these points inoculating salt (primarily chloride) can accumulate and cause potential initiation sites.

One of the driving forces for FFC is presence of the near surface damage layer, NSDL, which is induced by metal working at the surface, e.g., grinding processes. FFC initiates when aggressive species permeate through a defect in an organically coated metal producing FFC filaments. FFC filaments consist of an active, electrolyte-filled head and a tail of dry, porous corrosion product Once initiated, filaments tend to propagate away from the coating defect under the influence of differential aeration.[161,164,165,168,169]

The filaments were generally white, with a grey head. The head forms the active corrosion site, with corrosion propagation and filament growth taking place here. Filament heads were electrolyte-filled, containing metal cations and aggressive anions (such as Cl^-), and typically show a low pH toward their leading edge, as a consequence of cation hydrolysis.[164,165]

If the process within the electrolyte-filled head is conserved, FFC can continue for long periods of time, as long as the water and oxygen transport can continue to diffuse through the tail. The diffusion of the oxygen through the tail sets up a differential aeration cell in the head[187,188]

The leading edge of the head is oxygen deprived, therefore is the site of anodic activity[170:]

Anodic (metal dissolution): $Al \rightarrow Al^{3+} + 3e^{-}$ [10]

Aluminium cations produced at the leading edge of the filament-head migrate toward the trailing edge where OH^- induces cation hydrolysis. The trailing edge of the head can access the oxygen and is the site of cathodic activity:

Cathodic (oxygen reduction): $O_2 + 2H_2O + 4e^{-} \rightarrow 4OH^{-}$ [11]

This electrochemical cell and propagation of the filaments suggest that the FFC process is anodic undermining, rather than cathodic disbondment. Cl- ions migrate beneath the coating to preserve electroneutrality and water is drawn in by diffusion osmosis to produce an electrolyte droplet Cl^- anions continually migrate toward the anodic leading edge with the result that all water-soluble salt and, through osmosis, liquid water is retained in the filament head.[1]

The type of pre-treatment used prior to painting had an important influence on the subsequent occurrence of filiform corrosion, in particular, surface preparation. The introduction of a deformed surface layer, NSDL, either by thermomechanical processing or surface abrasion, and the significantly different microstructural, due to precipitation of intermetallic phases, and electrochemical properties that it had compared to that of the bulk alloy, increases the susceptibility of the alloy to FFC. [171] Afseth et al [91–94,172]found a strong relationship between the presence of deformed layers and FFC susceptibility. Additionally, FFC susceptibility is further increased by use of high temperature heat treatments. Afseth et al also found that the hot-rolled material is more susceptible to FFC attack than the cold-rolled material, and the susceptibility increases more with heat treatment.[91–93]

The type of FFC observed is seen to vary depending on the surface preparation. In the absence of a NSDL a slower, more deeply penetrating “successive pitting” FFC is observed, while, in the presence of a NSDL propagation of FFC becomes rapid and very superficial, limited only to the deformed surface layer itself.

FFC could be controlled using an acid or alkaline cleaner to remove the deformed layer. Caustic etching improved the FFC susceptibility of the alloy by removal of the active surface layer.[91] Etching also removed the substrate sensitivity to heat-treatment, thus indicating that the enhanced precipitation is associated with the deformed layer.[90]

1.3.11 Aluminium Corrosion

Aluminium is naturally passive and generally had excellent resistance to corrosion and gives years of maintenance-free service in natural atmospheres, fresh waters, seawater, many soils and chemicals, and most foods despite being a thermodynamically reactive metal.[22,73,122] Aluminium had excellent corrosion resistance because of an air-formed, thin layer of aluminium oxide (Al_2O_3), which adheres to the surface of the aluminium.

$$2Al + {}^{3}/_{2}\, O_2 \rightarrow Al_2O_3 \qquad [12]$$

The protective layer consists of an adherent, compact and stable inner layer of oxide film covered with a porous, less stable outer layer which is more susceptible to corrosion. The oxide layer protects the underlying metal and renders it inert to any further reaction the aluminium oxide (Al_2O_3) layer provides chemical and thermal stability, relatively good strength, thermal and electrical insulation characteristics making it an attractive choice for engineering applications.[173–175] However, the surface films contain many flaws that can become the initiation sites for corrosion. These flaws present easy routes for electronic conduction in the otherwise insulating oxide.[176] If the surface layer is deformed, and the aluminium underneath it is exposed to its environment, in most cases, the aluminium reacts to form more (Al_2O_3). The oxide film is naturally self-renewing and accidental abrasion, or other mechanical damage of the surface film is rapidly repaired. Due to the (Al_2O_3) having a stoichiometric value 1.5 times that of the pure metal, the (Al_2O_3) is under enough pressure to cover the surface continuously and handle a level of stress and deformation before splitting.[16,17]

Aluminium is found in group three of the periodic table; therefore, aluminium usually exists as Al^{3+} species. The large positive charge can be stabilised by water molecules arranged in octahedral co-ordination, $[Al\ (H_2O)_6]^{3+}$. Additionally, aluminium oxide reacts readily with water to form hydroxide, $Al(OH)_3$.[177] The formation of the adsorbed $Al(OH)_3$, which transforms into $Al_2O_3 \cdot 3H_2O$ in neutral media, leads to the observed passivity of aluminium and its alloys[177]. At neutral pH, the film formed is insoluble and grows to a sufficient thickness that limits reactivity of the aluminium substrate. However, aluminium is not resistant to corrosion in many mineral acids, except for acids with strong oxidising properties [17].

Aluminium alloys may corrode through several different pathways.[17] Recognising the pathway or the form of aluminium corrosion is a crucial step in determining the appropriate treatment for each problem. When a metal is placed in an aqueous environment it can behave in three ways: corrode, show immunity, or passivate. The level of acidity or alkalinity of the environment significantly affects the corrosion behaviour of aluminium alloys.[16]

The fundamental corrosion reactions of aluminium in the aqueous mediums involve the oxidation of aluminium in water, producing a trivalent cation $A1^{3+}$ and three electrons[71]:

$$Al \rightarrow Al^{3+} + 3e^{-} \quad [13]$$

Whilst simultaneously, a reduction of H^{+} protons produced from dissociation of water molecules:

$$H_2O \leftrightarrow H^{+} + OH^{-}\ 3H^{+} + 3e^{-} \rightarrow {}^{3}/_{2}\ H_2 \quad [14]$$

In summary, the corrosion of aluminium in aqueous media is via O_2 reduction:

$$A1 \rightarrow Al^{3+} + 3e^{-} \quad [15]$$

$$3H^{+} + 3e^{-} \rightarrow {}^{3}/_{2}\ H_2\ ;\ A1 + 3H^{+} \rightarrow A1^{3+} + {}^{3}/_{2}\ H_2 \quad [16]$$

$$A1 + 3H_2O \rightarrow Al(OH)_3 + {}^{3}/_{2}\ H_2 \quad [17]$$

Aluminium corrosion results in the formation of aluminium hydroxide $Al(OH)_3$, which is insoluble in water and precipitates as a white gel, which is found in corrosion pits as white gelatinous flakes.

1.3.12 Previous studies of corrosion driven failure on Aluminium Alloys of the 6000 series which have been organic-coated

In addition to the literature within the body of this report, this section highlights the literature that had been useful in understanding and planning this project.

Firstly, comparison of the ageing of, and mechanical behaviour of AA6014 to AA6011 found that: AA6014, in comparison with AA6111 offers a better control on ageing along with good formability characteristics and hence is a potential sheet body alloy for the automotive industry. [178]

The kinetics and mechanisms of filiform corrosion on AA6111 and Scanning Kelvin Probe Studies of Filiform Corrosion on Automotive Aluminium Alloy found that abrasion of aluminium alloys at T4 temper induces a NSDL which displays a significantly more negative potential than the bulk alloy with a potential difference between the NSDL and bulk alloy greater than 0.2 V with temperatures up to 350°C for AA6111 and at a temperature of 180°C for AA6016 0.2V. At the temperature continued to increase, to 350°C for AA6016 the potential difference increased to 0.5V [3,5]

Furthermore, for PVB (Polyvinyl butyral) coated aluminium alloys samples, with a defect injected with dilute aqueous HCl, FFC is observed for all tempers, both in the presence and absence of an NSDL. In the presence of an NSDL, a rapid, superficial attack, surface-active FFC, is observed in which the metal loss is limited to the thickness of the NSDL (i.e., <2μm). In the absence of a NSDL, a slower, more deeply penetrating FFC, successive-pitting FFC is observed. Successive- pitting FFC occurs both on samples which have been caustic etched to remove any NSDL, and as a secondary process on NSDL-bearing aluminium alloys after the NSDL had been removed by surface-active FFC. The bulk alloy is penetrated to depths of between 10 and 50μm.[5]

It is also found that the rates of both surface-active and successive-pitting FFC were greater on aluminium alloys which had been subject to a post-abrasion heat treatment between 100 and 350°C. The rates of both forms of FFC reach a maximum for heat treatment at 180°C. In both surface-active and successive-pitting FFC the appearance of the corroded surface is consistent with intergranular attack. For surfaces affected by

successive-pitting FFC, localized corrosion features were separable on a scale like grain size (20μm) of the bulk alloy. Where surface-active FFC had occurred, metal dissolution is localized on a much smaller scale (0.1–1μm).[5]

The lower potential and higher corrodibility of the NSDL were consistent with the NSDL being anodically activated relative to bulk aluminium alloys. A mechanistic scheme had therefore been proposed in which anodic activation to intergranular attack causes the NSDL to react sacrificially with respect to bulk aluminium alloys and contributes substantially to the driving force for surface-active FFC. Previous work on AA6111 also reported results that agree with papers but also found that the combination of mechanical grinding and paint baking heat treatment were responsible for the increased susceptibility of AA6111 alloy to filiform corrosion after rectification [3,5,179]

Investigation of filiform corrosion on painted 6000-series aluminium alloys, reported that the increased concentration of copper in the aluminium alloy composition led to a significant reduction in filiform corrosion resistance of the painted panel, environmental exposure at higher temperatures increased corrosion activity for the copper-containing aluminium alloy at a given humidity level and rolling direction had a clear effect on the direction of filiform and blister growth. Additionally, it reported that the low-copper AA6022 showed greater mean corrosion-affected area measurements, but the effect is not as severe as that observed for AA6111. [180]

Precipitation and corrosion behaviour of nano-structured near-surface layers on an AA6111 found that hot and cold rolling resulted in the formation of near-surface deformed layers with microstructures different from that of the underlying bulk alloy.[121,179,181,182] Between the outermost deformed layer and the bulk microstructure, a microband transition region of elongated grains aligned parallel to the working surface might also be present. Severe shear strains generated the recrystallization and the formation of microbands, therefore resulting in significant difference in the surface layer microstructure, i.e., the formation of a near-surface deformed layer. [182,183]

Investigation of filiform corrosion on coated aluminium alloys by FTIR micro-spectroscopy and scanning kelvin probe found the FFC of coated aluminium is investigated using SKP (Scanning Kelvin Probe) and FTIR micro-spectroscopy.[184] An active head with a Volta potential of approximately 400 mV lower than that of the tail

of the filament is identified. The head is filled with a partially hydrolysed aluminium chloride solution, containing monomeric and polymeric cations of aluminium. The aluminium ions produced by the anodic reaction in the front of the head were hydrolysed by the hydroxyl ions generated by the cathodic oxygen reduction, which occurs at the back of the head and the tail.

Complete neutralization of the aluminium chloride solution in the back of the head and in the tail leads to the formation of an aluminium hydroxide gel. During the precipitation process, carbonate ions were also incorporated in the gel. Crystals of the mineral, dawsonite, were formed in the scratch. The aluminium hydroxy compounds generated in the head were hygroscopic and form an acidic electrolyte with a high chloride content that maintains an active aluminium surface. Since the diffusion path of oxygen at the back of the head is longer than that at the front, the condition for a differential aeration cell is present.

Time-lapse potentiometric imaging of active filiform corrosion using a scanning Kelvin probe technique found that the scanning Kelvin probe (SKP) technique can generate time-lapse animations showing the dynamic evolution of free corrosion potential (E_{corr}) patterns associated with filiform corrosion (FFC). [1]

It is used to investigate the initiation, propagation, and termination of FFC filaments on a model system consisting of polyvinyl butyral coated AA2024-T3 and found that the intact PVB coated surface is passive, exhibiting an E_{corr} value of 2140 mV vs. SHE. Local E_{corr} values in the head region of actively propagating FFC filaments were c.a. 150 mV lower than those on the intact polymer coated surface, indicating aluminium depassivation. However, E_{corr} values in the filament tail were c.a. 100 mV higher than background, indicating super-passivation produced by deposition of hydrated aluminium oxide corrosion product.

Spatial analysis of instantaneous E_{corr} distributions indicated that anodic metal dissolution is concentrated at the leading edge, and cathodic oxygen reduction at the trailing edge, of active filament heads. From the findings, a mechanistic scheme is proposed whereby a differential oxygenation cell drives the filament propagation.[1]

Additionally, temporal analysis of time dependent E_{corr} distributions showed that actively propagating filaments tend to advance preferentially in the substrate rolling direction, at a constant speed and do not intersect.

Finally, it is observed that some of the FFC heads initiating at a coating defect subsequently deactivate producing filament termination. Furthermore, some FFC heads appeared to undergo cycles of deactivation and reactivation

Filiform Corrosion on 6000 Series Aluminium: Kinetics and Inhibition Strategies found that grinding the surface of 6000 series aluminium alloys causes susceptibility to FFC. Subsequent heat treatments above 180°C further increases susceptibility and results in faster delamination rates. And Polyaniline doped with phosphoric acid can significantly reduce FFC on a ground surface. [6]

Microstructural characteristics and paint-bake response of Al-Mg-Si-Cu alloy, specifically AA6022, found that the main phases in the as-cast microstructure of 6022 alloy with 0.3% Cu were Mg_2Si, Si, $Al_5Cu_2Mg_8Si_6$(Q), Al_5FeSi, α-Al(MnCrFe)Si and $CuAl_2$. During the homogenization process, most of Al_2Cu, Q and Mg_2Si were dissolved, and plate-like Al_5FeSi particles were transformed into multiple, spherical α-Al(MnCrFe)Si particles.[185] After deformation processing, the phase constituents in the alloy change less, except the precipitation of Mg_2Si. The Cu addition increases the paint-bake response of the 6022 alloys by facilitating the formation of β″ phase. Therefore, the strength of 6022 alloy with certain Cu addition is higher than that of 6022 alloys without Cu after paint-bake cycle. [185]

Earlier experiments suggest that the abrasion induced on the alloys with produce a NSDL that is likely to produce a more negative potential, than the bulk alloy, when measured with in-situ SKP scanning. A more negative potential would suggest that the NSDL is anodically activated compared to the bulk alloy. It is anticipated that FFC, for all PVB coated AA6xxxs samples, will be observed after HCl had been injected. [1–6]

Additionally, the earlier work proposes that it is likely that the nature of the FFC with, and without, the NSDL will differ. The NSDL should cause a rapid superficial attack to be observed, surface-active FFC, with metal loss limited to the thickness of the NSDL. Without NSDL should cause a less rapid response to the HCl but the FFC, successive-pitting FFC, should penetrate further into the sample. Some NSDL samples could undergo successive-pitting FFC after surface-active FFC had occurred. The appearance of the corroded surface will be consistent with intergranular attack with localised successive-pitting FFC features similar in size to the grain size of the alloy

and surface-active FFC features should be approximately the size of the NSDL grain size. Furthermore, samples that have been subjected to post-abrasion heat treatment, at elevated temperatures of 100 to 350°C, were likely to show more rapid FFC when compared to the as-received temper, for both types of FFC. Figure 1.3.12a shows results from previous work showing the different mechanisms and kinetics observed on AA6111 with and without the NSDL[3]

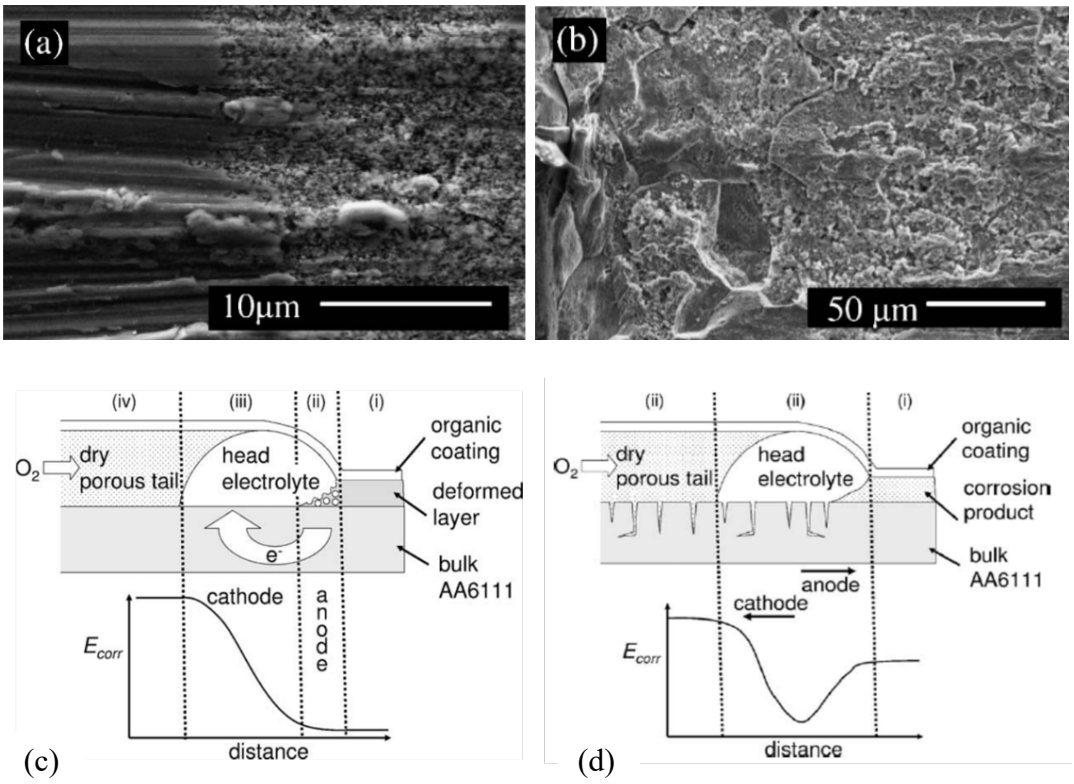

Figure 1.3.12a: Results from[3] showing the different mechanisms and kinetics observed with the AA6111 with and without the NSDL. Top images, a and b, show SEM images of corroded NSDL-bearing AA6111 (THT =180 ◦C) surface after ethanol stripping of the PVB coating and removal of corrosion product with chromate inhibited phosphoric acid. (a) The surface-active FFC front. (b) A region near the coating defect where successive-pitting FFC has also occurred. The lower diagrams, c and d, show schematic representation of proposed relationship between SKP measured E_{corr}– distance profiles and physical regions within the surface-active FFC corrosion cell and successive-pitting FFC corrosion cell respectively.

1.3.13 Coatings and corrosion inhibition

For a coating to prevent corrosion, it must remove at least one of the four essential components required for aqueous corrosion to occur. They are:

- Anodic sites (electron producing)
- Cathodic sites (electron consuming)
- The electrolyte (conduction solution)
- A conductive pathway between anode and cathode

Coatings are judged on how well they perform. They ideally must possess the following properties:

- Resistance to oxygen and water permeation
- Barrier to ion migration through the film, when wet
- Large electrical resistance of the coating
- Adhesion to the metal, especially when wet
- Presence of any corrosion inhibitors
- Good resistance to attack by an alkali

The first types of organic coatings used were primarily paint-based. They were used as it is assumed that they would prevent oxygen and water from reaching the metal surface. However, after investigating these coatings, it is concluded that due to the paint-based coatings already containing water, the metal surfaces experienced an increased rate of water arrival when compared to bare-metal samples. I.e., water easily diffuses through paint-based organic coatings. Another type of coating investigated is polymer coatings. Leng et al[186–189] 107 studied water and oxygen diffusion and found that the concentration of water at the metal/polymer interface is far greater than that in the bulk polymer and although slower than that observed on an uncoated metal surface, the reduction did not explain the significantly lower corrosion rates. It is therefore concluded that oxygen and water diffusion through the paint film were not a rate-determining step.[24,66]

Using coatings for corrosion inhibition also investigated the paint's ability to resist ionic activity/movement with the addition of pigments designed to inhibit anodic and cathodic reactions. The pigments are usual added to the primer layer, or the layer in

contact with the metal surface. The nature of the pigments has changed over time and as a result of investigative work being published. Pigments can be in the form of sparingly soluble salts or ion-exchange pigments.[190,191] The ion-exchange pigments either be used for cathodic inhibition or anodic inhibition, with the potential for some smart inhibitors performing roles over time. Cathodic inhibitor generally inhibits the corrosion by producing precipitates, insoluble salts formed by cations and hydroxide ions. The use of rare-earth metals has been particularly effective in the inhibition of aluminium alloys[234–244]. Anodic inhibitors come in two forms: anodic precipitation inhibitors, and oxidising inhibitors, sometime known as cathodic depolarisers. In a similar way to the cathodic precipitation inhibitors, anodic precipitation inhibitors form insoluble salts with the metal cations produced at the anodic site. The salts form a protective barrier film over the metal surface preventing any further mass transport to the anode, thereby eliminating one of the four requirements for corrosion, a conductive pathway between anode and cathode. Chromates and Phosphates are examples of efficient anodic precipitation inhibitors. The other type of anodic inhibition, oxidising inhibitors, have alternative cathodic reactions to the oxygen reduction reaction removing electrons from the system. A stable insoluble oxide or hydroxide forms on the metal surface. This causes a large shift in the free corrosion potential moving the metal into a passive region which protects against further corrosion.

Chapter 2 – Experimental methods

2.1 Materials

All Chemicals were acquired from Sigma Aldrich, now Merck, unless otherwise stated. They were all of analytical reagent or pigment grade. A general description of the experimental procedures used throughout the experimental work in this thesis are given in this chapter. Any details specific to a particular experiment are given in that particular chapter.

Polyvinyl-Butyral, PVB

Polyvinyl butyral-co-vinyl alcohol-co-vinyl acetate (PVB), molecular weight 70,000 – 100,000 is used as a model coating and also as a matrix for the suspension of inhibitors. PVB has been used in many investigations into corrosion kinetics and is why it is used in this work. The reasons PVB is widely used is in part due to its inert nature and visual appearance once dry as it forms a clear lacquer allowing observations to be made easily. Additionally, PVB is soluble in ethanol and is used to produce a 15.5 wt. % ethanolic solution of PVB. PVB maintains a good level of adhesion to the metal substrate as it consists of hydrophilic and hydrophobic monomers.

Metals

This thesis has focussed on AA6014-T4 and AA6022-T4 alloys, which are commercial AlMgSi(Cu) alloys and were supplied by BASF Coatings GmbH. Their compositions are shown in table 7:

Component Element	AA6014	AA6022
Aluminum, Al	≤ 97	96.7 - 98.7
Chromium, Cr	≤ 0.20	≤ 0.10
Copper, Cu	≤ 0.25	0.01 - 0.11
Iron, Fe	≤ 0.35	0.05 - 0.20
Magnesium, Mg	0.40 - 0.80	0.45 - 0.70
Manganese, Mn	0.05 - 0.20	0.02 - 0.10
Silicon, Si	0.30 - 0.60	0.80 - 1.5
Titanium, Ti	≤ 0.10	≤ 0.15
Zinc, Zn	≤ 0.10	≤ 0.25
Vanadium, V	0.05 - 0.20	-
Cr + Mn	-	-
Other, each	≤ 0.05	≤ 0.05
Other, total	≤ 0.15	≤ 0.15

Table 7: The compositions of earlier aluminium alloys investigated and AA6014 and AA6022 to be investigated: [88,204–208]

2.2 Sample Preparation

Sample preparation techniques conducted in earlier and similar work were followed to produce comparative results.[3–5,179] Individual chapters discuss the adaptations to the steps below. Both AA6014 and AA6022 were prepared in the same way. The aluminium alloy sheets were cut into coupons c.a. 40mm x 40mm followed by:

1. Alkali cleaning of the coupon in Sodium Hydroxide, NaOH, (10% w/v) (CAS 1310-73-2) to dissolves aluminium oxide. It removes several µm, including any NSDL. It is a vigorous reaction, and therefore time dependent. The coupons were submerged for c.a. 45s at a temperature of c.a. 60°C to allow the aluminium oxide to completely dissolve.
2. The coupons were rinsed with distilled water and acetone
3. Acid desmutting in concentrated Nitric Acid, HNO_3, (CAS 7697-37-2) to remove impurities such as copper and iron from the surface and passivate the aluminium surface. The coupons were submerged for c.a. 30s at a temperature of 25°C.
4. The coupons were rinsed with distilled water and acetone
5. When required, a NSDL is reintroduced by manual abrasion using 180 grit silicon carbide paper for 5 mins. The abrasion direction is orientated in the same direction as the rolling direction.

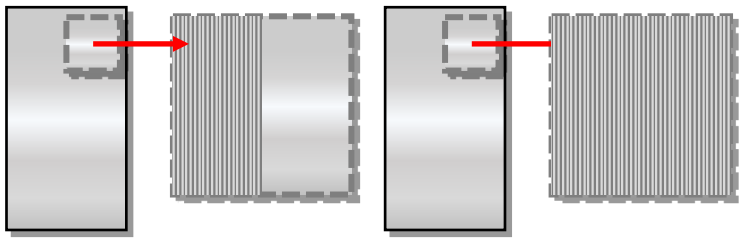

Figure 2.2a: The types of surfaces produced on the cut aluminium alloy samples.

6. The coupons were rinsed with distilled water and acetone prior to coating
7. Coupons were coated with 15.5% (w/w) ethanolic PVB solution (CAS 27360-07-2) to produce an air-dried PVB coating of thickness 30µm ± 5µm
8. 10mm defect(s) were scribed through the PVB layer normal (90°) to the rolling/NSDL direction with a scalpel. Due to economy of samples, most were scribed with 2 defects c.a. 13mm apart.[3,4]

9. FFC is initiated by injecting the scribe with 1μL of 2M aqueous hydrochloric acid using a glass micro-capillary dispenser. The HCl (CAS 7647-01-0) injection method is intended to create greater reproducibility than methods involving full sample exposure either by salt fog, HCl vapour, or immersion in aqueous electrolyte. [3,4]
10. the samples were placed in sealed containers, with a specific saturated salt solution to obtain the desired % relative humidity, and a digital hygrometer and temperature sensor (Lascar's EasyLog EL-USB-2-LCD+) is placed in each container.
11. *Any other adjustments to the sample preparation will be discussed in the relevant chapters.

2.3 Bar coating technique

A self-metering coating process performed using automated techniques or by hand. The coating weight is determined by the fluid rheology, substrate, substrate speed, rod geometry and the load(s) applied. Increasing fluid viscosity, increases film thickness. Changing the size of the rod and/or the pressure of the rod also affects film thickness; generally, the higher the pressures, the thinner the coating weight. The simplest technique of bar coating is tape casting, shown in figure 2.3a. Pieces of insulator tape were placed at the edges of the sample. The tape acts as the height guide. The PVB is placed at one end of the sample, as shown in figure 6 and a smooth bar drags the PVB along the length of the sample. The sample is air dried to remove the solvent, thus producing the final film weight. However, the thickness of the tape may vary whether between different rolls or within the same roll. The slightest variation in pressure and roller speed is difficult to reproduce and define.

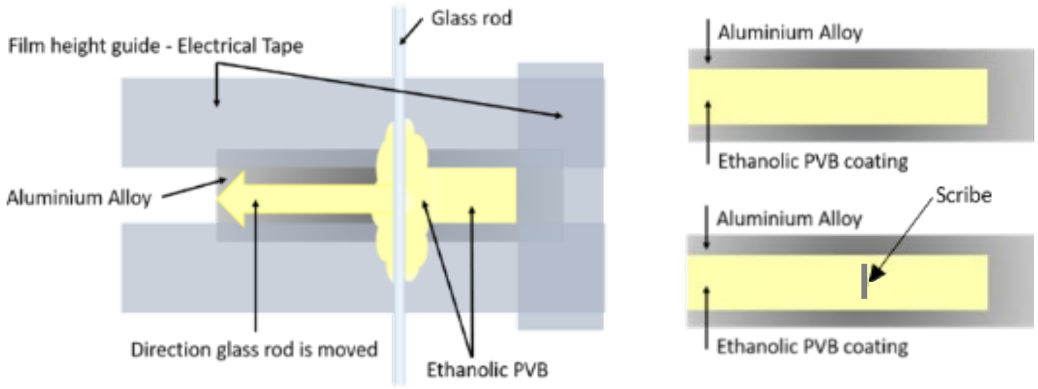

Figure 2.3a: Schematic of the bar coating technique

Additions were made to the PVB coating in some of the investigation and have been discussed in detail in chapter 6.

2.4 Image Analysis of FFC Experiments

Following FFC initiation samples were put in a sealed environment chamber which is maintained at 20°C and at the required relative humidities. Time-lapse photography is used to capture images of the samples periodically. A Canon EOS 750D DSLR camera with 18-55 mm f/3.5-5.6 lens is used to take the images. The images were uploaded to Photoshop and analysed by taking pixel measurements and converting them into area measurements to determine the total area of FFC on the surface. The data is inputted into various excel documents where the area of FFC w.r.t. time were produced, along with FFC propagation rates. Some of the data is used with surfer imaging software to provide potential imaging from selected SKP scans.

2.5 Electrochemical techniques

2.5.1 Scanning Kelvin Probe, SKP

Advances have been made in the study kinetics and the mechanisms of corrosion in aqueous environments due to the development of scanning electrochemical techniques. SKP, had seen substantial developments and improvements in recent years. Which has in turn led to improved quantitative electrochemical investigations of FFC.[121] The major advantage of the scanning techniques over other electrochemical methods were their ability to spatially resolve localised corrosion. This allows quantification of the corrosion processes and information on corrosion rates instead of surface average information for the area exposed to testing. The techniques use a microtip, which is not in direct contact with the substrate under investigation, to measure quantities (potential gradient, potential, current) that relate to the amount of corrosion activity on the surface. Additionally, the surface under investigation is not affected and thus the scanning procedure can be repeated, allowing a study of the dynamic evolution of localized corrosion processes. The fact that the microtip is not in direct contact with the surface means that the data signals received from the microtip were often complicated and inferences must be made to interpret them.

SKP, has seen substantial developments and improvements which has led to improved quantitative electrochemical investigations of FFC. The major advantage of the scanning techniques over previous electrochemical methods are their ability to spatially resolve localised corrosion. This allows quantification of the corrosion processes and information on corrosion rates instead of surface average information for the area exposed to testing[1–3,121]. The technique uses a microtip, which is not in direct contact with the substrate under investigation, to measure quantities (potential gradient, potential, current) that relate to the amount of corrosion activity on the surface. Additionally, the surface under investigation is not affected and thus the scanning procedure can be repeated, allowing a study of the dynamic evolution of localised corrosion processes. Unfortunately, the fact that the microtip is not in direct contact with the surface means that the data signals received from the microtip are

often complicated and inferences must be made to interpret them. This has unfortunately occurred in this initial scan.

The schematic of the SKP is shown in Figure 2.5.1a. The Scanning Kelvin Probe measures the work function of a surface. The Work function is the minimum work required to extract an electron through a conducting phase to a surface. Under certain circumstances the work function is determined by the electrode potential and therefore the Kelvin probe can measure local electrode or corrosion potentials. These can then be used to produce a map of corrosion potentials existing on a surface. The major advantage of the SKP over SVET and many other electrochemical techniques is that it does not require either the presence of a bulk electrolyte, allowing the SKP to measure atmospheric corrosion that is occurring both in-situ and under intact organic coatings.

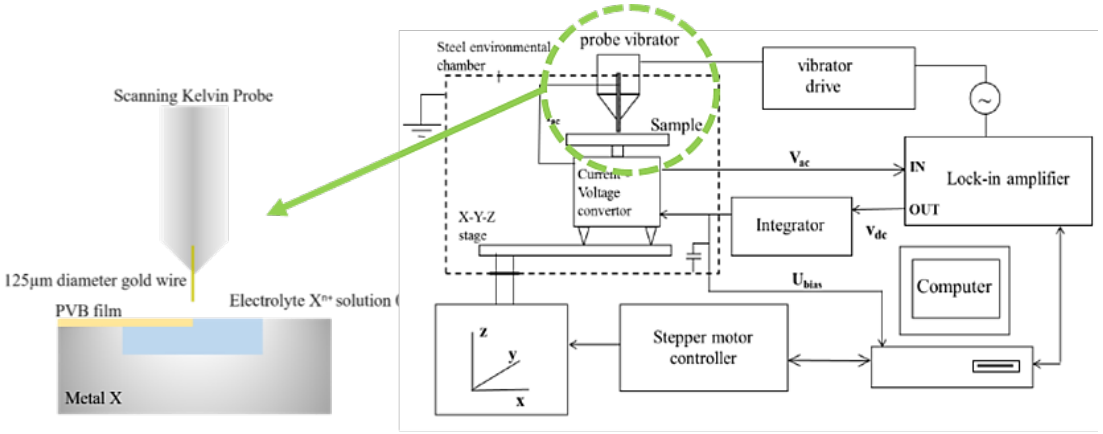

Figure [2.5.1a]: Schematic diagram showing the main components of a Scanning Kelvin Probe, SKP

This project used the SKP to study the mechanisms and kinetics of FFC as it has been used to find individual filament heads and their associated free corrosion potentials[169,209]Also, by repeatedly scanning in-situ it is possible to produce a series of time-dependent corrosion potential, E_{corr} maps. These provide information on the initiation of FFC and can be used to generate kinetic data associated with filiform propagation.[1,4,210]

Electrochemical polarisation measurements in dilute electrolyte solution and scanning Kelvin probe (SKP) measurements in humid air are used to demonstrate the free corrosion potential difference which exists between the surface deformed layer and the bulk alloy exposed by layer dissolution.

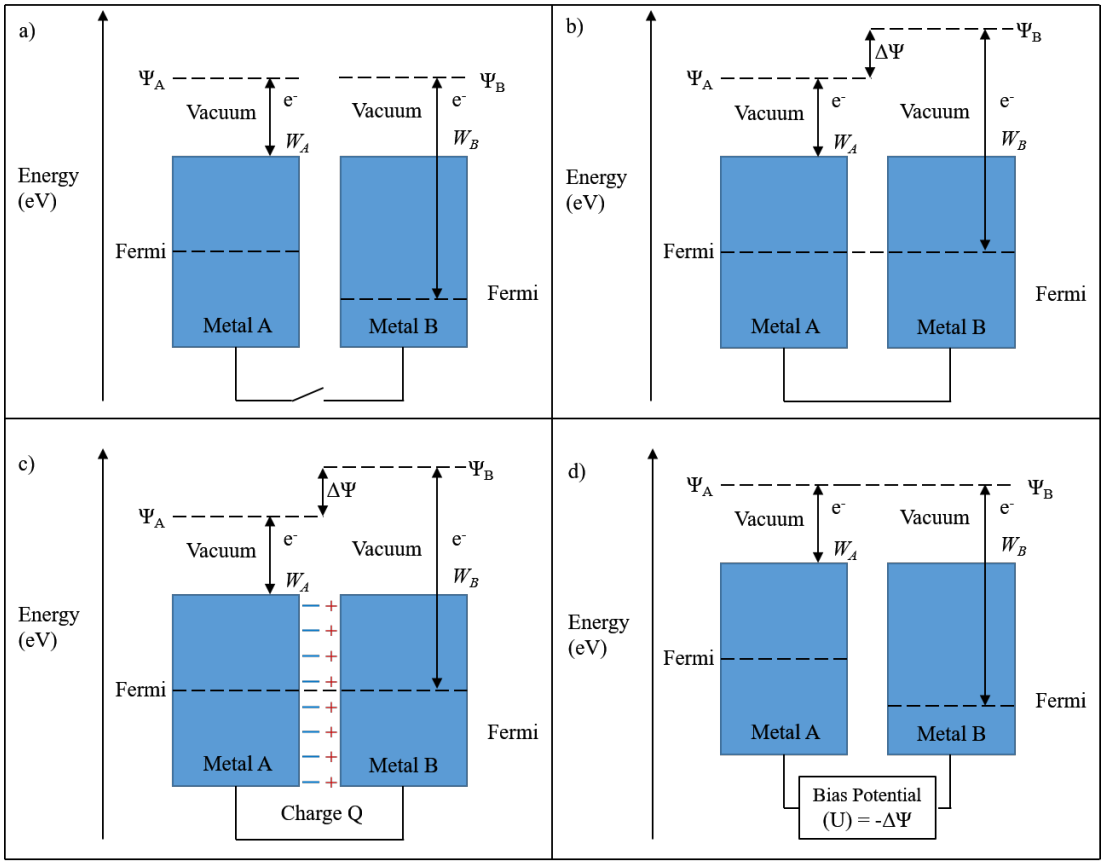

Figure 2.5.1b Schematic showing the mechanism to calculate the Volta potentials different, via an external bias potential

Figure 2.5.1b shows the schematic mechanism used to calculate the Volta potentials, via an external bias potential on a Scanning Kelvin Probe, SKP. The SKP investigates the effect of atmospheric conditions on metal surfaces, e.g., corrosion. It does not require the reference electrode to be immersed in electrolyte. It determines metallic work functions, W, minimum energy needed to remove electron from the Fermi level, to vacuum, and will produce data on the corrosion potential, E_{corr} with respect to the distance from the defect and the corrosion rate by using electrochemical mapping of localized corrosion that occurs beneath thin electrolyte films and polymer coatings.

The SKP measures the Volta potential difference, Δψ, between two metals, between two points, A, and B, in the vacuum, figure 2.5.1b, image c. Figure 2.5.1b, image d shows an external bias potential, U, is applied to the circuit until it equals the Volta potential difference, Δψ, (U = -ΔΨ). Volta potentials of the metals were now equal. ΔΨ can provide E_{corr} values by (A and B were determined via the calibration process):

$$E_{corr} = A + \Delta\psi \frac{Ref}{El} \qquad For\ Bare\ Metal \qquad [1]$$

Type equation here.

$$E_{corr} = B + \Delta\psi \frac{Ref}{Pol} \qquad For\ Polymer - Coated\ Metal \qquad [2]$$

SKP can use very small tips; useful when studying localised corrosion. It is non-perturbing; measurements were potentiometric. Potentials can be taken of surfaces covered in thin layers of electrolyte and films. The SKP resolution is limited to scan height and tip dimensions, as the height, and/or dimensions, of the tip increases, the resolution decreases because the potential gradient distribution at the surface spreads out and areas of dissimilar potentials can overlap. SKP does not detect electrical current directly; no corrosion rate data produced. Interpretation of the data can be difficult as additional potential differences can interfere with measurements. Galvanic coupling may occur if thick electrolytes were used or in the presence of low resistivity.

SKP Calibration and Setup

Potentiometric measurements were conducted using a 125µm diameter gold wire reference probe, vibrated normal to the sample surface at 280 Hz, with a 40µm peak-to-peak amplitude, and mid-amplitude probe–sample distance of 120µm, full details are found in previous work by Williams et al.[211] The SKP is calibrated using the technique described in previous work [1–5,212–214]:

Calibration of electrode potential is conducted using Ag/Ag^{+}, Cu/Cu^{2+}, Fe/Fe^{2+} and Zn/Zn^{2+} couples using an established procedure. Each metal is machine cut into discs measuring 15mm in diameter and a thickness of 5mm. Each disc consisted of a cavity which is 8mm in diameter with a depth of 1mm. During the calibration process, the cavity is filed with a 0.5 mol dm^{-3} aqueous solution of each of the respective metal-chloride salt. Once the readings became stable, the Volta potential difference, Ref/pol, is measured between the SKP reference probe and the surface. Additionally, the metal electrode potential is measured at the same time against the SCE (Standard Calomel Electrode). For a bare metal surface metal surface, film the free corrosion potential (E_{corr}) is found using equation [1]. For a metal surface coated in a hydrated PVB film the free corrosion potential (E_{corr}) is found using equation [2]. Calibration is repeated before and after each SKP experiment. All SKP measurement were carried out in static air at c.a. 20±1◦C % relative humidities relevant to each chapter.

The samples were placed in a thermostatic stainless-steel environment chamber, containing reservoirs of saturated salt solution to maintain the constant relative humidity dependant on the investigation requirements. The RH is monitored using a digital hygrometer, with a digital temperature sensor (Lascar's EasyLog EL-USB-2-LCD+)

SKP scans started immediately after the sample has been placed inside the chamber. The data produced by the scans is inputted into excel, and on occasion surfer software, to produce calibrated E_{corr} data and 2D E_{corr} potential maps.

2.5.2 Electrochemical measurements

Open circuit potential, OCP, and potentiodynamic polarisation were conducted on Gamry instruments interface 1010E, as shown in figure 2.5.2a and the software used is Gamry instruments version 7.8.4. All scans were setup as shown in figure 2.5.2b and 2.5.2c.

Figure 2.5.2a: Gamry instruments interface 1010E used to take open circuit potential, OCP, and potentiodynamic measurements

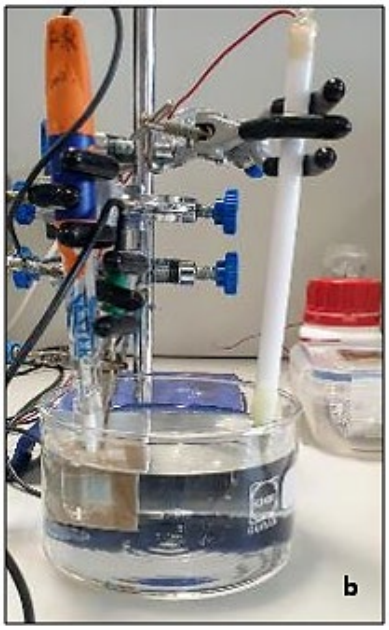

Figure 2.5.2b: photograph of setup

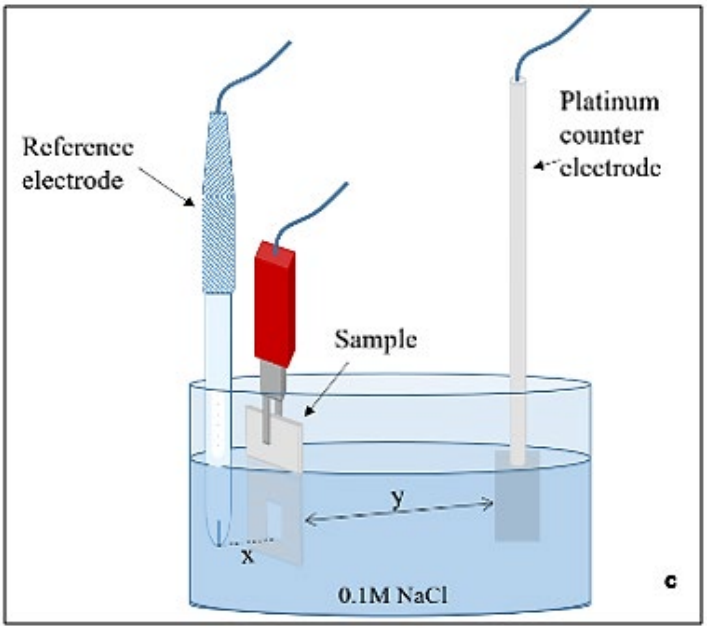

Figure 2.5.2c: diagram of setup.

- Samples were prepared as described in chapter 2.2.
- When required, the NSDL is reintroduced by manual abrasion using 180 grit silicon carbide paper/emery paper for 5 mins. The abrasion direction is orientated in the same direction as the rolling direction. Depending on whether the samples were to be aged or not, some samples were immediately used, zero aging, and others were left in an air environment at c.a. 20°C for the required time.
- The samples were taped with PTFE tape and a $1cm^2$ square is removed from the tape to expose a limited area of the sample.
- The samples were placed into a large cylinder with 0.1M sodium chloride solution, NaCl (aq) (CAS 7647-14-5):
- Referring to figures 2.5.2b and c, the sample is placed close to the reference electrode, where the bottom of the reference electrode is in-line with the bottom edge of the $1cm^2$ on the sample, as shown by 'x' in figure 2.5.2c.
- The sample is positioned at the furthest possible distance from the platinum counter electrode, as illustrated by 'y' in figure 2.5.2c.
- The electrodes and the sample were then connected to the Gamry interface.
- Open circuit potential, OCP, scans were set to run for 90 mins with potential measurements taken every 0.5s.
- The potentiodynamic experiments held the specimen at open circuit potential, OCP, for 90 mins prior to starting polarisation where a sweep rate of 1 mV/s is used.
- Cathodic potentiodynamic polarisation started at -0.9V vs SCE, in 0.1 M NaCl (aq) at pH 6.5, sweeping the applied potential in a positive direction at a rate of 1 mV/s.
- After completion of the experiment the data is converted to a format allowing results to be plotted in excel.

Dependent on the line of inquiry, the electrolyte is altered, as described in the relevant chapters.

2.6 Mechanical Deformation

During the car panelling process the sheet aluminium is cut, shaped and a folded hem is bent at each edge of the aluminium. Aluminium alloys provide “class-A” surface quality, meaning a freeform surface of high efficiency with ideal reflection quality[215].

Hemming is a mechanical joining process that uses plastic deformation to join the inner and outer panels together, whether on a door, bonnet, boot, roof, etc. Over time defect sites and/ or grain boundaries can form cracks. These cracks can propagate causing fractures along the apex of the hem. Although there have been studies regarding the bending of the AA6000 series, little is known about the surface deformation and performance[5,7–24].

Figure 2.6a shows how the mechanical deformation is achieved. The samples were cut so that part of the samples could be touched and manipulated into a bent sample, whilst the other part of the sample would remain untouched throughout to eliminate and shear forces on the surface. The samples were 50 x 15 mm^2. They were placed in a clamp with a lubricated pad to reduce friction and creating a NSDL (the section clamped is not used during the investigation, but precautions were still put in place), figure 2.6ai. Figure 2.6aii shows the inclusion of a 0.4 mm scalpel blade on the inner surface to bend the flange over. The flange is bent by applying a force to the top edge and pushing it over the blade. To create the shape shown in figure 2.6aiii, the sample is removed from the vice and wrapped in paper, to reduce shear forces, and placed back into the vice where the 2 short edges were pressed together to close the bend. The edge will not be investigated during the investigation. Figure 2.6b shows how the photographs were taken.

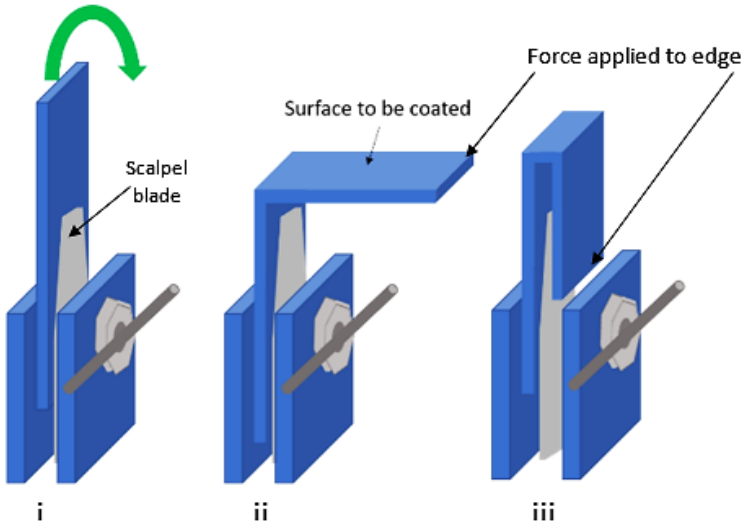

Figure 2.6a: a diagram of the bending technique used. i) Initial bending position in clamp with a scalpel blade on the inner surface. ii) Shows the flange being bent around the scalpel blade and iii) shows the flange in its final position.

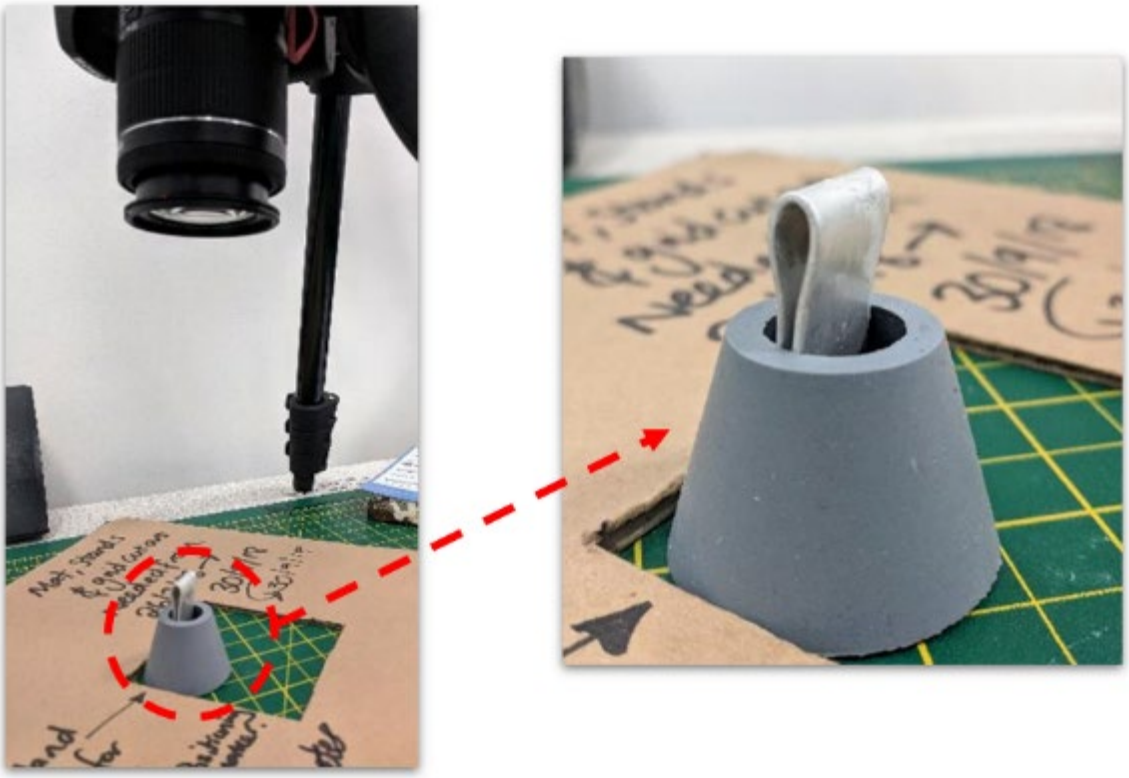

Figure 2.6b: how the images of the bent sample were taken

Chapter 3 - Understanding the surface potentials of AA6014 and AA6022 with and without a NSDL

3.1 Introduction

This chapter will investigate the kinetics and mechanism of filiform corrosion, FFC, on organically coated aluminium alloys AA6022 and AA6014 and determine the influence of surface preparation on the electrochemical behaviour of uncoated surfaces and the free corrosion potentials measured for both uncoated and organically coated surfaces. During the surface preparation of many aluminium alloys, especially involving abrasion and cold working and subsequent heat treatment, it is well known that a near surface deformed layer (NSDL) is formed, which has a significantly modified microstructure to the bulk[90,99,181,183,233–237]. This chapter will focus on whether NSDL formation affects the electrochemical behaviour of AA6022 and AA6014 alloy types and will seek to determine the influence this has on the susceptibility of FFC and its impact on the kinetics of FFC.

Previous work[3,5] found that abrasion of other 6000 series aluminium alloys, (AA6016 and AA6111) induces an NSDL which displays a more negative potential than the bulk alloy, with a potential difference between the NSDL and bulk alloy of ca. 0.2 V for AA6111, and between 0.2V to 0.5V for AA6016, after heat treatment at temperatures of up to 350°C. Additionally, PVB coated AA6000 series samples that had been scribed with a defect and injected with dilute aqueous HCl all showed signs of FFC. In the presence of a NSDL, a rapid superficial attack, surface-active FFC (*SA*-FFC), is observed in which the metal loss is limited to the thickness of the NSDL (i.e., approximately < 2μm). In the absence of a NSDL, a slower and deeper form of FFC is observed, known as successive-pitting FFC (*SP*-FFC). Successive pitting FFC has been found to occur on samples when either the NSDL has been removed during sample preparation, caustic etching, or once the NSDL has been removed during the surface active FFC process, as a secondary, slower, form of FFC[1–5,]. With both types of FFC, the appearance of the corroded surface is consistent with intergranular attack. Anodically activated intergranular attack could cause the NSDL to become sacrificial with respect to the bulk alloy and further contribute to the rate and driving force of the surface-active FFC as seen in previous work[1–5]. The work also found that localized

corrosion on the bulk metal displayed successive-pitting FFC features approximately 20 μm apart, similar to the grain size of the bulk alloy. In cases where surface-active FFC had occurred, metal dissolution seemed to be characterised by corrosion attack on a much smaller scale (approximately 0.1–1μm) [3,5].

The lower potentials and higher corrodibility due to the presence of a NSDL reported in these previous investigations are consistent with the NSDL being anodically activated relative to bulk AA6016 and AA6111. Furthermore, mechanistic schemes have therefore been proposed in which anodic activation to intergranular attack causes the NSDL to react sacrificially with respect to the bulk in these alloy types and contributes to the driving force for *SA*-FFC.

The aim of this chapter is to understand more about the changes in the electrochemical behaviour of AA6014 and AA6022 surfaces which have been mechanically abraded to induce an NSDL, when compared to specimens where the NSDL has been removed by alkaline cleaning. To this end the time-dependent variation of free corrosion potential is a corrosive electrolyte is used to follow the dissolution of the NSDL and potentiodynamic experiments are used to deduce the influence of the NSDL on the kinetics of both anodic dissolution and cathodic oxygen reduction. In addition, a scanning kelvin probe (SKP) is used to measure free corrosion potentials of model polymer coated surfaces, in the presence and absence of NSDL under atmospheric corrosion conditions at high relative humidity. Furthermore, SKP-derived potential distributions were also obtained for polymer coated specimens which are actively undergoing FFC after initiating corrosion by applying a controlled quantity of HCl to a penetrative scribed effect. Form previous work using AA6000 series alloys the presence of a NSDL will result in a more negative surface potential than the bulk alloy. The potential difference measured between NSDL and bulk surfaces for AA6014 and AA6022 will be compared to previously published findings. These experiments will also identify if there are a significant difference in the surface potentials for AA6014 and AA6022 which may act as a predictor of susceptibility towards enhanced rates of surface active FFC.

3.2 Experimental Details

3.2.1 Potentiostat Based Experiments

As discussed in chapter 2 the open circuit potential, OCP, and potentiodynamic polarisation were conducted on Gamry instruments interface 1010E, as shown in chapter 2 figure 2.5.2a and the software used is Gamry instruments version 7.8.4. All scans were setup as shown in chapter 2 Figure 2.5.2b and 2.5.2c.

Samples were prepared as described in chapter 2; Alkali cleaning of the samples in NaOH (10% w/v), for c.a. 45s at 60°C, to dissolve any aluminium oxide and any NSDL on the surface. Samples were rinsed with distilled water and acetone before acid desmutting using concentrated HNO_3 (15.6 molar) for 30s at 25°C to remove impurities such as copper and iron from the surface, and to passivates the surface. The samples were again rinsed with distilled water and acetone. Where required, the NSDL is reintroduced by manual abrasion using 180 grit silicon carbide paper/emery paper for 5 mins. The abrasion direction is orientated in the same direction as the rolling direction. Samples were rinsed with distilled water and acetone. Depending on whether the samples were to be aged or not, some samples were immediately used, zero aging, and others were left in an air environment at c.a. 20°C for the required time. The sample is taped with PTFE tape and a $1cm^2$ square is removed from the tape to expose a limited area of the sample. The samples were placed into a large cylinder with 0.1M sodium chloride solution, NaCl (aq). Referring to figures 2.5.2b and c, the sample is placed close to the reference electrode, where the bottom of the reference electrode is in-line with the bottom edge of the $1cm^2$ on the sample, as shown by 'x' in figure 2.5.2c. The sample is positioned at the furthest possible distance from the platinum counter electrode, as illustrated by 'y' in figure 2.5.2c. The electrodes and the sample were then connected to the Gamry interface.

The potentiodynamic experiments held the specimen at open circuit potential, OCP, for 90 mins prior to starting polarisation where a sweep rate of 1 mV/s is used. After completion of the experiment the data is converted to a format allowing plots of either Ecorr vs time or log i vs V to be plotted in excel.

3.2.2 SKP Experimentation

Scanning Kelvin Probe, SKP, investigates the effect of atmospheric conditions on metal surfaces, e.g., corrosion. It does not require the reference electrode to be immersed in electrolyte. It determines metallic work functions, Ψ, minimum energy needed to remove electron from the Fermi level, to vacuum, and will produce data regarding the corrosion potential, E_{corr}, with respect to the distance from the defect and the corrosion rate by using electrochemical mapping of localized corrosion that occurs beneath thin electrolyte films and polymer coatings. The SKP measures the Volta potential difference, Δψ, between the metal test specimen and the probe in the vacuum. An external bias potential, U, is applied to the circuit until it equals the Volta potential difference, Δψ, (U = -ΔΨ). Since the Volta potentials of the metals are now equal, ΔΨ can provide E_{corr} values by (A and B are constants which are determined experimentally via the calibration process):

$$E_{corr} = A + \Delta\psi \frac{Ref}{El} \qquad For\ Bare\ Metal \qquad [1]$$

Type equation here.

$$E_{corr} = B + \Delta\psi \frac{Ref}{Pol} \qquad For\ Polymer - Coated\ Metal \qquad [2]$$

A in equation in equation [1] is determined by simultaneous measurement of E_{corr} vs. a standard reference electrode and $\Delta\varphi \frac{Ref}{El}$ using the Kelvin probe. B in equation in equation [2] is determined by the simultaneous measurement of E_{corr} vs. a standard reference electrode and $\Delta\varphi \frac{Ref}{Pol}$, again using the Kelvin probe. Both sets of measurements are conducted using the calibration cell apparatus described in section 2.5.1.

Prior to the scan the samples were chosen for both AA6014 and AA6022. They were etched by the same process as described in chapter 2. Where required, the surface is abraded using 180 grit SiC paper to produce a NSDL or a 50:50 surface [no NSDL: NSDL] All samples undergoing FFC were coated with 15.5% w/w PVB. The bare samples were rinsed with acetone and D.I water prior to scanning.

Potentiometric measurements were conducted using a 125µm diameter gold wire reference probe, vibrated normal to the sample surface at 280 Hz, with a 40µm peak-to-peak amplitude, and mid-amplitude probe–sample distance of 120µm, full details are found in previous work by Williams, McMurray, and Worsley[211],. The SKP[1–5] is calibrated using the technique described in previous work [1–5,212–214].

Calibration of electrode potential is conducted using Ag/Ag^{+}, Cu/Cu^{2+}, Fe/Fe^{2+} and Zn/Zn^{2+} couples using an established procedure. Each metal is machine cut into discs measuring 15mm in diameter and a thickness of 5mm. Each disc consisted of a cavity which is 8mm in diameter with a depth of 1mm. During the calibration process, the cavity is filed with a 0.5 mol dm^{-3} aqueous solution of each of the respective metal-chloride salt. Once the readings became stable, the Volta potential difference, $\Psi_{Ref/pol}$, is measured between the SKP reference probe and the surface. Additionally, the metal electrode potential is measured at the same time against the SCE (Standard Calomel Electrode). For a bare metal surface metal surface, film the free corrosion potential (Ecorr) is found using equation [1]. For a metal surface coated in a hydrated PVB film the free corrosion potential (Ecorr) is found using equation [2]. Calibration is repeated before and after each SKP experiment.

All SKP measurement were carried out in static air at c.a. 20±1◦C and c.a.80% RH. The samples were placed in a thermostatic stainless-steel environment chamber, containing reservoirs of saturated salt solution, ammonium sulfate $(NH_4)_2SO_4$, to maintain the constant relative humidity of c.a. 80%. The RH is monitored using a digital hygrometer, with a digital temperature sensor (Lascar's EasyLog EL-USB-2-LCD+)

SKP scans started immediately after the sample has been placed inside the camber and scans will be repeated. The data produced by the scans were inputted into excel and surfer software to produce calibrated Ecorr data and 2D Ecorr potential maps.

3.3 Results and Discussions

3.3.1 Understanding the surface potentials of AA6014 and AA6022 with and without a NSDL using E_{corr} and polarisation curves for non-coated samples

All Samples for open circuit potential, OCP, and potentiodynamic polarisation were step up as described in Chapter 2. Open circuit potential, OCP, scans were set to run for 90 mins with potential measurements taken every 0.5s. Potentiodynamic polarisation scans were set to run from -0.9V to -0.1V with a scan rate of 1mV/s. AA6014 measured an average open circuit potential, OCP, of -0.67V, for samples with and without a NSDL. AA6022 measured an average open circuit potential, OCP, of -0.69V, for samples with and without a NSDL. Five tests of each sample, where used for the initial open circuit potential, OCP, investigations. Of the five samples, two did not have a NSDL, to show the potential of the bulk alloy, and three samples did have a NSDL. The three samples with a NSDL were allowed to age for different periods of time, at room temperature (c.a. 20°c), to see how this would affect the potential of the NSDL and the time taken to reach bulk potential. The results can be seen in figures 3.3.1a and 3.3.1b. Additionally, two samples of each alloy were used for the potentiodynamic scan, one without a NSDL and one with a NSDL. The results can be seen in Figures 3.3.1c to 3.3.1e.

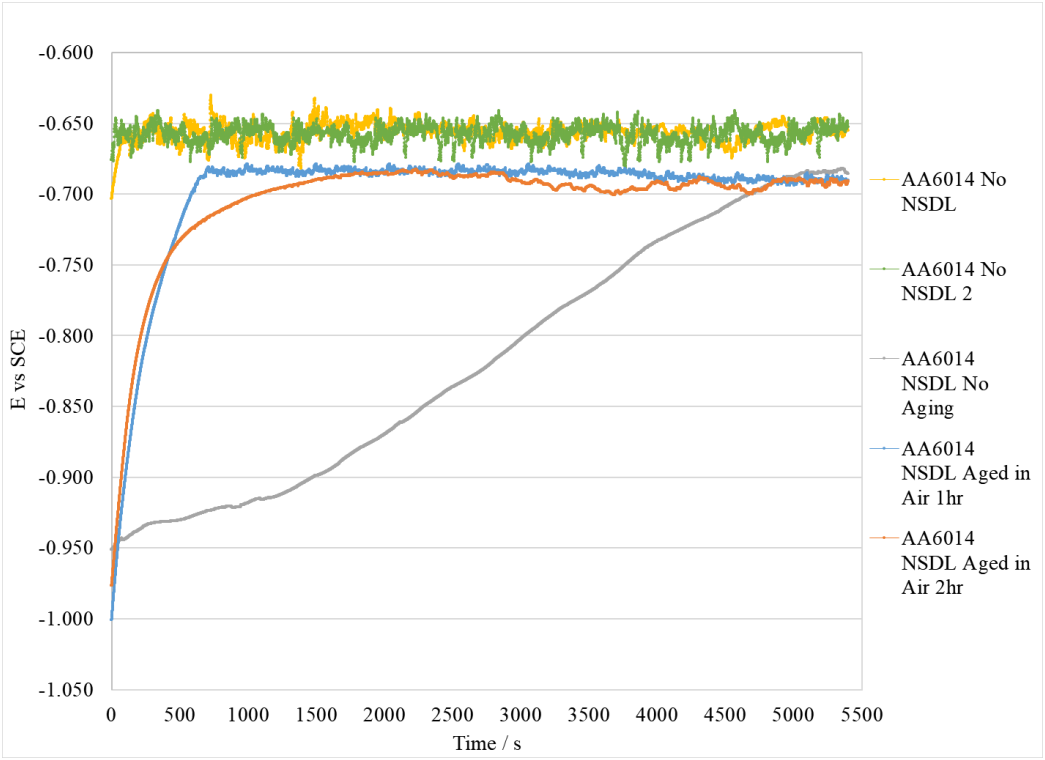

Figure 3.3.1a: Potentiodynamic polarisation scans of AA6014 open circuit potential, OCP, for no NSDL & NSDL at various aging times.

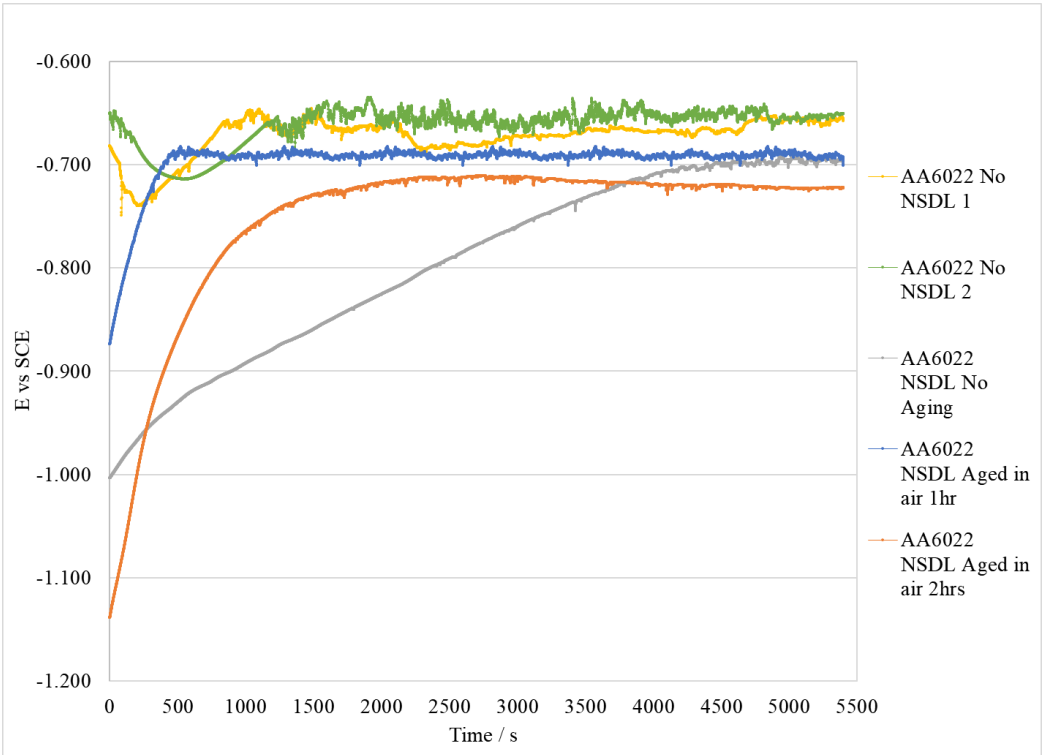

Figure 3.3.1b: Potentiodynamic polarisation scans of AA6022 open circuit potential, OCP, for no NSDL & NSDL at various aging times.

Overall, the results shown that for both alloys, the free corrosion potential of the alkaline cleaned (bulk) specimens is relatively constant over the 90 min immersion period. In the 0.1 mol/L electrolyte used, the Ecorr value established for the "bulk" AA6014 seems marginally more positive than that for the AA6022. The average open circuit potential, OCP, for AA6014, figure 3.3.1a, without a NSDL (Bulk metal) is -0.658V (sample 1) and -0.656V (sample 2) therefore of -0.657V for the two samples with a standard deviation of 0.0065V. The average open circuit potential, OCP, for AA6022, figure 3.3.1b, without a NSDL (Bulk metal) is -0.673V (sample 1) and -0.662V (sample 2) therefore an average potential of -0.668V (3dp) and a standard deviation of 0.0194V. The slightly more positive E_{corr} for AA6014 could be attributed to the slightly higher Cu content (≤0.25 for AA6014 and 0.01 to 0.11 for AA6022) however the Mg content is almost the same (0.4 to 0.8 for AA6014 and 0.4 to 0.7 for AA6022) so is unlikely to cause this rise in potential.

When a NSDL is present on AA6014 samples (figure 3.3.1a), initially the potential is significantly lower, -0.951V, -1.000V and -0.977V for no aging, 1 hour aging and 2-hour aging, respectively. They have an average initial potential of -0.976V and a standard deviation of 0.0245V. With zero aging samples with a NSDL take over 5000s (approximately 83 minutes) to stabilise and become close to the bulk potential (c.a. -0.682V at its lowest potential, a difference of 0.025V to the bulk metal). When the samples with a NSDL are allowed to age, the time taken for the surface potential to reach near bulk potential significantly decrease to 500s (8.3 mins) to 1500s (25 mins). In the results shown, the sample that has for 1 hour reaches the more stable potential quicker than the sample that has aged for 2 hours. Again, the aged samples never reach the bulk metal potential, but all the samples with a NSDL do reach a similar potential when they plateaux.

When a NSDL is present on AA6022 samples (figure 3.3.1b), initially the potential is significantly lower, -1.000V, -0.874V and -1.140V for no aging, 1 hour aging and 2-hour aging, respectively. They have an average initial potential of -1.005V and a standard deviation of 0.1325V. AA6022 appears to be less consistent, whether a NSDL is present or not, when compared to the values for AA6014. With zero aging the sample with a NSDL take approximately 4500s (approximately 75 minutes) to stabilise and become close to the bulk potential (c.a. -0.683V at its lowest potential, a difference of 0.015V to the bulk metal). When the samples with a NSDL are allowed to age, the

time taken for the surface potential to reach near bulk potential decrease to 500s (8.3 mins) to 2000s (41 mins). In the results shown, the sample that has for 1 hour reaches the more stable potential quicker than the sample that has aged for 2 hours, the same result as AA6014. However, the AA6022 does differ from AA6014 as the zero aged and 1hr aged reach a similar plateaux potential, however, the 2hr aged sample reaches a lower potential plateau of -0.711V with a difference to the bulk of 0.043V. Again, the aged samples never reach the bulk metal potential.

The open circuit potential, OCP, graphs show that, on average there is a difference in the initial potentials of 0.319V for AA6014 and 0.377V AA6022, when comparing surfaces with and without a NSDL. Which would suggest that AA6022 should have a greater corrosion rate than AA6014. The larger the potential difference the quicker the corrosion rate. The aging affect is interesting and one that could be investigated further as the results above show it has a significant effect on the surface potential.

Following the open circuit potential, OCP, versus time plots, the two alloys underwent cathodic potentiodynamic polarisation starting at -0.9V vs SCE, in 0.1 M NaCl (aq) at pH 6.5, sweeping the applied potential in a positive direction at a rate of 1 mV/s. Results are shown in figures 3.1.2c, 3.1.2d and 3.1.2e

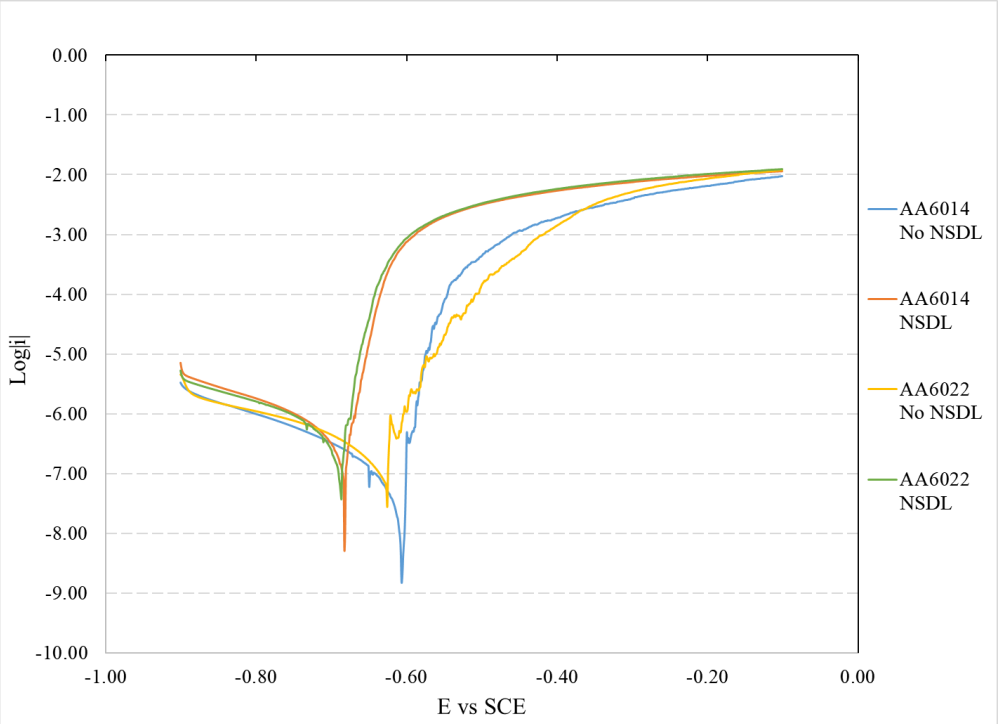

Figure 3.3.1c: Potentiodynamic polarisation scans for both AA6014 and AA6022 with and without a NSDL in 0.1 M NaCl (aq) at pH 6.5, sweeping at a rate of 1 mV/s

The free corrosion potential, E_{corr}, for AA6014 without a NSDL was -0.606V. When a NSDL was present the E_{corr} dropped to -0.682V, a difference of 0.076V. For AA6022 samples, the sample without a NSDL was -0.625V, whereas the sample with a NSDL dropped to -0.686V, with a difference in E_{corr} of 0.061V. AA6022 measured lower E_{corr} values for samples with and without a NSDL, compared to AA6014. Samples without had a difference in E_{corr} of 0.19V, however samples with a NSDL only had a difference in E_{corr} of 0.004V.

The bulk alloy, the AA2022 has a more negative Ecorr than the AA6014. In the presence of an NSDL, Ecorr is shifted in a more negative direction by about 0.06 – 0.08V. The difference between bulk-NSDL is lower in these experiments because they are being polarised at more negative potentials than E_{corr} to start. This might dissolve away some of the NSDL because the product of the cathodic reaction is OH^-, giving elevated pH which would activate an amphoteric surface layer. Or the NSDL specimens have aged so that immersion in NaCl for a few min before starting the experiment would be sufficient for some to dissolve away.

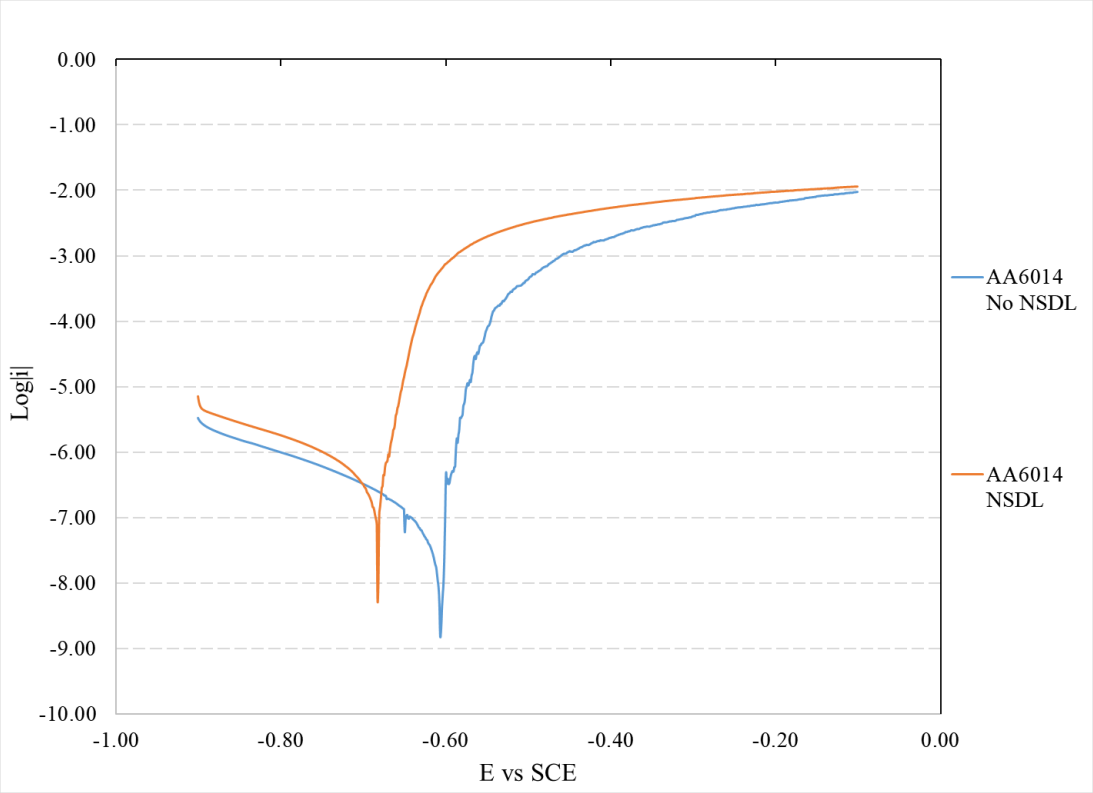

Figure 3.3.1d Potentiodynamic polarisation scans for AA6014 with and without a NSDL in 0.1 M NaCl (aq) at pH 6.5, sweeping at a rate of 1 mV/s

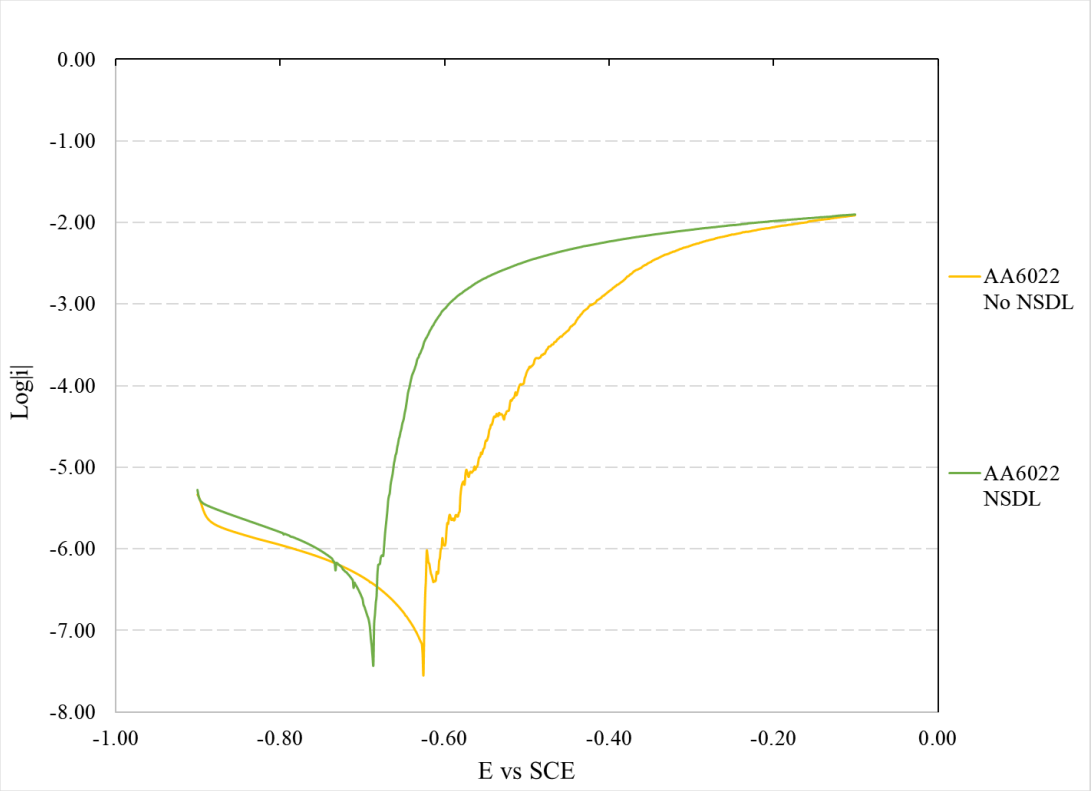

Figure 3.3.1e: Potentiodynamic polarisation scans for AA6022 with and without a NSDL in 0.1 M NaCl (aq) at pH 6.5, sweeping at a rate of 1 mV/s

The potentiodynamic polarisation, figures 3.1.2c to 3.1.2e, for AA6014 and AA6022 show that the Ecorr for the samples with a No NSDL are -0.606V and -0.625V, respectively. A difference of 0.019V, with standard deviation of 0.0134V. The open circuit potential, OCP, versus time plots, show that the average potential values for AA6014 and AA6022 were -0.657V and -0.668V, respectively. This difference between the two bulk metal samples is possibly due to their composition.

The potentiodynamic polarisation for AA6014 and AA6022 show that the Ecorr for the samples with a NSDL are similar, -0.682V and -0.686V, respectively. A difference of 0.004V, with standard deviation of 0.0028V. The open circuit potential, OCP, versus time plots, show that the lowest values at plateaux for AA6014 and AA6022 were -0.682V and -0.683V, respectively. This suggests that the presence of a NSDL provides a similar Ecorr value regardless of composition (within the same alloy group, i.e., AA6xxx)

Figures 3.3.1d and 3.3.1e compare the polarisation curves for AA6014 and AA6022 respectively in the presence and absence of NSDL, whereas figure 3.3.1c includes all

curves. For both alloys the cathodic branches show little difference in the magnitude of the observed net cathodic current. The Tafel slopes are also similar (Around 200 – 250 mV per decade of current). Therefore, the presence of the NSDL appears to have little influence on the cathodic reaction, (oxygen reduction, $A1^{3+} + 3OH^- \rightarrow Al(OH)_3$ and/or $Al_2O_3 + H^+$ evolution). If the measured current density values at an applied potential of -0.8V are compared, then the NSDL specimens produce a marginally higher net cathodic current density compared to the bulk. For AA6022, the bulk current density is c.a. $1x10^{-6}$ A/cm^2, compared to c.a. $2x10^{-6}$ A/cm^2 for the NSDL), the same is true for AA6014, the bulk current density is c.a. $1x10^{-6}$ A/cm^2, and c.a. $2x10^{-6}$ A/cm^2 for the NSDL.

There are however significant differences in the anodic behaviour of the NSDL bearing samples compared to the bulk alloy. The net anodic current density values measured over the -0.7 to -0.3 V range are markedly higher than for the alkaline etched surfaces. For example, comparing NSDL and bulk for AA6022, but at a potential of -0.5V; bulk is c.a. $1x10^{-4}$ A/cm^2, whereas NSDL is c. a. $3x10^{-3}$ A/cm^2. Similar increase is also observed for AA6014; bulk is c.a. $4x10^{-4}$ A/cm^2, whereas NSDL is c. a. $3x10^{-3}$ A/cm^2.

Again, the behaviour is consistent with abrasion producing a highly anodically susceptible surface layer. The greater increase in anodic current density values for NSDL compared to bulk for AA6022 suggests that the surface layer may be more reactive for this alloy.

The potentiodynamic polarisation show that, on average there is a difference in Ecorr of 0.075V for AA6014 and 0.061V AA6022, when comparing surfaces with and without a NSDL. This would suggest that the AA6014 should have a quicker corrosion rate than the AA6022, which is contrary to the open circuit potential, OCP, results. The driving force for anodic dissolution is greater for the 6014 alloy and as a result it would be expected that it would be dissolve more rapidly. However the E_{corr}-time plots suggest that the NSDL on 6022 is removed more easily. However, this doesn't take into account the relative thicknesses on the NSDL layer. The $E_{NSDL} - E_{bulk}$ difference might be greater for the 6014 alloy, but if the layer is also thicker then it will take longer dissolve away despite the greater driving force.

When an NSDL is present, for both alloys, the starting Ecorr is significantly more negative than observed for the bulk specimens. However, this rises progressively with

time, eventually equilibrating at potentials close to -0.7 to -0.65 over the duration of the 90 min immersion experiments. It was noted that when the NSDL specimens were immersed immediately after grinding, E_{corr} increased more slowly than sample which had been left in lab air for various times before starting experimentation. When specimens were stored in air for various times post abrasion, their OCP transient behaviours changed. Investigating this ageing effect showed that longer ageing times promoted significantly faster rates of E_{corr} increase after immersion. The results suggest the following:

1. The significantly more negative starting E_{corr} values observed after grinding is consistent with an anodically activated NSDL which the rapidly corrodes, leading to an increase in E_{corr} up to a point where the underlying bulk surface is exposed. At this point, the E_{corr} becomes relatively constant and similar to values established for alkaline cleaned surfaces (in the absence of NSDL)
2. The transient behaviour of E_{corr} provides a convenient means of following the dissolution of the NSDL for both alloys, where the time at which a constant potential is reached signifies the point when all the NSDL has been removed. It is possible that the ageing changes the NSDL layer thickness. It is possible that the original nano-grained structure changes with time, due to grain growth/aggregation, leaving only the outermost part of the NSDL remain the same as when it was originally generated.

3.3.2 Understanding the surface potentials of AA6014 and AA6022 with and without a NSDL using SKP analysis

Initial scans were conducted on bare metal samples. The samples chosen were prepared using process described in chapter 2. The surface was abraded using 180 grit SiC paper to produce a NSDL parallel to the rolling direction. The bare metal will consist of a 50:50 [no NSDL: NSDL] surface, see figure 3.3.2a. The half abraded bare alloy specimens were chosen to establish free corrosion potential differences between the NSDL and the bulk under atmospheric corrosion conditions, where only a thin film of adsorbed water will be present. This will also show if the results correspond or contradict with the OPEN CIRCUIT POTENTIAL, open circuit potential, OCP, and potentiodynamic scan results. Previous attempts with coated samples in the SKP resulted in a build-up of corrosion product and slight delamination at the defect sites which came into contact with the SKP tip. This caused the tip to become over-loaded and produce feedback affecting the result. Trying to account for the height of the tip to eliminate this issue led to poor signal to the tip to map the surface potential effectively.

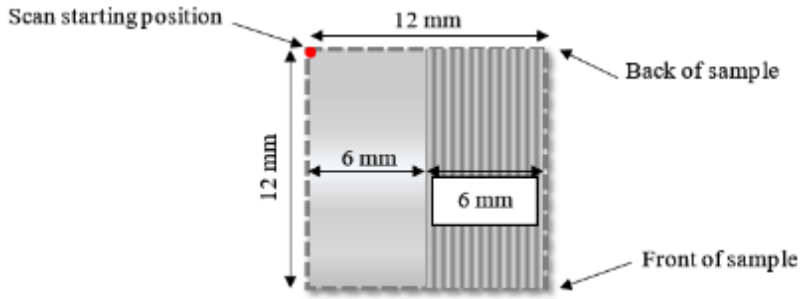

Figure 3.3.2a: sample setup for SKP with SKP starting position

The scans consist of the following samples:

1. AA6014 c.a. 50:50 [no NSDL: NSDL] with no PVB coating & no FFC initiation.
2. AA6022 c.a. 50:50 [no NSDL: NSDL] with no PVB coating & no FFC initiation.

The second set of scans were also prepared using process described in chapter 2. When required, the surface was abraded using 180 grit SiC paper to produce a NSDL parallel

to the rolling direction, this time covering the whole of the surface in a NSDL. The coupons were rinsed with distilled water and acetone prior to coating and were coated with 15.5% (w/w) ethanolic PVB solution to produce an air-dried PVB coating of thickness 30µm ± 5µm. 10mm defects were scribed through the PVB layer normal (90°) to the rolling/NSDL direction with a scalpel [3,4] with defects positioned c.a. 13mm apart[5]. FFC was initiated by injecting the scribe with 1µL of 2M aqueous hydrochloric acid using a glass micro-capillary dispenser. The HCl injection method was intended to create greater reproducibility than methods involving full sample exposure either by salt fog, HCl vapour, or immersion in aqueous electrolyte. [3,4]

The scans consist of the following samples:

1. AA6014 no NSDL with PVB coating & FFC initiation.
2. AA6014 NSDL with PVB coating & FFC initiation.
3. AA6022 no NSDL with PVB coating & FFC initiation.
4. AA6022 NSDL with PVB coating & FFC initiation.

The SKP[1–5] was calibrated using the technique described in previous work, in section 3.2.2 above, and in chapter 2 and setup ready to use as described in chapter 2. Potentiometric measurements were conducted using a 125 µm diameter gold wire reference probe, vibrated normal to the sample surface at 280 Hz, with a 40 µm peak-to-peak amplitude, and mid-amplitude probe–sample distance of 120 µm, as used in previous work[3,214]. All SKP measurement were carried out in static air at 20 ±1°C and 80% RH. The RH was monitored using a digital hygrometer, with a digital temperature sensor (Lascar's EasyLog EL-USB-2-LCD+). The sample to be scanned was placed in a thermostatic stainless-steel environment chamber, containing a reservoir of saturated salt solution, Ammonium Sulfate $(NH_4)_2SO_4$.

Once the SKP was calibrated and setup, scans started immediately after the sample has been placed and sealed inside the camber. The scans were repeated continuously with the final scans taken at 15 hours (AA6014) and 13 hours (AA6022). Each scan measured the potential over a 12 mm^2 area. The starting point of the scan was at the top left-hand corner of the 12 m^{m2} which was 6 mm away from the surface interface, See figure 3.3.2a. When the final scan finished, the samples were photographed in room air.

Values of $\Delta\Psi\frac{Ref}{Pol}$ obtained through the scans were used in equations [1] and [2], along with calibration values, to calculate the Ecorr across the surface of the scans and used in excel and surfer software to produce the graphs and images in sections 3.3.2.1 and 3.3.2.2. The data produced by the scan was inputted into excel and run through surfer software to produce calibrated E_{corr} data and 2D greyscale image maps showing the E_{corr} distribution over the scanned surface.

3.3.2.1 SKP for samples without a PVB coating, therefore no FFC initiated

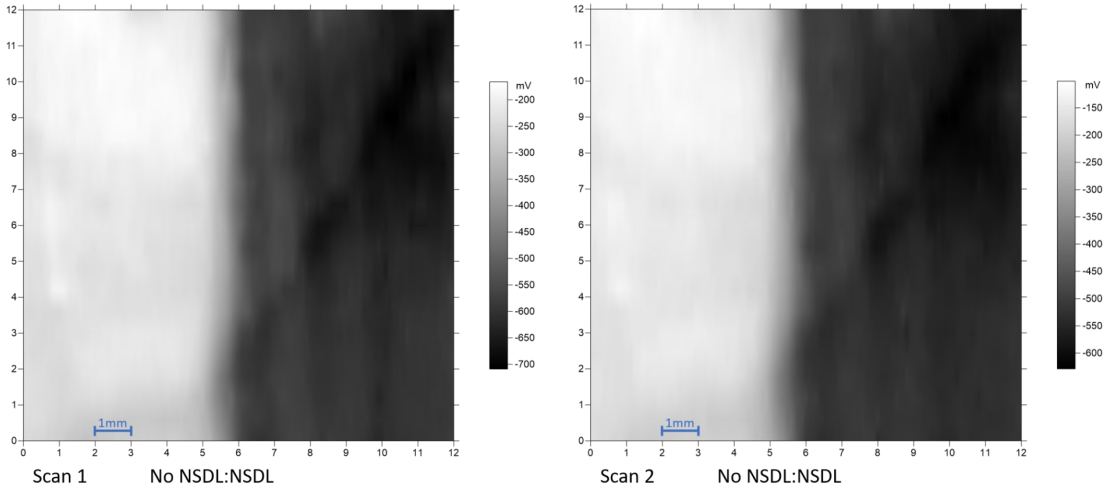

Figure 3.3.2.1a: Surface potential scans for AA6014; scan 1 at 0.6hrs and scan 2 at 14.92hrs, produced using Surfer software.

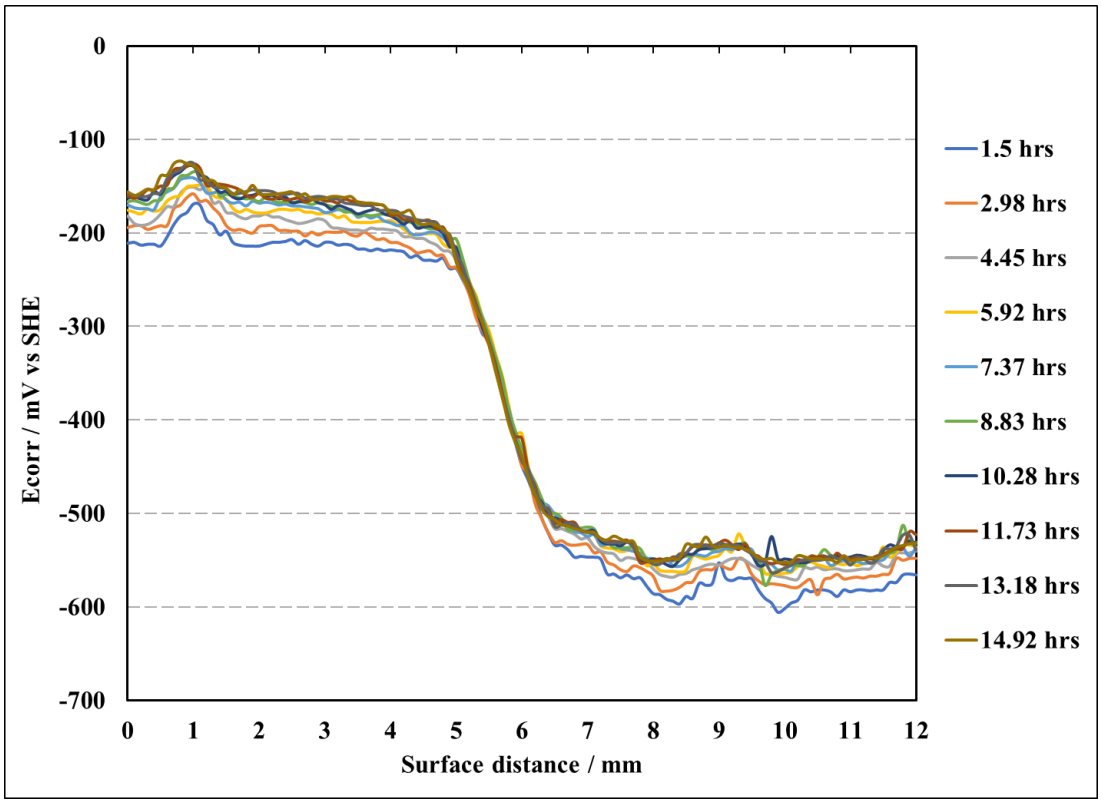

Figure 3.3.2.1b: SKP Electropotential SKP Electropotential profiles of SKP-derived E_{corr} versus distance recorded in humid air over a bare AA6014 alloy surface where the right-hand side has been abraded to form a NSDL.

The surfer images for AA6014, figure 3.3.2.1a, show the full surface potential during the initial and final scan, respectively. The images show a scan region of 12 mm^2. The scans show a stable and consistent potential for both regions of the sample and the clear difference between the 2 regions, noted above.

The graph (figure 3.3.2.1b) shows that when AA6014 is placed in these atmospheric corrosion conditions there is large potential difference between the section of the sample with no NSDL (LHS of the graph), an average potential of -183 mV (-0.183 V) compared to the section where a NSDL was present (RHS of the graph), an average potential of -548 mV (-0.548 V). The presence of a NSDL produces a more negative potential compared to the surface without the NSDL, on average there was a potential difference of 365 mV (0.365 V). The standard deviation across the scans were found to be 22.7 mv (0.023V) when no NSDL is present and 15.9 mv (0.016 V) when the NSDL was present.

When comparing the open circuit potential, OCP, scan for the two surfaces, the open circuit potential, OCP, , for AA6014 no NSDL had a potential of -0.657V, and the open circuit potential, OCP, for AA6014 NSDL had a potential of -0.976V, giving a difference of 0.319V. The potentials for the open circuit potential, OCP, differ quite considerably to that of the SKP scans. However, the difference between the two types of potential scans is not too dissimilar. They show that there is a potential difference between a NSDL and the bulk layer of at least 0.3V. The potential difference between the NSDL and the bulk metal could be why rates of corrosion and types of corrosion differ depending on the surface layer. Work conducted on AA6016[2,3] and AA6111[5,214] found that the presence of a NSDL reduces the open circuit potential, OCP, by more than 0.2V. One paper on AA6016[3] found that for temperatures up to 180°C the potential difference (ΔE_{intact} = E_{intact} surface deformed, E_{intact} bulk) is ca. − 0.2. Upon raising the temperature to 350°C, the potential different was measured to be c.a. -0.5V. Another paper found that regardless of heat treatment, AA6016 specimens with a NSDL produced a potential difference of c.a. -0.5V. Work conducted on AA6111[5] also found that the presence of a NSDL lowered the potential difference by more than -0.2V. This would put potential difference of AA6014 in line with that of AA6016 and AA 6111.

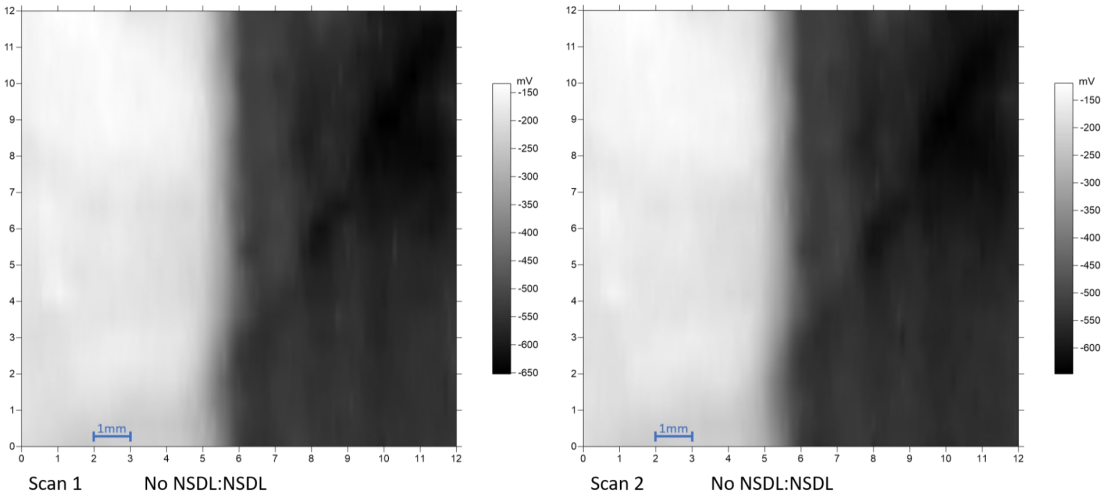

Figures 3.3.2.1c: Surface potential scans for AA6022; scan 1 at 1.14 hrs and scan 2 at 12.57 hrs, produced using Surfer software.

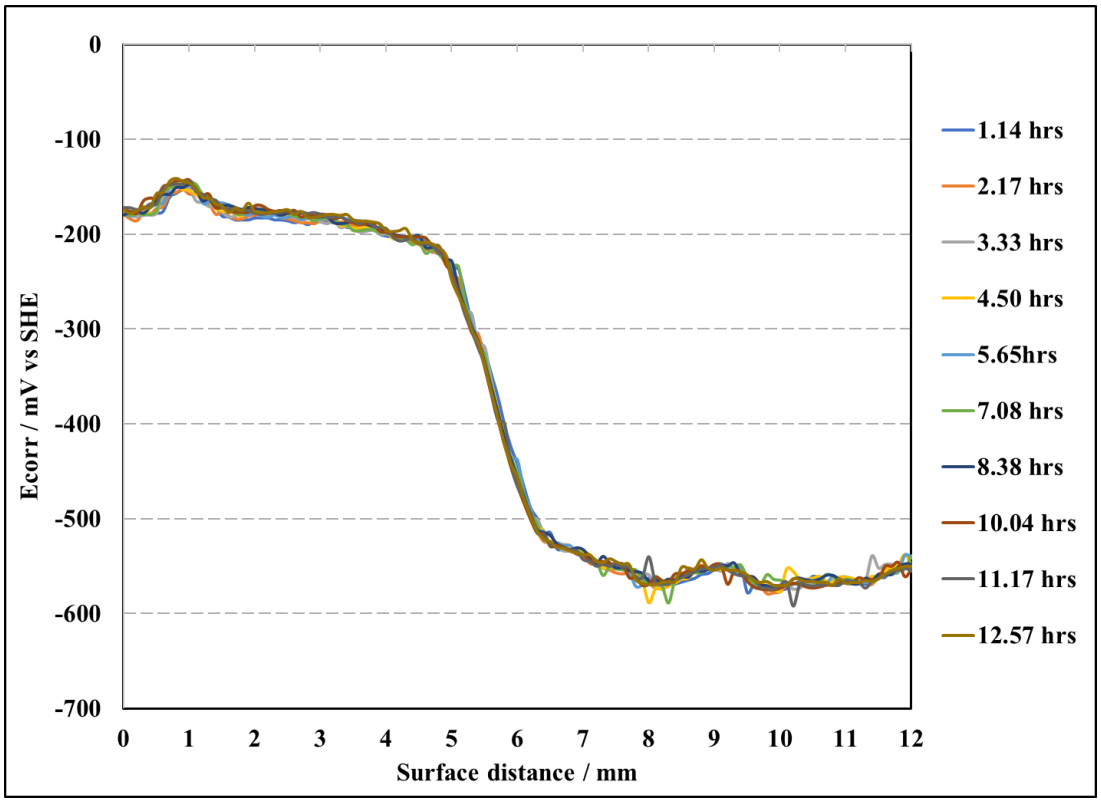

Figure 3.3.2.1d: SKP Electropotential profiles of SKP-derived E_{corr} versus distance recorded in humid air over a bare AA 6022 alloy surface where the right-hand side has been abraded to form a NSDL.

The surfer images, figures 3.3.2.1c, show the full surface potential during the initial and final scan, respectively. The images show a scan region of 12 mm^2. The scans show a stable and consistent potential for both regions of the sample and the clear difference between the 2 regions, noted above.

The graph (figure 3.3.2.1d) shows that when AA 6022 is placed in these atmospheric corrosion conditions there is large potential difference between the section of the sample with no NSDL (LHS of the graph), an average potential of -189 mV (-0.189 V) compared to the section where a NSDL was present (RHS of the graph), an average potential of -552 mV (-0.552 V). The presence of a NSDL produces a more negative potential compared to the surface without the NSDL, on average there was a potential difference of 363 mV (0.363 V). The standard deviation across the scans were found to be 15.1 mv (0.015V) when no NSDL is present and 8.87 mv (0.009 V) when the NSDL was present.

When comparing the open circuit potential, OCP, scan for the two surfaces, the open circuit potential, OCP, for AA 6022 no NSDL had a potential of -0.668V, and the open circuit potential, OCP, for AA 6022 NSDL had a potential of -1.005V, giving a difference of 0.337V. The potentials for the open circuit potential, OCP, differ quite considerably to that of the SKP scans. However, the difference between the two types of potential scans is not too dissimilar. They show that there is a potential difference between a NSDL and the bulk layer of at least 0.3V. The potential difference between the NSDL and the bulk metal could be why rates of corrosion and types of corrosion differ depending on the surface layer. As mentioned earlier, Work conducted on AA 6016[2,3] and AA 6111[5,214] found that the presence of a NSDL reduces the open circuit potential, OCP, by between 0.2V to 0.5V. This would also put the open circuit potential, OCP, measurements for AA 6022 in line with that of AA 6016 and AA 6111.

3.3.2.2 SKP for PVB coated samples with FFC initiated

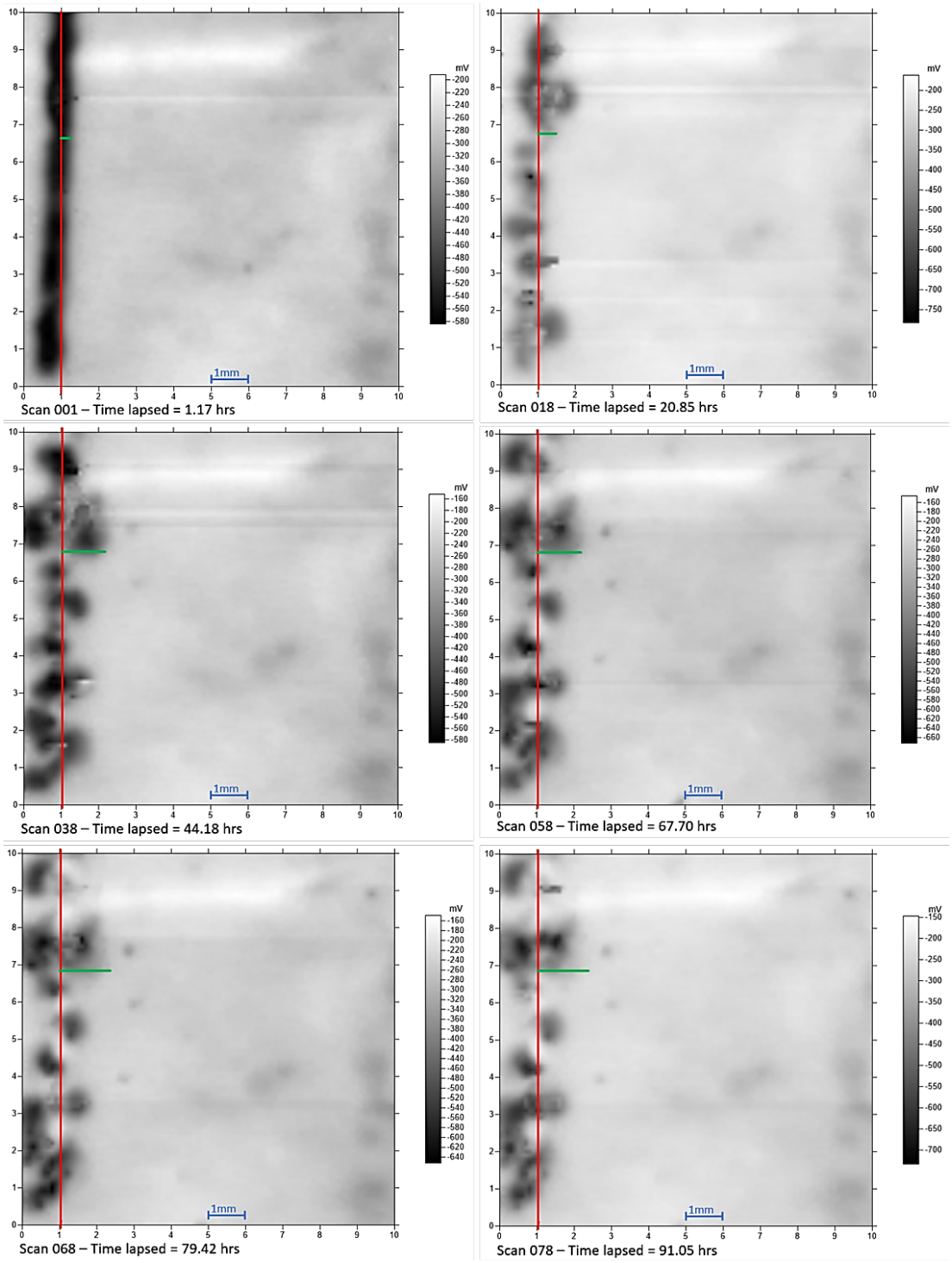

Figure 3.3.2.2a: Selection of scans of AA6014 with no NSDL and FFC initiated by 1µL of 2M HCl_{aq}, produced using Surfer software.

Across the scans, figure 3.3.2.2a, the corrosion area fluctuated in potential as well as increase in size. The fluctuation of potential suggests that the site has changes in its

chemical activity due to the corrosion mechanism producing both positive and negative ions. The images suggest that there is some development of SP-FFC over the first 50 hours, but thereafter any further progress is slow. A lower potential is observed after the corrosion zone.

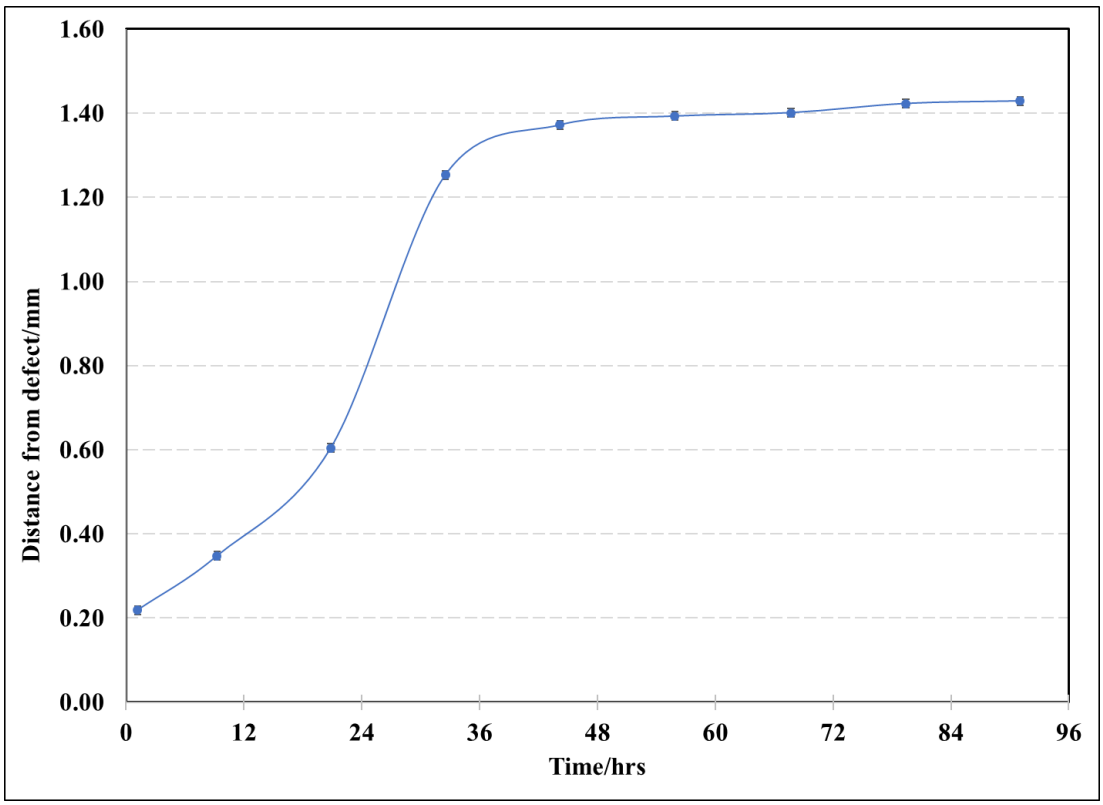

Figure 3.3.2.2b: Distance of corrosion from the defect, following the same point line over the duration of the scan for AA6014 with no NSDL and FFC initiated by 1µL of 2M HCl_{aq}

Figure 3.3.2.2b shows the distance of corrosion from the edge of the defect, following the same point line over the duration of the scan with an uncertainty of ±0.01mm. The graph shows that there is corrosion growth for the first 35 hours, however, over the first 35 hours the rate of corrosion starts to decrease. After 35 hours the distance of corrosion growth from the defect increases by small amounts and the rate of corrosion is continuing to decrease.

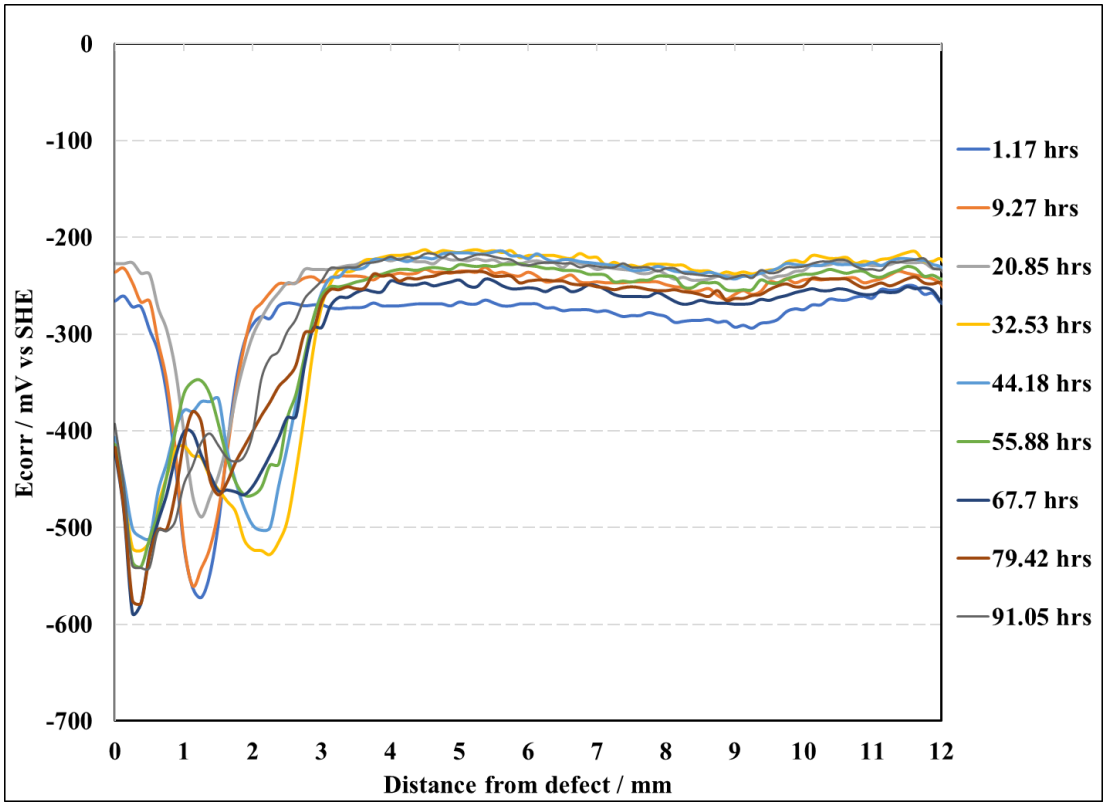

Figure 3.3.2.2c: Ecorr data for a selection of scans of AA6014 with no NSDL and FFC initiated by 1µL of 2M HCl_{aq}

The scans in figure 3.3.2.2c show the lowest potential at, and around, the defect edge. The negative potential surrounding the scribed defect is uniform, from c.a. 3mm, but within a 10 h the regions separate, between 0 to 3 mm (as discrete FFC heads from) which then move further underneath the PVB layer and start to move progressively further away from the scribe. A standard deviation of c.a. 97mv was measured between 0 and 3 mm. Around c.a. 3 mm the results show a less negative, and more stable, potential, with a standard deviation of c.a. 18mV.

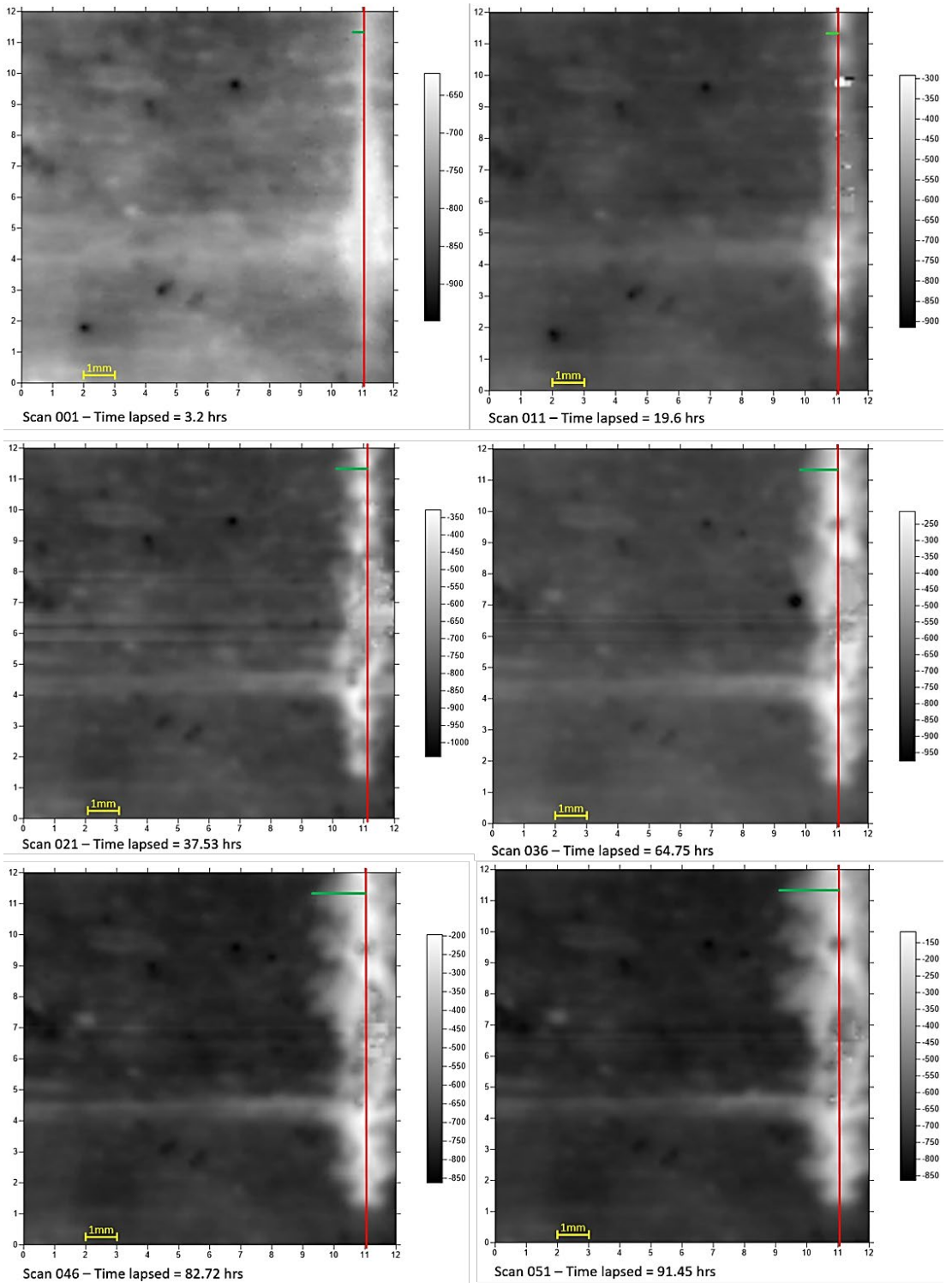

Figure 3.3.2.2d: Selection of scans of AA6014 with a NSDL and FFC initiated by 1µL of 2M HCl_{aq}, produced using Surfer software.

The scans in figure 3.3.2.2d have a red marker line for the defect and a green line indicating the corrosion distance measured across the scans, relative to the defect

marker line. Across the scans the corrosion area shows fluctuations in surface potential. The fluctuation of potential suggests that the site has changes in its chemical activity due to the corrosion mechanism producing both positive and negative ions.

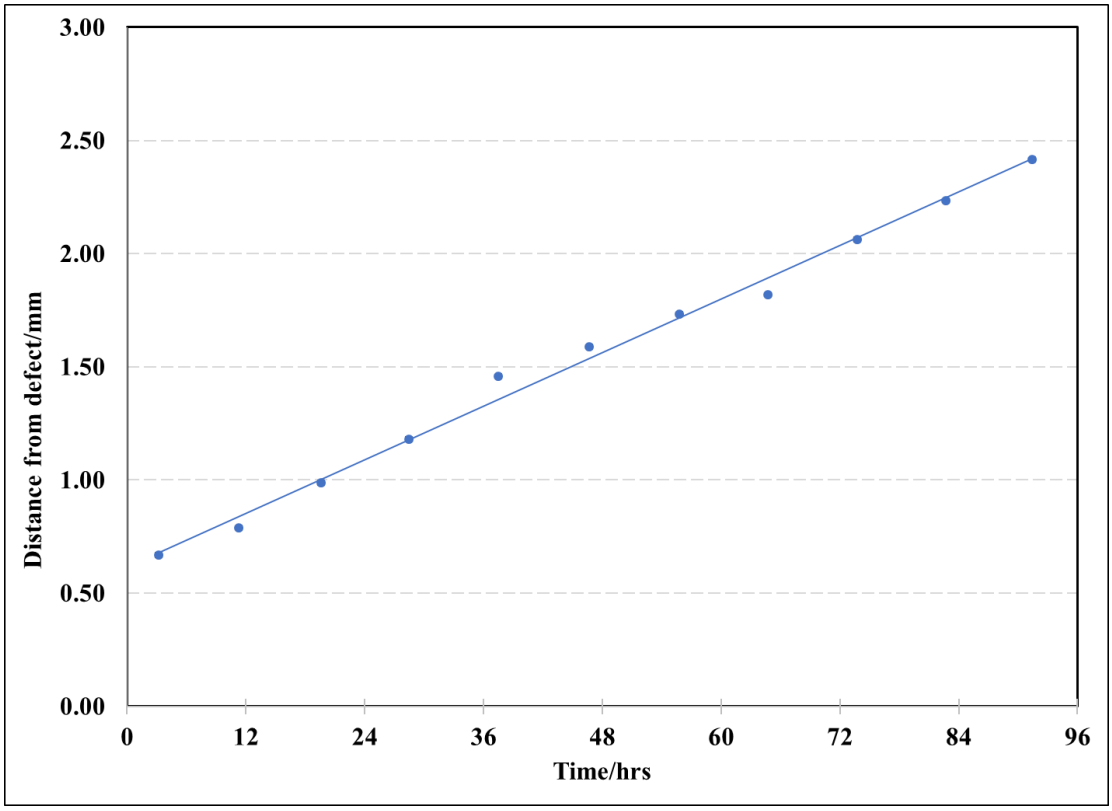

Figure 3.3.2.2e: Distance of corrosion from the defect, following the same point line over the duration of the scan for AA6014 with a NSDL and FFC initiated by 1µL of 2M HCl_{aq}

Figure 3.3.2.2e shows the distance of corrosion from the edge of the defect, following the same point line over the duration of the scan with an uncertainty of ±0.01mm. The graph shows that there is corrosion growth over the 90-hour period with a linear relationship between corrosion growth and time lapsed; as time increases, so does the distance of corrosion from the defect. As the graph does not show signs of a plateau, then it would suggest that the corrosion mechanism is still likely to continue past 91.45 hours, but at a relatively slow pace.

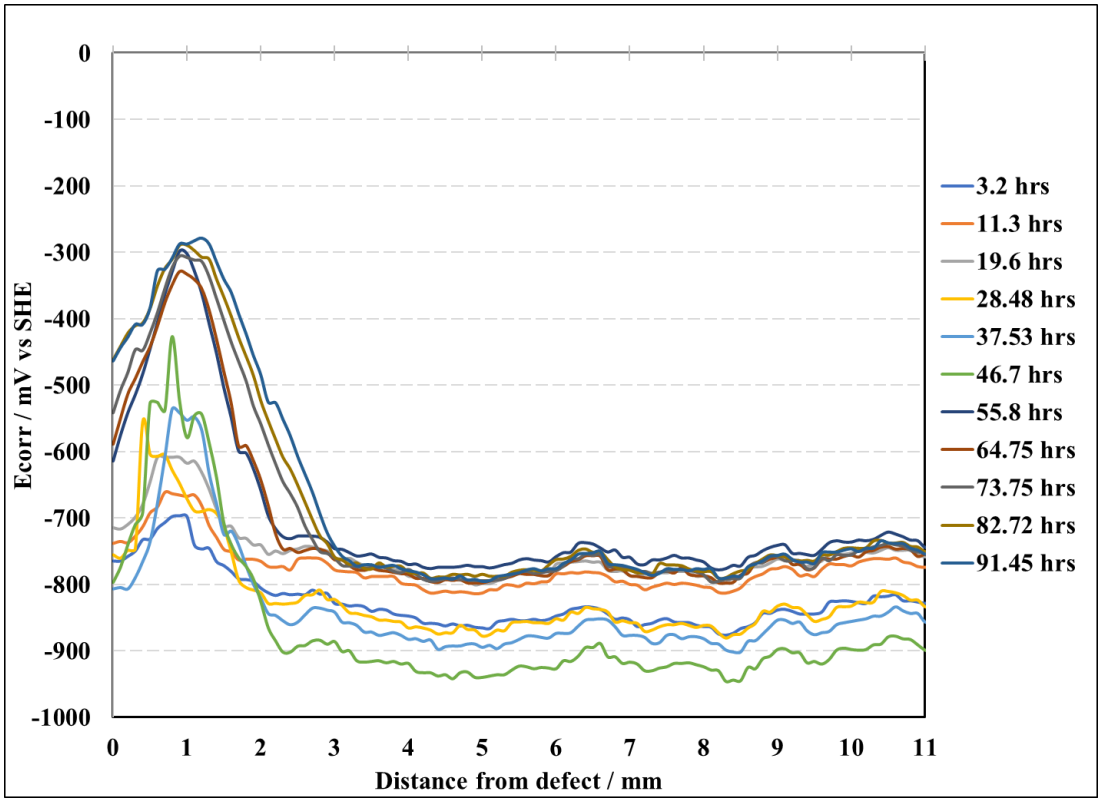

Figure 3.3.2.2f: E_{corr} data for a selection of scans of AA6014 with a NSDL and FFC initiated by 1µL of 2M HCl_{aq}

The scans in figure 3.3.2.2f show the least negative potential at and adjacent to the defect, c.a. 1 mm. As the scan moves away from the defect, onto the NSDL, the potential becomes more negative. Over time the scans spread apart and measure a less negative E_{corr}, i.e., the scans after 55.8 hours remain at a less negative E_{corr} for a greater distance. This is potentially linked the combination of the NSDL being etched away by the electrolyte and the formation of the corrosion product passivating the surface. Across the scans the potential fluctuated with a standard deviation in values between 0 to 3.5 mm measuring c.a. 168mV and between 3.6 and 12mm, c.a. 54 mV. This is potentially due to a change in surface chemistry since the HCl etches away the NSDL as the electrolyte moves away from the defect. Compared to AA6014 with no NSDL the average surface potential of the bulk alloy is between -200 to -300mV, the average E_{corr} in Figure 3.3.2.2f after c.a. 3.5mm is between -750 to -950 mV this suggest there is potentially a difference of between 550 to 650 mV between the NSDL and the bulk alloy underneath it, which would suggest that the corrosion mechanism is still likely to continue past 91.45 hours.

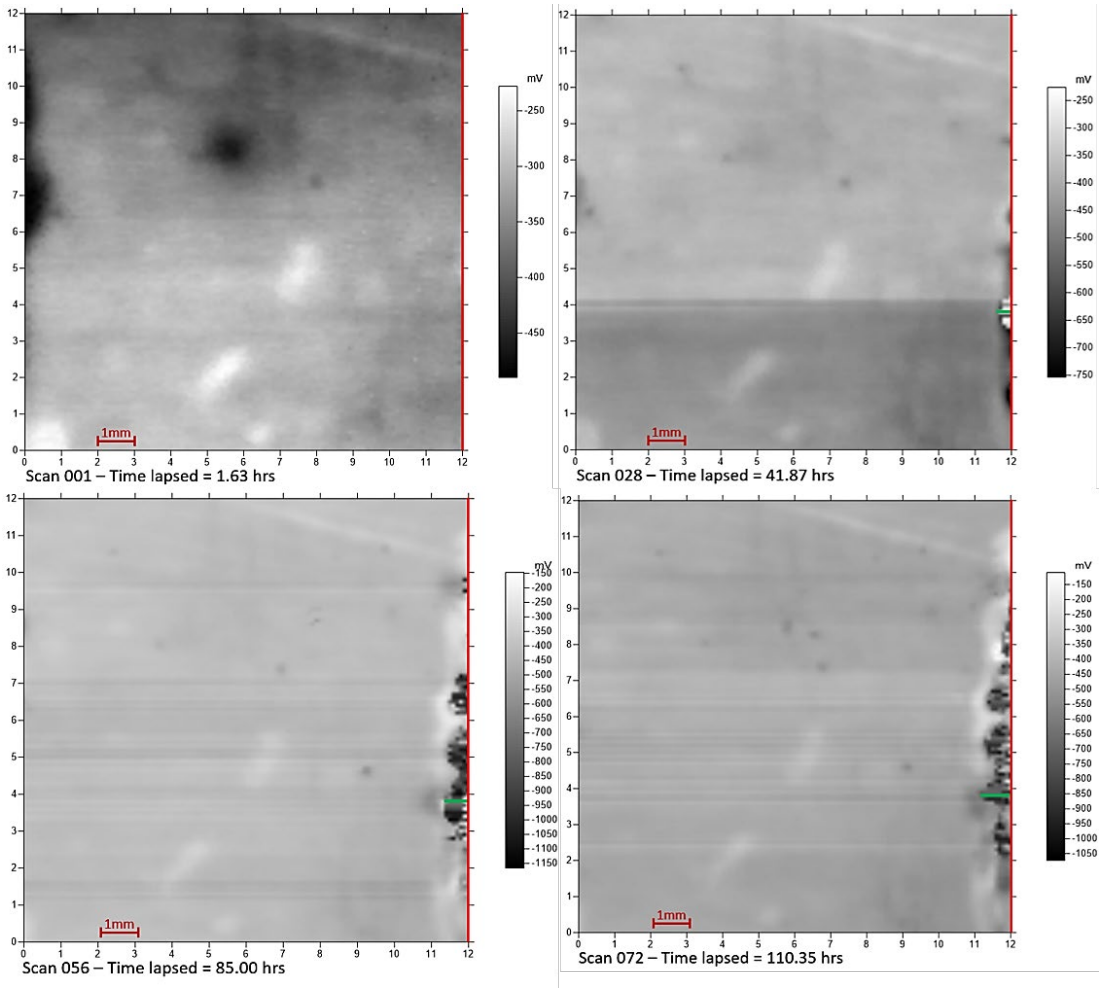

Figure 3.3.2.2g: Selection of scans of AA6022 with no NSDL and FFC initiated by 1µL of 2M HCl_{aq}, produced using Surfer software.

The scans in figure 3.3.2.2g have a red marker line for the defect and a green line indicating the corrosion distance measured across the scans, relative to the defect marker line. Across the scans the potential fluctuated, but the surface potential increased across the samples. The corrosion area is also increasing across the scans. The potential at the corrosion sites is more negative in places than the rest of the sample surface suggesting that the site has changes in its chemical activity due to the corrosion mechanism.

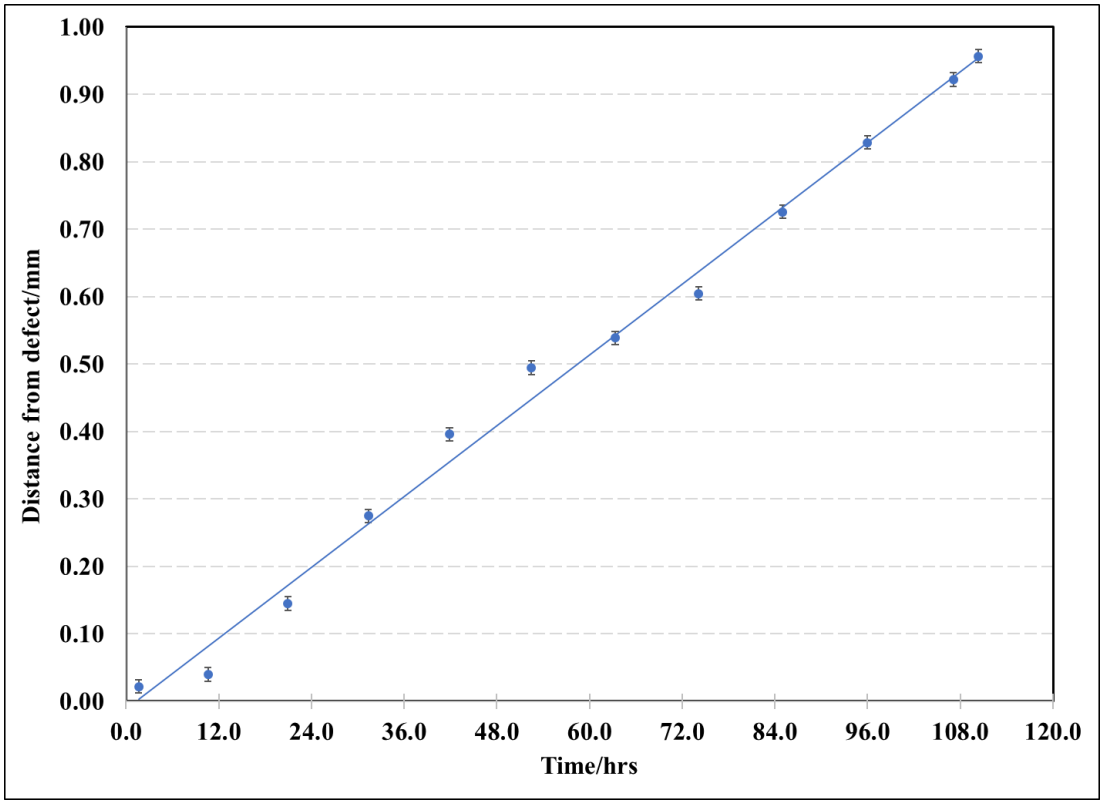

Figure 3.3.2.2h: distance of corrosion from the defect, following the same point line over the duration of the scan for AA6022 with no NSDL and FFC initiated by 1µL of 2M HCl_{aq}

Figure 3.3.2.2h shows the distance of corrosion from the edge of the defect, following the same point line over the duration of the scan with an uncertainty of ±0.01mm. The graph shows a linear corrosion growth from the defect with respect to time. Initially, up to c.a. 12 hours, the corrosion growth from the defect is < 0.1mm. The growth becomes more stable with time, potentially due to the abundance of electrolyte and FFC conditions being maintained.

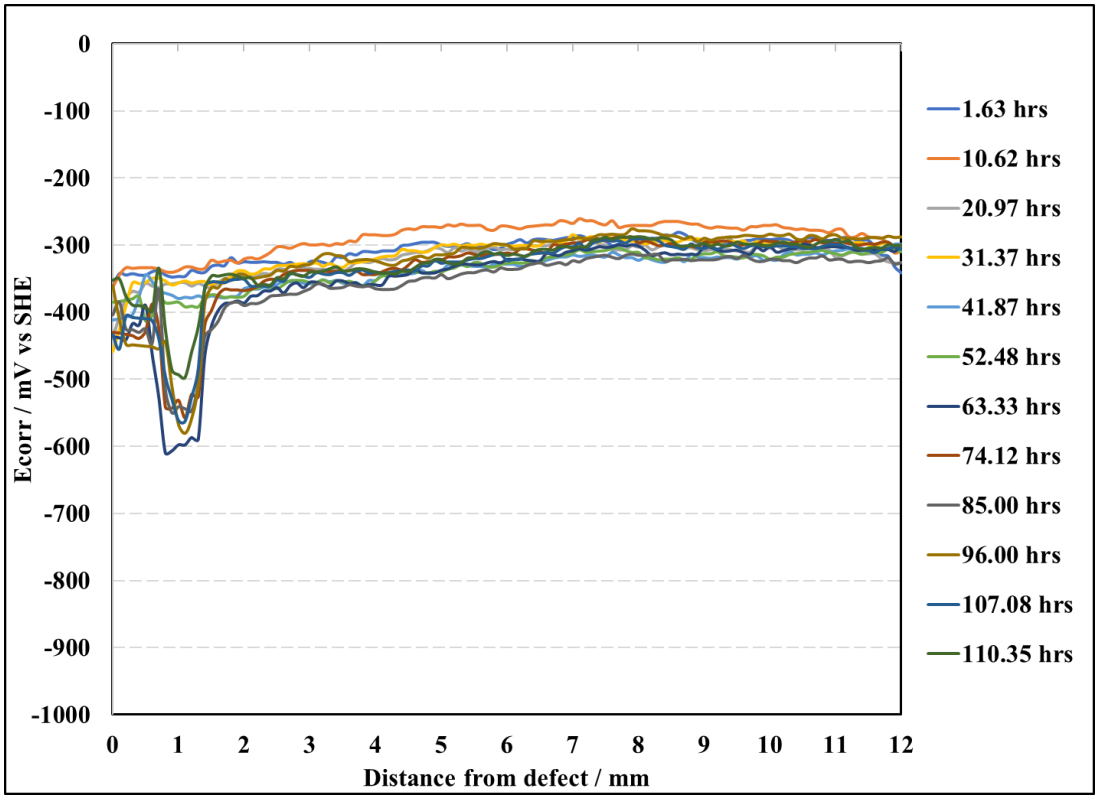

Figure 3.3.2.2i: Ecorr data for a selection of scans of AA6022 with no NSDL and FFC initiated by 1µL of 2M HCl_{aq}

Figure 3.3.2.2i shows that the scans become more negative as time increase, possibly due to the surface becoming more active. Scans after 52.48 hours show a drop in E_{corr} between c.a. 0.8 and 1.4mm potentially due to the SP-FFC mechanism and the formation of pits. The standard deviation in E_{corr} between 0.8 and 1.4mm was measured as c.a. 85mV, whereas the standard deviation between 1.5 to 12mm was c.a. 26mV. When compared to the scans for AA6014, for the bulk surface, the *SP*-FFC has yet to develop fully on AA6022 over the timescale of the experiment.

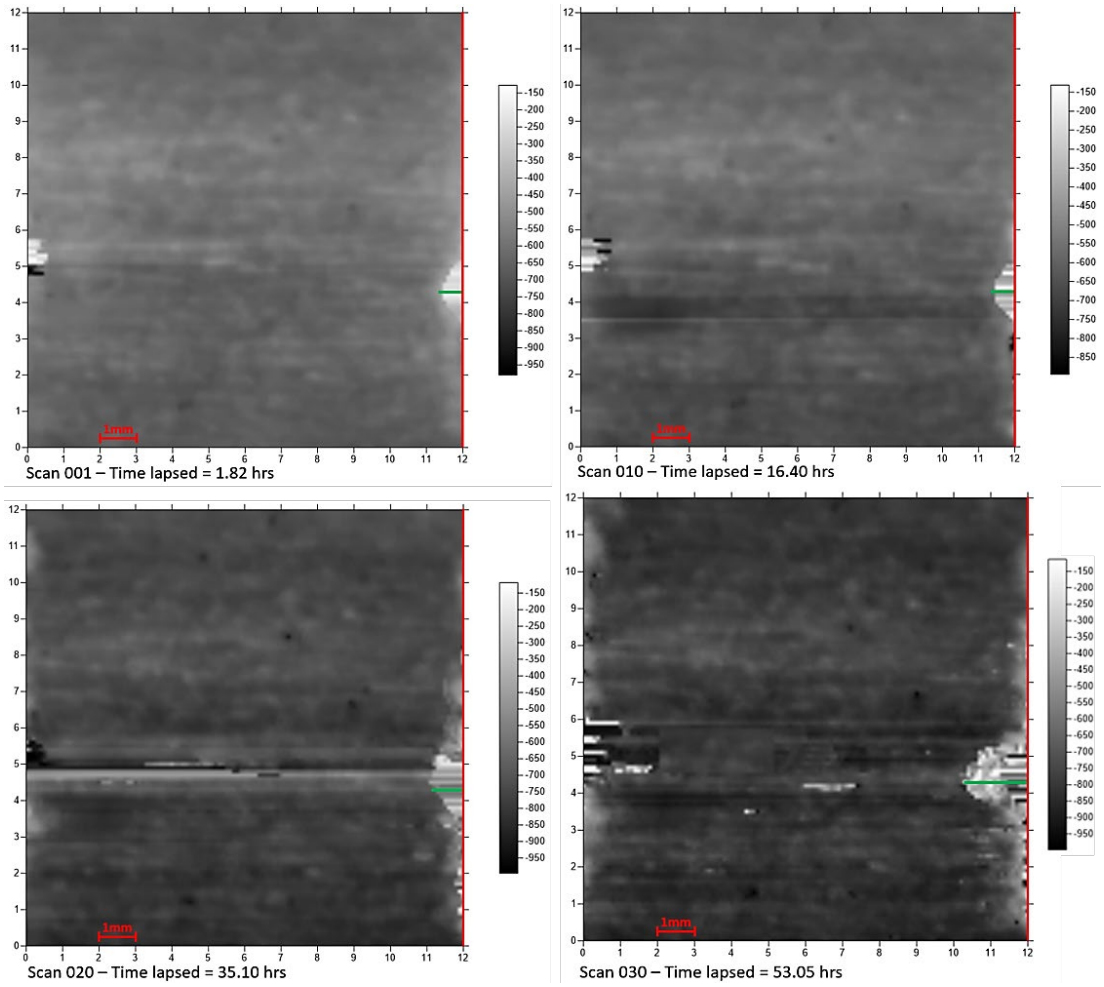

Figure 3.3.2.2j: Selection of scans of AA6022 with a NSDL and FFC initiated by 1µL of 2M HCl_{aq}, produced using Surfer software.

The scans in figure 3.3.2.2j have a red marker line for the defect and a green line indicating the corrosion distance measured across the scans, relative to the defect marker line. Across the scans the corrosion area shows fluctuations in surface potential. The fluctuation of potential suggests that the site has changes in its chemical activity due to the corrosion mechanism producing both positive and negative ions. Near the defect, between 10 to 12 mm the potential increases, as shown by the lighter colour. This is possibly due to the corrosion product produced being passive and having a lower potential than the rest of the sample. There is no notable evidence for fast FFC, but the significantly more negative intact potentials (compared to the PVB coated bulk specimen) is in line with previous measurements carried out on bare alloy samples.

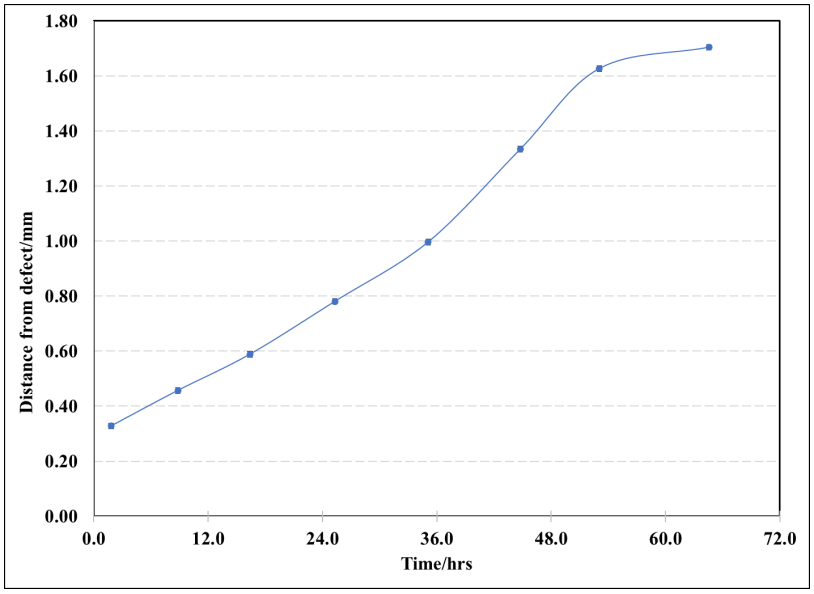

Figure 3.3.2.2k: Distance of corrosion from the defect, following the same point line over the duration of the scan for AA6022 with no NSDL and FFC i initiated by 1µL of 2M HCl_{aq}

Figure 3.3.2.2k shows the distance of corrosion from the edge of the defect, following the same point line over the duration of the scan with an uncertainty of ±0.01mm. The graph shows that there is a fairly linear relationship between corrosion growth and time lapsed; as time increases, so does the distance of corrosion from the defect, with a relatively large distance is moved from in c.a. 3 hours.

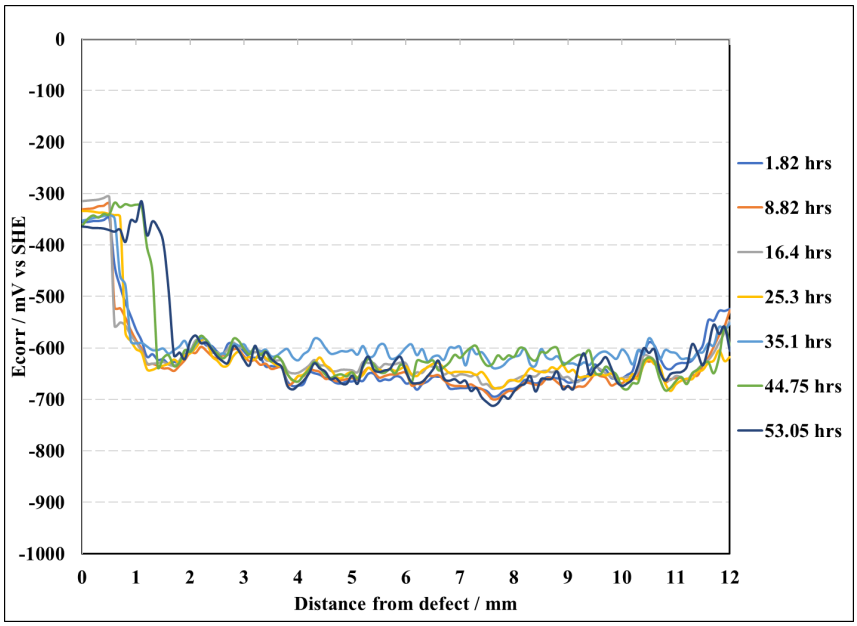

Figure 3.3.2.2l: Ecorr data for a selection of scans of AA6022 with NSDL and FFC initiated by 1µL of 2M HCl_{aq}

The scans in figure 3.3.2.2l show the least negative potential at and adjacent to the defect, between 0 and 1.6 mm. As the scans moves away from the defect, onto the NSDL, the potential becomes more negative. After 35.1 hours the scans spread apart and measure a less negative E_{corr}, i.e., the scans after 44.75 hours remain at a less negative E_{corr} for a greater distance from the defect. This is potentially linked the combination of the NSDL being etched away by the electrolyte and the formation of the corrosion product passivating the surface. Across the scans the potential fluctuated with a standard deviation in values between 0 to 1.6 mm measuring c.a. 127mV and c.a. 29 mV between 1.7 and 12mm. This is potentially due to a change in surface chemistry since the HCl etches away the NSDL as the electrolyte moves away from the defect. When compared to figure 3.3.2.2i AA6022 with no NSDL, the average surface potential of the bulk alloy is between -350 to -450 mV, the average surface potential in figure 3.3.2.2l is between -600 and -700 mV this suggest there is potentially a difference of c.a. 250mV between the NSDL and the bulk alloy underneath it, which would suggest that the corrosion mechanism is still likely to continue past 53.03 hours. The difference in potential here, compared with the AA6014 samples is lower. This could be for two reasons. 1. The composition of the alloys, or 2. The AA6022 samples were not able to run for the full time due to the SKP tip becoming overloaded. It is possible that, over a longer period, the AA6022 NSDL sample would reach a lower potential.

3.3.3 FFC mechanisms for PVB coated AA6014 and AA6022 alloys

Previous work [1,2,10] has suggested that the NSDL is anodically activated due to the difference in potential between the NSDL and the bulk. The more negative E_{corr} of the NSDL in relation to the bulk could be due to either (i) the NSDL is anodically activated with respect to the bulk alloy or (ii) the bulk could be cathodically de-activated in comparison with the NSDL.

This was seen in a similar alloy, AA6016, which had a difference in surface potential between the NSDL and bulk of 0.2V, at 180°C and 0.5V at 350°C[3]. At lower temperatures samples of AA6014 and AA6022, with FFC initiated, show an average difference of 0.5V and 0.375V, respectively. Both AA6014 and AA6022 are likely to have the same driving mechanism as found in AA6016 and AA6111. The consensus was that, due to the samples with a NSDL being more reactive than the samples without a NSDL, bulk alloy material, then the mechanism for FFC is driven by anodic activation, this is not to say that there is no cathodic activation, or deactivation, but that due to the net potential of the anodic region, this is the dominating feature.

If the corrosion mechanism, when a NSDL is present, is anodically activated, relative to the bulk alloy metal, and S.A.FFC is restricted to the presence of a NSDL, the mechanism underlying S.A.FFC can be dipicted as shown in figure 3.3.3a[3,214].

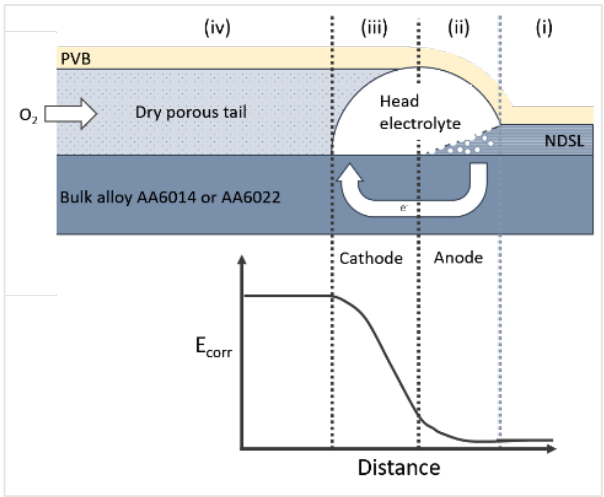

Figure 3.3.3a: Schematic model representing data and images from SKP scans and surfer seen earlier in this chapter.

The lower section of figure 3.3.3a shows a simlified version of the Ecorr profile from the SKP, note it is in reverse to te one in figure 3.3.2.2e due to the position of the

defect. The upper section of figure 3.3.3a is a simplified diagram showing how the lower section relates to the physics sample. The upper section has been split into four sections. Section (i) is the section of the sample where the NSDL is still present and where the PVB coating is still intact and adhered to the surface. Section (ii) head of the filament contining an electrolyte of HCl(aq) and partially hydrolysed $AlCl_3$(aq), comes into contact with the NSDL and starts to remove it via metal dissolution. This is the anodic site for the corrosion mechanism. Section (iii) is the region of the head where the NSDL has fully dissolved. The filament electrolyte in the head is now in contact with the bulk alloy and is the cathodic region of the head. This is due to the differential aeration* and the diffusion of gasses from the environment, through the poros tail. The diffusion of O_2 sets up cathodic oxygen reduction in this section. Section (iv), the tails contains the dry corrosion products by the hydrolysis of the Al^{3+}ions forming a mixture of aluminium oxide and aluminium hydroxide. This section is dry as it does not contain any water-soluble products or electrolyte. As a result, water is drawn to the head via osmosis. The dry, porous tail allows the easy diffusion of O_2 from the environment.

*Differential aeration is important in most localised corrosion mechanisms, FFC included. In SA-FFC the difference between the E-corr, for the NSDL compared with the bulk, is likely to be the main driving force as shown in figure 3.3.3a.

When a NSDL is not present, whether due to the removal during the sample preparation stage, or because the NSDL has been dissolved due to S.A.FFC, a different form of FFC is observed. Successive pitting FFC, S.P.FFC. S.P.FFC has more distinct filaments as well as grouped areas of pit-like features. S.P.FFC can be represented as shown in figure 3.3.3b. As descibed in other work[12–24] during the etching stage in the surface preparation, using NaOH, can cause aluminium alloys, with a high copper content, to have a copper-rich surface. The subsequent desmutting stage, using HNO_3, is not able to remove the copper from the surface. As mentioned in this work, aluminium alloys containing c.a. 0.95% can produce a copper-rich surface of c.a. 2nm under the oxide layer, when the samples have been etched. It has also been documented[3,199,249] that for surfaces without a NSDL present, the initial form of corrosion is intergranular. Due to anodic dissolution, whether through the corrosion process of a NSDL or because of sample preparation, it is likely that the surface that is in contact with the head electolyte is copper rich and may lead to cathodic reduction

and subsequent changes in cathodic activity. The tail will eventually become dehydrated and the corrosion mechanism stops. If there is a greater quantity of copper at intergranular boundaries at the surface then the quantity and distance of S.P.FFC is likely to increase. As found in previous work[5], S.P.FFC is only observed when an anodically activated NSDL is not present and therefore the surface is not cathodically protected. As there is no potential difference at the surface, then S.P.FFC is driven by differential aeration.

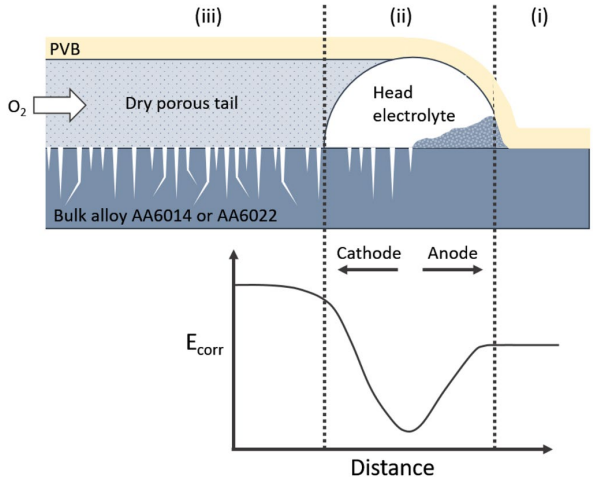

Figure 3.3.3b: Schematic model representing successive pitting FFC, S.P.FFC.

The image is split the same way as figure 3.3.3b; the lower section of shows a simlified version of the Ecorr profile from the SKP and the upper section is a simplified diagram showing how the lower section relates to the physics sample. This mechanism is split into three sections. Section (i) illustrates the region where the PVB is still intact and adheres to the surface of the bulk alloy, but some corrosion product can also be found here[3,5,214]. Section (ii) the head of the filament containing an electrolyte of HCl(aq) and partially hydrolysed $AlCl_3$(aq), moves under the PVB coating and is in contact with the bulk alloy. Due to the absence of a NSDL, the bulk alloy experiences cathodic O_2 reduction. Due to the cleaning process, or the dissolution of a NSDL, the bulk alloy is likely to have some copper-rich areas. Section (iii) as seen in figure 3.3.3b the tails contains the dry corrosion products by the hydrolysis of the Al^{3+}ions forming a mixture of aluminium oxide and aluminium hydroxide. This section is dry as it does not contain any water-soluble products or electrolyte. As a result, water is drawn to the head via osmosis. The dry, porous tail allows the easy diffusion of O_2 from the environment.

3.4 Conclusions

For uncoated samples, the presence of a NSDL reduces the surface potential compared to the bulk alloy. This has been observed through SKP and open circuit potential, OCP, scans. The NSDL is significantly more negative when compared to the bulk alloy. Where FFC is not induced, the potential difference observed between the NSDL and the Bulk for AA6014 and AA6022 has been measured. The open circuit potential, OCP, scans show that there is an average difference in the initial potentials of 0.319V for AA6014 and 0.377V AA6022. The SKP scans show that there is an average difference potential of 0.365V for AA6014 and 0.363V for AA6022. Both scans show a potential difference of over 0.3V for both alloys.

For PVB coated samples injected with 2M HCl (aq), FFC is observed for samples with and without a NSDL. The FFC observed differs depending on the surface. With a NSDL a fast form of superficial FFC is observed, known as surface active FFC. When a NSDL is not present, then a slower, more penetrating, form of FFC is observed, known as successive pitting FFC.

The potential difference between the two types of surfaces suggests that the samples with a NSDL are undergoing anodically activated driven corrosion, whereas the absence of a NSDL are more likely to be driven by differential aeration.

The scans show that there is only a small difference in potentials between the two alloys. There is no clear information to suggest one having more corrosion resistance than the other, therefore it is difficult to comment on the rate of corrosion between the two. This will be addressed in the next chapter.

Chapter 4 – The effect of relative humidity and presence of a NSDL on the type and rate of FFC on AA6014 and AA6022 using time-lapse photography

4.1 Introduction

Superficial corrosion, including FFC, on aluminium and aluminium alloys has been known about since c.a. 1960s, prior to this most FFC studies involved iron or steel substrates. The earliest reports of FFC on aluminium alloys were made on aeronautical alloys, followed by architectural alloys that had been exposed to extreme environmental conditions, in particular, very high levels of relative humidity and the presence of industrial and/or marine compounds. At present, the conditions above are leading to an increase in superficial attack via FFC in the automotive sector which is why research is required on new aluminium alloys designed for use in this sector.

Previous work[250] investigated FFC on steel sheets as there was a known range of %RH for FFC to occur. The work found that for %RH of 65% to 95%, the %RH in the environment, compared to the humidity within the corrosion cell, set up a difference in solute concentration allowing the diffusion of water from the environment to the cell via osmosis. If the water vapour pressure, from the environment, is greater than the water vapour pressure of the anodic region of corrosion cell within the head, then water will diffuse through the film and FFC will continue. Once the vapour pressures are in equilibrium, or if the water vapour pressure is greater within the filament head, then either FFC will cease to continue or will not occur. The work also found that for extremely high humidities, around 95%, they grow at such a quick rate that the filament heads become wider, or blisters occur. The work concluded that this diffusion, via osmosis, of moisture to the anodic site of the filament head, is a key component of FFC on steel substrates and thus could be on FFC of aluminium, and magnesium. It was concluded that the driving force of FFC, on steel, is dependent on the diffusion of water across a thick, semipermeable membrane. Although there was a known %RH range that iron was expected to show FFC, the work stated that although aluminium was also observed to corrode via FFC, no %RH range had been identified. Since aluminium undergoes FFC, then this work suggests that %RH could have an influence on the FFC of aluminium.

LeBozec[251] et al investigated the effect of climatic parameters on filiform corrosion of coated aluminium alloys of the 6000 series. This paper focused on AA6016 and one of the parameters investigated was temperature. The temperature in this investigation was an ambient temperature rather than a thermal treatment. Their work concentrated on the temperatures; 5°C, 25°C, 35°C, and 50°C. Samples were placed into chambers where the temperature was kept constant for six weeks. They found that as the temperature increased, the rate of corrosion also increased significantly. However, it was also noted that at 5°C a considerable number of FFC initiation sites were observed, but they did not progress into longer filaments. This paper looked into multiple corrosion factors alongside the effect of temperature and noted that the effect of ambient temperature differed depending on the pre-treatments and coatings used. The accelerated rated produced at 40°C and 50°C could provide improved testing conditions to obtain results in a shorter period of time, however they may not be valid for service conditions since they run tests at 10°C to 20°C. Another factor investigated was percentage relative humidity, %RH. They noted that %RH was affected by temperature with 5°C and 25°C producing substantially more underfilm corrosion at 85% RH when compared to 75% RH and 95% RH at the same temperatures. They also noted that at their highest ambient temperature, 50°C, 95% RH had the most favourable environment for corrosion growth.

Other work[164,252], states that environmental conditions, such as salinity, have a direct effect on the rate of corrosion emphasising that FFC initiates when organic coated metals are placed in an environment with a high %RH which allow salts in the atmosphere to dissolve on the surface of the coating[167]. The work agrees that the %RH should be within the range of 60% to 95% RH for FFC to occur[166,253], but very high %RH could lead to blistering. In general, the rate of corrosion, and the width of the filaments, increases as %RH increases, however this paper states that the optimum %RH for FFC to occur and develop is c.a. 80-85% RH. It also states that as well as a high %RH, some form of defect must be present in the coating that exposes the metal, that there must be oxygen present so that redox reaction can occur, there must be an aggressive species present, e.g. chloride[254], a high temperature (this is investigated in chapter 5), the substrate, as some are not prone to FFC and finally the surface preparation, pre and post-treatments, NSDL and cleaning were investigated in chapter 3. Other work[164,253] suggests that the permeability of the coating may also influence

FFC rates. This work also states that to reduce, or remove, the possibility of FFC that coated substrates should be stored in environments where the %RH is lower than 60%, preferably between 30-40% RH.

Following on from the findings above, Persson et al[184,255] states that no systematic investigation of temperature or %RH have been conducted for aluminium alloys. It does note the work conducted by Ruggeri and Beck 165 identified that FFC (filiform corrosion) can occur on coated substrates between 30-95% RH and Slabaugh et al 163 found that FFC can occur between 20-100% RH, but this range was depended on the initiating agent used. It is noted that at the lower humidities the filament becomes dehydrated, thereby stopping FFC, but it is still able to initiate. At extremely high humidities the results show blistering or general corrosion, rather than FFC. They found that an RH of between 85 to 95% showed the optimum conditions for FFC with %RH c.a. 85% producing wider filaments. If FFC can occur from 20% RH, then the storage environment noted in A. Bautista would not reduce or remove the likelihood of FFC. In the papers by Persson et al[184,255] the effect of %RH was investigated for five different %RH ranging from 40% to 95%. They used saturated salt solutions to control and maintain the %RH and conducted the tests over 6 weeks. It was noted that identifying the different corrosion types was challenging whether areas were showing small interconnecting blistering, or if it were FFC and that the filaments lead to cracks and imperfections in the coating which could lead to more general corrosion, something to be aware of during the investigations in this chapter. More specifically, they identified that at 40% RH no corrosion was identified, 60% RH did show FFC but the area of FFC was significantly smaller than the area of FFC at 75% RH, the largest FFC was observed when RH was at 85% and a drop in FFC area at 95% RH. Their results show an increase in FFC area as %RH increases, except for 95%. However, unlike some studies 256, they did observe rapid FFC growth at 95% RH. It was concluded that the optimal %RH for FFC was 85%, complementing previous work. They noted that the results for humidity were also affected by the pre-treatments and coatings used, as well as the temperature. They note that the combination of multiple variables complicated the tests.

Although the investigates above draw similar conclusions regarding the effect of %RH on FFC, they have not investigated any %RH below 40% and individually the spacing between the %RH is large, therefore important insights may have been missed.

Broudy, H. identified, in 1933[257], that the %RH of $AlCl_3$ at 27°C was 37% at a lower temperature of c.a. 20°C, it is reasonable to suggest that the %RH would be higher, but one might predict to observe some features akin to FFC around 40% RH. A systematic investigation of the effect of %RH on aluminium alloys is still required.

Iron undergoes FFC at %RH range of 65% to 95%. Following a systematic investigation conducted by Williams 258 on effect of %RH on FFC of magnesium alloys at a constant temperature of 20°C, it concluded that magnesium alloys undergo FFC at %RH between 52-95%. This work used far lower %RH than other work, ranging from 15% to 93%. It was found that no FFC occurred below 31% RH. This is likely due to the formation of $MgCl_2$ and its deliquescent point being ≥33% RH. As %RH increased above 31% the propagation rate of FFC increased. The investigation also resulted in a new mechanism for FFC on coated magnesium alloys. Where iron and aluminium are driven by differential aeration and are affected by %RH, magnesium is highly dependent on the presence of humid air, rather than the oxygen content of the air.

Further work on magnesium 259 investigated five different %RH with similar %RH[258], from 31% to 99% RH, at a constant temperature of 20°C for 21 days. The %RH were produced using saturated salt solutions. The results agreed with work conducted by Willams[258] with 31% RH not producing any features of FFC, RH of 53-93% producing FFC, with the area of FFC increasing as %RH increased. The area propagation relative to time for 93% showed that the area corroding towards the end of the investigation did not increase linearly compared with earlier results. It has been suggested in this work that the soluble chloride ions are not as readily available due to their more rapid use in the corrosion mechanism at the electrolytic head. A 99% RH did not yield any signs of FFC but did produce blistering around the defect. This work agreed that the presence of a humid environment is vital for FFC to be observed on magnesium alloys.

Since little is known about the influence of RH on FFC propagation on 6000 aluminium alloys, and based on the previous work mentioned above, the aim of this investigation, and section, was to investigate the influence of RH on the type of FFC corrosion and the rate of FFC propagation, both in the presence and absence of NSDL. The investigation also builds on the work in chapter 3 and will look at how the presence

of a NSDL also affects the type and rate of FFC. The following investigations followed the surface preparations and methodologies describe in earlier work[3,5] and comparable work[4,179]. Adaptations and modifications were made to the procedure due to equipment and environmental constraints [260]. Preliminary investigations were conducted on 2 high humidities to provide a base timeline of events. Following this, a greater range of humidities were investigated. Each sample and run of experiments in this section were prepared and conducted following the same method.

Little is known about the %RH of $AlCl_3$. Broudy, H. experimented with %RH of many saturated salt solutions, at a range of temperatures, and published his findings in 1933[257]. He identified that the deliquescence point of $AlCl_3$ at 27°C was at a RH of 37%. The final experiment in this chapter investigates a range of %RH from saturated salt solutions, including $AlCl_3 \cdot 6H_2O$. As well as finding how %RH effects the rate and type of FFC, it is hoped that a %RH will be identified for $AlCl_3 \cdot 6H_2O$.

4.2 Experimental

4.2.1. Sample preparation

Samples were prepared as described in Chapter 2.3 and 2.4; Alkali cleaning of the samples in NaOH (10% w/v), for c.a. 45s at 60°C, to dissolve any aluminium oxide and any NSDL on the surface. Samples were rinsed with distilled water and acetone before acid desmutting using concentrated HNO_3 (15.6 molar) for 30s at 25°C to remove impurities such as copper and iron from the surface, and to passivates the surface. The samples were again rinsed with distilled water and acetone. When required, the NSDL was reintroduced by manual abrasion using 180 grit silicon carbide paper/emery paper for 5 mins. The abrasion direction was orientated in the same direction as the rolling direction. Samples were rinsed with distilled water and acetone prior to coating with 15.5% (w/w) ethanolic PVB (Polyvinyl butyral) solution to produce an air-dried PVB coating of thickness 30µm ± 5µm. 10mm defects were scribed through the PVB layer normal (90°) to the rolling/NSDL direction with a scalpel [3,4] Due to economy of samples, most were scribed with 2 defects c.a. 13mm apart[3,4]. The number of defects used, have been identified in each section. FFC was initiated by injecting the scribe with 1µL of 2M aqueous hydrochloric acid using a glass micro-capillary dispenser. The HCl injection method was intended to create greater reproducibility than methods involving full sample exposure either by salt fog, HCl vapour, or immersion in aqueous electrolyte. [3,4]

For the first two trials, samples were placed in closed petri-dishes, with a specific saturated salt solution to obtain the desired % relative humidity. However, they were not airtight, and they were too small to contain a humidity sensor therefore the RH was not monitored. When the large-scale RH investigation was proposed the setup changed so that the samples were placed in sealed containers, with a specific saturated salt solution to obtain the desired % relative humidity, and a digital hygrometer and temperature sensor (Lascar's EasyLog EL-USB-2-LCD+) was placed in each container.

Photographs were taken periodically, and measurements obtained using Photoshop, as described in Chapter 2.5 A selection of graphs were produced to show corrosion growth with respect to time and to compare the rate and type of cosmetic corrosion observed.

4.2.2. Preliminary investigation – Rate of FFC propagation, both in the presence and absence of NSDL at 93% Relative Humidity

All samples were placed under the following conditions:

- A fixed relative humidity of 93%[3] - using a saturated salt solution of sodium sulfate-decahydrate. This was monitored using a digital hygrometer, with a digital temperature sensor (Lascar's EasyLog EL-USB-2-LCD+). All samples were placed in the same sealed container to maintain consistency.
- Average temperature throughout investigation c.a. 20 °C
- Duration of investigation – 72 hours
- 3 x 10mm scribes (c.a. 10mm separation) each injected with 1µl 2M HCl.

All samples were prepared as described in chapter 2, and above; Alkali cleaning of the samples in NaOH (10% w/v), for c.a. 45s at 60°C, followed by acid desmutting using concentrated HNO_3 (15.6 molar) for 30s at 25°C ; this is what is meant by surface treatment/cleaned samples in the images and results that follow. Some samples were abraded with 180 grit SiC paper to create the NSDL which has been identified in the image descriptions. Images of the test samples can be seen in figures below, (Figures 4.3.1a and 4.3.1b), followed by a graph showing the average area of corrosion around the defect with respect to time, a rate of FFC propagation chart, both in the presence and absence of NSDL, for both alloys at 93% RH and a table showing the difference in corrosion rates.

Furthermore, trial 4 of the AA6014 alloy, was left for a longer period to allow insight into the rate of complete surface corrosion. AA6014 was chosen due to its chemical composition, higher percentage of copper, and potentially a quicker corrosion rate. It was setup inside a camera box with a continuous light source. Images were taken every 30 minutes to allow a more thorough understanding of the corrosion growth.

4.2.3. Rate of FFC propagation, both in the presence and absence of NSDL at 80% Relative Humidity

All samples received the following:

- A fixed relative humidity 80% - using a saturated salt solution of ammonium sulfate. This was monitored using a digital hygrometer, with a digital temperature sensor (Lascar's EasyLog EL-USB-2-LCD+). All samples were placed in the same sealed container to maintain consistency.
- Average temperature throughout investigation c.a. 20 °C
- Duration of investigation – 453 hours
- 2 x 10mm scribes (c.a. 20mm separation) each injected with 1µl 2M HCl.

All samples were prepared as described in chapter 2, and above; Alkali cleaning of the samples in NaOH (10% w/v), for c.a. 45s at 60°C, followed by acid desmutting using concentrated HNO_3 (15.6 molar) for 30s at 25°C, no samples were used "as received. Some samples were abraded with 180 grit SiC paper to create the NSDL which has been identified in the image descriptions. Images were taken periodically, and the area of corrosion was measured around each defect using Photoshop measuring tools, and an average taken. Images of the test samples can be seen in figures below followed by a graph showing the average area of corrosion around the defect with respect to time, a rate of FFC propagation chart, both in the presence and absence of NSDL, for both alloys at 93% RH and a table showing the difference in corrosion rates.

The samples differed by surface preparation. Test samples 1 and 2 were as received and did not go through the sample preparation as described above, but samples 3 and 4 were prepared as described. Additionally, sample 1 and 3 did not have a NSDL, whereas test sample 2 and 4 did have NSDL.

4.2.4. How the rate of FFC propagation, both in the presence and absence of NSDL varies with different % relative humidity

This investigation followed the surface preparations and methodologies describe in previous work[3–5,179] and in chapter 2. All samples were prepared as described in chapter 2, and above; Alkali cleaning of the samples in NaOH (10% w/v), for c.a. 45s at 60°C, followed by acid desmutting using concentrated HNO_3 (15.6 molar) for 30s at 25°. Some samples were abraded with 180 grit SiC paper to create the NSDL which has been identified in the image descriptions, no samples were used "as received". The aluminium alloy sheets were cut into square samples, 45 mm x 45 mm. As described in chapter 2, images were taken periodically to show surface changes along with the corrosion growth and type of FFC. The images were uploaded to Photoshop where the corrosion area was measured for each image to produce a selection of graphs to identify the rate of FFC growth.

The enquiry consisted of 13 sealed boxes each with a different relative humidity. Relative humidities were achieved by using a different saturated salt solution in each box, as outlined in the table 8**,** however, the mass of the salts used was higher than the mass found on data sheets, therefore a '+' has been placed next to the required masses. The relative humidities, and temperature, were monitored throughout the enquiry using a data logger sensor. The selected humidities were: 12%, 19%, 33%, 40%, 46%, 53%, 58%, 65%, 71%, 75%, 80%, 85%, and 93%. Samples were routinely photographed and the area surrounding the defects were measured. Measurements were taken around two defects on each sample and each of the 3 samples had a different surface; 1. No NSDL, 2. NSDL, 3. c.a. 50:50 no NSDL: NSDL

Figure 4.2.4a – laboratory setup- relative humidity and its effect on FFC

Each relative humidity [261–266] was produced by adding salt to deionised water. Each salt requires a minimum g/100ml to achieve the desired relative humidity. The table below shows the minimum salt/water ratio required. The boxes with the desired relative humidities we set up and left for a minimum of 24 hours. The RH was monitored using a digital hygrometer and temperature sensor (Lascar's EasyLog EL-USB-2-LCD+). The RHs were checked before initiating the corrosion, with 2M HCl, and the samples were placed in the relevant sealed containers. With the RHs below 50% more than 24 hours was required. This was due to the %RH being too high on checking. Therefore, more salt was added and a further 24 hours allowed for the salt to dissolve and stabilise.

Relative Humidity %	Name of Salt	Salt Formula	Ratio minimum salt: deionised water g/100ml at c.a. 20°C	CAS Number
12	lithium chloride	LiCl	57+	7447-41-8
19	calcium bromide hydrate	$CaBr_2 \cdot xH_2O$	143+	71626-99-8
33	magnesium chloride hexahydrate	$MgCl_2 \cdot 6H_2O$	47+	7791-18-6
40	sodium iodide	NaI	17+	7681-82-5
46	aluminium chloride hexahydrate	$AlCl_3 \cdot 6H_2O$	133+	7784-13-6
53	magnesium nitrate hexahydrate	$Mg(NO_3)_2 \cdot 6H_2O$	42+	13446-18-9
58	sodium bromide	NaBr	95+	7647-15-6
65	cobalt(ii)chloride hexahydrate	$CoCl_2 \cdot 6H_2O$	19+	7791-13-1
71	strontium chloride hexahydrate	$SrCl_2 \cdot 6H_2O$	54+	10025-70-4
75	sodium chloride	NaCl	32+	7647-14-5
80	ammonium sulfate	$(NH_4)_2 SO_4$	77+	7783-20-2
85	lithium sulfate monohydrate	$Li_2SO_4 \cdot H_2O$	13+	10102-25-7
93	sodium sulfate decahydrate	$Na_2SO_4 \cdot 10H_2O$	32+	7727-73-3

Table 8: Salts used for the different %RH.

4.3 Results and Discussion

4.3.1. Preliminary investigation – rate of FFC propagation, both in the presence and absence of NSDL at 93% Relative Humidity

This investigation was conducted to identify the rate of FFC propagation, both in the presence and absence of NSDL, of both aluminium alloys, AA6014 and AA6022. A saturated salt solution of sodium sulfate-decahydrate was used to create a relative humidity (R.H.) of 93% to try and identify the quickest corrosion rate. Earlier work used 80% R.H. but at a higher temperature than was possible in the environment this experiment was conducted in, therefore, a higher RH of 93% was chosen [3]. During this preliminary investigation, some of the samples used did not undergo the sample preparation stage and were used as 'as received' samples. The following figures use the terms "no surface treatment" and "surface treatment. "No surface treatment" is the as received sample from BASF with no cleaning; "Surface treatment" shows the samples that have been cleaned with an alkali and an acid, as described in the sample preparation in section 4.2.1. The reason for this was to investigate if there would be a difference in the resulting cosmetic corrosion.

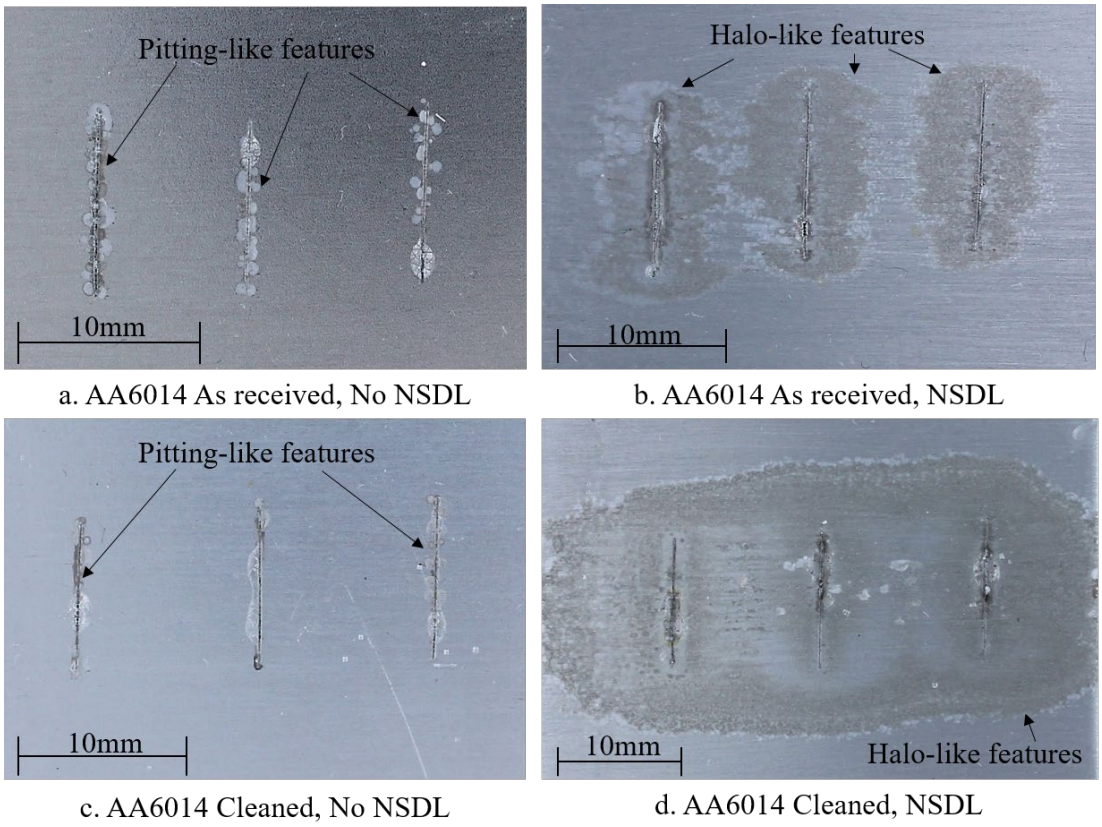

a. AA6014 As received, No NSDL

b. AA6014 As received, NSDL

c. AA6014 Cleaned, No NSDL

d. AA6014 Cleaned, NSDL

Figure 4.3.1a: aluminium alloy 6014 final images – a. no surface treatment, without NSDL at 72Hrs, b. No surface treatment, with NSDL, at 72hrs, c. surface treatment, without NSDL, at 72hrs, d. surface treatment, with NSDL, at 144hrs. Samples at 20°C and 93% RH, injected with 1µL of 2M HCl.

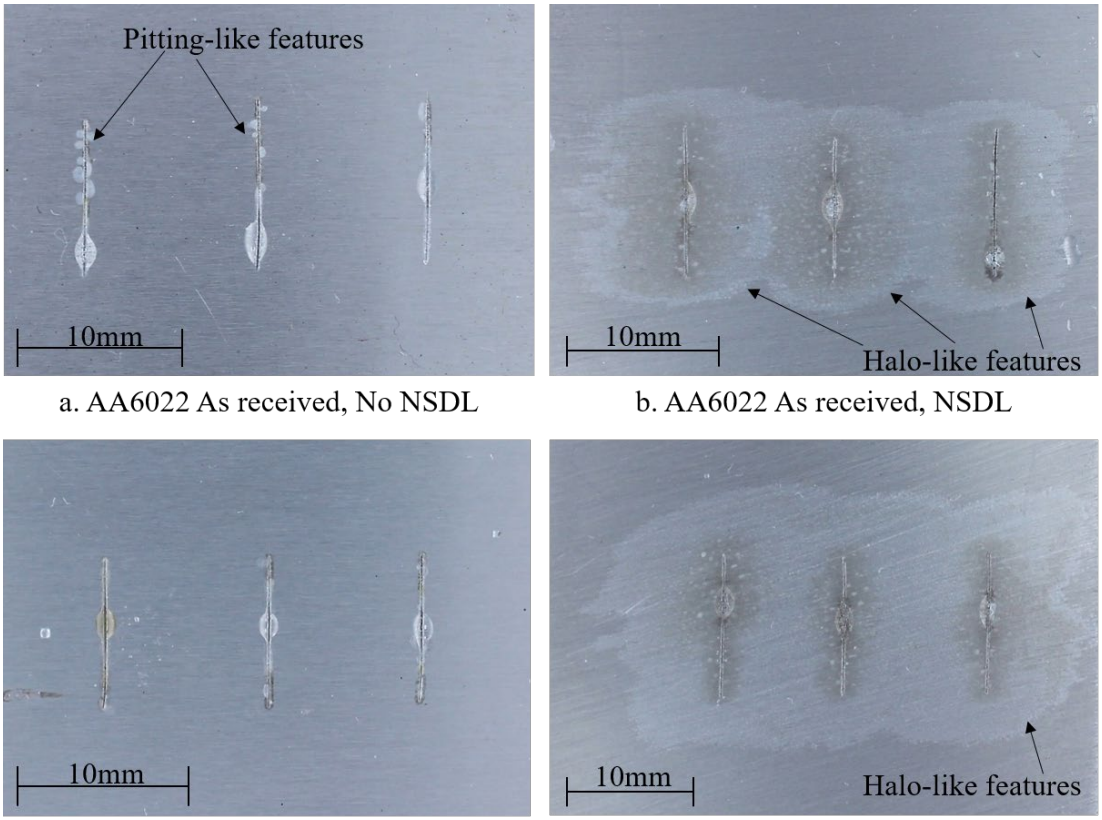

a. AA6022 As received, No NSDL

b. AA6022 As received, NSDL

c. AA6022 Cleaned, No NSDL

d. AA6022 Cleaned, NSDL

Figure 4.3.1b: aluminium alloy 6014 final images after 72 hours – a. no surface treatment, without NSDL. b. No surface treatment, with NSDL. c. surface treatment, without NSDL. d. surface treatment, with NSDL. Samples at 20°C and 93% RH, injected with 1µL of 2M HCl.

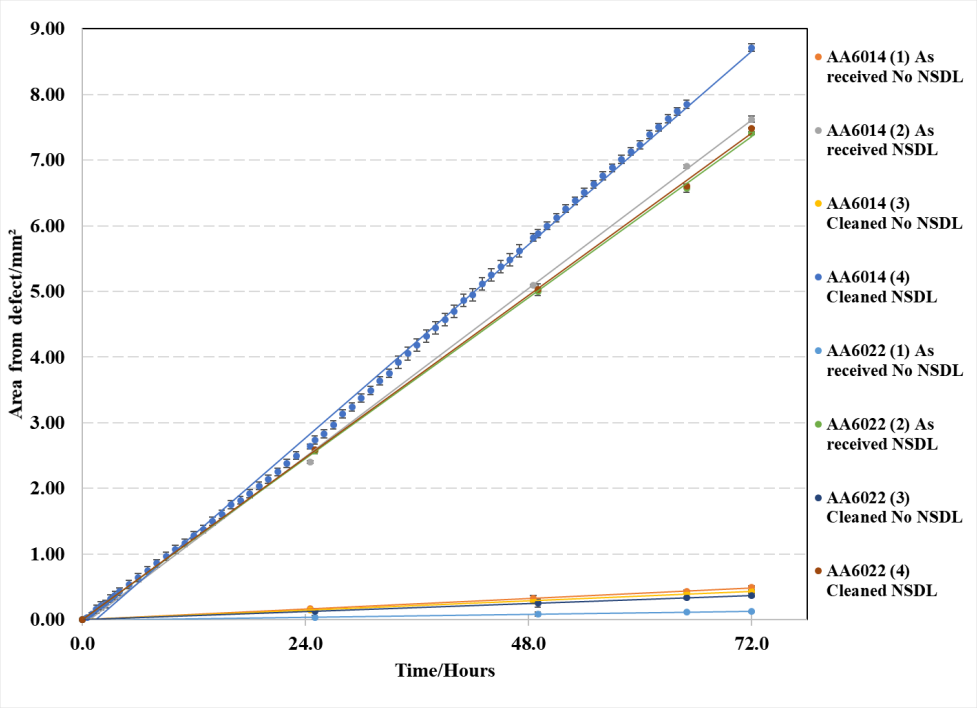

Figure 4.3.1c: Average area of corrosion around the defect with respect to time. Samples at 20°C and 93% RH, injected with 1µL of 2M HCl for 72 hours. Y-error bars included.

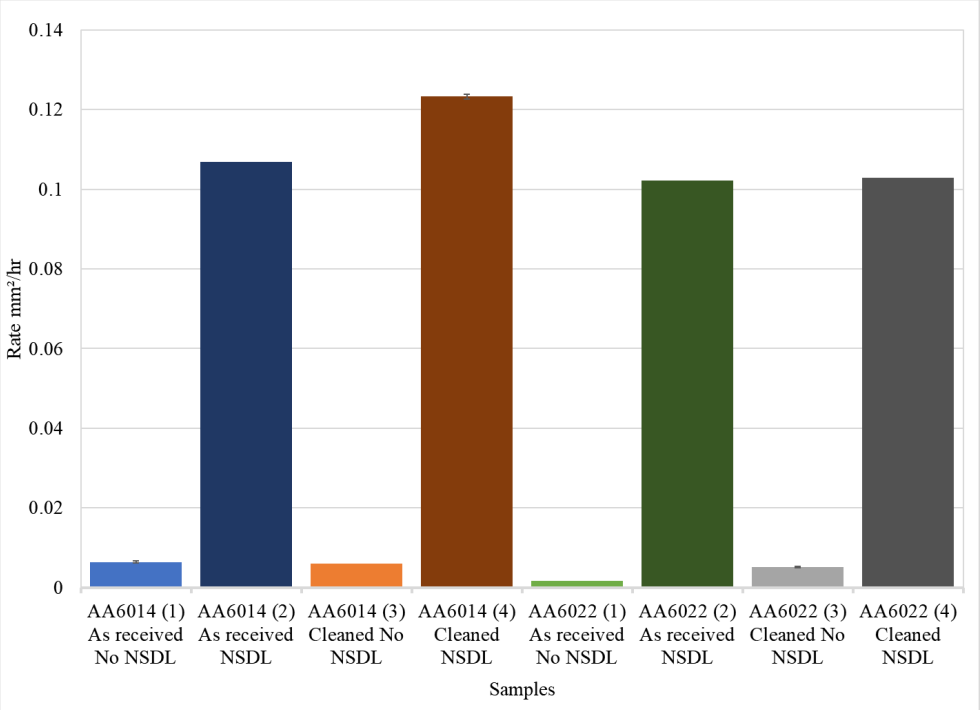

Figure 4.3.1d: Rate of FFC propagation, both in the presence and absence of NSDL for both alloys at 93% RH. Y-error bars included.

	Rate of FFC propagation mm²/hr at 93% RH					
	AA6014			AA6022		
Sample type	No NSDL	NSDL	Difference	No NSDL	NSDL	Difference
As received	0.0064	0.1069	0.1005	0.0017	0.1021	0.1004
Cleaned	0.0061	0.1233	0.1172	0.0052	0.1028	0.0976
Difference	0.0003	0.0164	0.0167	0.0035	0.0007	0.0028

Table 9: Rates of FFC propagation, both in the presence and absence of NSDL for both alloys at 93% RH. With the difference between rates shown.

The images, figure 4.3.1a on show the final images of the samples at 72 hours for images a to c and at 144 hours for image d. The images b and d that have a NSDL contain a halo-like feature, indicating surface active FFC. However, images a and c, samples without a NSDL, do not contain a halo, indicating surface active FFC was not present. However, images a and c do show some apparent successive pitting type filaments adjacent to defect, visible as dimple-features. However, the time taken to obtain the results was dictated by earlier work and as the samples without a NSDL show, more time was required.

Like the images in figure 4.3.1a for AA6014, the images in figure 4.3.1b for AA6022 show the final images of the samples. Again, the images b and d that have a NSDL contain a halo-like feature, indicating surface active FFC. However, images a and c, samples without a NSDL, do not contain a halo, indicating surface active FFC was not present. However, images a and c do show potential pitting sites adjacent to the defect. However, the time taken to obtain the results was dictated by earlier work and as the samples without a NSDL show, more time was required.

Based on data from figure 4.3.1c to the rate of FFC propagation for each of the 4 cleaned samples was calculated and shown in figure 4.3.1d. (The clean samples were

chosen as during the experimental work that followed all the samples went through the sample preparation as described in Chapter 2).

Throughout the experiment a series of images were taken for all samples. AA6014 with a NSDL having more images due to the additional enquiry mentioned above. The images were opened in Photoshop where area measurements were taken, as described in chapter 2**.** The measurements were put into excel where the above graph, and others, were produced. The mean standard deviation for the samples were as follows: AA6014 no NSDL as received 0.015mm, AA6014 no NSDL cleaned 0.022mm, AA6014 NSDL as received 0.006mm, AA6014 NSDL cleaned 0.067mm, AA6022 no NSDL as received 0.013mm, AA6022 no NSDL cleaned 0.03mm, AA6022 NSDL as received 0.021mm, AA6022 NSDL cleaned 0.03mm. Figure 4.3.1c shows: 1. as time passes, the area of corrosion increases, 2. The AA6014 samples have travel further from the defect compared to the AA6022, regardless of a NSDL, 3. The NSDL does influence the distance of corrosion from the defect as both the AA6014 and AA6022 corrosion area was larger when a NSDL was present.

Figure 4.3.1d shows: 1. the presence of a NSDL increases the rate of FFC propagation significantly, 2. Whether a NSDL is present or not and that AA6014 has a larger rate of FFC propagation than AA6022, particularly after the surface has been cleaned. The mean standard deviation for the samples were as follows: AA6014 no NSDL as received 0.00023mm/h, AA6014 no NSDL cleaned 0.0006mm/h, AA6014 NSDL as received 0.00021mm/h, AA6014 NSDL cleaned 0.0009mm/h, AA6022 no NSDL as received 0.00015mm/h, AA6022 no NSDL cleaned 0.00031mm/h, AA6022 NSDL as received 0.00038mm/h, AA6022 NSDL cleaned 0.00035mm/h.

Table 9 shows that the presence of a NSDL significantly increase the rate of FFC propagation, with an average difference in the rate of FFC propagation of c.a. 0.11mm^2/hr for AA6014 and c.a. 0.10mm^2/hr for AA6022. However, at 93% RH there is not a significant difference between AA6014 and AA6022.

This preliminary investigation suggested that the presence of the NSDL does promote corrosion and the existence of surface active FFC. It also suggested that the samples without the NSDL were more susceptible to pitting corrosion. This preliminary experiment also suggests that the AA6014 more readily corrode compared to the AA6022. As shown in chapter 3, the presence of a NSDL lowers the surface potentials

significantly. In this experiment, the lower potential has increased the rate of FFC propagation for these samples. This experiment has also shown that AA6014 has a larger rate of FFC propagation with a NSDL than the AA6022 sample. This was not clear in the results shown in chapter 3 as there was not a significant difference between the surface potentials when a NSDL was present. There was less of a difference when a NSDL was not present, in chapter 3, and this is shown in these results as there is little between the corrosion rates for the samples without a NSDL. This set of results agrees with the first, that AA6022 is potentially more corrosion resistant than AA6014.

4.3.2. Rate of FFC propagation, both in the presence and absence of NSDL at 80% Relative Humidity

Following on from the preliminary investigation, an additional relative humidity was investigated, 80% ammonium sulfate saturated salt solution. This was chosen due to its use in previous work. The same sample preparations and method were followed as described in chapter 3.3.1, with the exception being the saturated salt solution. Due to the drop in relative humidity, and the limited results without a NSDL seen in chapter 3.3.1, the investigation was conducted for a longer period, 453hrs.

**Note, some images show reflections of the camera lens. They have been identified in the images. They were not an effect of experiment or a corrosion phenomenon.*

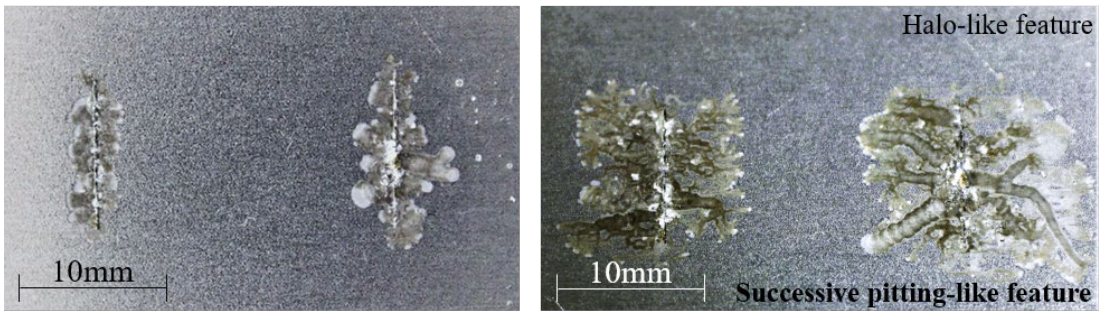

Figure 4.3.2a: aluminium alloy 6014 – as received sample with no NSDL. Sample at 20°C and 80% RH, injected with 1µL of 2M HCl at i) 120 hours and ii) at 453 hours.

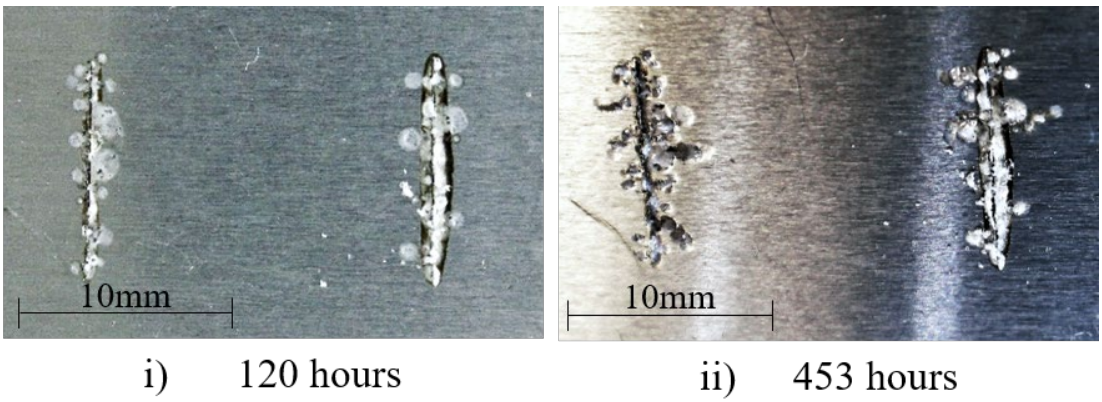

Figure 4.3.2b: aluminium alloy 6022 – as received sample with no NSDL. Sample at 20°C and 80% RH, injected with 1µL of 2M HCl at i) 120 hours and ii) at 453 hours.

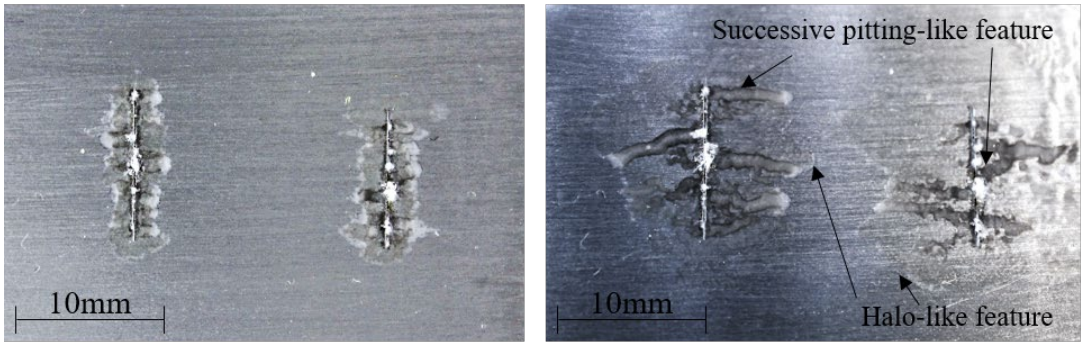

Figure 4.3.2c: AA6014 – as received sample with a NSDL. Sample at 20°C and 80% RH, injected with 1µL of 2M HCl at i) 120 hours and ii) at 453 hours.

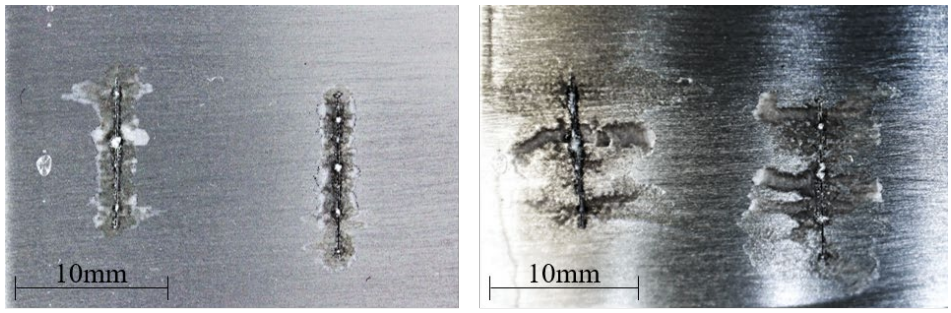

Figure 4.3.2d: AA6022 – as received sample with a NSDL. Sample at 20°C and 80% RH, injected with 1µL of 2M HCl at i) 120 hours and ii) at 453 hours.

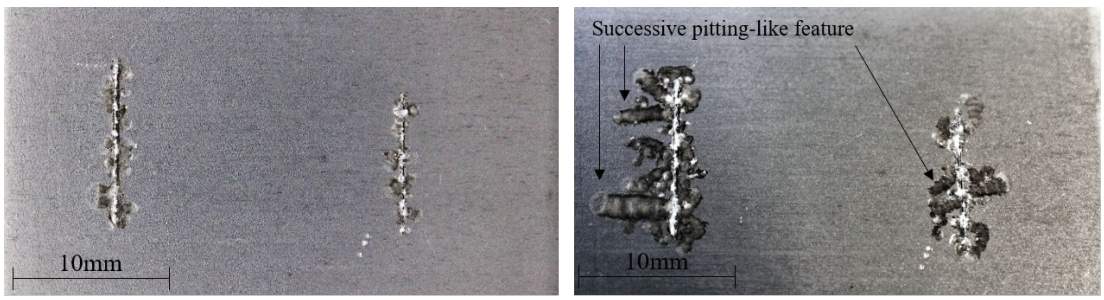

Figure 4.3.2e: AA6014 – alkaline cleaned and desmutted sample with no NSDL. Sample at 20°C and 80% RH, injected with 1µL of 2M HCl at i) 120 hours and ii) at 453 hours.

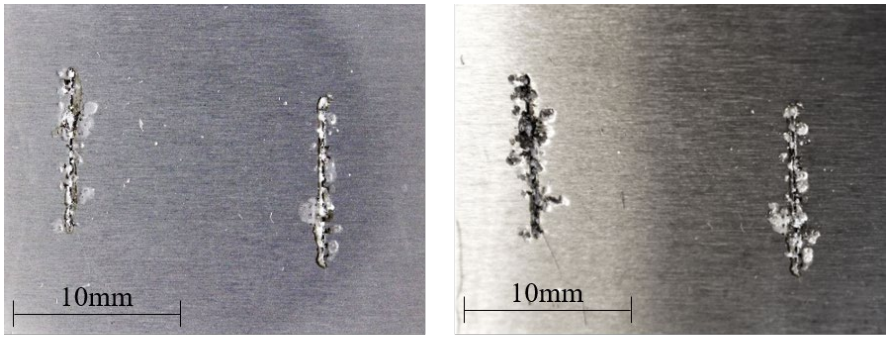

i) 120 hours ii) 453 hours

Figure 4.3.2f: AA6022 – alkaline cleaned and desmutted sample with no NSDL. Sample at 20°C and 80% RH, injected with 1µL of 2M HCl at i) 120 hours and ii) at 453 hours.

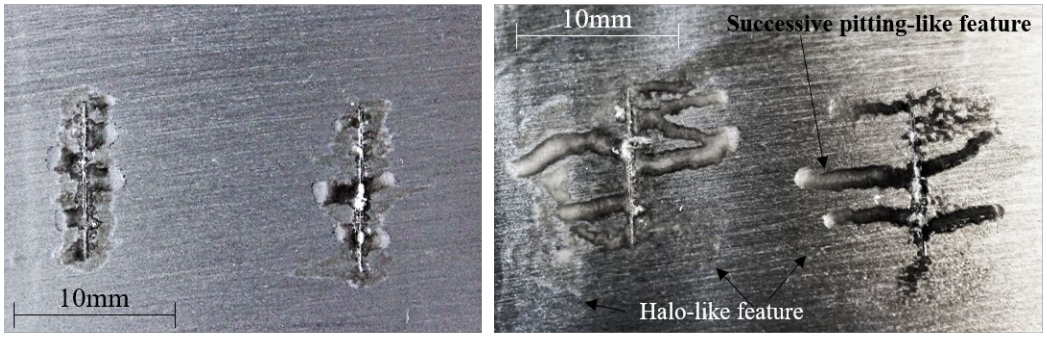

i) 120 hours ii) 453 hours

Figure 4.3.2g: aluminium alloy 6014 – alkaline cleaned and desmutted sample with a NSDL. Sample at 20°C and 80% RH, injected with 1µL of 2M HCl at i) 120 hours and ii) at 453 hours.

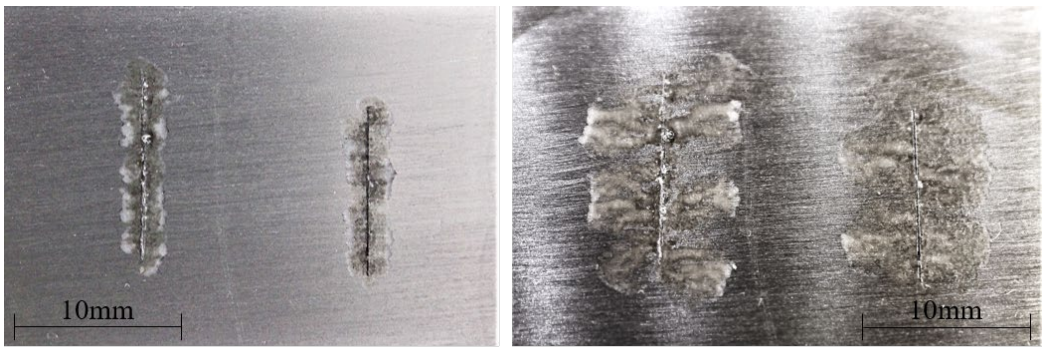

i) 120 hours ii) 453 hours

Figure 4.3.2h: aluminium alloy 6022 – alkaline cleaned and desmutted sample with a NSDL. Sample at 20°C and 80% RH, injected with 1µL of 2M HCl at i) 120 hours and ii) at 453 hours.

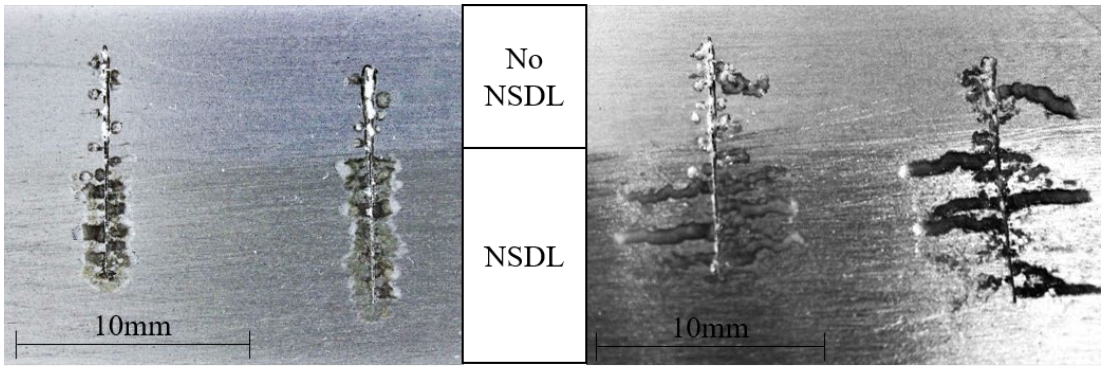

Figure 4.3.2i: aluminium alloy 6014 – alkaline cleaned and desmutted sample with c.a. 50:50 no NSDL. Sample at 20°C and 80% RH, injected with 1µL of 2M HCl at i) 120 hours and ii) at 453 hours.

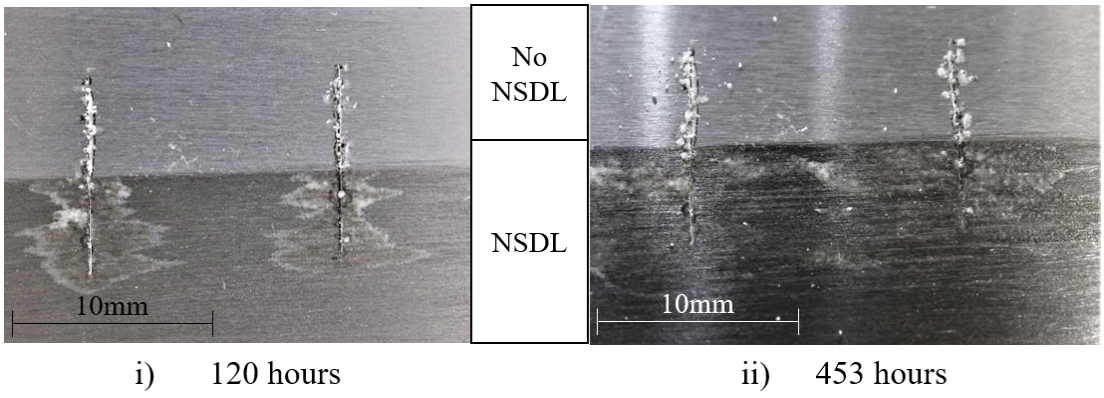

Figure 4.3.2j: aluminium alloy 6022 – alkaline cleaned and desmutted sample with c.a. 50:50 no NSDL. Sample at 20°C and 80% RH, injected with 1µL of 2M HCl at i) 120 hours and ii) at 453 hours.

The as received samples of AA6014 and AA6022 without a NSDL show a combination of both successive pitting and cosmetic FFC, with AA6014 suffering from more underfilm corrosion than the 6022. The AA6022 shows features comparable to successive pitting FFC, with no obvious surface active FFC, with little corrosion growth from the defect. The AA6014 shows both surface active and successive pitting FFC and corrosion further from the defect.

The as received samples of AA6014 and AA6022 with a NSDL show a combination of both successive pitting and surface active FFC that have travelled some distance

from the defect. The halo on the AA6014 appears to have travelled further from the defect. Filaments for both samples appear to travel outwards along the rolling direction and contain light heads and dark tails. The defects are covered with a bright, semi-translucent, liquid product likely to be the formation of aluminium hydroxide $Al(OH)_3$, which was insoluble in water and precipitates as white gelatinous flakes. In this case, there were no conclusive discussions at this point that would suggest one alloy is more susceptible to FFC than the other. This could be the effect of the how the NSDL is produced on the alloys.

The alkaline cleaned and desmutted samples of AA6014 and AA6022 without a NSDL both display successive pitting FFC with the filaments in the AA6014 travelling further from the defect than the AA6022. The AA6022 shows features comparable to successive pitting FFC, with little corrosion growth from the defect. In this case the AA6014 appears to be more susceptible to FFC, after 120 hours. This could be due to the composition of the alloy and the higher percentages of Cu and Mg, as shown in chapter 1. Surface treatment, caustic etching, would appear to depress the corrosion growth. Which was in-keeping with previous work on FFC on aluminium[267,268]

The alkaline cleaned and desmutted samples of AA6014 and AA6022 with a NSDL show a combination of both successive pitting and surface active FFC. AA6022 has a much clearer halo and very narrow and faint filaments compared to the AA6014. The halo on the 6014 appears to have travelled slightly further from the defect. The filaments and halo for both samples appear to travel outwards along the rolling direction. In this case, there are no conclusive discussions at this point that would suggest one alloy is more susceptible to FFC than the other. Again, this could be the effect of the how the NSDL is produced on the alloys.

The alkaline cleaned and desmutted samples of AA6014 and AA6022 with a c.a. 50:50 [no NSDL: NSDL] ([Top of image: bottom of image] respectively) show that the region of the AA6014 and AA6022 samples with no NSDL shows a slower FFC corrosion growth with more pit-like areas forming. The samples are similar until 453 hours where the AA6014 sample had one clear filament forming in each defect but the AA6022 sample does not. The NSDL region of the AA6014 and AA6022 shows a halo which is in keeping with discussion of surface active FFC which has travelled from the defect along the roll and NSDL direction. However, the halo is more clearly seen

on the AA6022 sample. The AA6014 sample also shows the defects appear to have filament formation and show corrosion growth in the roll and NSDL direction, where this is less clear for the AA6022 sample. The filaments on the AA6014 sample have the appearance of successive pitting FFC. Distance from the defect appears greater in the AA6022 when compared to the AA6014 which contradicts previous result. However, once the areas had been measured the results were in keeping with previous work as the corrosion areas were more clearly seen when using Photoshop.

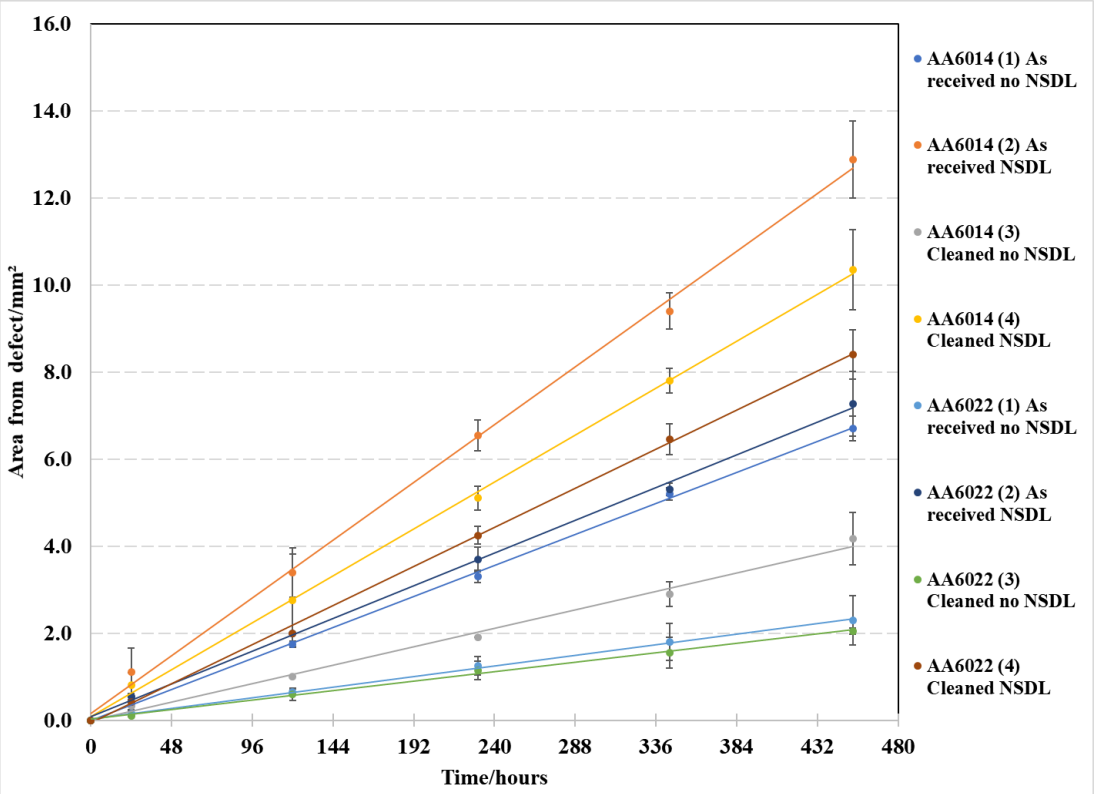

Figure 4.3.2k: Area of corrosion with respect to time for AA6014 and AA6022 samples. (1) Denotes aluminium alloy as received and a NSDL absent. (2) Denotes aluminium alloys as received and a NSDL present. (3) Denotes aluminium alloys cleaned and a NSDL absent. (4) Denotes aluminium alloys cleaned and a NSDL present. Samples at 20°C and 80% RH, injected with 1µL of 2M HCl for 453 hours. Y-error bars included.

Figure 4.3.2k shows a linear relationship between the 2 variables, as time increases, the area of corrosion increases. As no plateau is observed the corrosion mechanism has been maintained throughout the 453 hours and still has not terminated. This could be due to the sealed container and negligible loss in humidity or changes in temperature which has allowed the corrosion mechanism to continue. The graph also shows that

the presence of a NSDL influences the area of corrosion observed. When a NSDL is present a greater area of corrosion is observed. The samples that do not have a NSDL show they are less susceptible to FFC. The mean standard deviation for the samples were as follows: AA6014 no NSDL as received 0.11mm, AA6014 no NSDL cleaned 0.47mm, AA6014 NSDL as received 0.16mm, AA6014 NSDL cleaned 0.47mm, AA6022 no NSDL as received 0.22mm, AA6022 no NSDL cleaned 0.21mm, AA6022 NSDL as received 0.13mm, AA6022 NSDL cleaned 0.22mm.

Based on the data from figure 4.3.2k, the rate of FFC propagation for each of the 4 cleaned samples were calculated and can be seen in figures 4.3.2l and 4.3.2m. (The clean samples were chosen as during the experimental work that followed all the samples went through the sample preparation as described in Chapter 2). In general, Figure 4.3.2k shows: 1. as time passes, the area of corrosion increases, 2. The AA6014 samples have travel further from the defect compared to the AA6022, regardless of a NSDL, 3. The NSDL does influence the distance of corrosion from the defect as both the AA6014 and AA6022 corrosion area was larger when a NSDL was present.

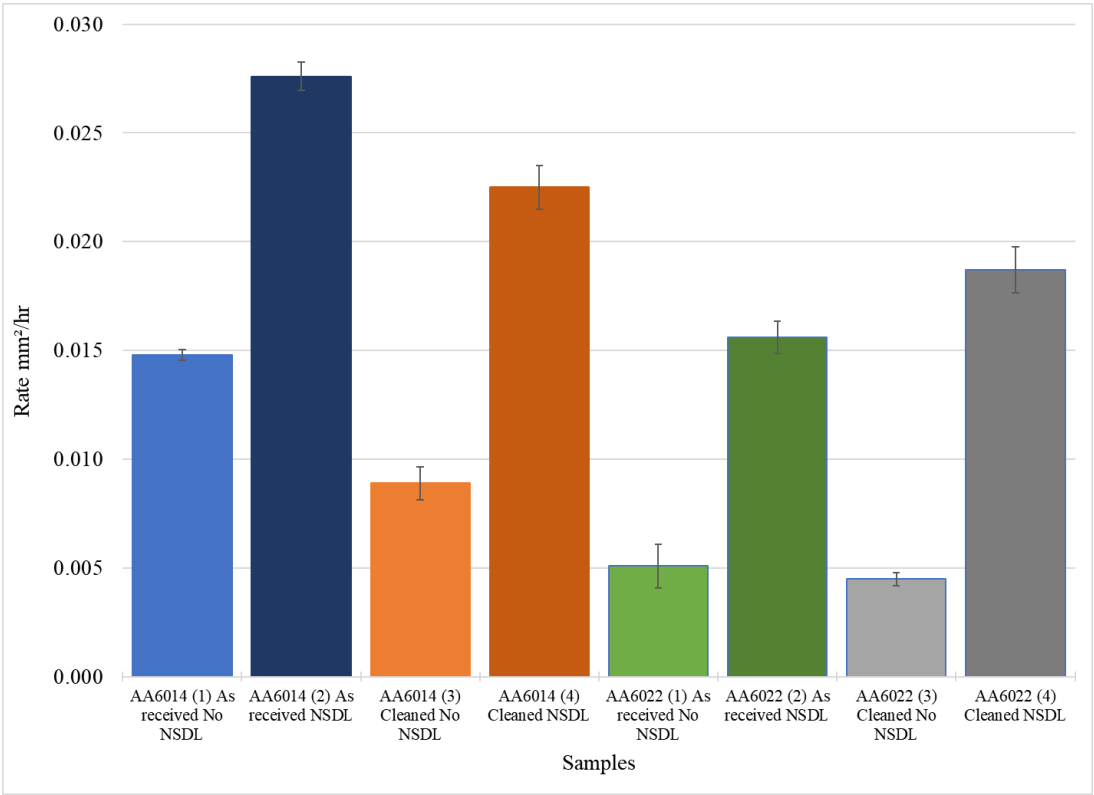

Figure 4.3.2l: Rate of FFC propagation, both in the presence and absence of NSDL for both alloys at 80% RH. Y-error bars included.

Figure 4.3.2l shows a difference in corrosion rate between the as received and the cleaned for samples with and without a NSDL. The mean standard deviation for the samples were as follows: AA6014 no NSDL as received 0.00025mm/h, AA6014 no NSDL cleaned 0.00065mm/h, AA6014 NSDL as received 0.00075mm/h, AA6014 NSDL cleaned 0.001mm/h, AA6022 no NSDL as received 0.001mm/h, AA6022 no NSDL cleaned 0.00075mm/h, AA6022 NSDL as received 0.0003mm/h, AA6022 NSDL cleaned 0.00105mm/h.

It is possible that the as received AA6014 has passivated more with time, whereas the AA6022 is more readily corroding. This would need further investigating is the samples where to be used as received, however, all other experiments were conducted on cleaned samples.

Sample type	No NSDL	NSDL	Difference	SD	No NSDL	NSDL	Difference	SD
As received Sample a	0.0151	0.0283	0.0132	0.0066	0.0061	0.0164	0.0103	0.0052
As received Sample b	0.0146	0.0270	0.0124	0.0062	0.0041	0.0149	0.0108	0.0054
Difference	0.0005	0.0013	0.0008	0.0004	0.0020	0.0015	0.0005	0.0002
Cleaned Sample a	0.0096	0.0235	0.0139	0.0070	0.0048	0.0198	0.0150	0.0075
Cleaned Sample b	0.0081	0.0215	0.0134	0.0067	0.0042	0.0177	0.0135	0.0068
Difference	0.0015	0.0020	0.0005	0.0003	0.0006	0.0021	0.0015	0.0008

Table 10: Rates of FFC propagation, both in the presence and absence of NSDL for both alloys at 80% RH. With the difference between rates shown.

Table 10 shows: 1. the presence of a NSDL increases the rate of FFC propagation significantly, 2. in most cases, whether a NSDL is present or not AA6014 has a larger rate of FFC propagation than AA6022. The only exception above is for samples AA6014 (4) and AA6022 (4) where the samples were cleaned prior to the experiment. This could be linked to the composition of the alloys, chapter 1. AA6022 only has between 0.01 to 0.11% of copper and 0.05 to 0.2% of iron present whereas AA6014 has approximately 0.25% copper and approximately 0.35% of iron, this potentially increases the number density of the existing Cu-rich and Fe-rich intermetallic phases

when making the alloy and tempering it for use. This investigation suggests that the main condition for FFC to continue to propagate, at elevated rates, is the presence of a NSDL. As the NSDL has a more andocially susceptible surface layer, as seen in chapter 3.

In this experiment, the lower potential has increased the rate of FFC propagation for these samples. Finally, the graph shows that 6022 is less susceptible to both SA-FFC (in the presence of an NSDL) and SP-FFC (in the absence of NSDL) when compared to AA6014, this was not clear from the results obtained in chapter 3. This set of results show that AA6022 has a slower corrosion rate, and therefore slightly more corrosion resistant compared to AA6014 which supports the first set of results in this chapter.

4.3.3. A systematic investigation of the influence of RH on the rate of FFC propagation

Based on the results in the previous sections, the difference in rates calculated suggest that an RH of 80% has a quicker rate of FFC propagation than 93%, a systematic investigation was conducted to establish the effect of RH on the rate of FFC propagation and type of cosmetic corrosion. The investigation used the same surface treatment regimens and quantity of initiating HCl for all specimens of both alloys as noted in the sections above.

The following images show images across the range of humidities at 1872 hours (78 days), followed by graphs showing the area of corrosion with respect to time from the defect at all % RHs. The images shown below have been chosen as the corrosion can be seen clearly. Some of the samples were positioned at angles to reduce the reflection as well as show the corrosion. Different versions of these images were used to take measurements. These images were taken so that no parallax errors were encountered. Between the two images a clearer understanding of the surface corrosion was found, and a more accurate area measurement was recorded.

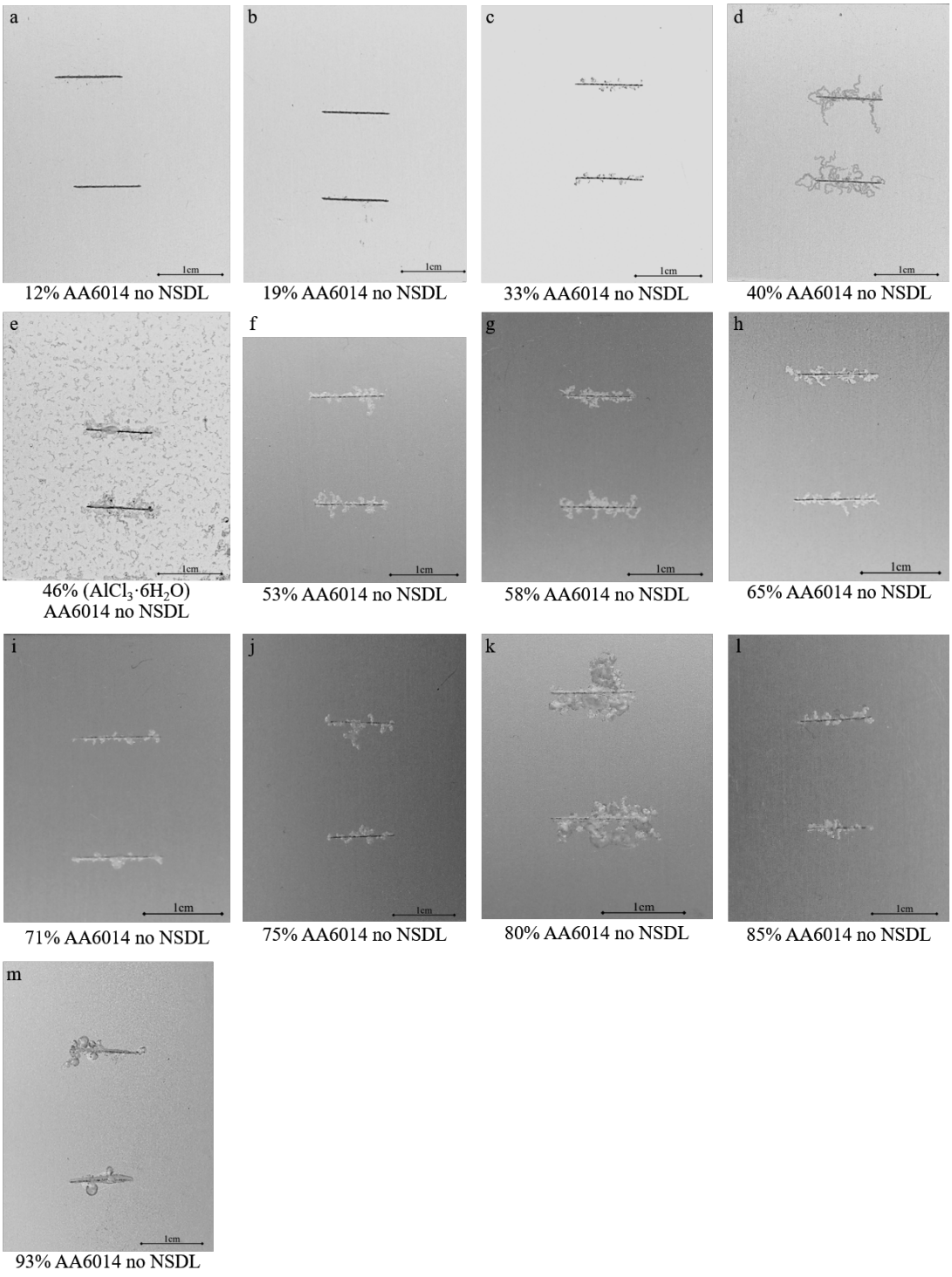

Figure 4.3.3a: AA6014 without NSDL – FFC after 1872 hrs. Samples at 20°C and injected with 1µL of 2M HCl

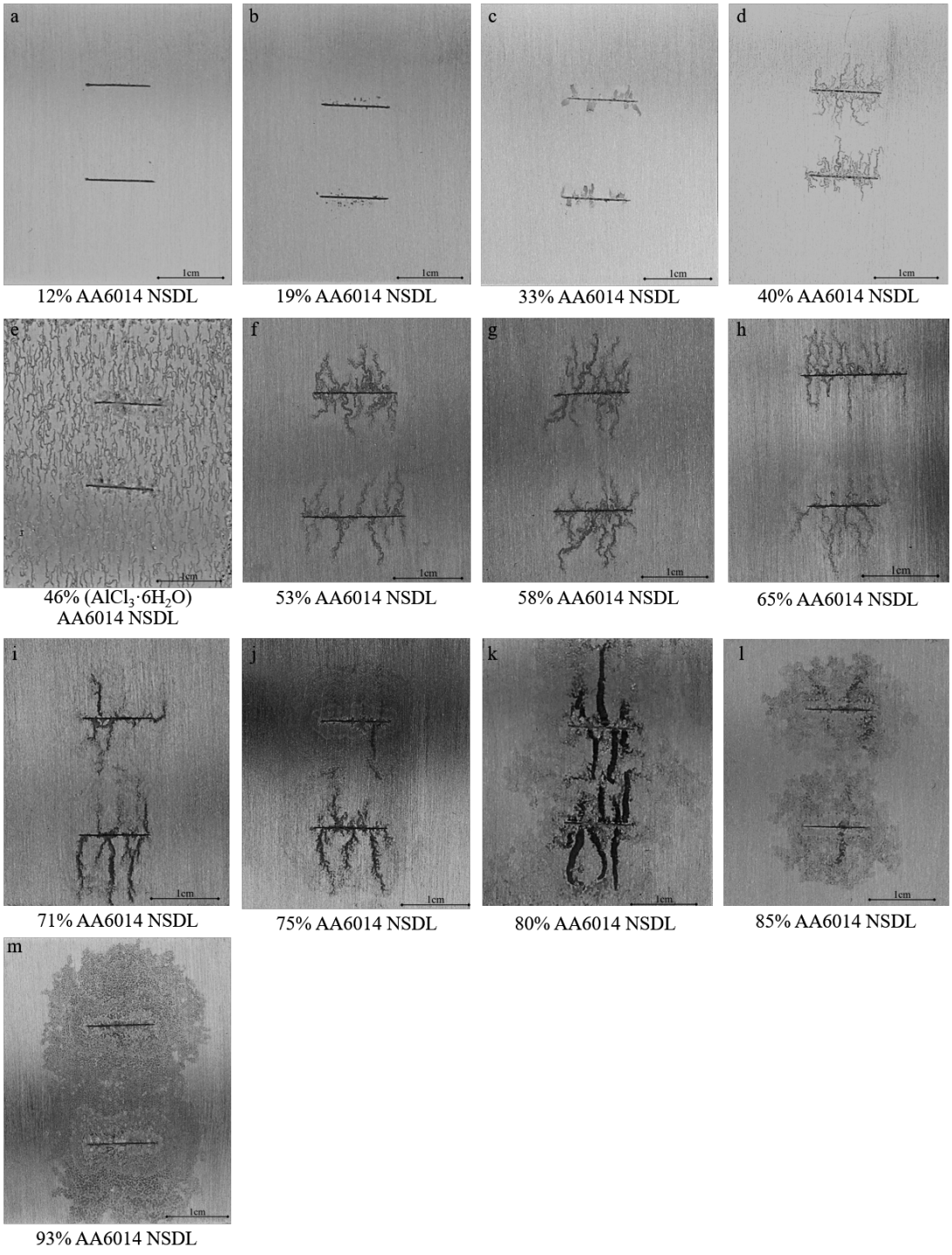

Figure 4.3.3b AA6014 with NSDL – FFC after 1872 hrs. Samples at 20°C and injected with 1µL of 2M HCl

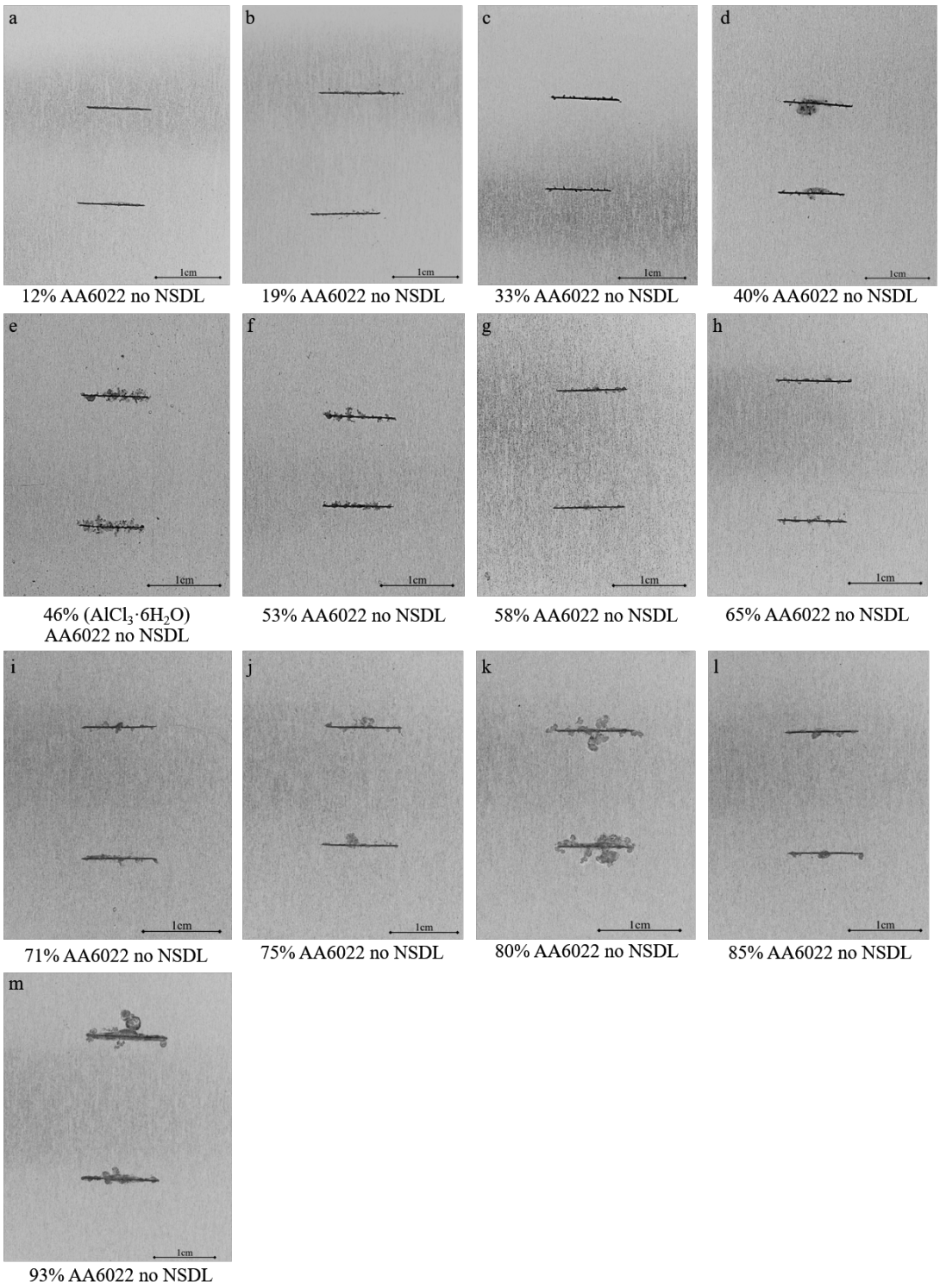

Figure 4.3.3c: AA6022 without a NSDL – FFC after 1872 hrs. Samples at 20°C and injected with 1µL of 2M HCl

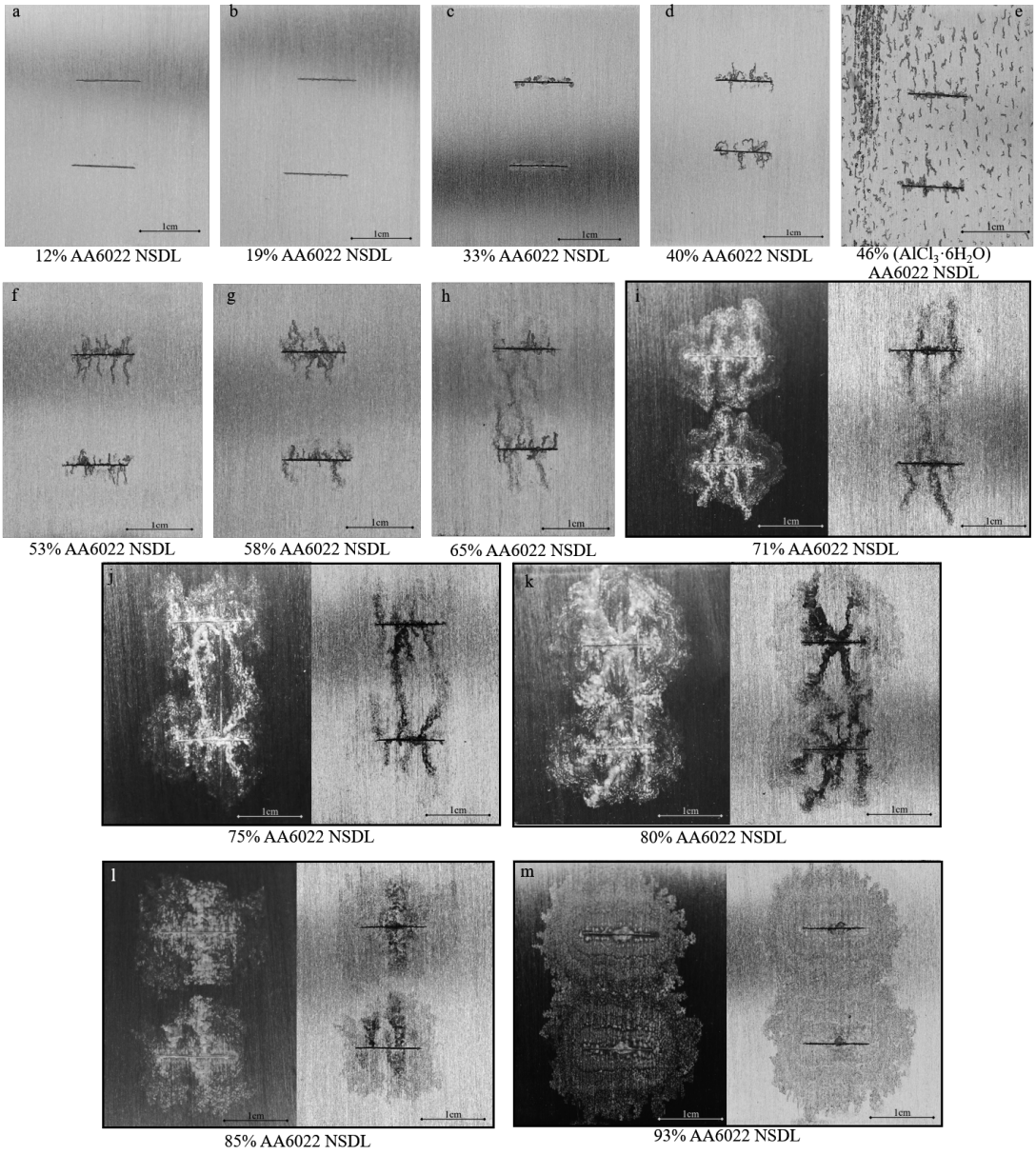

Figure 4.3.3d: AA6022 with a NSDL – FFC after 1872 hrs. Samples at 20°C and injected with 1µL of 2M HCl. Images i to m show the same sample photographed at different angles to show the corrosion area more clearly. The lighter of the 2 images is of a flat samples and the darker is of the same sample raised at a shallow angle (<5°).

Figure 4.3.3a for AA6014, no NSDL, and FFC is observed from 19% to 93% the FFC observed is SP-FFC with no features to suggest SA-FFC. 40% has many thin filaments that have travelled a large distance from the defect, relative to all other AA6014 no NSDL samples. This could be a factor of having a RH close to that of $AlCl_3$ and slight fluctuations in RH when the samples were removed for photographing. 53% RH to 75% RH show SP-FFC but there is no clear indication of size of growth, or rate, from the images alone. 80% RH shows a significant increase in the number of filaments, width of filaments and length of filaments. 85% and 93% RH images are more in line with the results seen for 53% to 75% RH, fewer filaments and close to the defect.

Figure 4.3.3b for AA6014, NSDL, show at RH 53% there is a faint halo, associated with the presence of SA-FFC, and filaments associated with SP-FFC.; RH 58% & 65% showed an increase in the area covered by the FFC, but had similar features to 53%; RH 71% & 75% showed an increase in the area covered by the SA-FFC but fewer filaments for SP-FFC; RH 80% the sample surface is almost completely covered with SA-FFC and contains a few wide filaments for SP-FFC. These filaments are wider than the samples at lower RH and darker. The darkness could be a result of surface roughness due to the corrosion product, it could be due to the depth of the filament, or both. It could be more detrimental if the corrosion reaction penetrated the bulk alloy. RH 85% & 93% - there are no clearly observable SP-FFC filaments. There is an increase of SA-FFC area as RH increases, but this area is smaller than that seen for 80% RH. From 71% Rh to 93% RH the samples appear to have multiple halos suggesting a 2^{nd} & 3^{rd} generation corrosion growth of SA-FFC from the defect. This is less clear in 80% RH and could be the reason behind the larger SA-FFC area and presence of the SP-FFC filaments.

Figure 4.3.3c for AA6022, No NSDL, FFC is observed from 19% to 93% the FFC observed is SP-FFC with no features to suggest SA-FFC. 33% RH to 75% RH show SP-FFC but there is no clear indication of size of growth, or rate, from the images alone. 80% RH shows a significant increase in the number of filaments, width of filaments and length of filaments. 85% and 93% RH images are more in line with the results seen for 53% to 75% RH, fewer filaments and close to the defect. Although like the images seen in Figure 4.3.3a for AA6014 with no NSDL, the images in figure 4.3.3c appear to show less FFC, suggesting that AA6022 with no NSDL is more corrosion resistant compared to AA6014 with no NSDL.

Figure 4.3.3d for AA6022, NSDL, shows that FFC is present from 33%, with some pitting observed. RH 40% shows an increase in SP-FFC, again, this could be a result of fluctuation in RH due to the samples being removed from the 40% RH environment to allow images to be taken. RH 53% there is a faint halo, associated with the presence of SA-FFC, and filaments associated with SP-FFC.; RH 58% & 65% showed an increase in the area covered by the FFC, but had similar features to 53%; RH 71% & 75% showed an increase in the area covered by the SA-FFC but fewer filaments for SP-FFC; RH 80% the sample surface has a more dense and slightly larger covering of SA-FFC and contains a few wide filaments for SP-FFC. Compared to the 80% RH sample for AA6014 NSDL, the corrosion growth is smaller and the growth of AA6022 NSDL is more in line with the growth across the RHs. RH 85% the SA-FFC is smaller than that of 80% and less densely populated with corrosion features. It has some faint filaments, therefore some SP-FFC is present. RH 93% - there are no clearly observable SP-FFC filaments. There is an increase of SA-FFC, like AA6014 NSDL samples at 80% RH. From 71% Rh to 93% RH the samples appear to have multiple halos suggesting a 2^{nd} & 3^{rd} generation corrosion growth of SA-FFC from the defect.

The images for both alloys show small amounts of FFC observed on both alloys from 19% to 46%. This could be a result of removing samples for photographing and a brief increase in the RH. This is not an expected result as during the investigation it was found the RH of the more likely corrosion products $AlCl_3$ has an RH of 46% ±2%. Once the RH is above 46% it is likely to see corrosion, which can be seen in figures 4.3.3a to 4.3.3d.

There is a significant amount of background activity away from the scribed area when the saturated salt $AlCl_3$ is used as the RH controlling electrolyte. This is because hydrolysis of acidic Al^{3+} cations lead to acidification with time and an increase of HCl in the solution, some of which will be volatile. Therefore, HCl vapour will be present in the chamber which will tend to inoculate FFC at pin holes or other defects in the nominally intact PVB coating. Since some FFC was observed at RH levels well below the deliquescence point of $AlCl_3$ (46%), then it is possible that $AlCl_3$ is not the only salt present in the head electrolyte.

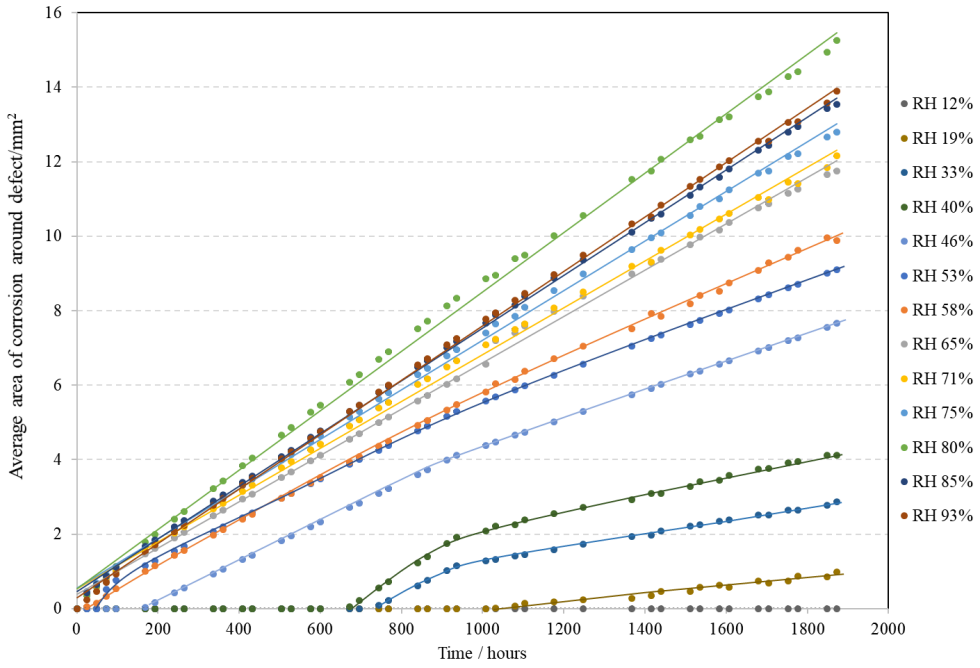

Figure 4.3.3e: Corrosion area with respect to time for percentage RH from 12% to 93% for AA6014 without a NSDL. Samples at 20°C and injected with 1µL of 2M HCl. Y-error bars included.

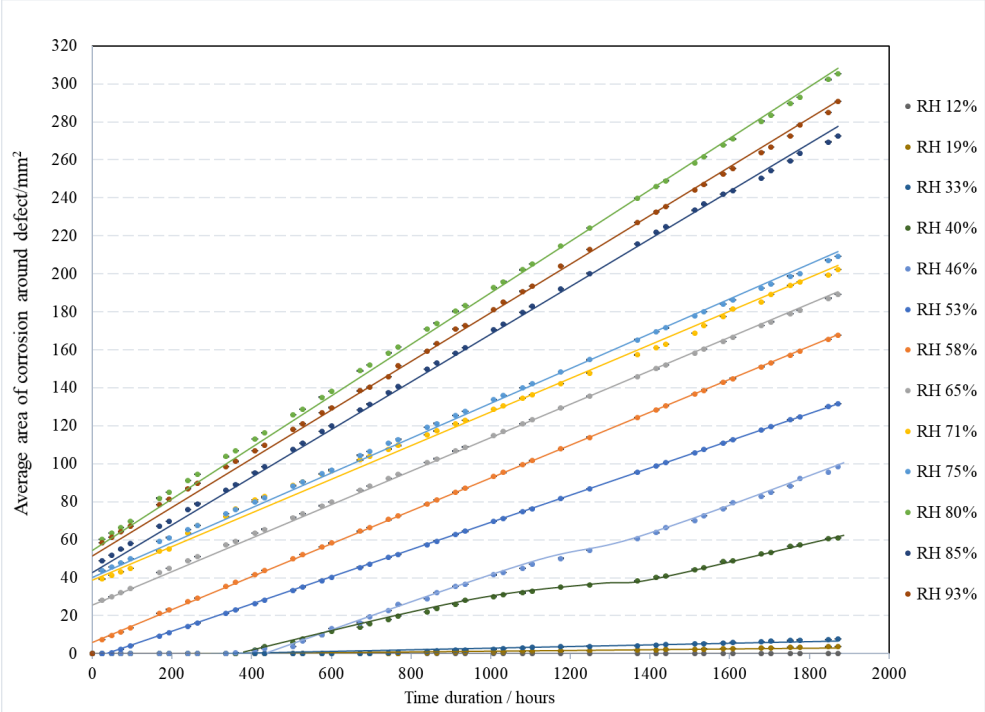

Figure 4.3.3f: Corrosion area with respect to time for percentage RH from 12% to 93% for AA6014 with a NSDL. Samples at 20°C and injected with 1µL of 2M HCl. Y-error bars included.

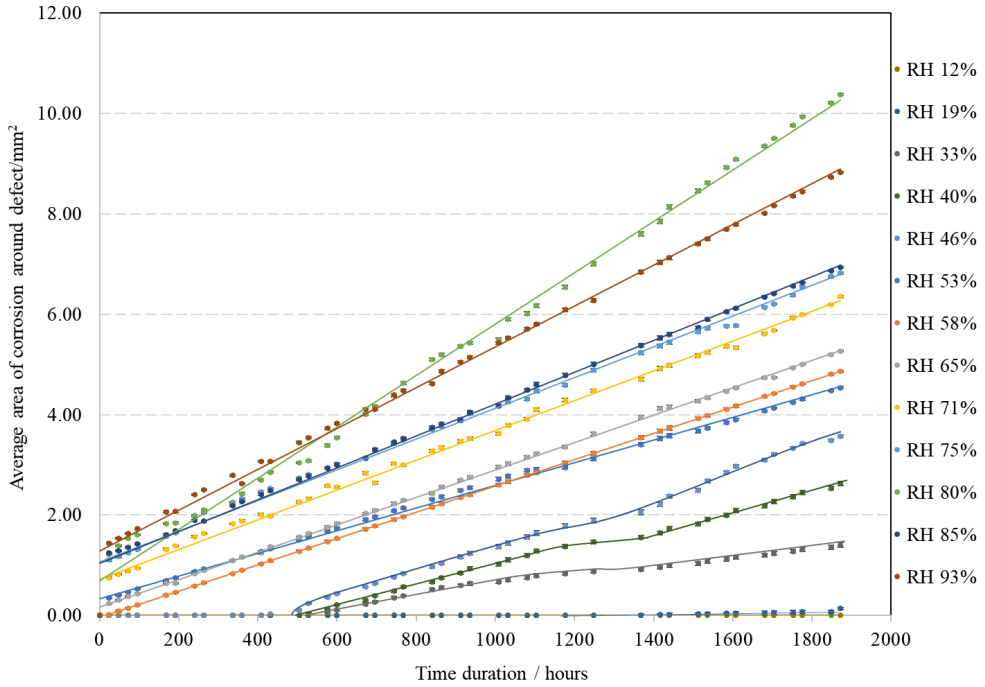

Figure 4.3.3g: Corrosion area with respect to time for percentage RH from 12% to 93% for AA6022 without a NSDL. Samples at 20°C and injected with 1µL of 2M HCl. Y-error bars included.

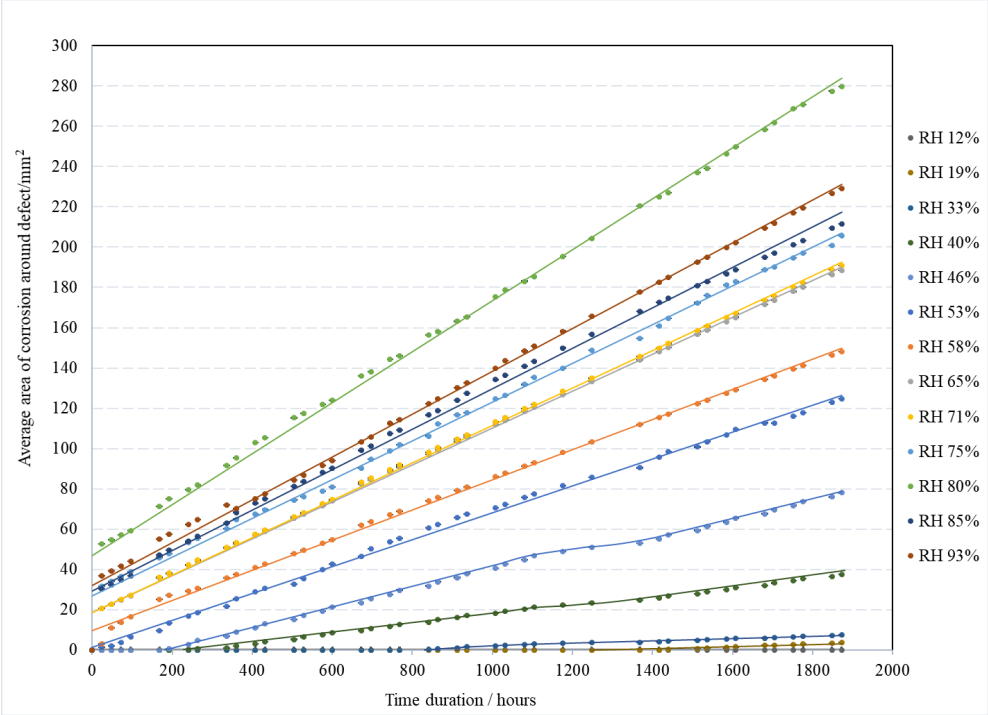

Figure 4.3.3h: Corrosion area with respect to time for percentage RH from 12% to 93% for AA6022 with a NSDL. Samples at 20°C and injected with 1µL of 2M HCl. Y-error bars included.

Figures 4.3.3e to 4.3.3h illustrate that the area and rate of FFC increases as the relative humidity increases and that the corrosion growth in all samples is linear which agrees with most investigations of FFC on Aluminium alloys which report that the rate of FFC advance has a linear relationship between area (or length) vs time. The standard deviations in the corrosion area for the samples can be seen in Table 11 below:

Sample	AA6014 no NSDL	AA6014 NSDL	AA6022 no NSDL	AA6022 NSDL
%RH	mm^2	mm^2	mm^2	mm^2
12	0.0000	0.0000	0.0000	0.0000
19	0.0044	0.0244	0.0080	0.0070
33	0.0059	0.0339	0.0204	0.0115
40	0.0074	0.0372	0.0213	0.0207
46	0.0114	0.0376	0.0214	0.0205
53	0.0120	0.0493	0.0222	0.0228
58	0.0103	0.0500	0.0219	0.0269
65	0.0115	0.0487	0.0217	0.0297
71	0.0111	0.0504	0.0223	0.0296
75	0.0109	0.0477	0.0216	0.0307
80	0.0114	0.0500	0.0231	0.0301
85	0.0125	0.0503	0.0220	0.0305
93	0.0115	0.0500	0.0216	0.0300
Av	0.0093	0.0407	0.0190	0.0223

Table 11: Standard deviation of the corrosion area for the different samples

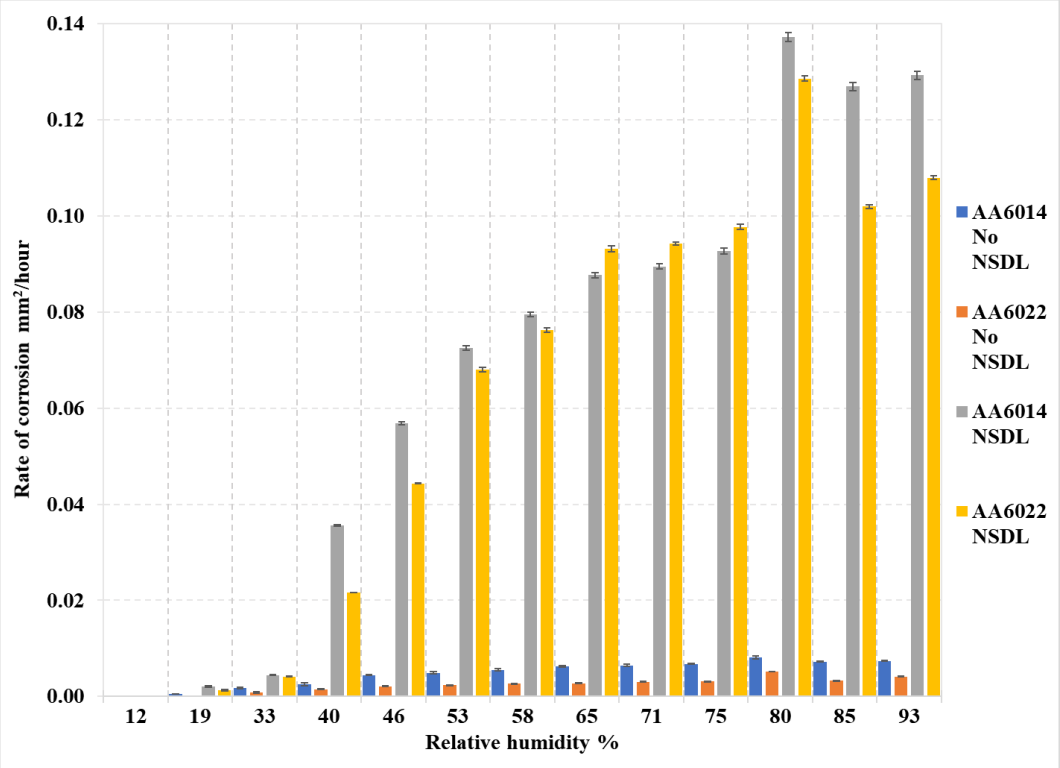

Figure 4.3.3i: How the rate of FFC propagation, both in the presence and absence of NSDL varies with % RH for AA6014 and AA6022. Y-error bars included.

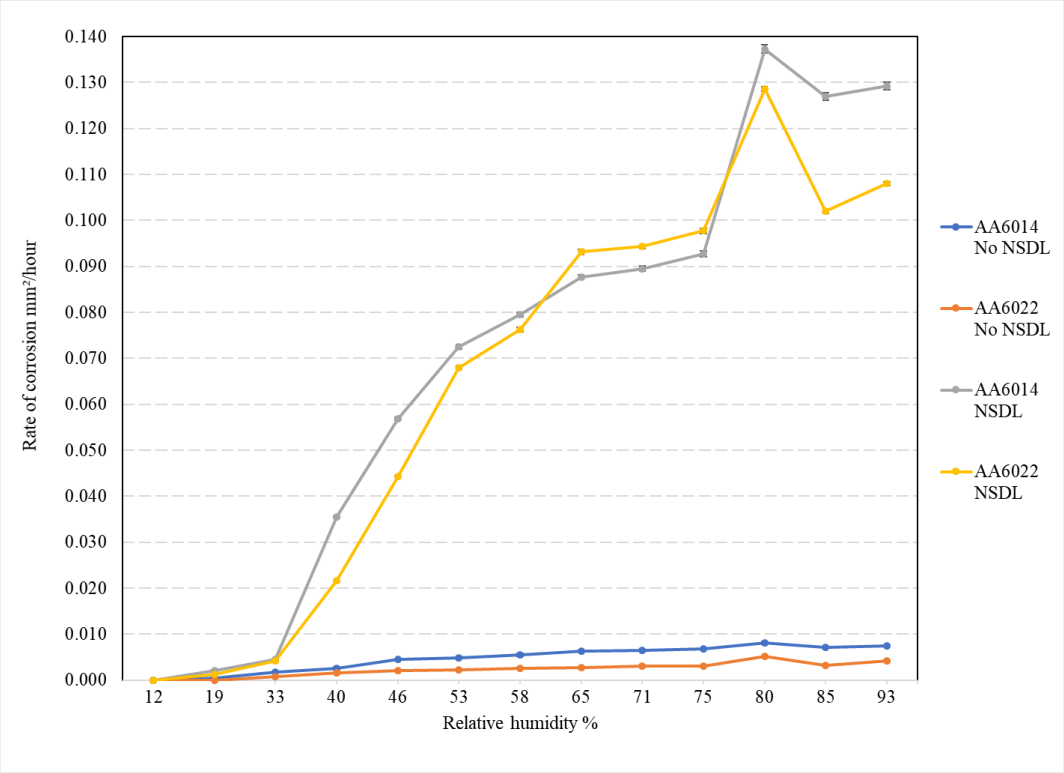

Figure 4.3.3j: How the rate of FFC propagation, both in the presence and absence of NSDL varies with % RH for AA6014 and AA6022. Y-error bars included.

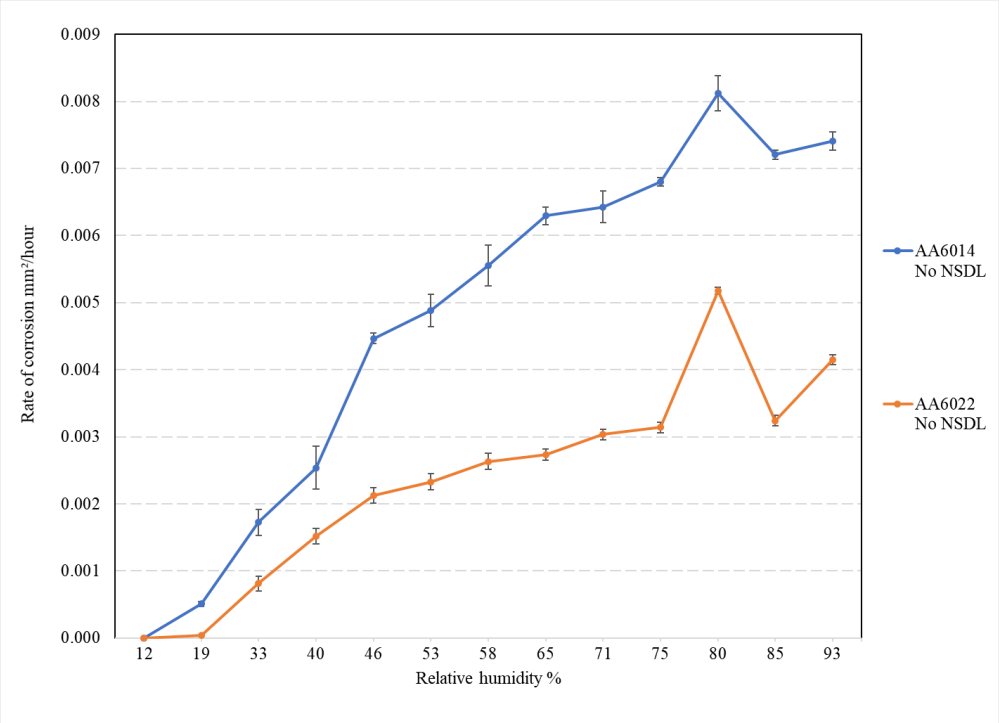

Figure 4.3.3k: How the rate of FFC propagation varies with % RH – AA6014 and AA6022 without a NSDL. Y-error bars included.

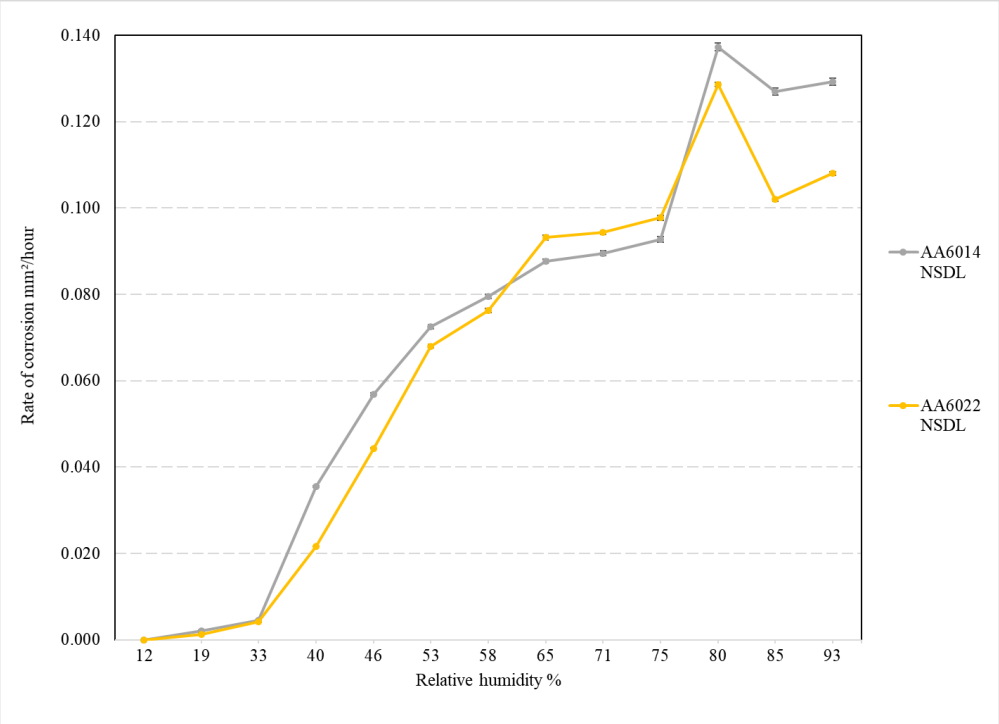

Figure 4.3.3l: How the rate of FFC propagation varies with % RH – AA6014 and AA6022 with a NSDL. Y-error bars included.

The graphs in figures 4.3.3i to 4.3.3l shows that there is little fluctuation in corrosion growth, relative to relative humidity, with samples without a NSDL, however corrosion growth for the AA6014 samples is slightly more elevated than the AA6022. In figures 4.3.3i, 4.3.3j and 4.3.3l, when a NSDL is present, AA6014 has the quicker corrosion rate until 58% to 75% rh, where AA6022 had the more elevated rate. From 80% RH AA6014 has the higher corrosion rate. The standard deviations in the corrosion rate for the samples can be seen in table 12 below:

	AA6014					
	No NSDL			NSDL		
%RH	sample 1 mm²/hour	sample 2 mm²/hour	SD mm²/hour	sample 1 mm²/hour	sample 2 mm²/hour	SD mm²/hour
0	0.0000	0.0000	0.00000	0.0000	0.0000	0.00000
19	0.0005	0.0005	0.00003	0.0022	0.0018	0.00019
33	0.0019	0.0015	0.00019	0.0044	0.0045	0.00008
40	0.0022	0.0029	0.00032	0.0354	0.0357	0.00015
46	0.0045	0.0044	0.00008	0.0566	0.0572	0.00032
53	0.0046	0.0051	0.00024	0.0721	0.0729	0.00044
58	0.0059	0.0053	0.00030	0.0790	0.0800	0.00049
65	0.0062	0.0064	0.00013	0.0871	0.0882	0.00055
71	0.0062	0.0067	0.00024	0.0889	0.0901	0.00056
75	0.0069	0.0067	0.00007	0.0922	0.0933	0.00059
80	0.0084	0.0079	0.00026	0.1364	0.1382	0.00092
85	0.0073	0.0071	0.00007	0.1261	0.1278	0.00084
93	0.0073	0.0075	0.00014	0.1284	0.1302	0.00086

	AA6022					
	No NSDL			NSDL		
	sample 1 mm²/hour	sample 2 mm²/hour	SD mm²/hour	sample 1 mm²/hour	sample 2 mm²/hour	SD mm²/hour
	0.0000	0.0000	0.00000	0.0000	0.0000	0.00000
	0.0000	0.0000	0.00000	0.0014	0.0012	0.00011
	0.0009	0.0007	0.00011	0.0043	0.0040	0.00012
	0.0016	0.0014	0.00011	0.0216	0.0216	0.00001
	0.0022	0.0020	0.00012	0.0442	0.0445	0.00012
	0.0024	0.0022	0.00012	0.0676	0.0684	0.00044
	0.0028	0.0025	0.00012	0.0768	0.0759	0.00046
	0.0027	0.0028	0.00008	0.0926	0.0937	0.00056
	0.0030	0.0031	0.00008	0.0947	0.0939	0.00036
	0.0031	0.0032	0.00008	0.0983	0.0972	0.00058
	0.0051	0.0052	0.00005	0.1281	0.1291	0.00053
	0.0032	0.0033	0.00008	0.1024	0.1016	0.00040
	0.0041	0.0042	0.00007	0.1084	0.1076	0.00043

Tables 12: Standard deviation of the corrosion area for the AA6014 and AA6022 respectively.

Previous work[250,4] investigated FFC on steel sheets as there was a known range of %RH for FFC to occur. The work found that for FFC to occur a %RH of 65% to 95% was required with an RH of between 85 to 95% showing the optimum conditions for FFC with %RH c.a. 85% producing wider filaments however an RH of 95% produced blisters[5, 6, 10, 11]. Similar results have been found for aluminium alloys, Persson et al[184,255] , the largest FFC was observed when RH was at 85% and a drop in FFC area at 95% RH. Their results show an increase in FFC area as %RH increases, except for 95%. It was concluded that the optimal %RH for FFC was 85%, complementing previous work. However, the work in this chapter has repeatedly shown that an RH of 80% produces the largest area and rate of corrosion for both AA6014 and AA6022. There was a significant difference, for both alloys, between the corrosion rates for surfaces with and surfaces without a NSDL, as seen in table 13, below:

Mean	Rate mm²/hour					
	AA6014			AA6022		
%RH	No NSDL	NSDL	Difference	No NSDL	NSDL	Difference
12	0.00000	0.00000	0.00000	0.00000	0.00000	0.00000
19	0.00051	0.00202	0.00152	0.00004	0.00132	0.00128
33	0.00172	0.00446	0.00274	0.00081	0.00416	0.00335
40	0.00254	0.03552	0.03299	0.00152	0.02162	0.02010
46	0.00447	0.05690	0.05244	0.00213	0.04436	0.04223
53	0.00489	0.07249	0.06761	0.00233	0.06801	0.06568
58	0.00556	0.07948	0.07392	0.00263	0.07632	0.07368
65	0.00629	0.08768	0.08139	0.00273	0.09318	0.09044
71	0.00643	0.08950	0.08308	0.00304	0.09429	0.09126
75	0.00680	0.09274	0.08594	0.00314	0.09775	0.09461
80	0.00812	0.13729	0.12918	0.00518	0.12860	0.12342
85	0.00721	0.12697	0.11976	0.00324	0.10201	0.09877
93	0.00741	0.12930	0.12189	0.00415	0.10800	0.10385

Table 13: Rates and difference in rate between NSDL and no NSDL for all % RH for AA6014 and AA6022 respectively.

Previous work on AA6016 found that, at 80% RH and 40°C, the corrosion propagation rates were c.a. 0.1 mm h^{-1} and 0.01 mm h^{-1} for samples with and without a NSDL, respectively[2,3]. Equivalent results were obtained for AA6111 for samples at 60% RH and 40°C. The corrosion propagation rates were c.a. 0.04 mm h^{-1} and 0.01 mm h^{-1} for samples with and without a NSDL, respectively[5,214]. The corrosion propagation rates

obtained in this investigation found that for AA6014, at 80% RH and 20°C, were c.a. 0.1 mm h^{-1} and 0.01 mm h^{-1} for samples with and without a NSDL, respectively, and the corrosion propagation rates for AA6022, at 80% RH and 20°C were c.a. 0.1 mm h^{-1} and 0.004 mm h^{-1} for samples with and without a NSDL, respectively.

Previous work[3,5] discussed that when a NSDL is removed due to the anodic dissolution, SP-FFC is observed as a secondary FFC attack. As shown in the images in this chapter, when a NSDL is not present the type of FFC observed is SP-FFC. This suggested that the samples with a NSDL that exhibit SP-FFC are likely to have had the NSDL removed during SA-FFC for this observation to exist. Additionally, previous work found that the features associated with SP-FFC tended to trail the SA-FFC front when a NSDL is present. This is evident in the images in figures 4.3.1a (trial 4), 4.3.2a-c, e, g and i, and 4.3.3b and d where the filaments are observed to be some distance behind the halo feature. Therefore, it can be inferred, based on previous work that the SP-FFC is penetrating the bulk metal either due to the samples having no NSDL or after the NSDL has been removed suggesting that SP-FFC does not depend on surface deformation. As the images in this chapter show, when SP-FFC is present, the filaments do not always have a specific direction. On samples where a NSDL was present, the filaments move slightly more in the roll direction, or the direction of the NSDL. But they do move sideways as well as forward, this was also noted in previous work. Also noted in previous work, and in figures 4.3.3b and e, the filaments do not cross, neither do the halos. It is possible that due to the head and edge of the filaments, and the leading edge of the halo, undergoing anodic dissolution, $Al \rightarrow Al^{3+} + 3e^-$ and cathodic reduction in the trailing (tail) region of the filament or inner part of the halo, $O_2 + 2H_2O + 4e^- \rightarrow 4OH^-$ that the filament is polarised and experiencing a repulsive force between filaments and when two halos approach. This would explain some of the area shapes seen in figures 4.3.3b and d.

As found in previous work[164,165,184,238,239,269,270], the NSDL in the head has dissolved and the electrolyte within the head is in direct contact with the bulk alloy. The tail contains the dry corrosion products by the hydrolysis of the Al^{3+}ions forming a mixture of aluminium oxide and aluminium hydroxide. This section is dry as it does not contain any water-soluble electrolyte. As a result, water is drawn to the head via osmosis. If the %RH of the environment is low, then the water is drawn from the corrosion product, thereby drying it. If the environment is at a higher %RH, then water is drawn

from the environment as well as from the corrosion product. Once the corrosion product can no longer donate H^+ from the hydrolysis reaction of:

$Al(H_2O)_6^{3+}$, $Al(H_2O)_6^{3+} \rightarrow Al(H_2O)_5(OH)^{2+} + H^+$,

followed by $Al(H_2O)_5(OH)^{2+} \rightarrow Al(H_2O)_4(OH)^{2+} + H^+$, etc.,

Then the corrosion mechanism stops. If the sample is in an environment of higher %RH, then the H^+ evolution is maintained for longer and is produced at a quicker rate and therefore the corrosion rate increases with the increase of humidity. The dip in corrosion rate after 80% RH suggests that the tail could be saturated which could reduce the rate, and/or quantity of oxygen diffusion through the tail.

It has also been documented[5,249] that for surfaces without a NSDL present, the initial form of corrosion is intergranular. If there is a greater quantity of copper at intergranular boundaries at the surface then the quantity and distance of SP-FFC is likely to increase. As the images in this chapter show, AA6014 had more SP-FFC on samples without a NSDL, and with samples with a NSDL, than the AA6022. This could be attributed to the composition found in table 4 in chapter 1. The schematic model representing SP-FFC can be seen in figure 3.3.3b.

Other work[2,10,51], identified that during the etching stagein the surface preparation, using NaOH, can cause aluminium alloys containing c.a. 95%, with a high copper content, to have a copper-rich surface. The aluminium content is up to 97% for AA6014 and between 96.7% and 98.7% for AA6022. So although the Al percentage is greater than 95% there is still a possibility of Cu-rich surfaces. The Cu content for AA6014 contains up to 0.25% where AA6022 only contains between 0.01 to 0.11%. So although both alloys have a high Al content, AA6014 has a higher quantity of Cu present. This could explain why AA6014 generally has a higher corrosion rate than AA6022.

Previous work[164] identified that the inclusion of other elements in the alloy composition can reduce corrosion resistance, for example copper, iron, lead, magnesium, and zinc all have a negative effect on corrosion protection but may be vital for the intended use of that alloy. AA6014 contains a great % of copper and iron than AA6022 and a similar quantity of magnesium. AA6022 contains a higher quantity of zinc, as shown in table 4 in chapter 1.

4.4 Conclusions

- All AA6014 and AA6022 samples in %RH greater than 12% exhibited corrosion. %RH below 46% showed pitting corrosion, rather than successive pitting as no filaments were observed. The only exception being AA6014 with a NSDL at 40%.
- At lower %RH there the rate of FFC propagation was small and increases at c.a. 33% - 40%. This could be due to the sample boxes being opened briefly to monitor the %RH and to remove samples for images.
- For %RH between 53% and 80%, both alloys with a NSDL exhibited a mixture of rapid SA-FFC and a secondary, slower SP-FFC. After 80% both alloys show a reduction in SP-FFC with zero SP-FFC observed at 93% RH.
- The samples without a NSDL exhibit a mix of pitting and SP-FFC. SP-FFC occurs due to the absence of a NSDL. The surfaces with no NSDL see a slight change in corrosion rate between %RHs of 53% to 75% but do have a peak corrosion at 80% RH.
- In all cases 80%RH has the largest rate of FFC propagation and showed most clearly the 2 types of FFC: surface active and successive pitting. Prior to 80%RH successive pitting is the more dominant FFC. Beyond 80%RH surface active FFC is more dominant.
- AA6014 surfaces, with and without a NSDL, exhibit a higher rate of FFC propagation than the AA6022 samples. This result was not apparent in chapter 3 based on their surface potentials alone as there were no significant differences between the surface potentials. This could potentially be due to the composition of the alloys. Since there is more Cu and Fe in the AA6014, then the bulk alloy will be a marginally better cathode. So if the NSDL is acting sacrificially then a more effective cathode on the bulk alloy will produce a faster rate of dissolution.
- This investigation suggested that the optimum conditions required for FFC initiate and propagate is a RH of 80% and the presence of a NSDL. This is like the findings discussed in the introduction. A considerable number of previous works focused on 75%, 85% and 95% RH and omitted 80%, as a result they may have missed some important result, and it is also possible that these alloys behave slightly differently to those investigated before.
- Although they were not measured, visually it is clear that the samples with a NSDL show the filament width increasing as %RH increases, up until 80% RH, after which

the filament disappears. Again, this is in line with work discussed in the introduction to this chapter.

- A saturated salt solution of Aluminium Chloride hexahydrate produced a % RH of 46% at 20°C. This is higher that the %RH for aluminium chloride at 27°C which had a RH of 37%. This %RH saw an increase in corrosion rate, but also a difference in surface corrosion appearance. The corrosion rate increases with the increase of %RH.

Chapter 5 – The effect of thermal treatment and presence of a NSDL on the type and rate of FFC on AA6014 and AA6022 using time-lapse photography, and SKP.

5.1 Introduction

Aluminium sheet alloys of the 6000 of the T4 temper, have several desirable characteristics, strength, and formability. The sheets can then undergo a further thermal treatment, known as paint bake. This process increases the strength of the alloy by forming intermetallic precipitates. The paint bake process is dependent on the initial formation of the sheet alloys, therefore a variety of techniques and treatments are used to increase the paint bake response 96. Although Aluminium Alloys of the 6000 series are relatively resistant to corrosion, the presence, and increase, of intermetallic precipitates increases their possibility of undergoing intergranular corrosion, IGC (Intergranular corrosion)[97]. AA6xxx series alloys show a considerable increase in strength due to the addition of c.a. 1 wt. % magnesium and silicon. They have been used in industry for c.a. 90 years and have been continually tested and new alloys produced. The phases of the AA6xxx series have been investigated for over 70 years.[277,278].

He et al[97] investigated the dissolution of Mg_2Si during solution treatment in AA6014. They looked at the effect of solution heat treatment conditions on the Mg_2Si particle size distribution and volume fraction using multiple methods and analysis techniques. They found that higher thermal treatment temperatures resulted in an increase in grain size. It was also found that the higher temperatures, c.a. 570°C, almost removed all the Mg_2Si.

Previous work by Slabaugh et al[279] investigated the effect of temperature on underfilm corrosion. They varied the temperature from room temperature to 60°C. They concluded that there was no significant influence of temperature on the amount of corrosion observed, but that they did observe the greatest corrosion rate at 40°C. Contrary to this, sometime later, Scheck 280 also investigated the effect of temperature on FFC and found that by increasing the temperature from 23°C to 70°C the area of filiform corrosion increased significantly.

By 1995 Bautista[281] compiled a review paper that stated that there are several causes and factors that lead to FFC and that one of the factors identified was temperature. The paper states a correlation between an increase of temperature and the increase of corrosion rate, although it also states that a raised temperature is not necessary for corrosion.

As shown in previous work and in previous chapters, shear deformation of the surface of aluminium alloys, when thermomechanical processed, can produce a large potential difference that could be attributed to a deformed surface layer (several μm thick) that has a different microstructure to the bulk alloy below it[47,90,92–94,165,234,235,268,282–284]. Previous work has found that the deformed layer, although only being several μm thick, consists of fine sub-micrometre-sized grains with second phase intermetallic particles which prevent recrystallization. The work also found that the presence of the deformed layer, as well as the presence of thermal produced intermetallic precipitates in the deformed layer due to thermal treatment, increase the alloys susceptibility to FFC [47,90,92–94,234,235,268,282,284–286].

Due to the findings noted above, AA sheets of the 6000 series are typically etched using an alkaline and/or an acidic cleaner to remove any deformed layer produced by rolling. However, during automotive manufacturers processes and post manufacture maintenance deformed layers are re-introduced by grinding and other surface abrasion and mechanical processes. Subsequently, this reactivates the surface, and the sheet alloy is more prone to FFC. If the sheet has undergone the paint bake process, then the sheet alloy is also susceptible to IGC 286. The dissolution of Al, and Mg, during the etching process can produce Cu-enrichment at the surface. As mentioned earlier the presence of Cu at the surface, or at grain boundaries, whether it is initially present or reintroduced increases the susceptibility of FFC and IGC as well as increasing the rate of under-film corrosion and eventual disbondment of the coating[3,6,283,286–291].

Previous work by McMurray et al[2,3] on AA6016 looked at three thermal treatment temperatures; 25°C, 180°C, and 350°C. They concluded that the bulk form of AA6016 is relatively corrosion resistant at all thermal treatment temperatures showing a slower, more penetrative FFC, known as successive pitting FFC. However, when a NSDL is introduced a rapid form of FFC is observed, surface active FFC, which was limited to the depth of the NSDL, c.a. 2μm. Once the NSDL has been removed as a result of

surface active FFC, successive pitting FFC is observed, with the corrosion attack penetrating down to a depth of 50μm. Both types of FFC produce a surface which is in-keeping with the type of attack produced by IGC. The thermal treatments of 180°C, and 350°C was found to increase the surface-active rates by up to 184%. The inclusion of thermal treatment was found to increase the difference in surface potential between the bulk alloy and the NSDL; at 180°C the potential difference was -0.2V, and at 350°C the potential difference was -0.5V.

Previous work on the 6000 series, AA61115 179, where a surface deformed layer was produced by abrasion with silicon carbide paper, found that this method of surface deformation produces a NSDL of c.a. 2μm and a grain diameter ranging from 50nm to 150nm. The boundary between the NSDL and bulk material was observed as a clear transition from one to the other. The samples were heat treated at 180°C and subjected to HCl inoculation[86,292]. Rapid FFC was observed along with a corrosion depth equal to the depth of the NSDL, 2μm. The work concluded that IGC was found within the NSDL and that the precipitates within the layer increased the susceptibility to corrosion. Further work was conducted into the effect of heat treatment on the open-circuit potential of both bulk and NSDL-bearing (SiC abraded) AA6111 by McMurray et al[5]. using the techniques and methods from Liu et al.[179] assuming the same microstructure is maintained.

Work conducted on aluminium alloys of the 6000 series by McMurray et al[5] focused on four different thermal treatment temperatures; 25°C, 100°C, 180°C, and 350°C and their effect on AA6111. They found comparable results to those identified for AA6016, they concluded that the potential difference between a NSDL and the bulk alloy remained above 0.2V regardless of any thermal treatment up to 350°C. They observed FFC at all temperatures whether a NSDL was present or not, with a NSDL producing surface active FFC which was limited to the depth of the NSDL. When a NSDL is not present, or when it has been removed due to initial surface active FFC, a slower, more penetrative (up to 50μm deep), form of FFC is observed, successive pitting FFC. The study also found that when the samples were subject to thermal treatments of 100°C, 180°C, and 350°C that the rate of both types of FFC increased, with 180°C generating the greatest corrosion rate. Both forms of FFC produce a corroded surface which is consistent with IGC.

Although some work has been done on the potential link between temperature and corrosion rates, whether it is ambient temperature of thermal treatment and corrosion rates, there are large gaps between the temperatures and the same temperatures appear to be used repeatedly, even though the alloy composition changes. This chapter investigates the effect of thermal treatment on AA6014 and AA6022 across the same range of temperatures, but with finer divisions between the temperatures to see if the peak aging temperature agrees with previous work, or whether its composition has an effect. Ambient temperature was not varied, but kept to 20°C.

5.2 Experimental

5.2.1 Experimental method for preparing samples for thermal treatment and the process of obtaining the temperatures to conduct the thermal treatment.

For consistency samples were prepared as stated in previous chapters. Prior to heating, the samples were subject to; Alkali cleaning of the samples in NaOH (10% w/v), for c.a. 45s at 60°C, to dissolve any aluminium oxide and any NSDL on the surface. Samples were rinsed with distilled water and acetone before acid desmutting using concentrated HNO_3 (15.6 molar) for 30s at 25°C to remove impurities such as copper and iron from the surface, and to passivates the surface. The samples were again rinsed with distilled water and acetone. When required, the NSDL was reintroduced by manual abrasion using 180 grit silicon carbide paper/emery paper for 5 mins. The abrasion direction was orientated in the same direction as the rolling direction.

The samples, AA6014-T4 and AA6022-T4, were heated in the following way; once the oven had reached the desired temperatures (25°C, 100°C, 140°C, 160°C, 180°C, 210°C, 250°C, 300°C, and 350°C) after 10 additional minutes samples were placed into the oven using a small hatch. The additional time and small hatch opening reduced the heat loss and large fluctuation in temperature. Once the temperature of the oven had reached the desired temperature, a further 10 minutes was given to allow the temperature to stabilise. After these 10 minutes the stopwatch was initiated, and the samples were kept at the desired temperature for 2 hours to allow all parts of the samples to reach the desired temperature. After the 2 hours, the samples were removed and allowed to cool in air to room temperature, c.a. 20°C.

Samples were rinsed with distilled water and acetone prior to coating with 15.5% (w/w) ethanolic PVB (Polyvinyl butyral) solution to produce an air-dried PVB coating of thickness 30µm ± 5µm. 10mm defects were scribed through the PVB layer normal (90°) to the rolling/NSDL direction with a scalpel [3–5,214] . Samples were scribed with 2 defects c.a. 13mm apart [3–5,214]. FFC was initiated by injecting the scribe with 1µL of 2M aqueous hydrochloric acid using a glass micro-capillary dispenser. The HCl injection method was intended to create greater reproducibility than methods involving full sample exposure either by salt fog, HCl vapour, or immersion in aqueous electrolyte [3–5,214]. Samples were placed into a sealed container with a saturated salt

solution of ammonium sulfate to achieve an 80% relative humidity and a digital hygrometer and temperature sensor (Lascar's EasyLog EL-USB-2-LCD+). The container will have samples with and without a NSDL at each temperature. Photographs were taken periodically, and measurements obtained using Photoshop, as described in Chapter 2.5 A selection of graphs were produced to show corrosion growth with respect to time and to compare the rate and type of cosmetic corrosion observed.

5.2.2 Experimental method for preparing samples and the process of obtaining surface potential scans using the SKP:

Scanning Kelvin Probe, SKP, scans were taken across the surfaces of some samples. Samples used were chosen based on previous work[3–5] and the results obtained from the initial thermal treatment inquiry stated above. Potentiometric measurements were conducted using a 125µm diameter gold wire reference probe, vibrated normal to the sample surface at 280 Hz, with a 40µm peak-to-peak amplitude, and mid-amplitude probe–sample distance of 120µm. The SKP was calibrated using the technique described in previous work[1–5,212–214]

Prior to the scan the samples were chosen for both AA6014 and AA6022 and prepared and heated in the same way described at the start of this section. Half of the samples' surface was abraded using 180 grit SiC paper to produce a 50:50 [no NSDL: NSDL] surface. Scans were conducted across uncoated samples and were rinsed with acetone and D.I water prior to scanning.

All SKP measurement were conducted in static air at c.a. 20±1◦C and c.a.80% RH. The samples were placed in a thermostatic stainless-steel environment chamber, containing reservoirs of saturated salt solution, ammonium sulfate $(NH_4)_2SO_4$, to maintain the constant relative humidity of c.a. 80%. The RH was monitored using a digital hygrometer, with a digital temperature sensor (Lascar's EasyLog EL-USB-2-LCD+). SKP scans started immediately after the sample has been placed inside the camber and scans will be repeated. The data produced by the scans were inputted into excel to produce calibrated Ecorr data.

5.3 Results and Discussion

5.3.1 Effect of thermal treatment temperatures

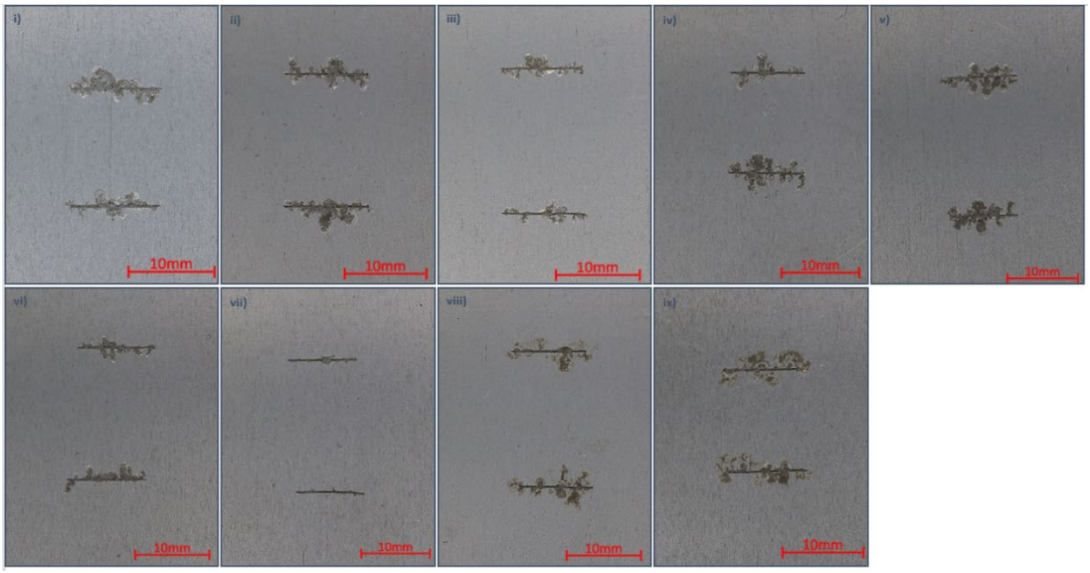

Figure 5.3.1a: aluminium alloy 6014 samples without a NSDL injected with 1µL of 2M and kept at 80% RH. Images shown are after 312 hours, thermal treatments: i) 25°C ii) 100°C iii) 140°C iv) 160°C v) 180°C vi) 210°C vii) 250°C viii) 300°C ix) 350°C.

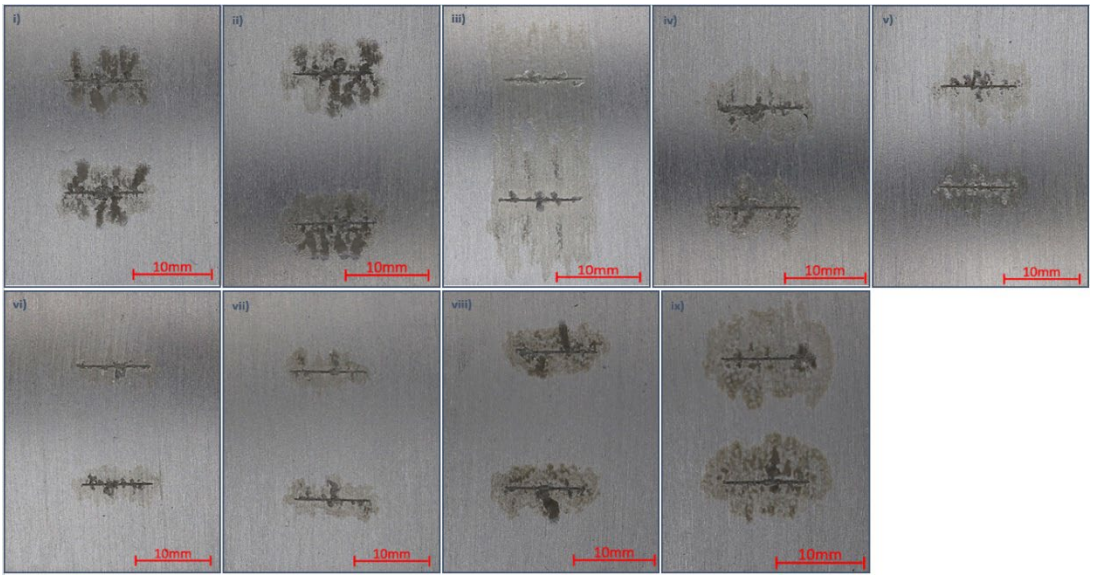

Figure 5.3.1b: AA6014 samples with a NSDL injected with 1µL of 2M and kept at 80% RH. Images shown are after 312 hours, thermal treatments: i) 25°C ii) 100°C iii) 140°C iv) 160°C v) 180°C vi) 210°C vii) 250°C viii) 300°C ix) 350°C

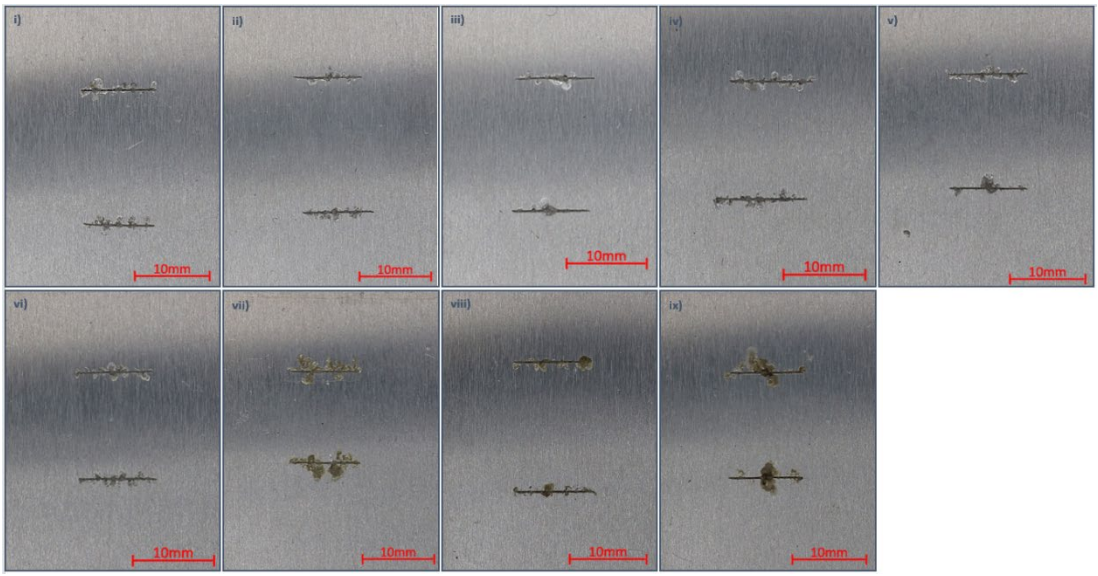

Figure 5.3.1c: aluminium alloy 6022 samples without a NSDL injected with 1µL of 2M and kept at 80% RH. Images shown are after 312 hours, thermal treatments: i) 25°C ii) 100°C iii) 140°C iv) 160°C v) 180°C vi) 210°C vii) 250°C viii) 300°C ix) 350°C

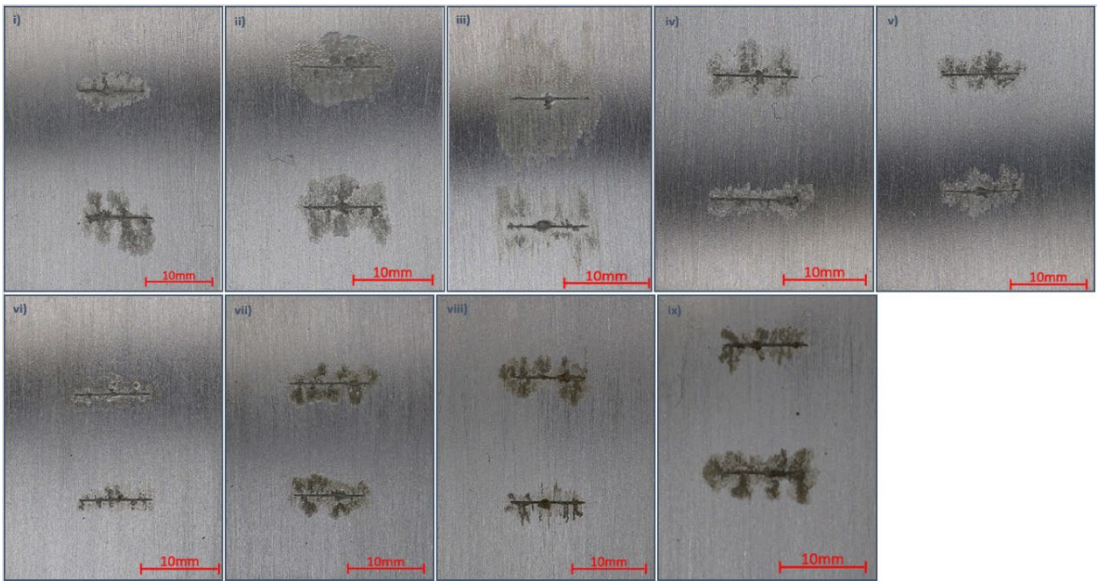

Figure 5.3.1d: AA6022 samples with a NSDL injected with 1µL of 2M and kept at 80% RH. Images shown are after 312 hours, thermal treatments: i) 25°C ii) 100°C iii) 140°C iv) 160°C v) 180°C vi) 210°C vii) 250°C viii) 300°C ix) 350°C

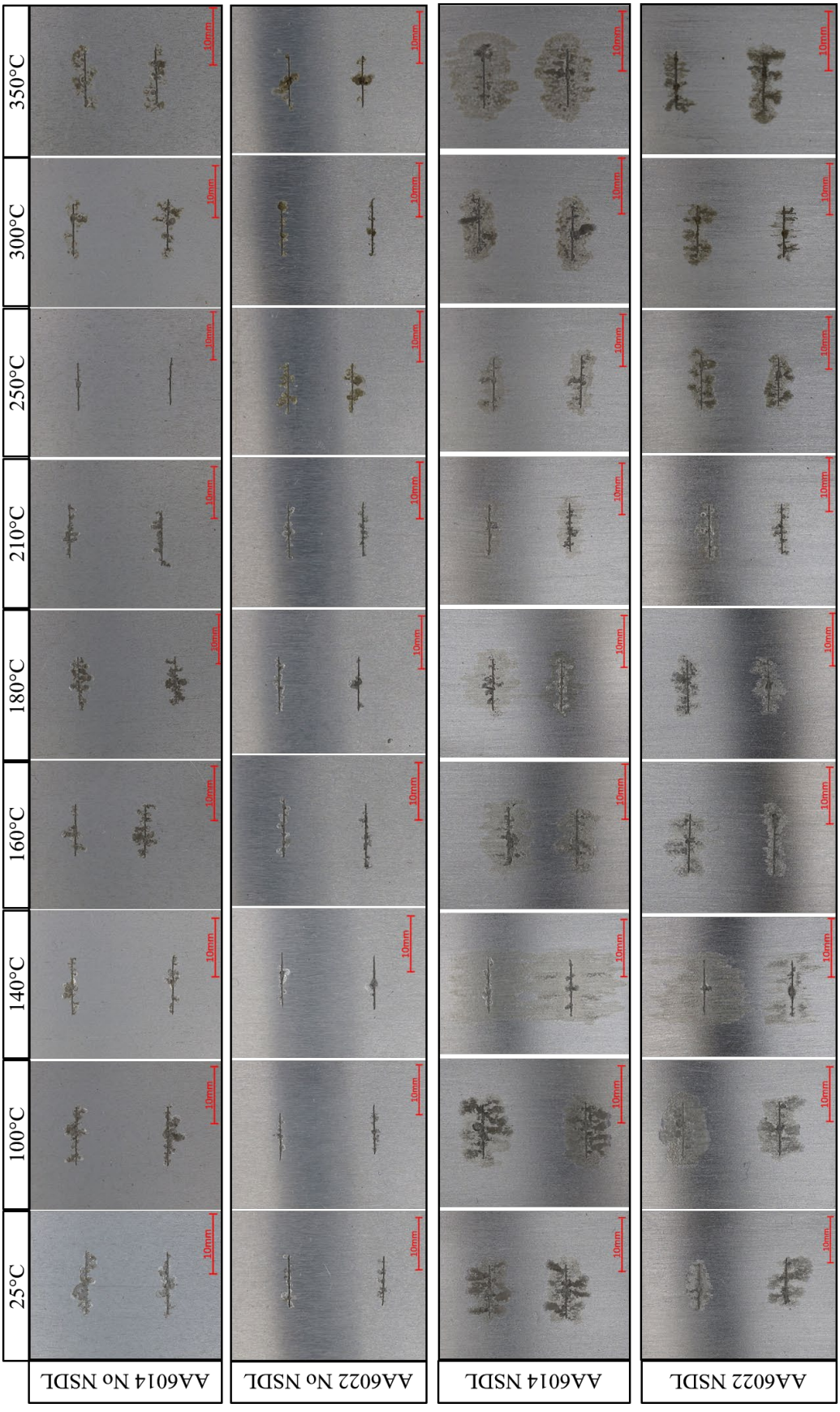

Figure 5.3.1e: AA6014 and AA6022 all samples across the thermal treatment range placed in 80% RH after 312 hours.

Samples where the NSDL is not present display more pit-like formations with some samples ultimately displaying successive pitting FFC, shown in figures 5.3.1a and 5.3.1c. The figures show that the presence of a NSDL accelerated the rate of corrosion. In-keeping with results from the previous chapter, the presence of a NSDL displays surface active FFC, prior to any secondary successive pitting, shown in figures 5.3.1b and 5.3.1d.

From the images alone, samples without a NSDL have no clear correlation between the thermal treatment temperature and the quantity of corrosion observed. The samples with a NSDL show varying degrees of FFC with samples that have been subjected to thermal treatment at 140°C, showing a more accelerated FFC with the majority of the surface covered with corrosion. Visually, figure 5.3.1e shows that a thermal treatment temperature of between 210°C and 250°C has the least amount of corrosion present for samples with and without a NSDL.

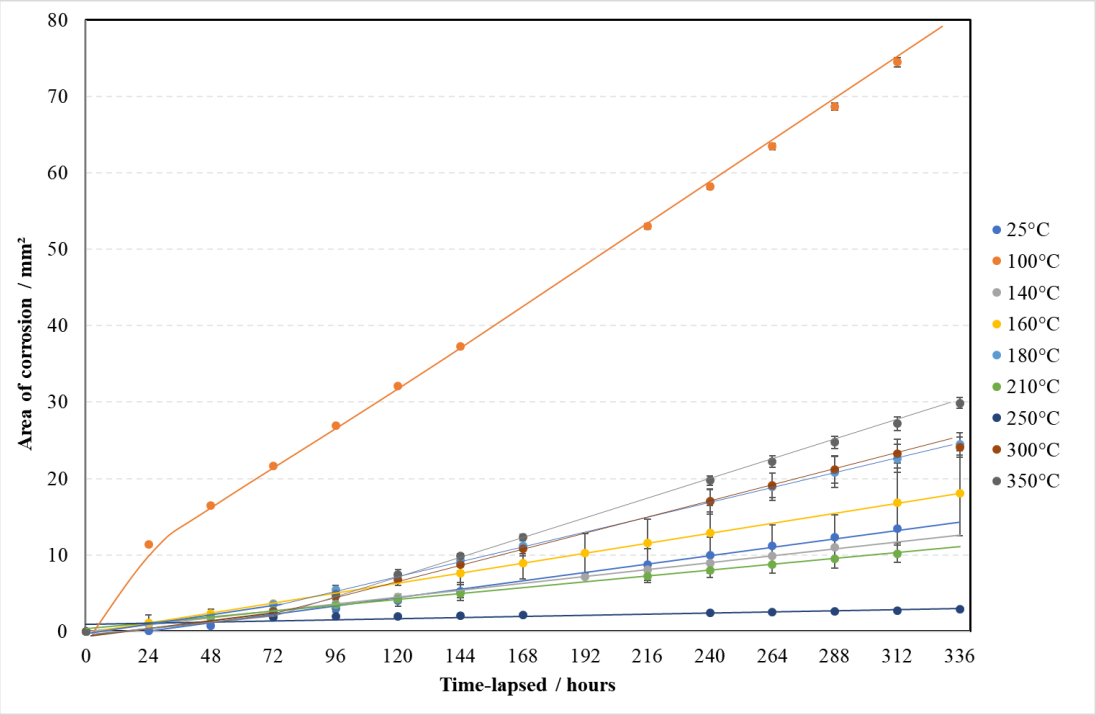

Figure 5.3.1f: Corrosion propagation of AA6014 samples with no NSDL placed in 80% RH. At thermal treatment temperatures ranging from 25°C to 350°C. Y-error bars included.

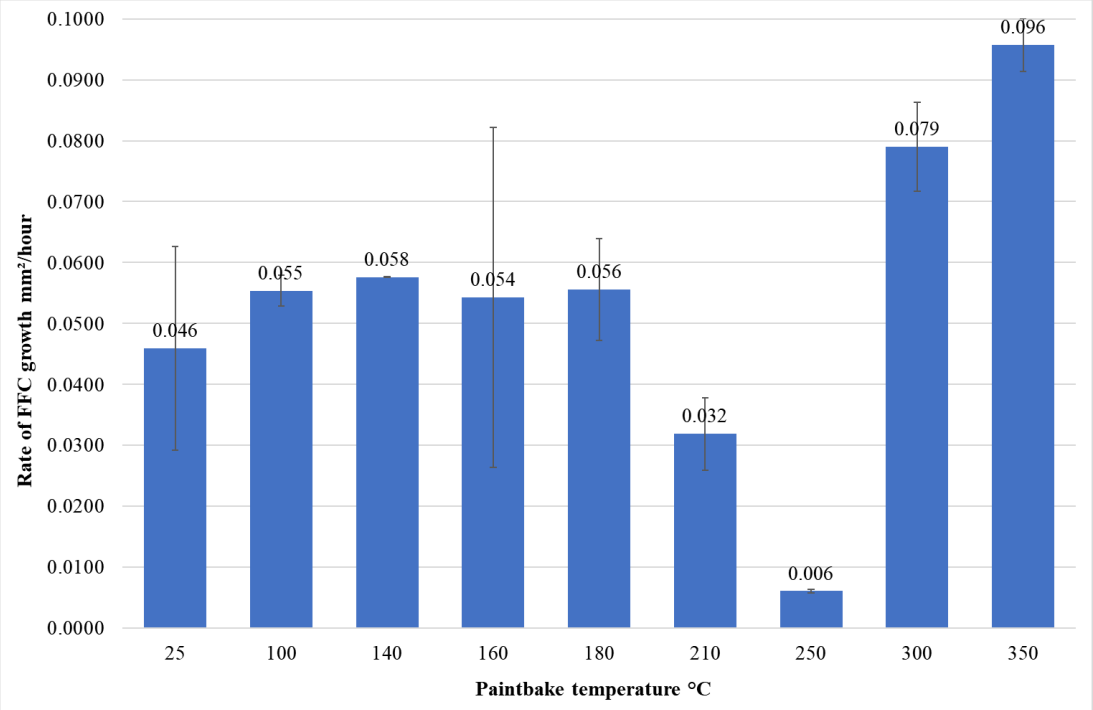

Figure 5.3.1g: Corrosion rates of AA6014 samples with no NSDL placed in 80% RH. At thermal treatment temperatures ranging from 25°C to 350°C. Y-error bars included.

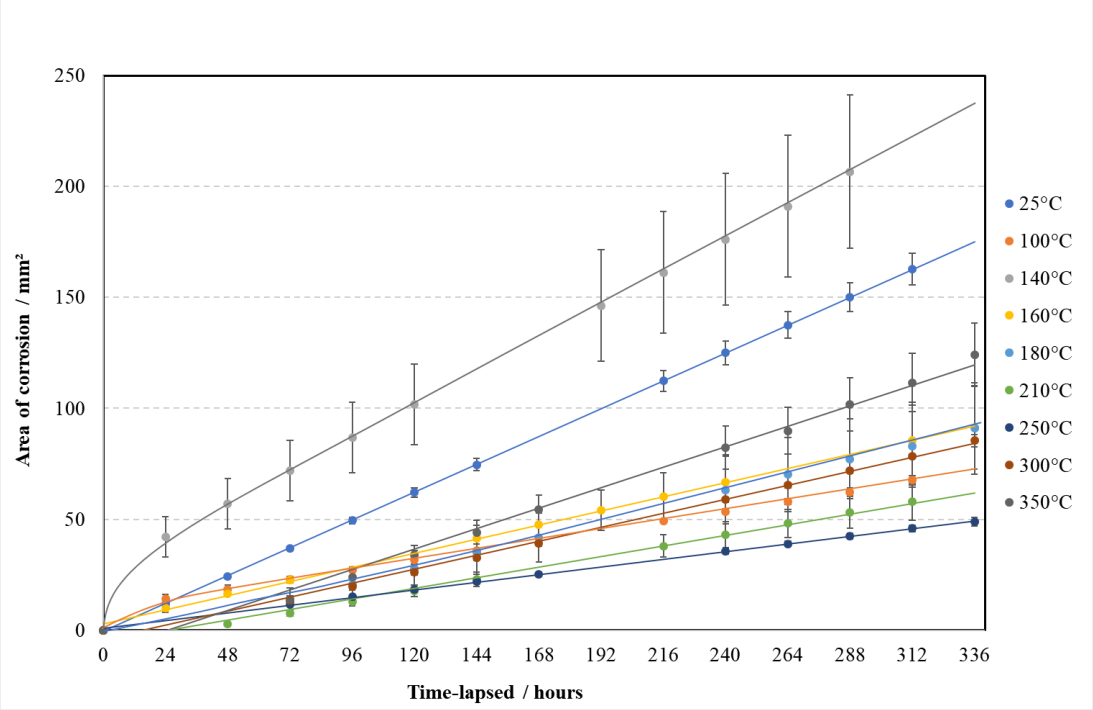

Figure 5.3.1h: Corrosion propagation of AA6014 samples with a NSDL placed in 80% RH. At thermal treatment temperatures ranging from 25°C to 350°C. Y-error bars included.

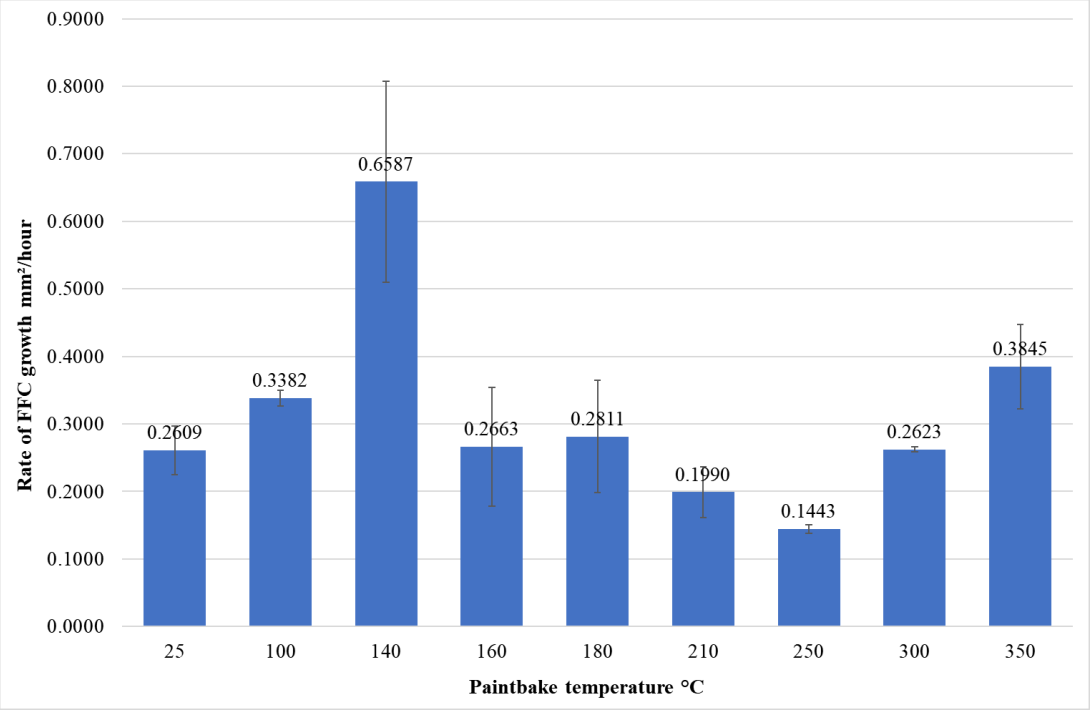

Figure 5.3.1i: Corrosion rates of AA6014 samples with a NSDL placed in 80% RH. At thermal treatment temperatures ranging from 25°C to 350°C. Y-error bars included.

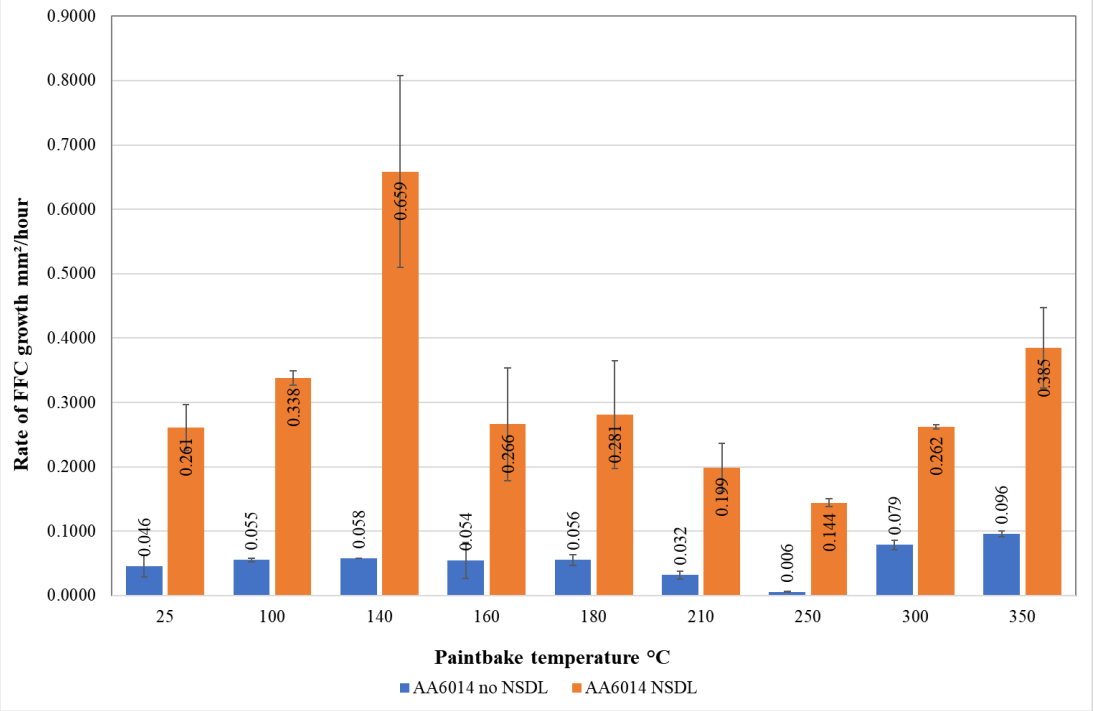

Figure 5.3.1j: Corrosion rates of AA6014 samples with and without NSDL placed in 80% RH. At thermal treatment temperatures ranging from 25°C to 350°C. Y-error bars included.

Figures 5.3.1f to 5.3.1j show the area of corrosion propagation and rate of FFC propagation graphs. The standard deviation of the areas measured and the rates for all AA6014 samples can be seen below in table 14:

Temperature °C	AA6014 no nsdl	AA6014 nsdl	AA6014 no nsdl	AA6014 nsdl
	area s.d/mm²	area s.d/mm²	rate s.d mm²/hour	rate s.d mm²/hour
25	1.3506	3.1269	0.0167	0.0356
100	0.2358	1.2190	0.0025	0.0114
140	0.2232	19.6820	0.0001	0.1486
160	2.3103	7.7076	0.0279	0.0876
180	1.1031	11.8230	0.0083	0.0832
210	0.6252	3.8466	0.0059	0.0374
250	0.0234	0.9679	0.0003	0.0061
300	1.0590	1.3492	0.0074	0.0035
350	0.4101	7.3470	0.0044	0.0626

Table 14: Standard deviations in the corrosion area and corrosion rate, for all AA6014 samples.

The differences in the standard deviation could be due to: 1. The length of the defect was not always 10mm, but varied from 9.5 to 10.5mm, this could have allowed the HCL to settle less-evenly, the quality of the NSDL is likely to have varied across the surface, which would mean there may be some areas of the surface where it is more density populated with a NSDL and would allow for more rapid growth, finally, the PVB coating may have inconsistency with respect to adhesion therefore corrosion maybe more favourable in sections where there is a weak adhesion. The area of corrosion propagation graphs, figures 5.3.1f and 5.3.1h show that the once initiated, the corrosion area propagation is linear with respect to time. Unfortunately, these graphs do not present a clear understanding of any trend or correlation between thermal treatment and corrosion. Therefore, the data from these graphs was used to calculate the rate of corrosion and produce the corrosion rate charts shown in figures 5.3.1g, 5.3.1i and 5.3.1j.

Figure 5.3.1g shows the rates of FFC propagation for AA6014 samples without a NSDL. Up to 180°C there is little difference in the corrosion rates, c.a. 0.05mm^2/hr, but it could be interpreted to have a slight peak at 140°C. There is a drop in corrosion

rate at 210°C with the thermal treatment temperature most resistant to corrosive attack noted at 250°C, with a FFC propagation rate of c.a. 0.001 0.05mm^2/hr. There is a sudden increase in corrosion rate at 300°C and another increase at 350°C, to c.a. 0.1 mm^2/hr. This sudden increase could be due to the sudden increase in the temperature as prior to this the increments were smaller. Nonetheless, for AA6014 with no NSDL present, the peak aging time is 350°C and the lowest corrosion rate is at 250°C

Figure 5.3.1i shows the rates of FFC propagation for AA6014 samples with a NSDL. Figure 5.3.1i shows the rate decreases until it reaches its slowest rate at 250°C and then shows an increase in rate at 300°C and 350°C. Figure 5.3.1i shows that peak aging occurs at 140°C and the lowest corrosion rate is at 250°C. Figure 5.3.1j shows that there is a similar trend to the results for AA6014 without a NSDL, however the results for the NSDL show a prominent peak at 140°C rather than a subtle one. Figure 5.3.1j also shows that as with the relative humidity enquiry, the samples with NSDL produce a more accelerated FFC when compared to the samples without NSDL.

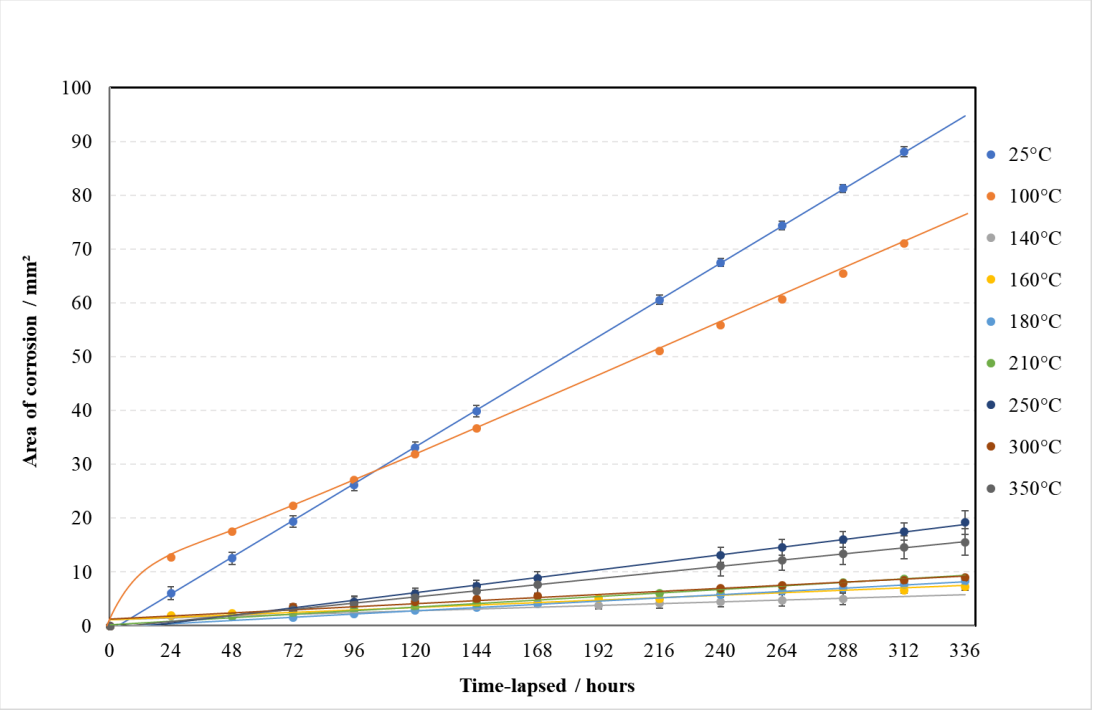

Figure 5.3.1k: Corrosion propagation of AA6022 samples with no NSDL placed in 80% RH. At thermal treatment temperatures ranging from 25°C to 350°C. Y-error bars included.

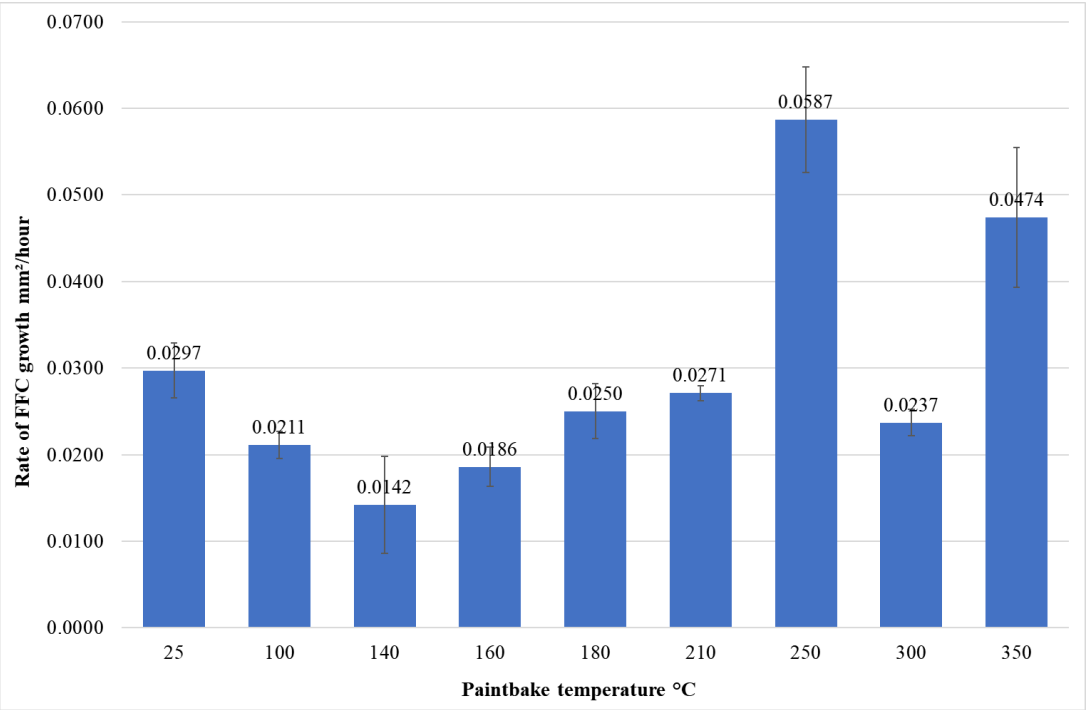

Figure 5.3.1l: Corrosion rates of AA6022 samples with no NSDL placed in 80% RH. At thermal treatment temperatures ranging from 25°C to 350°C. Y-error bars included.

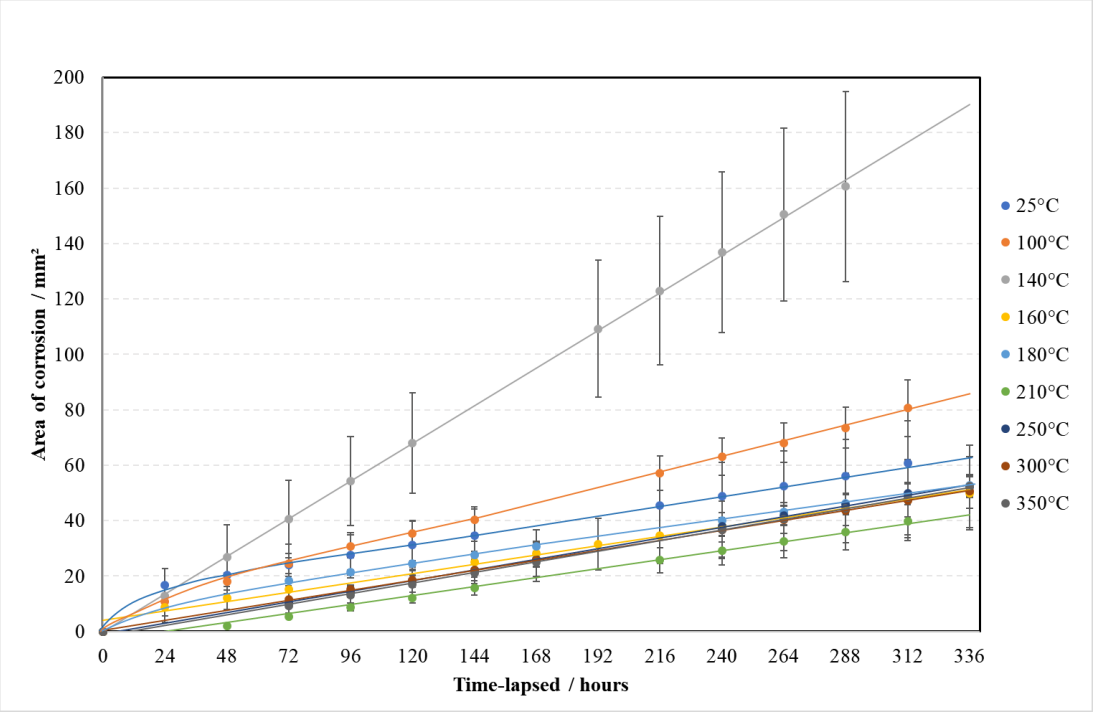

Figure 5.3.1m: Corrosion propagation of AA6022 samples with a NSDL placed in 80% RH. At thermal treatment temperatures ranging from 25°C to 350°C. Y-error bars included.

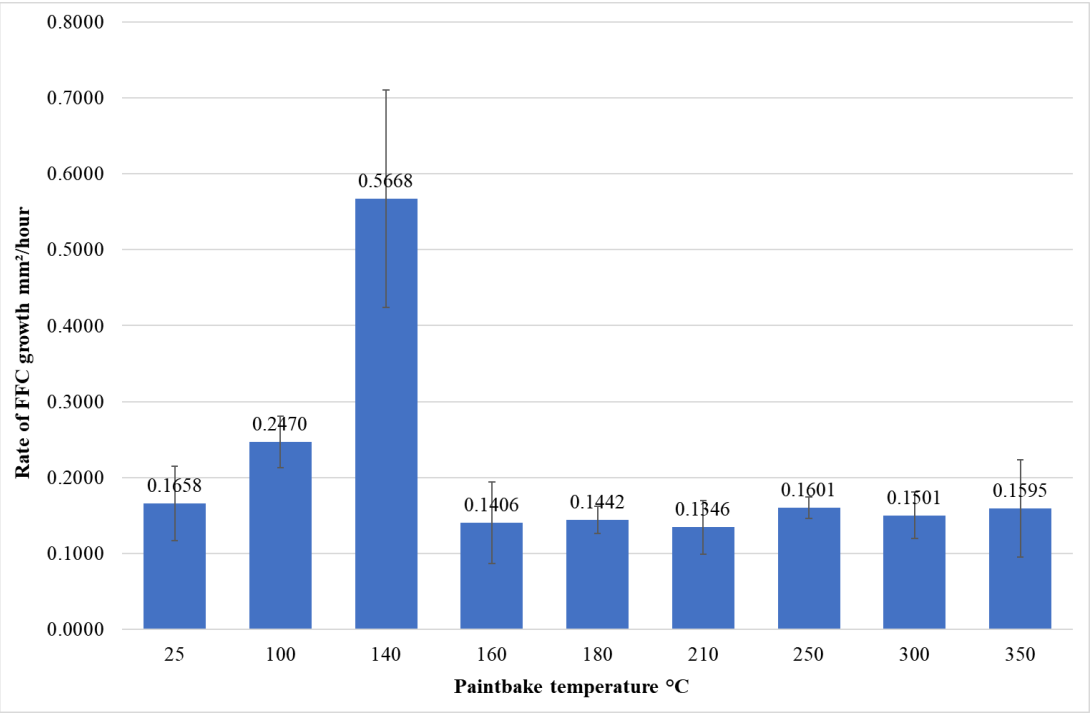

Figure 5.3.1n: Corrosion rates of AA6022 samples with a NSDL placed in 80% RH. At thermal treatment temperatures ranging from 25°C to 350°C. Y-error bars included.

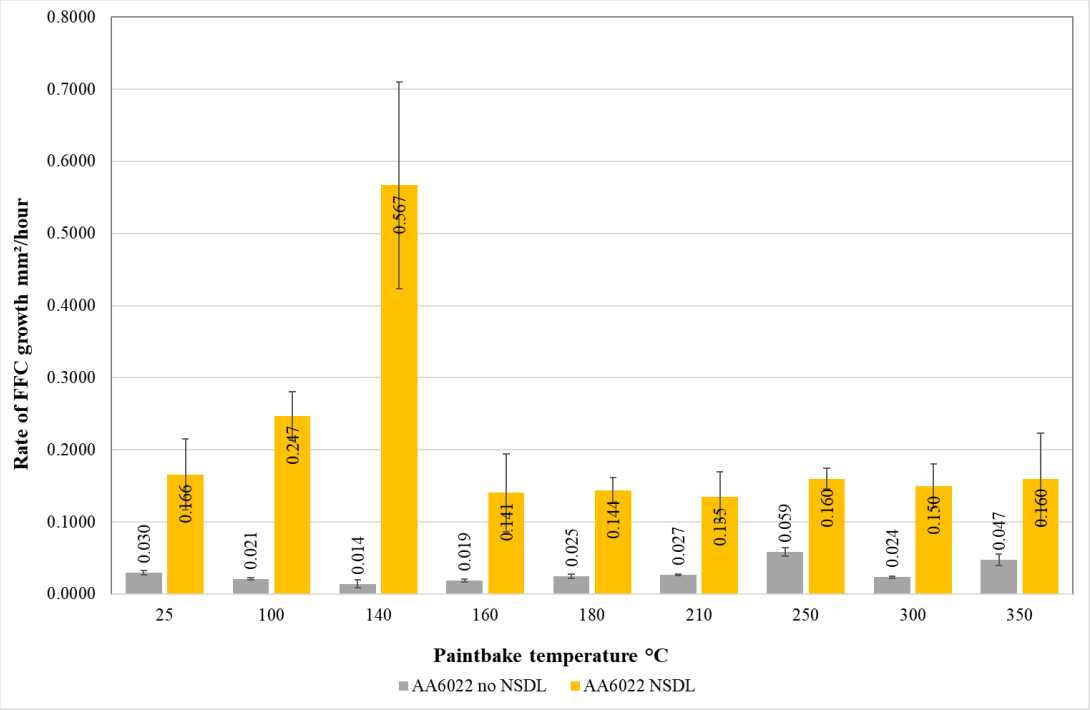

Figure 5.3.1o: Corrosion rates of AA6022 samples with and without NSDL placed in 80% RH. At thermal treatment temperatures ranging from 25°C to 350°C. Y-error bars included.

Figures 5.3.1k to 5.3.1o show the area of corrosion propagation and rate graphs. The standard deviation of the areas measured and the rates for all AA6022 samples can be seen below in table 15:

Temperature °C	AA6022 no nsdl	AA6022 nsdl	AA6022 no nsdl	AA6022 nsdl
	area s.d/mm²	area s.d/mm²	rate s.d mm²/hour	rate s.d mm²/hour
25	0.9025	9.2464	0.0032	0.0492
100	0.1795	5.0043	0.0016	0.0341
140	0.5618	19.6015	0.0056	0.1431
160	3.6756	34.2718	0.0023	0.0539
180	0.4214	2.0849	0.0032	0.0176
210	0.0911	3.2308	0.0008	0.0351
250	1.2374	2.6408	0.0061	0.0142
300	0.2158	3.0571	0.0016	0.0306
350	1.5544	7.8803	0.0081	0.0641

Table 15: Standard deviations in the corrosion area and corrosion rate, for all AA6022 samples.

The differences in the standard deviation could be due to: 1. The length of the defect was not always 10mm, but varied from 9.5 to 10.5mm, this could have allowed the HCL to settle less-evenly, the quality of the NSDL is likely to have varied across the surface, which would mean there may be some areas of the surface where it is more density populated with a NSDL and would allow for more rapid growth, finally, the PVB coating may have inconsistency with respect to adhesion therefore corrosion maybe more favourable in sections where there is a weak adhesion.

The area of corrosion propagation graphs, figures 5.3.1k and 5.3.1m, show that the once initiated, the corrosion area propagation is linear with respect to time. Unfortunately, these graphs do not present a clear understanding of any trend or correlation between thermal treatment and corrosion. Therefore, the data from these graphs was used to calculate the rates of FFC propagation and produce the corrosion rate charts shown in figures 5.3.1l, 5.3.1n, and 5.3.1o.

Figure 5.3.1l shows the rates of FFC propagation for AA6022 samples without a NSDL. Unlike the AA6014 samples, AA6022 shows the slowest corrosion rate at 140°C, c.a. 0.01mm^2/hr, with the greatest rate of FFC propagation, peak aging, at 250°C, c.a. 0.06mm^2/hr. This is then followed by a decrease in rate at 300°C followed by another, but lower, peak at 350°C. The results of AA6022 appear to have a trend that is the exact opposite of AA6014 when no NSDL is present. The highest 3 temperatures cover a 100°C range and would benefit from more temperatures between 210°C and 350°C to see if there is any trend overlooked by this set of data. Figure 5.3.1n shows the rates of FFC propagation for AA6022 samples with a NSDL present. It shows that there is a similar trend to the results for AA6014 with a NSDL, with a prominent peak at 140°C, c.a. 0.6mm^2/hr. The rates of FFC propagation decrease significantly after 140°C with all corrosion rates for thermal treatment between 160°C to 350°C being similar, between 0.14 mm^2/hr to 0.16 mm^2/hr. The slowest corrosion rate, most corrosion resistant, is found at 210°C. Figure 5.3.1n shows that, unlike AA6014, AA6022 does not exhibit a similar trend from one type of surface (no NSDL) to the other (NSDL). Figure 5.3.1n also shows that as with the relative humidity enquiry, the samples with NSDL produce a more accelerated FFC when compared to the samples without NSDL.

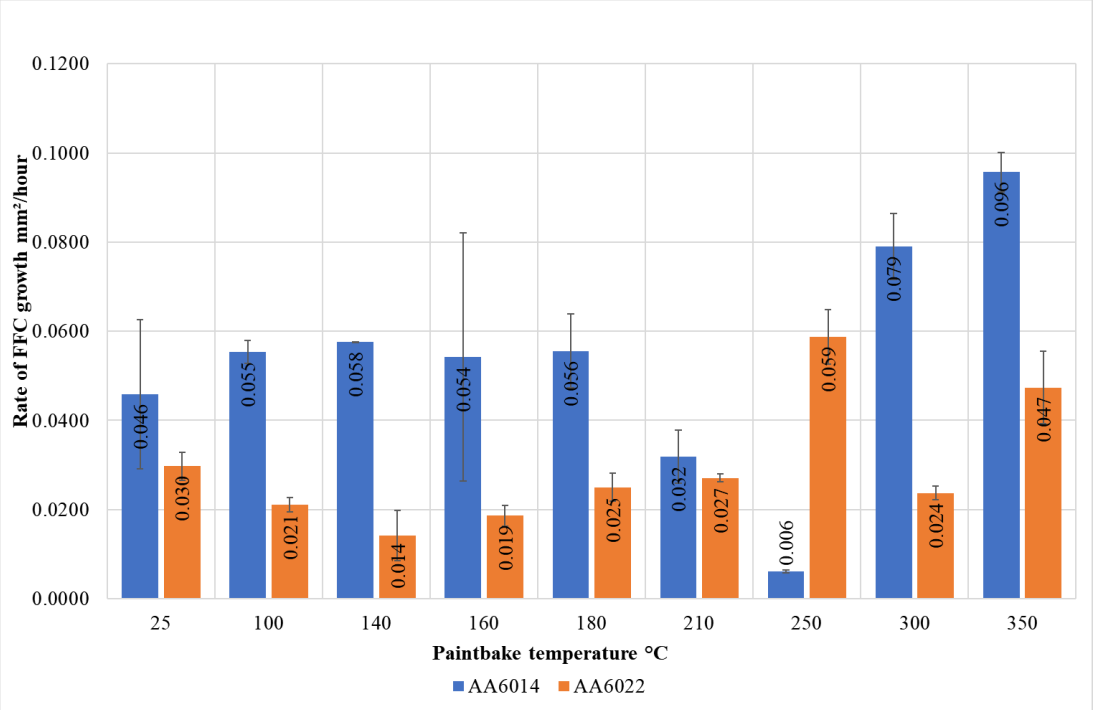

Figure 5.3.1p: Corrosion rates of AA6014 and AA6022 samples with no NSDL placed in 80% RH. At thermal treatment temperatures ranging from 25°C to 350°C. Y-error bars included.

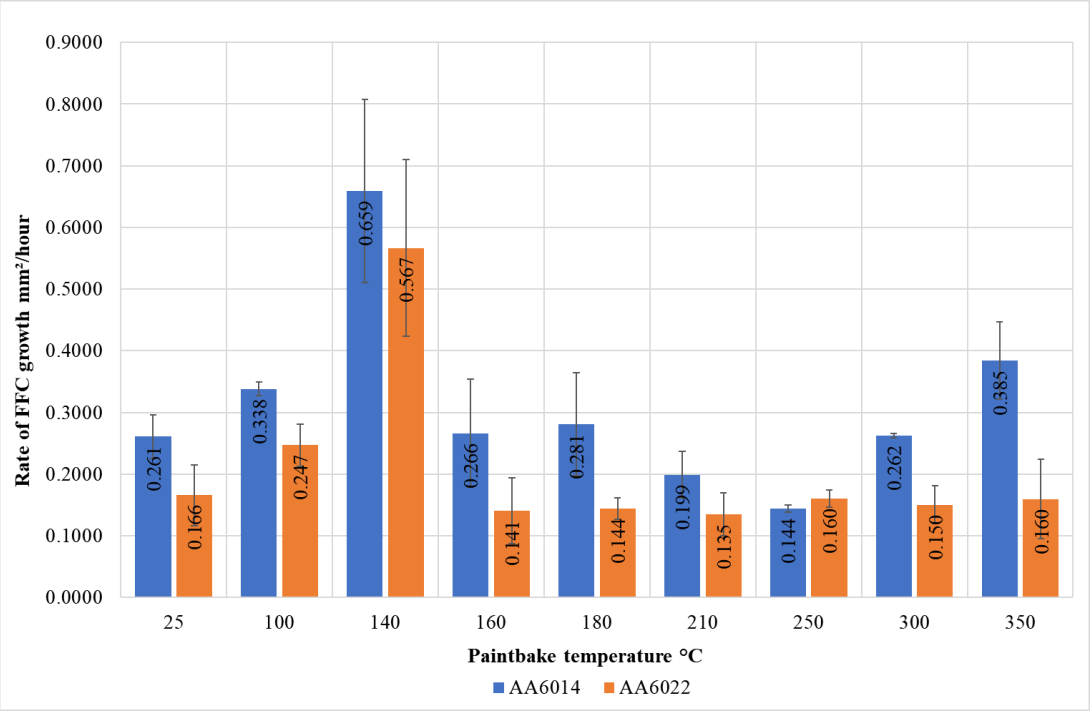

Figure 5.3.1q: Corrosion rates of AA6014 and AA6022 samples with a NSDL placed in 80% RH. At thermal treatment temperatures ranging from 25°C to 350°C. Y-error bars included.

Figure 5.3.1p shows the corrosion rates for AA6014 and AA6022 when no NSDL is present. AA6014 has the higher corrosion rate across the majority of the thermal treatment temperatures, with 250°C being the only exception. The temperature range; 25°C to 210°C show the opposite nature of the alloys with 210°C having a similar rate for both alloys. Figure 5.3.1q shows the corrosion rates for AA6014 and AA6022 when a NSDL is present. As with figure 5.3.1p, AA6014 has the higher corrosion rate across the majority of the thermal treatment temperatures, with 250°C being the only exception. Both AA6014 and AA6022 start with a similar trend, when a NSDL is present. They show an increase in the corrosion rate from 25°C to 140°C followed by a decrease in corrosion rate to 210°C and 250°C. However, after 140°C the similarities disappear. The lowest corrosion rate for AA6014 is at 250°C and for AA6022 is at 210°C. After 250°C AA6014 corrosion rate starts to increase, whereas the corrosion rate for AA6022 seem to fluctuate showing no trend.

This investigation has shown that the presence of a NSDL is a greater driving force than the temperature used for heat treatment. It also shows that for the majority of the samples 210°C to 250°C reduced the rate of FFC propagation, especially for samples when a NSDL is present. Since cosmetic corrosion is significantly accelerated around 140°C, this temperature should be avoided in industrial practices.

5.3.2 Effect of thermal treatment temperatures – SKP Scans

The following pages show Free corrosion potential (V vs SHE) as a function of distance across the interface of the NSDL and "bulk" alloy surfaces for uncoated 50:50 (no NSDL: NSDL) for select thermal treatment temperatures for AA6014 and AA6022. Followed by the difference in surface potentials at the same temperatures. The temperatures were chosen due to their significance from the rate results and based on previous work[3,5,6,214].

The free corrosion potential measured by the scans was used in conjunction with equation [1] to calculate the average free corrosion potential of AA6022 samples with and without a NSDL placed in 80% RH at thermal treatment temperatures ranging from 25°C to 350°C of the alloys.

Figures 5.3.2a to 5.3.2d shows the free corrosion potential and the average free corrosion potentials of AA6014 and AA6022 samples, with and without a NSDL placed in 80% RH. Error bars have been included in figures 5.3.2b and 5.3.2d and show an average standard deviation of: c.a. 0.03V for AA6014 without a NSDL, 0.05V for AA6014 with a NSDL, 0.03V for AA6022 without a NSDL and c.a. 0.04V for AA6022 with a NSDL. The surfaces with a NSDL show a slightly larger standard deviation, this is potentially due to the quality of the NSDL produced on the surface is likely to have varied across the surface, which would mean there may be some areas of the surface where it is more density populated with a NSDL and is likely to have more grain boundaries, therefore more intermetallic precipitates present which would alter the surface potential. As seen in previous chapters the presence of a NSDL lowers the potential.

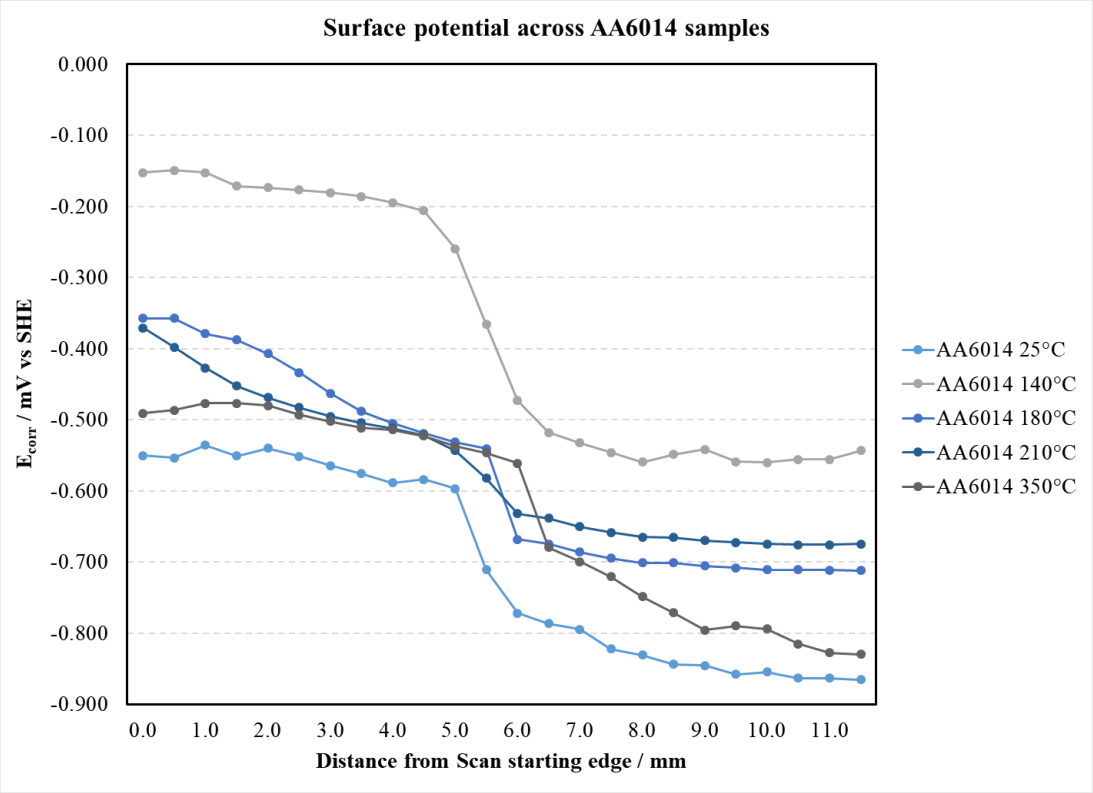

Figure 5.3.2a: Free corrosion potential (V vs SHE) as a function of distance across the interface of the NSDL and "bulk" alloy surfaces of AA6014 placed in 80% RH. 0mm to c.a. 5mm = no NSDL present, c.a. 6mm to 12mm = NSDL present. At thermal treatment temperatures ranging from 25°C to 350°C.

Figure 5.3.2a shows that the sample thermally treated at 140°C potential is not in the same range as the other samples and could be a result of the formation of thermally promoted intermetallic precipitates at the surface. In general, all of the temperatures have different potentials at 0mm, bulk material, and at 12mm (NSDL) which could be a direct result of the thermally promoted intermetallic precipitates and the quantity present at the surface layer as areas of strain are more likely to promote intermetallic precipitates during thermal treatment, even at low temperatures. Since NSDLs increase the number of grain boundaries at the surface increasing thereby strain across the surface allowing for a greater number of intermetallics to precipitate at a NSDL. This could be why the potentials across the surface vary significantly.

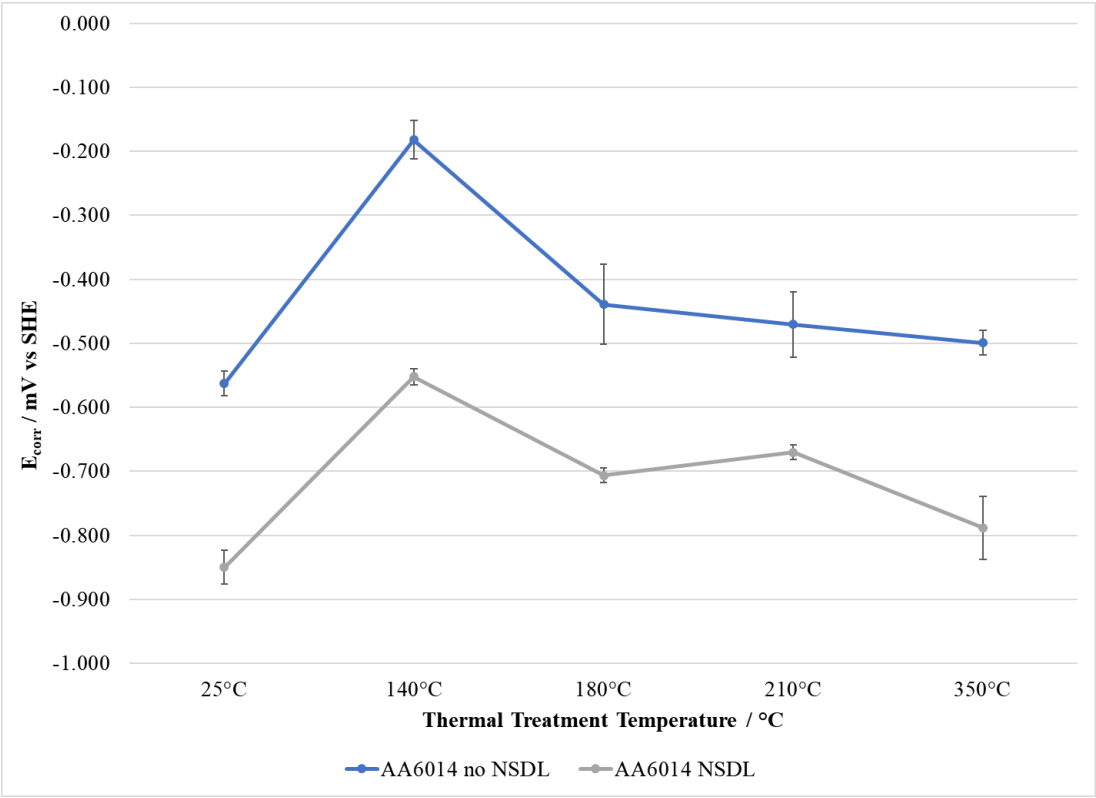

Figure 5.3.2b: Average free corrosion potential of AA6014 samples with and without a NSDL placed in 80% RH. At thermal treatment temperatures ranging from 25°C to 350°C. Y-error bars included.

Figure 5.3.2b shows the difference in surface potential of AA6014 samples with and without a NSDL placed in 80% RH. At thermal treatment temperatures ranging from 25°C to 350°C. The separate sections, no NSDL and NSDL, of the sample surface potentials were averaged and plotted, along with the difference in potential between the two surface sections. The greatest potential difference was found at 140°C (0.370 V) and the smallest potential difference was found at 210°C (0.200 V). This is reflective of the corrosion rates found earlier in the chapter for AA6014 samples with a NSDL; the greatest potential difference produces the quickest corrosion rate and the smallest potential difference produced one of the slowest corrosion rates for AA6014 (the slowest rate was 0.1443 mm^2/hr for 250°C followed by 0.199 mm^2/hr for 210°C).

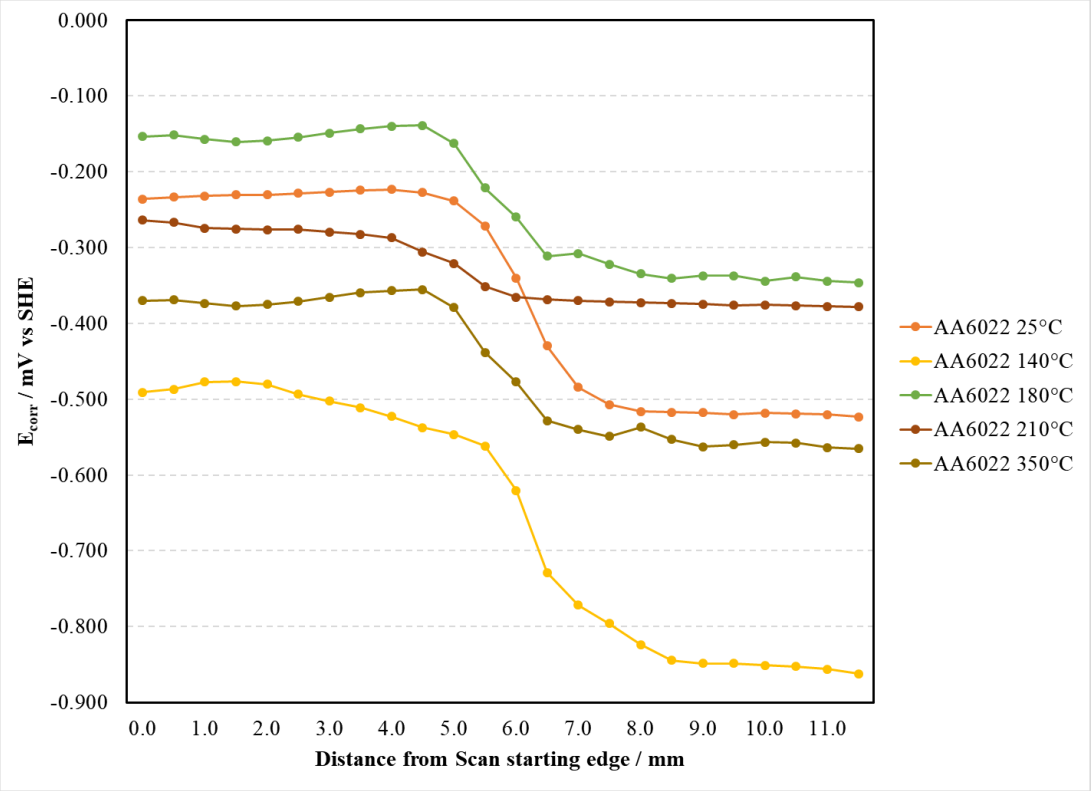

Figure 5.3.2c: Free corrosion potential (V vs SHE) as a function of distance across the interface of the NSDL and "bulk" alloy surfaces of AA6022 placed in 80% RH. 0mm to c.a. 5mm = no NSDL present, c.a. 7mm to 12mm = NSDL present. At thermal treatment temperatures ranging from 25°C to 350°C.

Figure 5.3.2c shows SKP surface scans of AA6022 samples with and without a NSDL placed in 80% RH. At thermal treatment temperatures ranging from 25°C to 350°C. The samples were positioned so that between 0mm to c.a. 5mm no NSDL was present and between c.a. 7mm to 12mm a NSDL was present with the boundary between the surfaces between 5mm and 7mm. As seen in previous chapters the presence of a NSDL lowers the potential. Similar to the result for AA6014, figure 5.3.2c shows that the sample thermally treated at 140°C potential is not in the same range as the other samples and could be a result of the formation of thermally promoted intermetallic precipitates at the surface. In general, all of the temperatures have different potentials at 0mm, bulk material, and at 12mm (NSDL) which could be a direct result of the thermally promoted intermetallic precipitates and the quantity present at the surface layer for the same reason noted above.

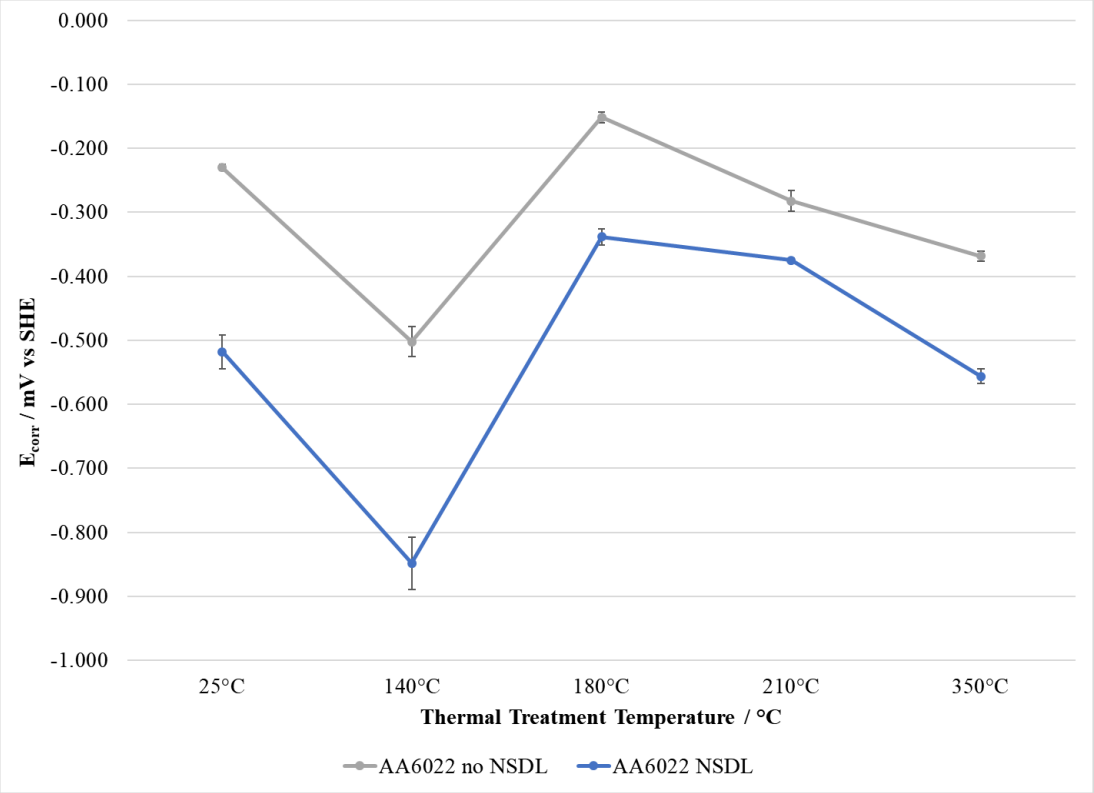

Figure 5.3.2d: Average free corrosion potential of AA6022 samples with and without a NSDL placed in 80% RH. At thermal treatment temperatures ranging from 25°C to 350°C. Y-error bars included.

Figure 5.3.2d shows the difference in surface potential of AA6022 samples with and without a NSDL placed in 80% RH. At thermal treatment temperatures ranging from 25°C to 350°C. As with AA6014 the separate sections, no NSDL and NSDL, of the sample surface potentials were averaged and plotted, along with the difference in potential between the two surface sections. The greatest potential difference was found at 140°C (0.346 V) and the smallest potential difference was found at 210°C (0.188 V). This is reflective of the corrosion rates found earlier in the chapter for AA6022 samples with a NSDL; the greatest potential difference produces the quickest corrosion rate (0.5668 mm^2/hr), and the smallest potential difference produced the slowest corrosion rate (0.1346 mm^2/hr) for AA6022.

As mentioned in the chapter introduction, previous work 293 has found that the alloy surface can become enriched in copper when the alloys undergo alkaline etching, and the Cu cannot be removed by the subsequent desmutting with nitric acid. Both alkaline etching and nitric acid desmutting are used when preparing AA6014 and AA6022. The same work 293 found that when an aluminium alloy has a copper content of c.a. 0.95% it produces a c.a. 2nm Cu-enriched layer beneath the surface oxide film after alkaline etching, which has been known to increase the surface potential of the alloy at temperatures below 100°C. For temperatures above 100°C the Cu is more likely to form intermetallic precipitates and reduce the Cu-rich layer. This is in keeping with work by H.N. McMurray on AA6111[5]. AA6014 contains ≤ 0.25% copper and AA6022 contains 0.01 to 0.10% copper, less than that found in the alloys investigated previously. Since there is more Cu and Fe in the AA6014, then the bulk alloy will be a marginally better cathode. So if the NSDL is acting sacrificially then a more effective cathode on the bulk alloy will produce a faster rate of dissolution.

Previous work on the AA6000 series (AA6016 and AA6111[3,5,214]) found that there was a potential difference of 0.2V and c.a.0.3V, respectively, for samples subjected to thermal treatment of 180°C. The potential difference for AA6014 and AA6022 when subjected to thermal treatment of 180°C were 0.267V and 0.186V, respectively, which is not too dissimilar. The same work found that AA6016 and AA6111 samples subjected to thermal treatment of 350°C had a potential difference of 0.5V and c.a.0.3V, respectively. The potential difference for AA6014 and AA6022 when subjected to thermal treatment of 350°C were 0.289V and 0.188V, respectively, which is quite different to previous work and could be due to the composition of the alloys and the intermetallic precipitates formed. However, the work conducted on AA6016 and AA6111 were conducted at 40°C and 80%RH and at 40°C 60%RH, respectively, whereas the results in this chapter were obtained at a temperature of 20°C and a RH of 80%.

The aging temperature, produced by thermal treatment, for both AA6016 and AA6111 was found to be 180°C which does not reflect the potential differences found in the SKP scans. Whereas the peak aging temperature, produced by thermal treatment, for to AA6014 and AA6111 was found to be 140°C which does reflect the potential differences found in the SKP scans.

Figures 5.3.2e and 5.3.2f below, seem to suggest that greater FFC rates are produced at temperatures where the bulk/NSDL potential difference is greatest, but it there is very weak correlation, and less with AA6014 in figure 5.3.2e. Although this is something that could be investigated further.

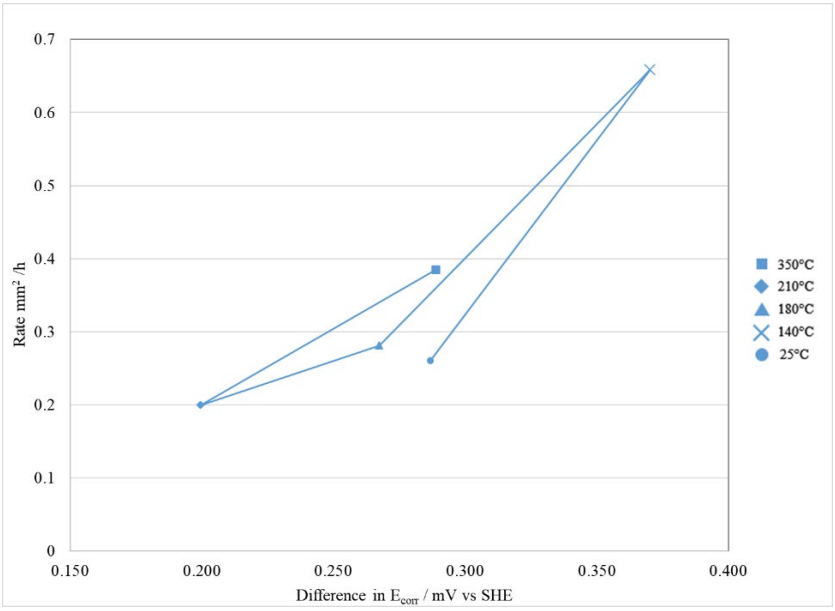

Figure 5.3.2e: Comparison of the difference in free corrosion potential (V vs SHE) between the NSDL and "bulk" alloy surfaces and the rate of FFC propagation at different temperatures for AA6014.

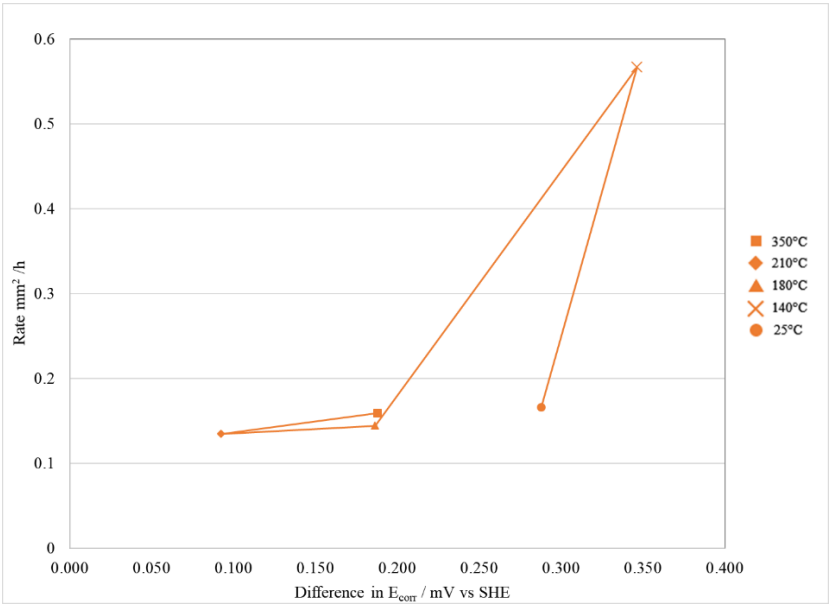

Figure 5.3.2f: Comparison of the difference in free corrosion potential (V vs SHE) between the NSDL and "bulk" alloy surfaces and the rate of SA-FFC propagation at different temperatures for AA6022.

5.4 Conclusions

The presence of a NSDL remains to have the most significant influence on the type and rates of FFC propagation after thermal treatment of the alloy specimens, prior to the application of an organic coating. When a NSDL is present then a rapid form of corrosion is observed, surface active FFC followed by a second type of slower more penetrative corrosion, successive pitting corrosion. When a NSDL is not present only the slower successive pitting is observed. When comparing both alloys, there is not a significant difference in corrosion area for AA6014 and AA6022 visually. However, AA6014 samples with no NSDL have a greater corrosion area relative to AA6022. There is a slight difference in corrosion areas with a NSDL, again with AA6014 displaying a greater corrosion area. Generally, AA6014 has a greater rate of corrosion, i.e., AA6022 is more corrosion resistant. this could be due to the higher percentage of copper in the composition of AA6014 and a higher percentage of copper leading to a greater chance of a copper-rich surface as a result of thermal treatment and why the surface potentials of both AA6014 and AA6022 vary quite substantially across a range of thermal treatment temperatures whether a NSDL is present or not. The presences of a NSDL lowers the surface potential, relative to the bulk alloy, in a range of 0.2V to 0.37V for AA6014 and 0.093V to 0.346V for AA6022 and could be why AA6014 shows a slight increase in corrosion rates.

The effect of thermal treatment has little influence on surfaces without a NSDL with little change in corrosion morphologies over corroded areas and corrosion rates. The observations is unexpected because thermal treatment, especially at higher temperatures within the range used, would be expected to change the precipitate distribution. This suggests that SP FFC is not strongly influenced by changes in the distributions of the precipitates present. AA6014 shows more of a trend for samples with and without a NSDL. The effect of thermal treatment is more clearly seen on surfaces with a NSDL with both AA6014 and AA6022 showing the greatest corrosion rates and greatest potential difference at 140°C. The thermal treatment temperatures of 210°C to 250°C showed the greatest corrosion resistance, with the slowest corrosion rates and smallest potential difference. This could be ascribed to the greater Cu and Fe content within the AA6014. It is possible that the 210°C to 250°C range produces a change in the precipitate distribution which may render the bulk a less active cathodic surface when coupled to the NSDL.

Chapter 6 – The effect of inhibitors and presence of a NSDL on the type and rate of FFC using time-lapse photography.

6.1 Introduction

During FFC, filaments are produced which consist of an active head, containing a concentrated aqueous electrolyte, and a tail, containing dry semi-porous corrosion products 210. Due to differential aeration, the leading edge of the active head undergoes anodic metal dissolution, whilst the trailing edge of the active head experiences cathodic oxygen reduction[276,281]. These reactions lead to the partially hydrolysed $[Al(H_2O)_6]^{3+}$ cations continuously moving towards the cathode in trailing edge of the active head, and the OH^- and Cl^- anions continuously moving towards the anode at the leading edge of the active head, giving it a low pH, c.a. pH 1. The reactions can continue for prolonged periods of time and result in filaments which are several centimetres long.

Aluminium alloys with a copper content can form copper-rich intermetallic particles at the surface and grain boundaries when the alloys undergo thermal treatment. The presence of the copper-rich intermetallic particles produces a surface that is highly susceptible to localised corrosion when an aqueous chloride-based electrolyte is present. The presence of copper-rich intermetallic particles, along with iron intermetallics, such as Q-phase ($Al_5Mg_8Si_6Cu_2$ and $Al_4Cu_2Mg_8Si_7$), θ-phase (Al_2Cu) as well as Al_5FeSi and α-Al(MnCrFe)Si phases, within the alloy, may setup regions of anodic attack and cathodic oxygen reduction due to Mg dealloying and leaving behind a copper-rich sponge, similar to that seen with AA2024[294]. After corrosion has been initiated, the copper-rich regions on the surface produce changes in local electrochemical activity towards cathodic oxygen reduction [71,131,295,296]. AA6014 and AA6022 contain ≤0.25 Cu, ≤0.35 Fe and 0.01-0.11 Cu, 0.05-0.2 Fe, respectively. This is significantly lower than AA2024-T3 (3.8-4.9 Cu, ≤0.5 Fe) and lower than AA6016 (≤0.2 Cu, ≤0.5 Fe) and AA6111 (0.5-0.9 Cu, ≤0.4 Fe). It is possible that the inhibitors that displayed an effective resistance to FFC in AA2024-T3 may have a positive effect on AA6014 and AA6022, but there should be more correlation between the alloys investigated in this chapter and that of AA6016 and AA6111 since the compositions are more aligned.

For decades ways of reducing corrosion have been investigated, with some excellent inhibitors identified. The most effective corrosion inhibitors for aluminium, and steel, contain pre-treatments and primer pigments containing chromate.[170,297–299] Chromium (VI) oxyanions reduce the effect of localised corrosion on thermally treated aluminium due to the passivation of the S-phase intermetallic particles, thereby preventing anodic dealloying[297,299–304]. The work has also found that chromium (VI) oxyanions inhibit the cathodic oxygen reduction on copper-rich sites[297,305,306]. However, due to the production of chromates, the sparingly soluble nature of the inhibitor and risks associated with them (toxicity and carcinogenicity), they have been prohibited by REACH (Registration, Evaluation, Authorization, and Restriction of Chemicals)[307–309]. Therefore, alternatives have been investigated. For this chapter, work on the following inhibitors and associated inhibitors will be discussed; hydrotalcite, benzotriazole, diethyldithiocarbamate and smart inhibitors using cations and anions.

Since the need for alternative corrosion inhibitors was identified, studies have been conducted looking at different compounds, additions to coatings and different mechanisms such as smart-release pigments or sol-gel-based coatings to reduce corrosion rate 23. Smart-release pigment inhibitors release corrosion inhibitors when placed in certain environments such as pH extremes, when there are electrochemical potential differences, or when they interact with ionic species. Smart-release pigments work efficiently, especially when they interact with ionic species (of specific ionic strength), as they release the inhibitors only when required, meaning they could work over a prolonged period. During these interactions there will be ion-exchange, whereby the corrosion causing ions are exchanged for corrosion inhibiting ions. Cathodic inhibitors typically produce an insulating film either by reacting with cathodically evolved hydroxide ions to form insoluble precipitates, preventing electron transfer between the metal substrate and cathodic site. An alternative theory suggests that cathodic inhibition involves the removal of free radical intermediates by using free radical scavengers (trans-cinnamate, benzoate, salicylate) to negatively shift the E_{corr} and I_{corr}[186]. Some anodic inhibitors may also act as oxidising agents.

One of the more effective inhibitor carriers and release compound is hydrotalcite, HT. HT is an anion exchange clay, which when used in the as-received condition will contain stored carbonate anions. It is a layered double hydroxide that has shown a positive inhibiting effect on aluminium and its alloys. Hydrotalcite

$Mg_6Al_2CO_3(OH)_{16}\cdot 4(H_2O)$, as mentioned previously, has a layered double hydroxide of positively charged layers of magnesium and aluminium ions which can be substituted with other metal ions, M^{2+} and M^{3+}. The positive layers are ionically balanced by layers of weakly bound anions, typically carbonates, which can also go through ion-exchange which makes hydrotalcite an interesting inhibitor mechanism as it can affect both cathodic and anodic corrosion sites[1,23,38,40,48–57]. Hydrotalcite, as well as hydrotalcite-like compounds, have several properties that make them a viable alternative to chromates. They can neutralise aqueous acids when they are in the form of calcined hydrotalcite. They actively search for and react with halides in aqueous solutions and halogens in polymers 334. They simultaneously exchange aggressive anions, Cl^-, for either nonaggressive or corrosion-inhibiting anions by neutralising the electrolyte in the filament head[192,210,342].

Studies 23 have been conducted looking at how rare-earth metal (REM) ions, such as cerium (III) and yttrium (III), whether in smart-release pigments or sol-gel-based coatings affect the rate of FFC propagation. When the REM ions, known as cathodic precipitation inhibitors, are added to corrosive electrolytes they effectively inhibit corrosion on aluminium alloys when they are submerged in said electrolyte. The REM ions react with OH^- ions that are produced during cathodic oxygen reduction. The reactions result in insoluble hydroxide precipitates at the metal-electrolyte interface. It has also been noted that when Ce (III) oxidises to Ce (VI), due to hydrogen peroxide from the cathodic oxygen reduction process, this also aids in corrosion inhibition due to the formation of dense CeO_2 films 317. It has been shown that smart-release pigments, when combined into organic polymer binders, could match, potentially surpass, the effectiveness of the chromate inhibitors 195. The pigments can simultaneously release the inhibitor species and sequester aggressive ions from the aqueous environment.

Benzotriazole is a heterocyclic, amphoteric, aromatic organic compound. It can exist in neutral, anionic, or cationic forms, depending on the pH. It has been shown to effectively inhibit the corrosion of copper, and alloys containing copper, whether it is atmospheric corrosion or corrosion due to samples being submerged[345,346]. Other work has shown benzotriazole, and the benzotriazole-anion (when exchanged into a hydrotalcite layered double hydroxide, LDH), is an effective corrosion inhibitor of aluminium, and its alloys, as well as zinc[196,347–349]. The benzotriazolium cation,

$BTAH_2^+$, should be able to be released through an exchange equilibrium with cations present in an aqueous electrolyte, at any pH. However, at alkaline dominating sites, where there is localised cathodic activity, any $BTAH_2^+$ released will quickly be deprotonated and the exchange equilibrium will be constantly skewed in favour of more $BTAH_2^+$ to be released, making the process acutely efficient.

Work by Williams et al.[4,192,210,339], and other work by Buchheit[78,300,324,350–353], found that anion exchange pigments (CO_3^{2-}, NO_3^- and CrO_4^{2-}) based on hydrotalcite-like compounds had a positive effect on the inhibition of FFC on AA2024-T3 due to the pigments ability to remove aggressive Cl^- anions from the concentrated aqueous electrolyte in the active head of the filament. It is thought that this process aids in the repassivation of the metal surface. The work also noted that the hydrotalcite matrix could act as a generic delivery system for other anions making it a very versatile method for corrosion inhibition.

Coleman et al[6,192,199,339,354,355] also looked at the effect of hydrotalcite on aluminium alloys, AA6016 and AA6111, as well as other inhibitors. They found that the presence of hydrotalcite, in its untreated form, i.e., no anion additions, did reduce the amount of FFC, but stated that it was insignificant as it only reduced the area of FFC by just over $50mm^2$. However, it was noted that the effect of the hydrotalcite may have been restricted due to the concentration of the electrolyte used, 2M HCl, and the exchange capacity attained very quickly allowing FFC to continue. The hydrotalcite-like compound showed a slight improvement to corrosion inhibition, but not noteworthy.

Aluminium alloys containing copper-rich intermetallics, or copper dealloying intermetallics or the bulk alloy, increases the likelihood for to FFC to occur and propagate at a quicker rate [71,240,297,356,357]. Therefore, inhibitors that reduce the anodic dealloying processes and cathodic oxygen reduction processes have been investigated previously, with chromate again showing the more successful outcome[297,299,357,358]. Work by Williams et al[6,192,196,210,339] on AA2024-T3 which contains 3.8-4.9% of copper investigated the effect of benzotriazolate (BTA^-) along with other anions, ethyl xanthate and oxalate. Benzotriazolate is widely known to inhibit copper corrosion due to the numerous studies conducted over the last sixty years[300,359–366]. Williams and McMurray found that hydrotalcite containing organic anions were able to inhibit FFC propagation on PVB (Polyvinyl butyral) coated AA2024-T3, with the combined

hydrotalcite-benzotriazolate (HT-BTA^-) pigment producing the greatest inhibition of FFC. However, it was also noted that although the (HT-BTA^-) produced a good result, it was not able to reproduce, or better, the inhibition produced when a chromate anion is combined with the hydrotalcite (HT-CrO_4^{2-}). Other work has shown that copper complexants, 2,5-dimercapto-1,3,4-thiadiazolate (DMTD), also has an inhibiting effect by suppressing cathodic oxygen reduction on pure copper[199,367,368].

Further work by Williams et al.[199] looked at the inhibition of AA2024-T3 pitting corrosion by copper complexing compounds making use of DEDTC and BTA, along with other reagents (EDTA and DMTD) that should interact with the aqueous cations. DEDTC is a form of HT this in this form the carbonate has been replaced with DEDTC inhibitor ions by calcining the HT and then re-dispersing in a solution containing DEDTC ions. They found that DEDTC and DMTD, which form the copper complexants, appeared to produce precipitates on the metal surfaces and successfully inhibited the localised corrosion. BTA also produced a surface film and showed to inhibit the corrosion mechanisms, but less than DEDTC and DMTD. They also found that although EDTA produced little to no inhibition of localised corrosion, it did suggest that Cu^{2+}ions were sequestered by the EDTA as no copper re-plating was observed on the surface of the aluminium and that cathodic oxygen-reduction can be sustained, due to the copper-rich intermetallic particles, despite the absence of copper re-plating.

Williams and McMurray investigated the effect of smart-release inhibitors on AA2024-T3, the effect of anion-exchange hydrotalcite based pigments, along with cationic pigments, bentonite pigments with cerium (III) and yttrium (III) cations[192,196,339]. They found that the bentonite pigments were not an effective inhibitor of FFC on AA2024-T3. They deduced that due to lower-than-expected pH in the filament-head electrolyte, there were no REM-hydroxide precipitates at cathodic oxygen reduction sites. However, the anion-exchange hydrotalcite pigments were shown to provide effective corrosion inhibition, especially when copper specific anionic reagents were combined. Their work, via SKP (Scanning Kelvin Probe) potentiometry, also showed that BTA, EDTA and DEDTC anions interact with the intact metal surface and depress the free corrosion potential. DEDTC was shown to be the least effective corrosion inhibitor out of BTA, EDTA and DEDTC. The work also

found that the copper-specific exchange anions provide an inhibition comparable and surpassing that of the baseline inhibition effect of hydrotalcite-carbonate pigments.

The effect of cationic exchange pigments has been investigated on hot dip galvanised, HDG, steel by Richards et al.[369] They used a novel corrosion inhibitor, cationic benzotriazole, CBP. This BTA containing pigment is a cation exchange resin (amberlite), which is prepared by dispersing the as-received resin beads in a solution of BTA. The acidic nature of the resin protonates the BTA, and the cationic form of the BTA (BTAH+) gets incorporated within the resin beads. After filtering and drying, these are pulverised to a fine powder, which is then used as the inhibitive pigment which acts as a smart-release store of BTAH+ cations. The acidic nature of the CBP suggests that it should be compatible with other processes that remove impurities, intermetallic particles, and other unwanted particles from the metal's surface like etch-primers and/or acid-based pre-treatment primers, thereby passivating the surface. During this process, the $BTAH^+$ is converted to BTA^-. The BTA^- was able to inhibit both anodic and cathodic sites effectively, with the anodic zinc dissolution having the predominated effect and the cathodic oxygen reduction also having a profound inhibitive effect on the zinc surface of the HDG. When CBP was present in the organic PVB coating it was noted that an increase in the pigment volume fraction, Φ_{CBP}, reduced the delamination rates; with the greatest inhibition and lowest rate when a Φ_{CBP} of 0.1 was used. The work went on to propose two points; one, that the CBP pigment acts to produce a rapid and efficient release of BTA^- into the alkaline catholyte under the organic coating, and two, the high pH of the catholyte, along with the absence of aggressive anion, lead to the formation of a BTA^- film at the zinc surface, thereby inhibiting the underfilm cathodic oxygen reduction.

Recent work, conducted on PVB coated HDG steel, using hydrotalcite-based organic and inorganic anions as smart release corrosion inhibitors in the organic PVB coating found that most of the inhibitors reduced the rate of cathodic disbondment. The anions used were carbonate (CO_3^{2-}), nitrate (NO_3^-), tungstate (WO_4^{2-}), molybdate MoO_4^{2-} and phosphate (PO_4^{3-}) and the cathodic and mixed corrosion inhibitors used were chromate (CrO_4^{2-}), trans-cinnamate, benzoate, salicylate and benzotriazole. It was noted that the inhibition was dependent on the anion present in the hydrotalcite. Relative to the performance of chromate, none of the inorganic anions were able to produce a similar, or better outcome, however some of the organic anions, in particular $HT\text{-}BTA^-$, were

able to match the results seen with chromate. HT-BTA^- was observed to reduce the rate of FFC propagation by delaying the cathodic delamination process. Three main modes of inhibition were observed: ion-exchange between the BTA^- and the Cl^- and OH^- at the defect. HT-BTA inhibits the cathodic disbondment mechanism by anodically inhibiting the bare zinc surface at the defect site either forming an insoluble zinc-benzotriazole salt or a metal-polymeric film[186–188,252,370]. The HT-BTA^- inhibits the cathodic front within the delamination region.

This chapter evaluates a selection of novel inhibitive pigment technologies in terms of their relative efficiency in slowing down the rates of FFC on AA6014 and AA6022, both in the presence and absence of an NSDL. The reason for these inhibitors is that the as-received HT[192,196,210,339,371–373] has already been shown to effectively inhibit FFC on AA2024 and that when a copper-specific inhibitor is present (DEDTC[196,199]), that its efficiency can be improved. This strategy is tested out here using Mg-Si containing Al alloys which comprise significantly less Cu content than AA2024. CBP has been selected because of its efficiency in slowing coating failure rates on Zn, but also because its stored inhibitor (BTA, although in its anionic form) is also known to inhibit FFC on AA2024[369].

6.2 Experimental

Corrosion propagation and rate study:

Samples were prepared as described in Chapter 2.3 and 2.4; Alkali cleaning of the samples in NaOH (10% w/v), for c.a. 45s at 60°C, to dissolve any aluminium oxide and any NSDL on the surface. Samples were rinsed with distilled water and acetone before acid desmutting using concentrated HNO_3 (15.6 molar) for 30s at 25°C to remove impurities such as copper and iron from the surface, and to passivate the surface. The samples were again rinsed with distilled water and acetone. When required, the NSDL was reintroduced by manual abrasion using 180 grit silicon carbide paper/emery paper for 5 mins. The abrasion direction was orientated in the same direction as the rolling direction.

The HT-DEDTC was used as received from Sigma-Aldrich, as Sodium diethyldithiocarbamate trihydrate, and is produced as described in previous work[192]. The method for producing cationic BTA containing pigment (CBP) has been described in previous work[369]. The base coating was 15.5% (w/w) ethanolic PVB solution with different inhibitors at different pigment volume factions, Φ, added to the PVB to produce an air-dried PVB coating of thickness 30µm ± 5µm. The inhibitors investigated were cationic benzotriazolium, CBP, diethyldithiocarbamate, DEDTC, and Hydrotalcite, HT, with densities of 1.2 gcm^{-3}, 1.1 gcm^{-3} and 2.1 gcm^{-3}, respectively. The pigment volume fractions used were 0 (no inhibitor), 0.01, 0.025, 0.05, 0. 1, and 0.2. The mass of the pigment added to the PVB (mass of 15.5 g and density of 1.08 gcm^{-3}), based on pigment volume fractions, was calculated using 374:

$$M_{pig} = \frac{\varnothing \times M_{pol} \times \rho_{pig}}{(1 - \varnothing) \times \rho_{pol}}$$

Where M_{pig} is the mass of the pigment in g, M_{pol} is the mass of the polymer coating in g, ρ_{pig} is the density of the pigment in g cm^{-3}, ρ_{pol} is the density of the pigment in g cm^{-3} and Φ is the pigment volume fraction.

When adding the inhibitors to the PVB additional ethanol was added to the PVB to create a slurry to allow the inhibitor to mix more readily with the PVB. The additional ethanol evaporated off during the coating stage. The PVB and inhibitor mixture was mixed with a shear mixer until there were no signs of the inhibitor present. This was

adjusted for each pigment volume fraction, but a minimum time of 10 minutes was used.

Samples were rinsed with distilled water and acetone prior to coating. Once coated and the coating had dried and adhered to the surface, 10mm defects were scribed through the PVB layer normal (90°) to the rolling/NSDL direction with a scalpel. Due to economy of samples, most were scribed with 2 defects at least 13mm apart[2–4,214]. The number of defects used, have been identified in each section. FFC was initiated by injecting the scribe with 1µL of 2M aqueous hydrochloric acid using a glass micro-capillary dispenser. The HCl injection method was intended to create greater reproducibility than methods involving full sample exposure either by salt fog, HCl vapour, or immersion in aqueous electrolyte[2–4,214].

Samples were placed in sealed containers and kept at 20°C and at 80% relative humidity by using a saturated salt solution of Ammonium sulfate. A digital hygrometer and temperature sensor (Lascar's EasyLog EL-USB-2-LCD+) was placed in each container. Each container contained their own control samples, i.e., where the pigment volume fraction was 0.

Photographs were taken periodically, and measurements obtained using Photoshop, as described in Chapter 2.5 A selection of graphs were produced to show corrosion growth with respect to time and to compare the rate and type of cosmetic corrosion observed.

Polarisation curves obtained using Potentiodynamic experiment

The electrolyte used varied. Some samples were placed in 0.1M NaCl, others were placed in 0.1M NaCl with the addition of an inhibitor. When producing the solutions for both potentiodynamic and open circuit potential, OCP, (Open Circuit Potential) measurements, the inhibitors are either dissolved BTA or the sodium salt of DEDTC. Both are highly water soluble (although BTA only at pH values of >8 where it forms an anionic species). To dissolve the BTAH into the 0.1M NaCl the pH was increases to pH 8.5. The DEDTC readily dissolves into NaCl. The following inhibitor additions were used: 0.01 ML^{-1} CBP, 0.01 ML^{-1} DEDTC, and 0.001 ML^{-1} DEDTC. HT does not readily dissolve into NaCl, so it was not investigated at this time.

The samples were not coated but were covered using PTFE tape leaving a 10 mm^2 section of the samples exposed to the electrolyte. The samples were connected to a potentiodynamic sweep as described in chapter ##. The potentiodynamic experiments held the specimen at open circuit potential, OCP, for 20 mins prior to starting polarisation where a sweep rate of 1 mV/s was used. After completion of the experiment the data was converted to a format allowing plots of either Ecorr vs time or log i vs V to be plotted in excel, seen in section 6.3.2.

6.3 Results and Discussion

6.3.1 Effect of inhibitors – time lapse

The next slides show the final image of each inhibitor for each pigment volume fractions and at the 2 thermal treatment temperatures. The first image in each sections shows surfaces with no NSDL, and the second image shows surfaces with NSDL.

6.3.1.1 AA6014 and AA6022 Inhibitor A = Cationic benzotriazole at 140°C and 20°C

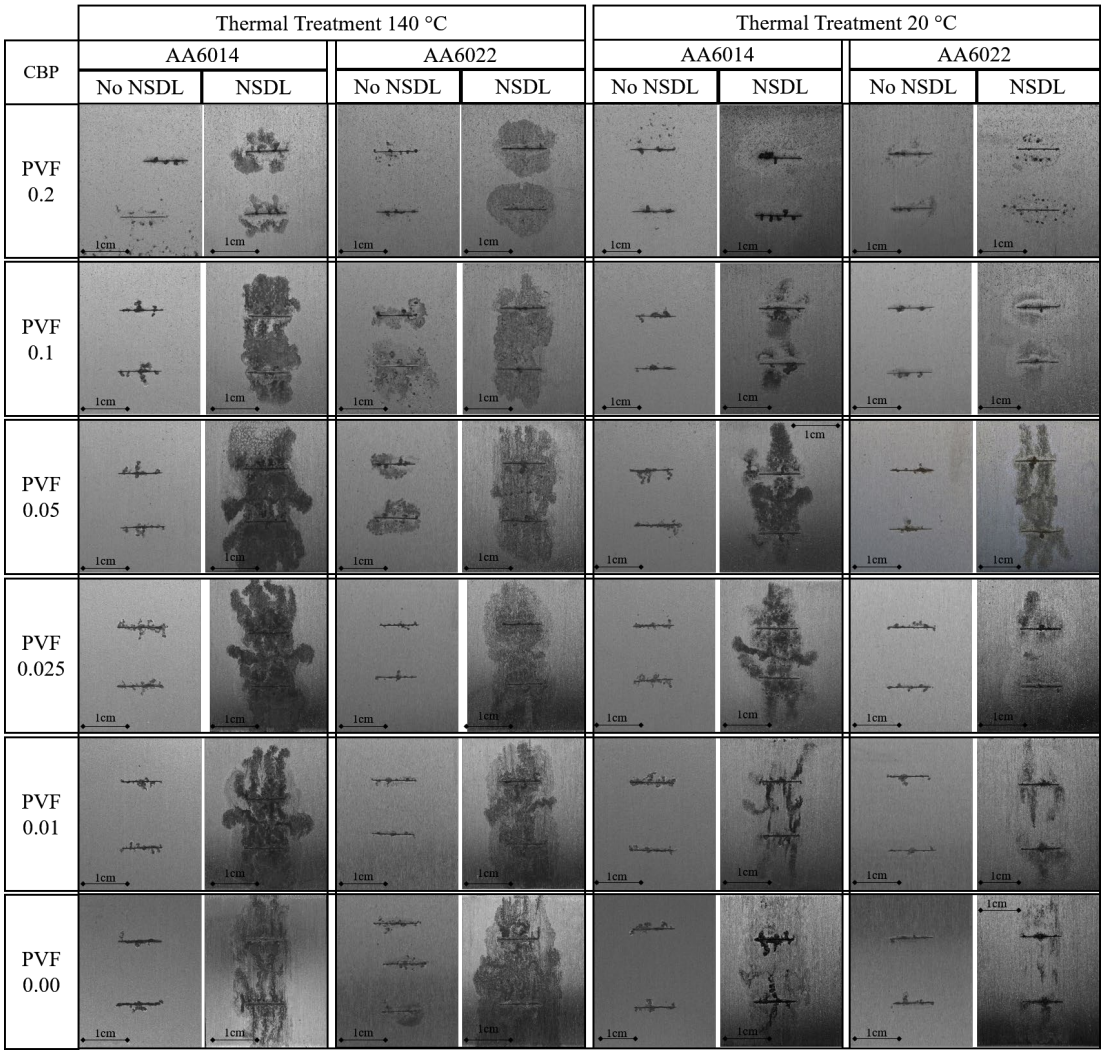

Figure 6.3.1.1a: AA6014 and AA6022 samples with cationic benzotriazole at 140°C and 20°Cat c.a. 700 hours

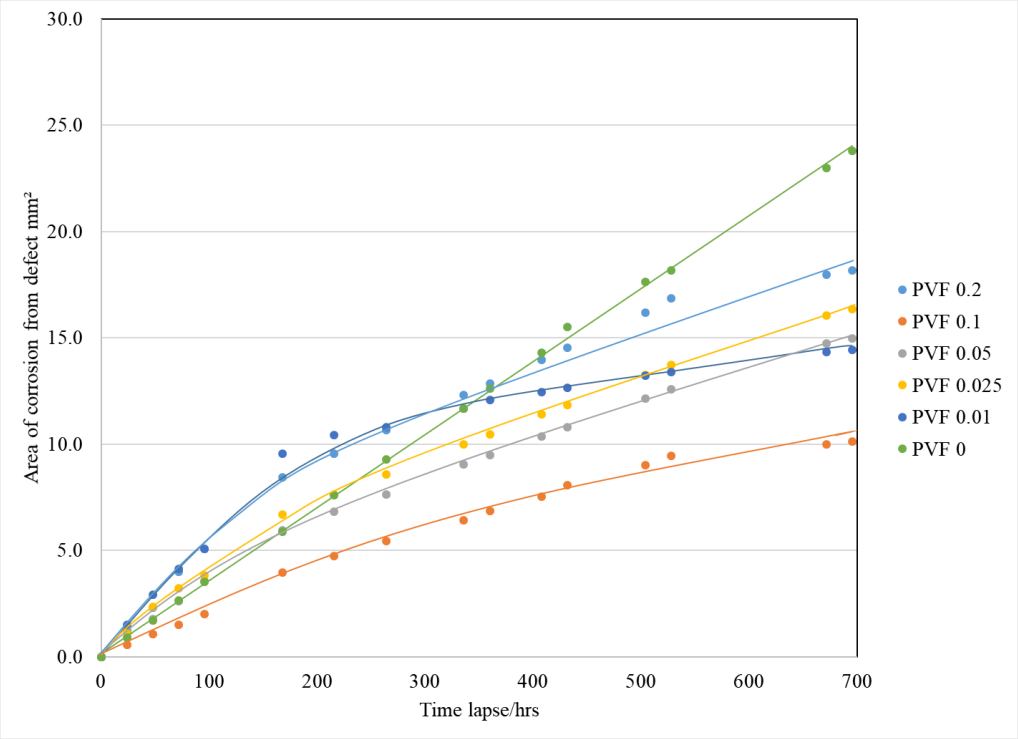

Figure 6.3.1.1b: Area of corrosion for AA6014 samples without a NSDL for each pigment volume fractions at 20°C. Samples were injected with 1µL of 2M and kept at 80% RH.

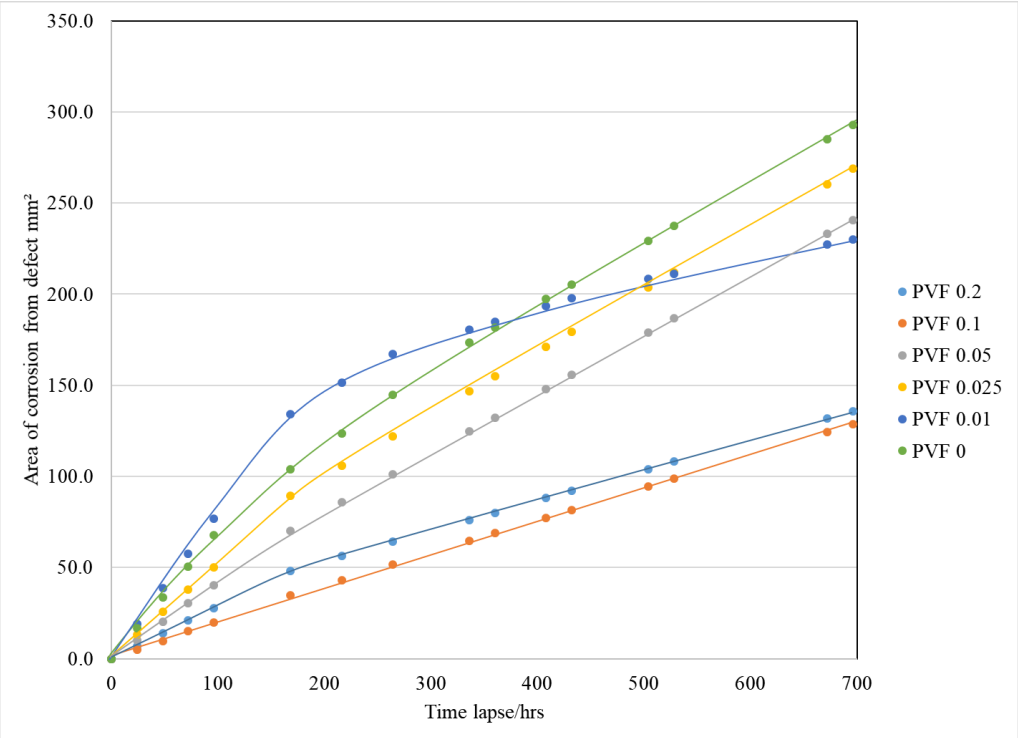

Figure 6.3.1.1c: Area of corrosion for AA6014 samples with a NSDL for each pigment volume fractions at 20°C. Samples were injected with 1µL of 2M and kept at 80% RH.

Error bars are not shown on the graphs to maintain clarity of the results. The standard deviations for the corrosion area for AA6014 with and without a NSDL can be seen in table 16 below:

PVF of CBP	AA6014 No NSDL	AA6014 NSDL
	Mean SD area mm^2	Mean SD area mm^2
0	0.6606	16.7232
0.01	2.2792	0.4200
0.025	0.6072	3.6978
0.05	0.3061	10.2164
0.1	1.2653	4.5195
0.2	1.1739	11.7010

Table 16: Standard deviations of the corrosion area for all samples of AA6014 with different PVF of CBP.

Figure 6.3.1.1a shows that the presence of a NSDL increases the corrosion area. It also shows that the type of FFC differs from having a NSDL present to it being absent with a NSDL showing both rapid S.A.FFC followed by, in some cases, a slower, more penetrative, SP-FFC. The graph for AA6014 without a NSDL at 20 °C figure 6.3.1.1b, and with a NSDL at 20 °C figure 6.3.1.1c, shows that when the pigment volume fraction (PVF) is zero, i.e., the control sample, then the area of corrosion propagates in a linear fashion, as found in previous chapters. However, when the PVF is present, whether a NSDL is present or not, then the area propagations tend away from a linear relationship.

For AA6014 samples at 20°C without a NSDL, figures 6.3.1.1b, when PVF is at 0.2, 0.025 and 0.01 the initial area of corrosion measured was larger than the control, and approximately linear up to c.a. 200 hrs. For AA6014 at 20°C, the PVF of 0.025 and 0.01 showed a reduction in the area propagation between c.a. 200 hours and 700 hours with the final area of corrosion measured being less than the control PVF of 0.2 also showed a slight reduction in corrosion area propagation after 200 hours, but nothing significant as it produced the greatest area of corrosion after the control sample. It is possible that PVF of 0.025 and 0.01 have insufficient pigment for ionic exchange initially and a limited amount after c.a. 200 hours. PVF of 0.1 appeared to reduce the corrosion area by the greatest amount. PVF 0.1 produce a fairly linear trend between

area and time, similar to the control. This indicates that although there is some degree of corrosion produced there is sufficient ionic exchange to reduce the area of corrosion at a steady rate.

For AA6014 samples at 20°C with a NSDL present, figure 6.3.1.1c, the PVF of 0.01 also produced a larger measurable area initially than the control sample, for measurements taken up to c.a. 350 hours followed by a reduction in the area propagation and the final area of corrosion measured being less than the control. The PVF of 0.025 produced the largest corrosion area after the control sample. It is possible that when PVF = 0.025 and 0.01, then there is insufficient pigment for ionic exchange. PVF of 0.2 and 0.1 appeared to have the strongest effect in reducing the corrosion area overall and have less corrosion production in the initial 200 hours at both thermal treatment temperatures. The PVF of 0.1 inhibits corrosion production more than the PVF of 0.2. PVF 0.1 has a fairly linear trend between area and time indicating that although there is some degree of corrosion produced there is sufficient ionic exchange to reduce the area of corrosion at a steady rate. AA6014 samples at 140°C produced a similar trend to the results shown above, and the rates for both temperatures are shown below.

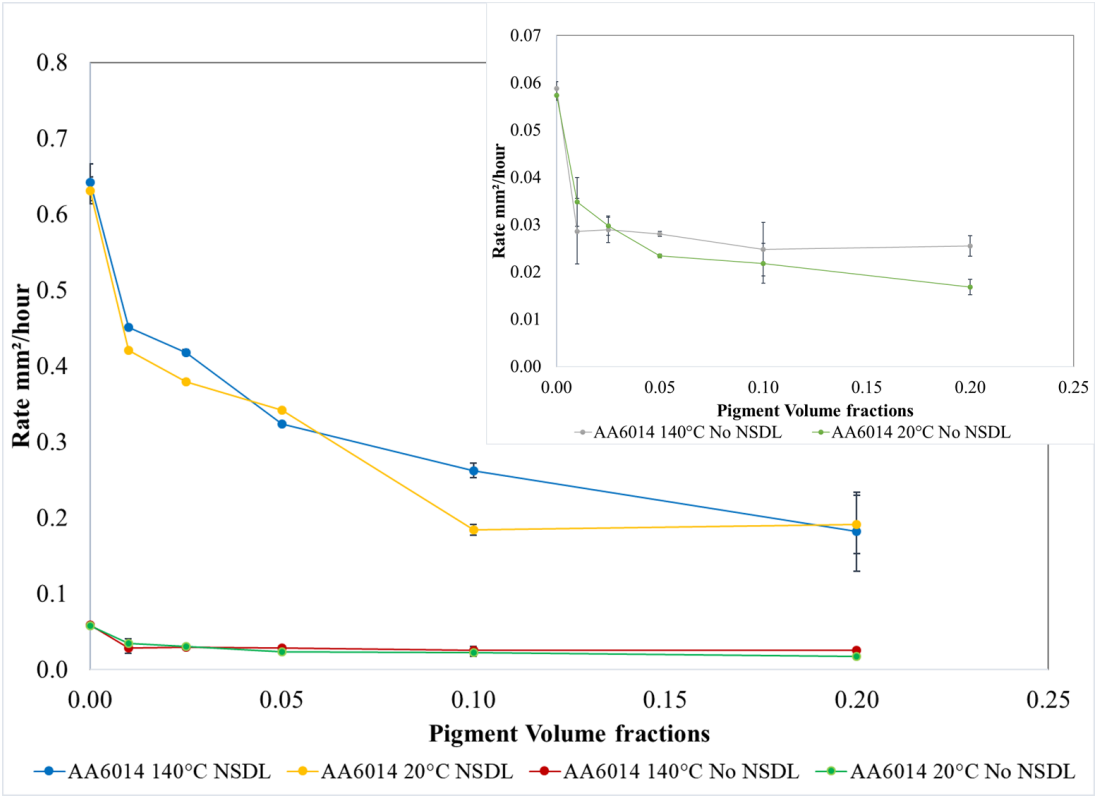

Figure 6.3.1.1d: Rate of FFC propagation for AA6014 samples, with and without a NSDL, with inhibitor cationic benzotriazole present across all pigment volume fractions at 20°C and 140°C. With the rate of FFC propagation for AA6014 samples without a NSDL shown in the top right-hand-corner. Y-error bars included.

Figure 6.3.1.1d shows the rate of FFC propagation for AA6014 samples, with and without a NSDL, with inhibitor cationic benzotriazole present across all pigment volume fractions at 20°C and 140°C. The standard deviation for each AA6014 sample is shown in table 17 below:

PVF of CBP	Standard deviation mm²/hour			
	AA6014 20°C No NSDL	AA6014 20°C NSDL	AA6014 140°C No NSDL	AA6014 140°C NSDL
0.000	0.0011	0.0181	0.0015	0.0243
0.010	0.0052	0.0005	0.0069	0.0007
0.025	0.0020	0.0027	0.0027	0.0036
0.050	0.0004	0.0006	0.0005	0.0008
0.100	0.0042	0.0072	0.0057	0.0097
0.200	0.0016	0.0387	0.0022	0.0521

Table 17: Standard deviation at each PVF of CBP for each AA6014 samples.

Figure 6.3.1.1d shows that the rate of FFC propagation is greater when a NSDL is present. The inset graph shows the rate of FFC propagation for AA6014 samples, without a NSDL, with inhibitor cationic benzotriazole present across all pigment volume fractions at 20°C and 140°C. Contrary to the final areas seen in figure 6.3.1.1b, PVF at 20°C show an increase in corrosion inhibition as the PVF increases, with the PVF of 0.2 having the slowest corrosion rate. PVF at 140°C also shows an increase in corrosion inhibition as the PVF increases, however the inhibition effect appears to plateau between PVF of 0.1 and 0.2. The rates appear to decrease exponentially as the PVF increases. Figure 6.3.1.1d, w.r.t the samples with a NSDL, shows an exponential decline as more PVF is added, with the PVF of 0.2 having the slowest rate. A PVF of between 0.1 and 0.2 would produce a significant corrosion inhibition whether the surface has a NSDL present or not and at both a low temperature and the temperature shown to produce the greatest rate of FFC propagation, as shown in chapter 5.

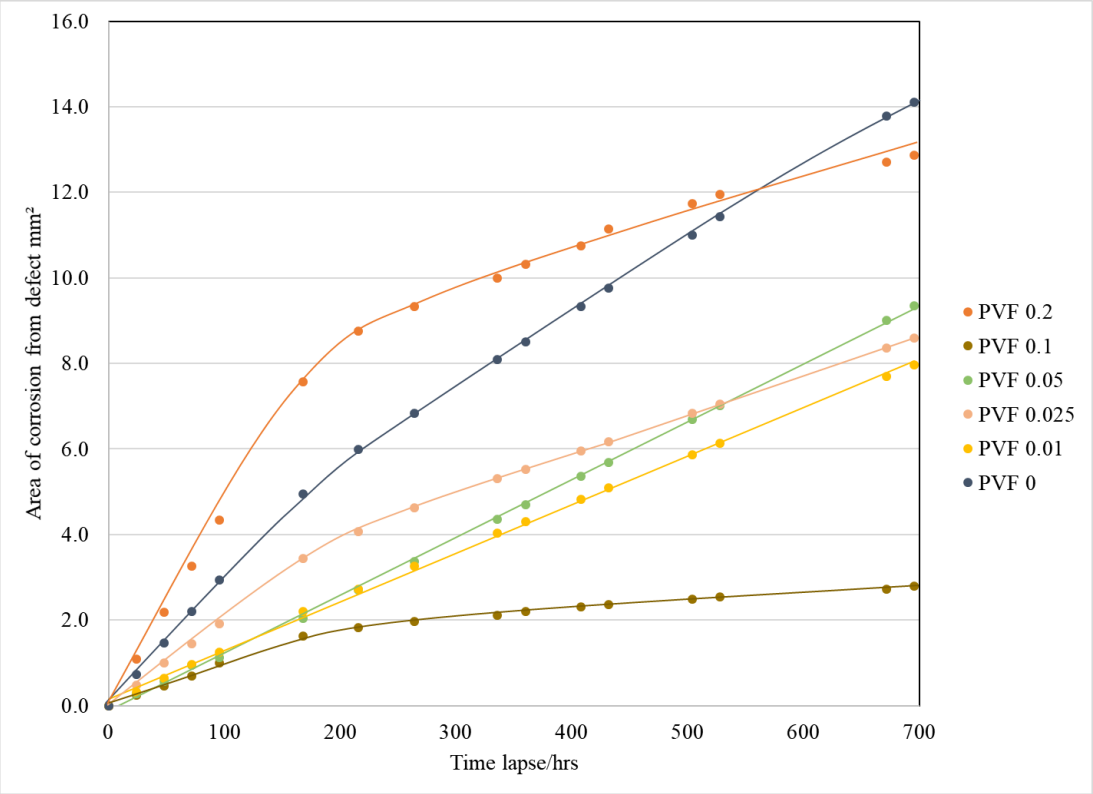

Figure 6.3.1.1e: Area of corrosion for AA6022 samples without a NSDL for each pigment volume fractions at 20°C. Samples were injected with 1µL of 2M and kept at 80% RH.

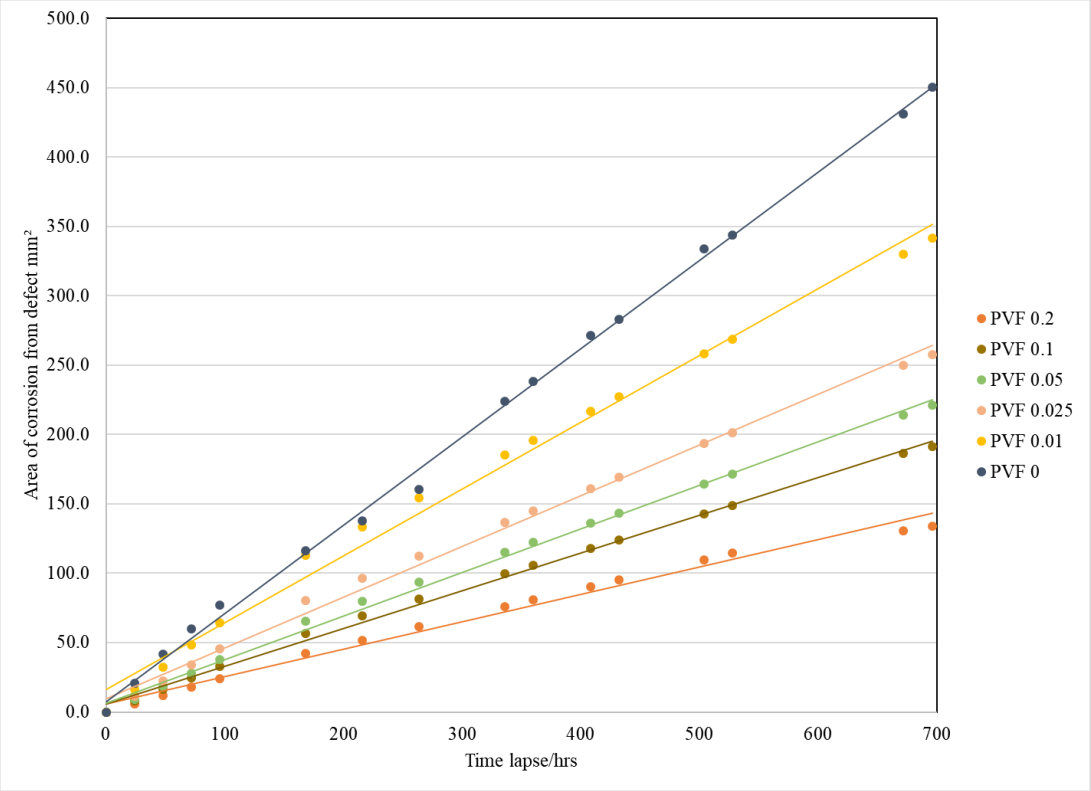

Figure 6.3.1.1f: Area of corrosion for AA6022 samples with a NSDL for each pigment volume fractions at 20°C. Samples were injected with 1µL of 2M and kept at 80% RH.

Error bars are not shown on the graphs to maintain clarity of the results. The standard deviations for the corrosion area for AA6022 with and without a NSDL can be seen in table 18 below:

PVF of CBP	AA6022 No NSDL	AA6022 NSDL
	Mean SD area mm^2	Mean SD area mm^2
0	0.4576	4.4206
0.01	0.7696	13.4785
0.025	0.9488	7.4808
0.05	0.6556	6.6177
0.1	0.0899	14.1591
0.2	1.5600	3.4629

Table 18: Standard deviations of the corrosion area for all samples of AA6022 with different PVF of CBP.

Figure 6.3.1.1a shows that the presence of a NSDL increases the corrosion area. It also shows that the type of FFC differs from having a NSDL present to it being absent with a NSDL showing both rapid S.A.FFC followed by, in some cases, a slower, more penetrative, SP-FFC. The graphs for AA6022 without a NSDL at 20 °C figure 6.3.1.1e, and with a NSDL at 20 °C figure 6.3.1.1f, show that when the pigment volume fraction (PVF) is zero, i.e., the control sample, then the area of corrosion propagates in a linear fashion, as found in previous chapters. However, when the PVF is present, whether a NSDL is present or not, then the area propagations tend away from a linear relationship.

For AA6022 sample at 20°C, without a NSDL, figure 6.3.1.1e, when PVF is at 0.2 the initial area of corrosion measured was larger than the control, and approximately linear up to c.a. 150 hrs. Although the increase in corrosion area propagation appeared to slow down with PVF = 0.2, the corrosion area measured at c.a. 700 hours was not too dissimilar to the control area measured. The PVF of 0.1 produced the smallest area of corrosion for the AA6022 sample at 20°C, potentially showing the most efficient ratio of pigment-coating mix for ionic exchange inhibition. The samples of PVF of 0.01 and 0.05 produce a fairly linear trend between area and time, indicating that although there is some degree of corrosion produced there is sufficient ionic exchange to reduce the area of corrosion at a steady rate.

AA6022 samples at 20°C with a NSDL, figure 6.3.1.1f, show when PVF is present the area of corrosion produced is less than the control sample. PVF of 0.2 produced the smallest area of corrosion, followed by 0.1. All PVF have a positive effect when inhibiting corrosion with all areas measured being smaller than the control area at all point on the graph. All PVF show fairly linear trends indicating that the PVF works at a steady rate, with the greater PVF having the more favourable results. The next largest corrosion area, after the control sample, was produced by PVF 0.01, then 0.025 and finally 0.05 suggesting that there is insufficient pigment for ionic exchange at the lover PVF. AA6022 samples at 140°C produced a similar trend to the results shown above, and the rates for both temperatures follow.

Figure 6.3.1.1f shows the rate of FFC propagation for AA6022 samples, with and without a NSDL, with inhibitor cationic benzotriazole present across all pigment volume fractions at 20°C and 140°C. This graph shows clearly that the rate of FFC

propagation is greater when a NSDL is present. The graph inset figure 6.3.1.1f shows the rate of FFC propagation for AA6022 samples, without a NSDL, with inhibitor cationic benzotriazole present across all pigment volume fractions at 20°C and 140°C. At 20°C most effective PVF was 0.1 followed by 0.01. the rates shown in figure 6.3.1.1f show that the most effective PVF at 140°C was at 0.05 and the most effective PVF at 20°C was at 0.1. Although the PVF differs between the area and rate graphs, generally figure 6.3.1.1f does show that for the most part, as the PVF increases the rate decreases, exponentially, but an increase in rate is observed at both temperatures at PVF = 0.2, which could be a potential outlier. This suggests that the optimum PVF for AA6022, for either temperature, should be between PVF 0.05 to 0.1, which also agrees with the results from the area measurements. The PVF in this range should be enough to effectively reduce the corrosion rate, without saturating the organic coating.

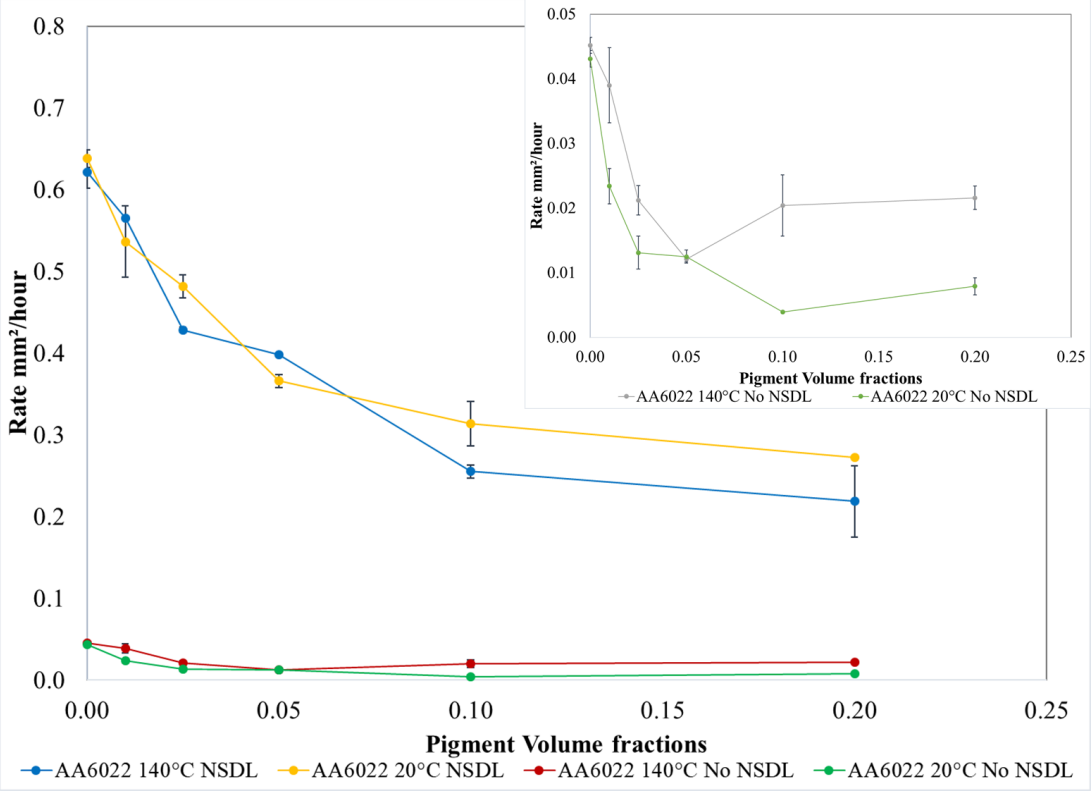

Figure 6.3.1.1g: Rate of FFC propagation for AA6022 samples, with and without a NSDL, with inhibitor cationic benzotriazole present across all pigment volume fractions at 20°C and 140°C. With the rate of FFC propagation for AA6014 samples without a NSDL shown in the top right-hand-corner. Y-error bars included.

Figure 6.3.1.1g shows the rate of FFC propagation for AA6022 samples, with and without a NSDL, with inhibitor cationic benzotriazole present across all pigment volume fractions at 20°C and 140°C. The standard deviation for each AA6022 sample is shown in table 19 below:

PVF of CBP	Standard deviation mm²/hour			
	AA6022 20°C No NSDL	AA6022 20°C NSDL	AA6022 140°C No NSDL	AA6022 140°C NSDL
0.000	0.0013	0.0107	0.0012	0.0203
0.010	0.0028	0.0435	0.0058	0.0006
0.025	0.0026	0.0143	0.0023	0.0030
0.050	0.0010	0.0078	0.0005	0.0007
0.100	0.0002	0.0273	0.0047	0.0081
0.200	0.0013	0.0009	0.0018	0.0436

Table 19: Standard deviation at each PVF of CBP for each AA6022 samples.

Figure 6.3.1.1g, w.r.t. samples with a NSDL present, shows an exponential decline in rate as more PVF is added, with the PVF of 0.2 having the slowest rate at both temperatures. Figure 6.3.1.1g shows a plateau between the PVF of 0.1 to 0.2. A PVF of 0.2 would produce a significant corrosion inhibition at both temperatures, with PVF 0.1 also producing effective results. If the sample surface is likely to contain a NSDL then a PVF of 0.2 would be the most favourable PVF to use. However, due to the likelihood of a mixed surface, and a PVF of 0.2 performing poorly on the bulk samples, it may be more beneficial to use a PVF of c.a. 0.1 to reduce the corrosion rate whether the surface has a NSDL present or not and at both a low temperature and the temperature shown to produce the greatest rate of FFC propagation, as shown in chapter 5.

6.3.1.2 AA6014 and AA6022 Inhibitor B = Diethyldithiocarbamate at 140°C and 20°C

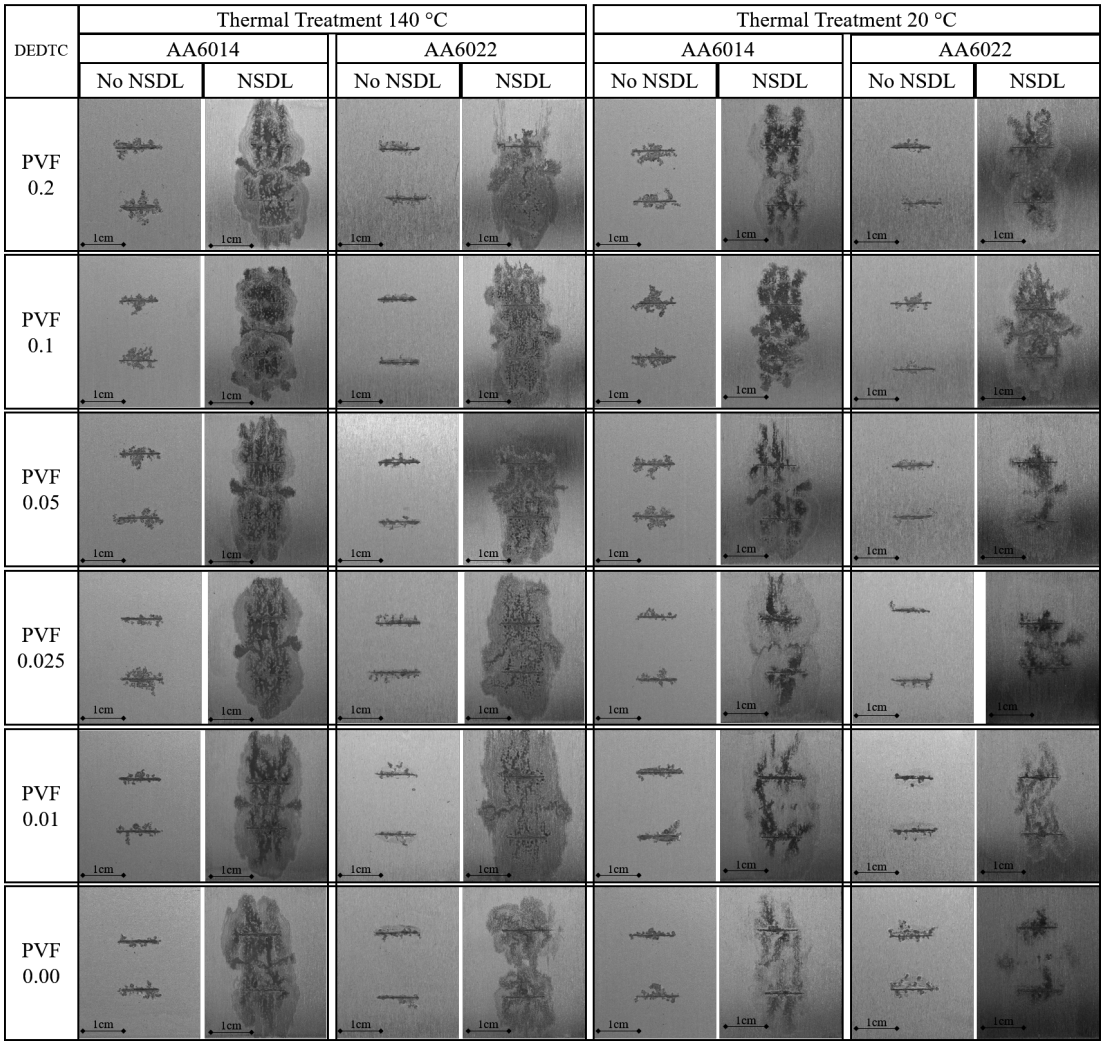

Figure 6.3.1.2a: AA6014 and AA6022 samples with diethyldithiocarbamate at 140°C and 20°C at c.a. 700 hours.

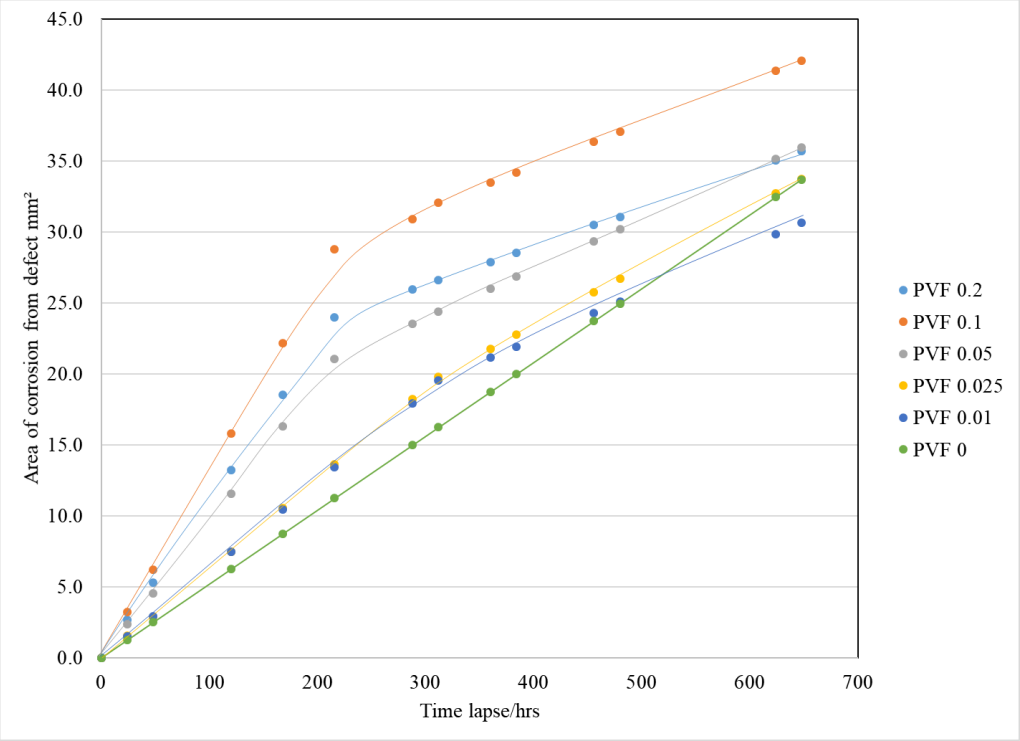

Figure 6.3.1.2b: Area of corrosion for AA6014 samples without a NSDL for each pigment volume fractions at 20°C. Samples were injected with 1µL of 2M and kept at 80% RH.

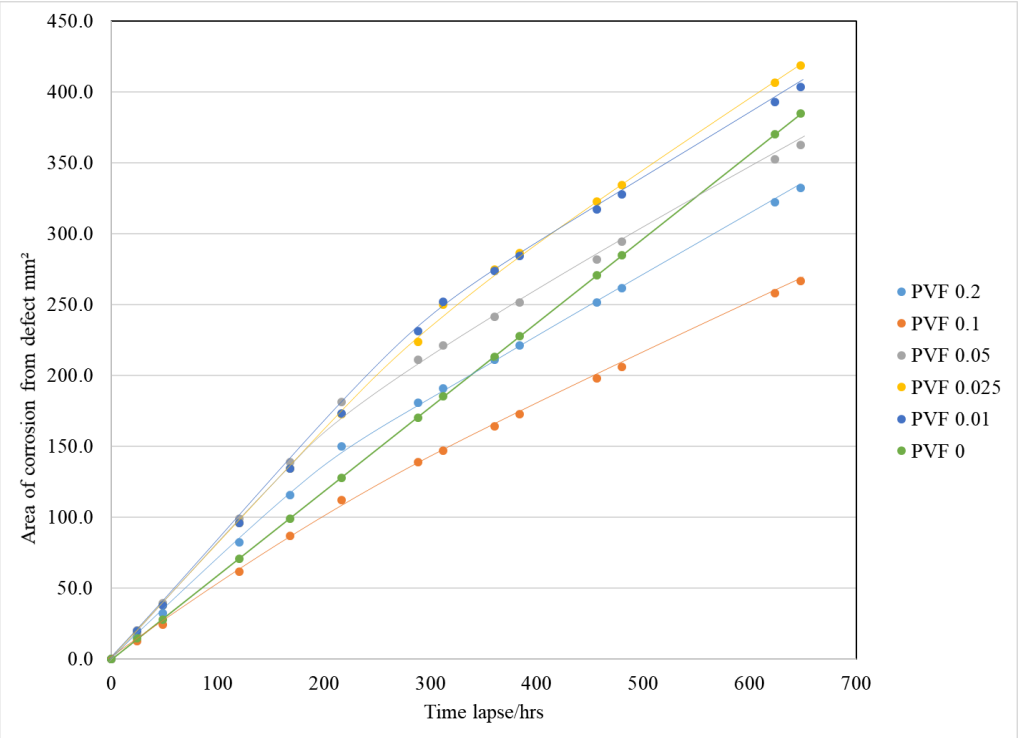

Figure 6.3.1.2c: Area of corrosion for AA6014 samples with a NSDL for each pigment volume fractions at 20°C. Samples were injected with 1µL of 2M and kept at 80% RH.

Error bars are not shown on the graphs to maintain clarity of the results. The standard deviations for the corrosion area for AA6014 with and without a NSDL can be seen in table 20 below:

PVF of DEDTC	AA6014 No NSDL	AA6014 NSDL
	Mean SD area mm^2	Mean SD area mm^2
0	3.0224	5.9989
0.01	1.6019	21.1743
0.025	1.9358	4.8869
0.05	2.1518	2.6207
0.1	2.9220	15.3557
0.2	2.7931	6.3399

Table 20: Standard deviations of the corrosion area for all samples of AA6014 with different PVF of DEDTC.

Figure 6.3.1.2a shows that the presence of a NSDL increases the corrosion area. It also shows that the type of FFC differs from having a NSDL present to it being absent with a NSDL showing both rapid S.A.FFC followed by, in some cases, a slower, more penetrative, SP-FFC. The graph for AA6014 at 20 °C without a NSDL, figure 6.3.1.2b, and with a NSDL, figure 6.3.1.2c, show that when the pigment volume fraction (PVF) is zero, i.e., the control sample, then the area of corrosion propagates in a linear fashion, as found in previous chapters. However, when the PVF is present, whether a NSDL is present or not, then the area propagations tend away from a linear relationship.

AA6014 samples at 20°C without a NSDL, figure 6.3.1.2b, show that when PVF is present most of the PVF have initial areas of corrosion that are larger than the control. This trend continues until c.a. 450 hours when the area of corrosion with PVF of 0.01 drops below the control and measures a slightly smaller area. Figure 6.3.1.2b suggests that the presence if the PVF increased the area of corrosion on the samples, compared with the control in most cases. Overall, all samples had a corrosion area between c.a. $22mm^2$ to c.a. $47mm^2$ and the presence of the inhibitor had negligible effect. For AA6014 samples at 20°C with a NSDL, figure 6.3.1.2c, show that there is slight difference between samples with PVF and the control and they all show a fairly linear trend. However, at c.a. 200 hours PVF 0.1 shows a smaller corrosion area, compared

to all other samples, for the remaining time. At the end of the investigation the samples with PVF of 0.025 and 0.01 have the largest area of corrosion, respectively, with the control sample having the next largest area. PVF of 0.2, 0.05, 0.025 and 0.01 fell within a range of 100 mm^2.

There is no significant information from the figures to indicate whether the inhibitor, at any PVF, has an effect, whether good or bad, on the area of corrosion, except that PVF 0.1 does has some effect on reducing the area when a NSDL is present, but increases corrosion area when there is no NSDL. AA6014 samples at 140°C produced a similar trend to the results shown above, and the rates for both temperatures are shown below.

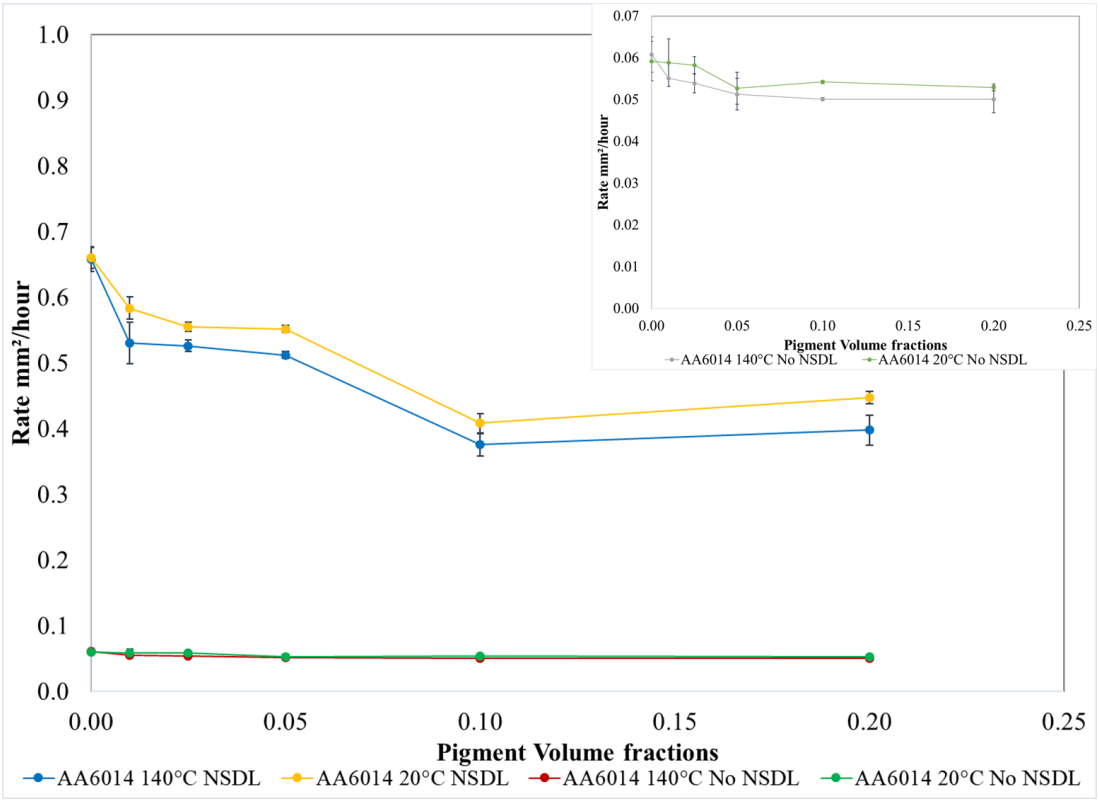

Figure 6.3.1.2d: Rate of FFC propagation for AA6014 samples, with and without a NSDL, with inhibitor diethyldithiocarbamate present across all pigment volume fractions at 20°C and 140°C. With the rate of FFC propagation for AA6014 samples without a NSDL shown in the top right-hand-corner. Y-error bars included.

Figure 6.3.1.2d: shows the rate of FFC propagation for AA6022 samples, with and without a NSDL, with inhibitor diethyldithiocarbamate present across all pigment

volume fractions at 20°C and 140°C. The standard deviation for each AA6014 sample is shown in table 21 below:

PVF of DEDTC	Standard deviation mm²/hour			
	AA6014 20°C No NSDL	AA6014 20°C NSDL	AA6014 140°C No NSDL	AA6014 140°C NSDL
0.000	0.0047	0.0162	0.0042	0.0186
0.010	0.0057	0.0173	0.0002	0.0314
0.025	0.0021	0.0076	0.0023	0.0087
0.050	0.0039	0.0048	0.0038	0.0056
0.100	0.0003	0.0146	0.0004	0.0168
0.200	0.0008	0.0097	0.0032	0.0226

Table 21: Standard deviation at each PVF of DEDTC for each AA6014 samples.

The larger graph in figure 6.3.1.2d shows the rate of FFC propagation for AA6014 samples, with and without a NSDL, with inhibitor diethyldithiocarbamate present across all pigment volume fractions at 20°C and 140°C. These graphs show that the rate of FFC propagation is greater when a NSDL is present. The PVF at 140°C and 20°C show a trend between PVF and rate of a weak exponential decay. There is a slight increase in corrosion inhibition as the PVF increases, with the PVF of 0.1 having the slowest corrosion rate. However, all the rates are within a c.a. 0.3 $mm^2\ hr^{-1}$ range, and why there is little difference in corrosion area on the sample, figure 6.3.1.2a, and graph, figure 6.3.1.2c.

The smaller graph shows the rate of FFC propagation for AA6014 samples, without a NSDL and with inhibitor diethyldithiocarbamate present across all pigment volume fractions at 20°C and 140°C. The PVF at 140°C and 20°C show a slight increase in corrosion inhibition as the PVF increases, with the PVF of 0.2 having the slowest corrosion rate. However, all the rates are within a c.a. 0.01 $mm^2\ hr^{-1}$ range, and why there is barely any difference in corrosion area on the samples, figure 6.3.1.2a, and graph, figures 6.3.1.2b.

Diethyldithiocarbamate has an insignificant effect on AA6014 when a NSDL is not present, whether at 20°C and 140°C. However, there may be some inhibition on samples with a NSDL with a PVF of 0.1. Unfortunately, a PVF of 0.1 was shown to increase rate and area of corrosion on surfaces without a NSDL so it is unlikely to be a useful inhibitor for AA6014.

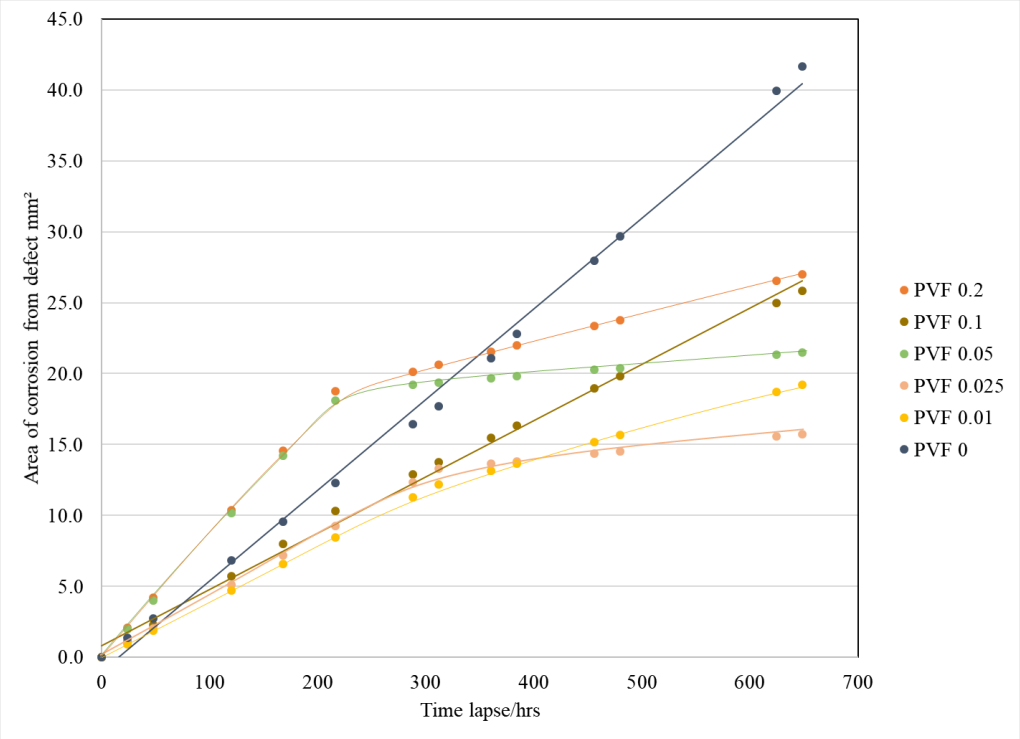

Figure 6.3.1.2e: Area of corrosion for AA6022 samples without a NSDL for each pigment volume fractions at 20°C. Samples were injected with 1µL of 2M and kept at 80% RH.

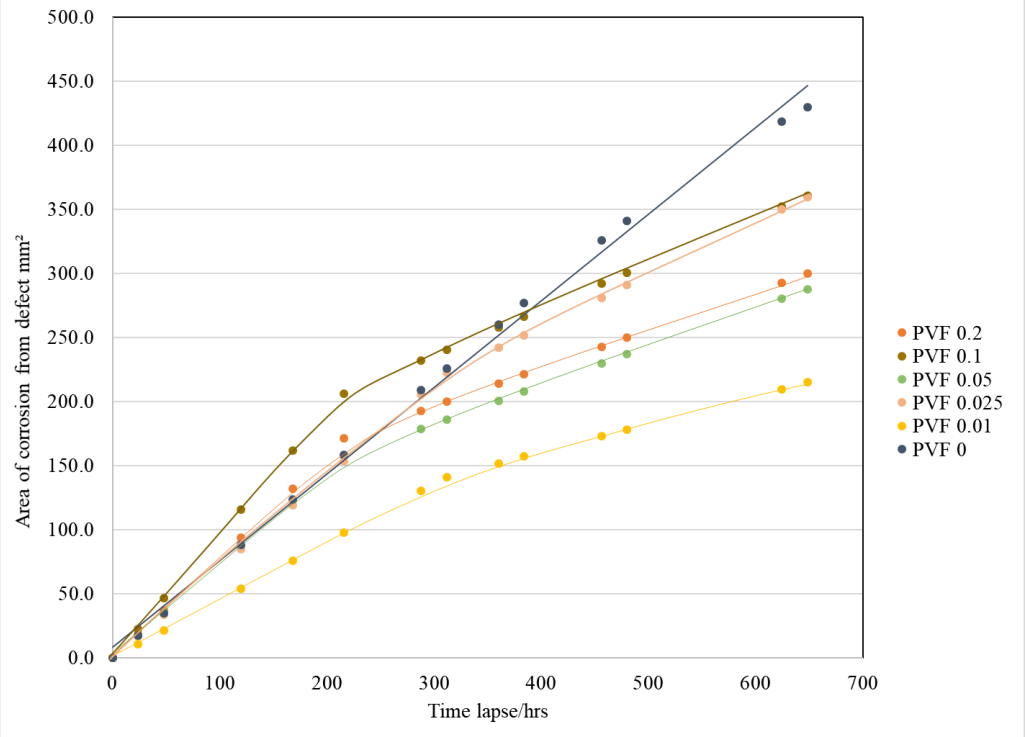

Figure 6.3.1.2f: Area of corrosion for AA6022 samples with a NSDL for each pigment volume fractions at 20°C. Samples were injected with 1µL of 2M and kept at 80% RH.

Error bars are not shown on the graphs to maintain clarity of the results. The standard deviations for the corrosion area for AA6022 with and without a NSDL can be seen in table 22 below:

PVF of DEDTC	AA6022 No NSDL	AA6022 NSDL
	Mean SD area mm^2	Mean SD area mm^2
0	2.1958	17.0356
0.01	1.5390	3.6708
0.025	2.1393	11.2117
0.05	1.0540	2.9714
0.1	1.8899	6.4886
0.2	5.3463	3.9615

Table 22: Standard deviations of the corrosion area for all samples of AA6022 with different PVF of DEDTC.

Figure 6.3.1.2a shows that the presence of a NSDL increases the corrosion area. It also shows that the type of FFC differs from having a NSDL present to it being absent with a NSDL showing both rapid S.A.FFC followed by, in some cases, a slower, more penetrative, SP-FFC. The graphs for AA6022 at 20 °C without a NSDL, figure 6.3.1.2e, and with a NSDL, figure 6.3.1.2f, show that when the pigment volume fraction (PVF) is zero, i.e., the control sample, then the area of corrosion propagates in a linear fashion, as found in previous chapters. However, when the PVF is present, whether a NSDL is present or not, then the area propagations tend away from a linear relationship.

AA6022 samples at 20°C without a NSDL, figure 6.3.1.2e, show that when PVF is present most of the PVF have initial areas of corrosion that are smaller than the control, except for PVF 0.02 and 0.05, which are above the control sample. PVF 0.2 and 0.05 continue to stay above the control until c.a. 350 hours when they drop below the control sample line. The final area measurements show that all samples with PVF produce a smaller corrosion area than the control with PVF 0.025 producing the smallest corrosion area. The control sample and PVF 0.1 and 0.01 have fairly linear trendlines, however the samples with PVF 0.02, 0.05, and 0.025 do not. They have two distinctive linear sections. The first section starts at 0 hour and stops within a range of c.a. 200 to 300 hours where the increase in area with respect to time is fairly large. However,

between c.a 200 and c.a. 300 hours the line becomes less steep, and the area of corrosion produced, with respect to time, decreases. AA6022 samples at 140°C produced a similar trend to the results shown above and both the 140°C and 20°C results potentially implies that the diethyldithiocarbamate may work as a slow-release inhibitor and would be of interest if combined with a fast-release inhibitor for a prolonged effect on AA6022.

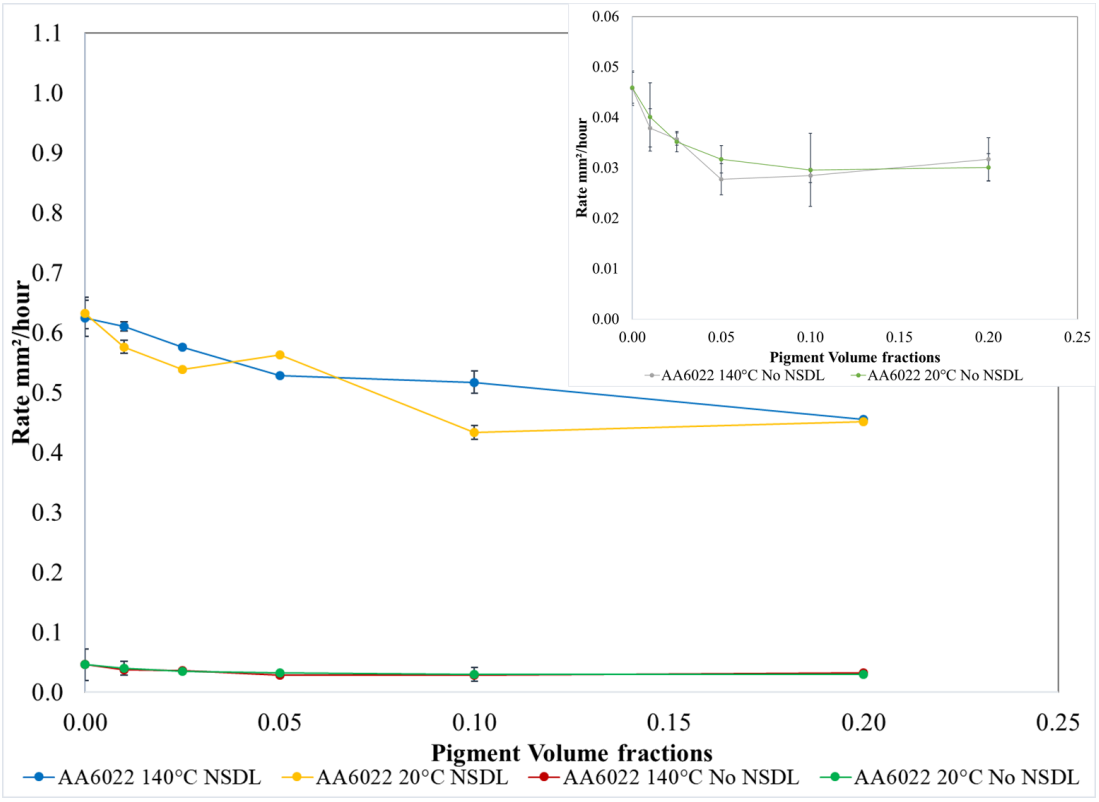

Figure 6.3.1.2g: Rate of FFC propagation for AA6022 samples, with and without a NSDL, with inhibitor diethyldithiocarbamate present across all pigment volume fractions at 20°C and 140°C. With the rate of FFC propagation for aluminium alloy 6014 samples without a NSDL shown in the top right-hand-corner. Y-error bars included.

Figure 6.3.1.2g shows the rate of FFC propagation for AA6022 samples, with and without a NSDL, with inhibitor diethyldithiocarbamate present across all pigment volume fractions at 20°C and 140°C. The standard deviation for each AA6022 sample is shown in table 23 below:

PVF of DEDTC	Standard deviation mm²/hour			
	AA6022 20°C No NSDL	AA6022 20°C NSDL	AA6022 140°C No NSDL	AA6022 140°C NSDL
0.000	0.0031	0.0265	0.0034	0.0300
0.010	0.0067	0.0113	0.0038	0.0075
0.025	0.0021	0.0034	0.0012	0.0028
0.050	0.0028	0.0013	0.0031	0.0015
0.100	0.0073	0.0115	0.0014	0.0186
0.200	0.0027	0.0008	0.0043	0.0009

Table 23: Standard deviation at each PVF of DEDTC for each AA6022 samples.

Figure 6.3.1.2g shows the rate of FFC propagation for AA6022 samples, with and without a NSDL, with inhibitor diethyldithiocarbamate present across all pigment volume fractions at 20°C and 140°C. This graph shows clearly that the rate of FFC propagation is greater when a NSDL is present. The larger graph shows the rate of FFC propagation have a very slight exponential decline in rate as more PVF is added, with the PVF of 0.2 having the slowest rate at 140°C and the PVF of 0.1 producing the slowest corrosion rate at 20°C. However, all the rates are within a c.a. 0.2 mm^2 hr^{-1} range, and why there is a limited difference in corrosion area on the samples, figure 6.3.1.2a, and graphs, figures 6.3.1.2c and 6.3.1.2e.

The smaller graph in figure 6.3.1.2g shows the rate of FFC propagation for AA6022 samples without a NSDL. The samples at 140°C show a very slight exponential decline with the PVF until the PVF of 0.05, but then shows it start to increase as PVF 0.1 and 0.2 rather than plateau. The PVF at 20°C shows a slight increase in corrosion inhibition as the PVF increases to PVF 0.1, but then shows it start to increase as it moves towards PVF 0.2. The most effective PVF to reduce the corrosion rate for AA6022, without a NSDL, at 140°C and 20°C is 0.05 and 0.1, respectively. However, all the rates are within a c.a. 0.02 mm^2 hr^{-1} range, and why there is a limited difference in corrosion area on the samples, figure 6.3.1.2a, and graphs, figures 6.3.1.2c and 6.3.1.2e.

Diethyldithiocarbamate has an insignificant effect on AA6022 whether a NSDL is present or not. This is true whether at 20°C and 140°C. However, there may be some inhibition on samples when a PVF of 0.1 is used as it does have some inhibition across the various AA6022 samples.

6.3.1.3 AA6014 and AA6022 Inhibitor C = Hydrotalcite at 140°C and 20°

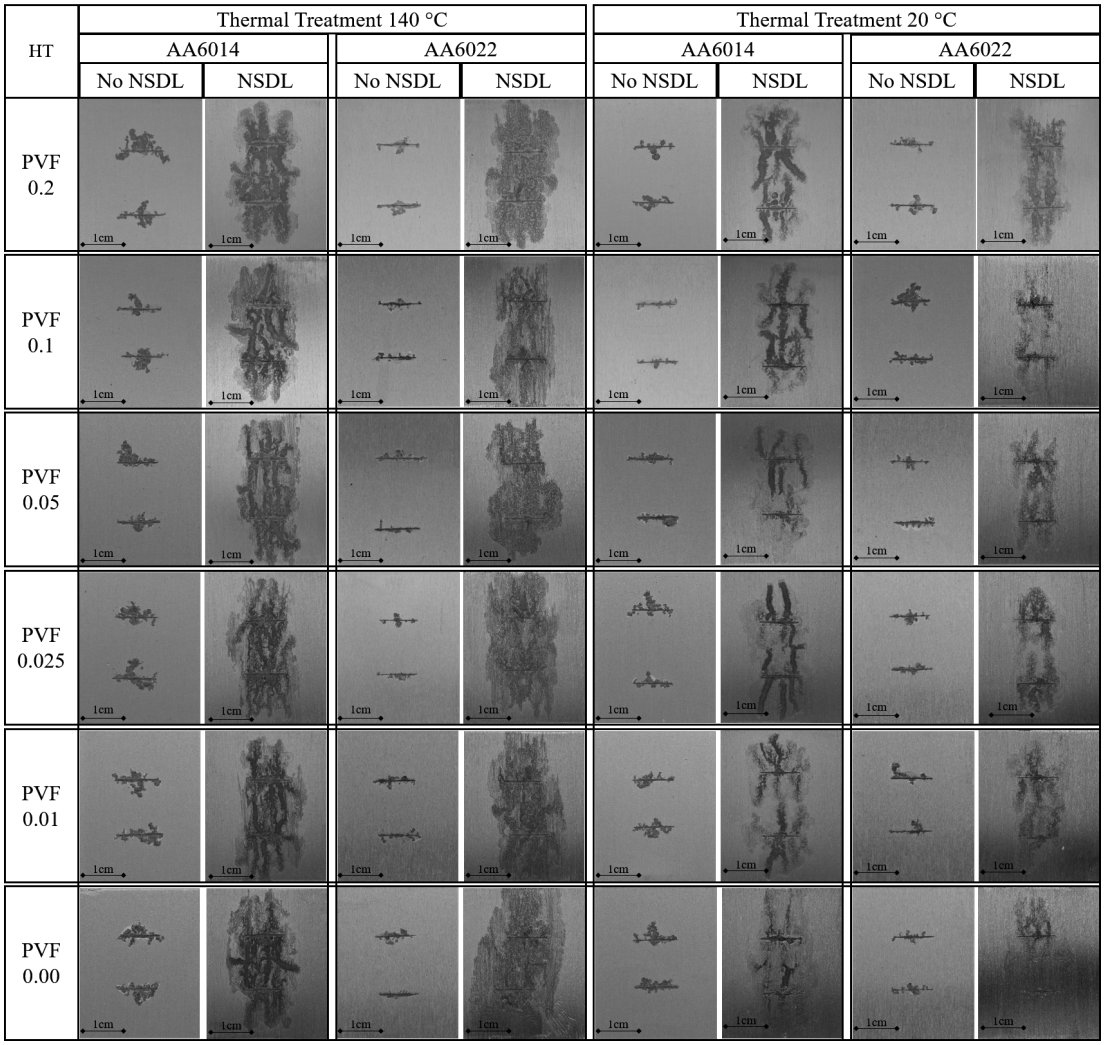

Figure 6.3.1.3a: AA6014 and AA6022 samples with diethyldithiocarbamate at 140°C and 20°C at c.a. 700 hours.

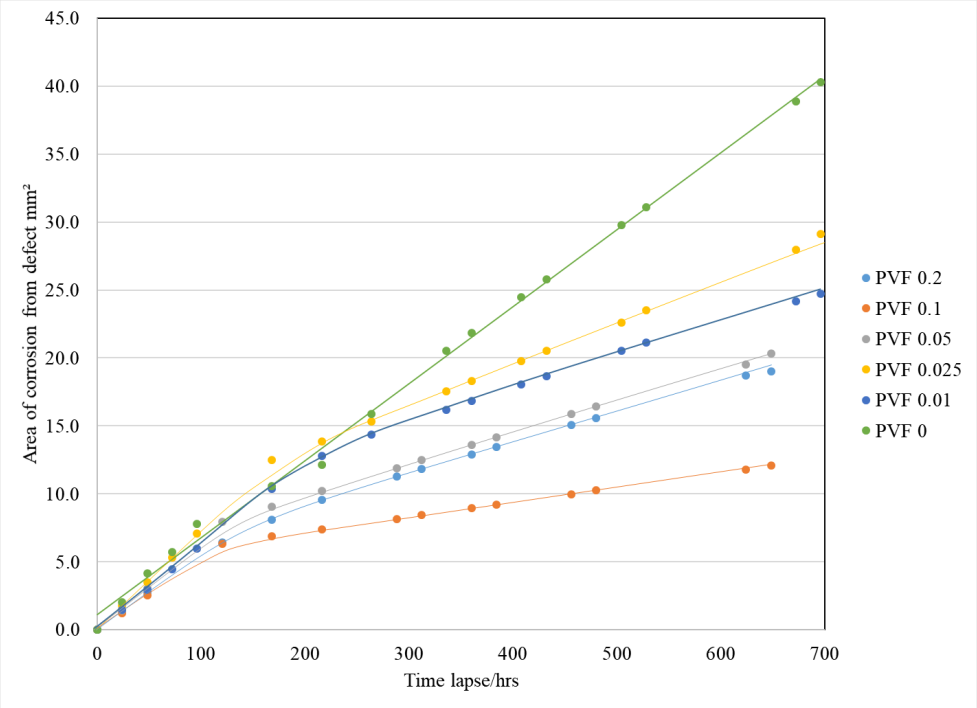

Figure 6.3.1.3b: Area of corrosion for AA6014 samples without a NSDL for each pigment volume fractions at 20°C. Samples were injected with 1µL of 2M and kept at 80% RH.

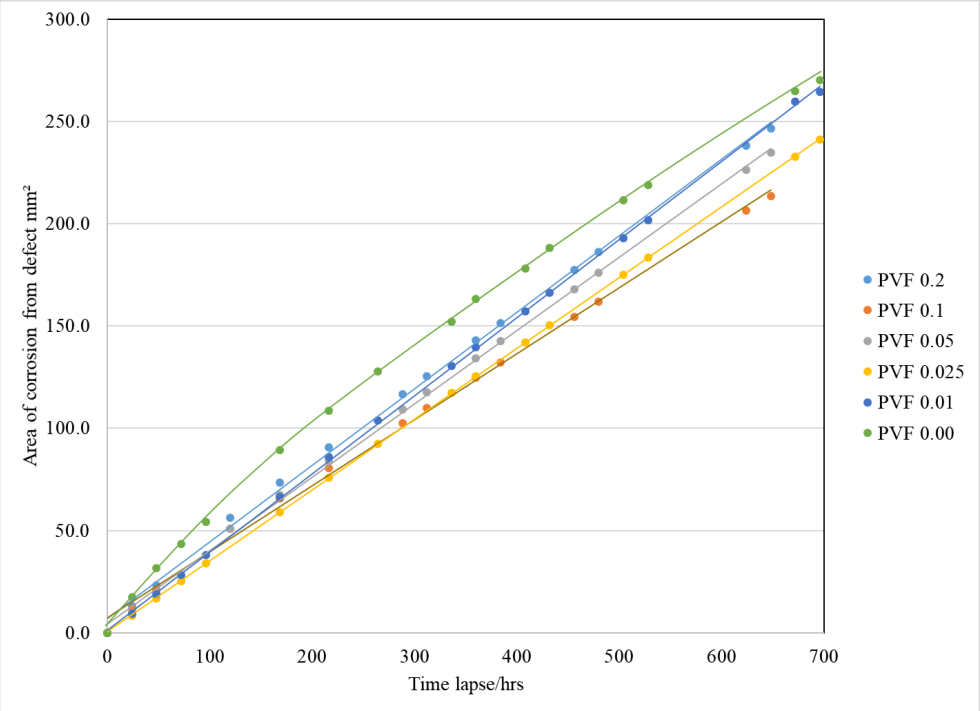

Figure 6.3.1.3c: Area of corrosion for AA6014 samples with a NSDL for each pigment volume fractions at 20°C. Samples were injected with 1µL of 2M and kept at 80% RH.

Error bars are not shown on the graphs to maintain clarity of the results. The standard deviations for the corrosion area for AA6014 with and without a NSDL can be seen in table 24 below:

PVF of Hydrotalcite	AA6014 No NSDL	AA6014 NSDL
	Mean SD area mm^2	Mean SD area mm^2
0	1.6099	1.9186
0.01	2.4405	2.9432
0.025	3.0604	7.0760
0.05	1.2532	7.8242
0.1	0.7011	3.6838
0.2	0.6811	26.2165

Table 24: Standard deviations of the corrosion area for all samples of AA6014 with different PVF of Hydrotalcite.

Figure 6.3.1.3a shows that the presence of a NSDL increases the corrosion area. It also shows that the type of FFC differs from having a NSDL present to it being absent with a NSDL showing both rapid S.A.FFC followed by, in some cases, a slower, more penetrative, SP-FFC.

The graph for AA6014 at 20 °C without a NSDL, figure 6.3.1.3b, and with a NSDL, figure 6.3.1.3c, shows that when the pigment volume fraction (PVF) is zero, i.e., the control sample, then the area of corrosion propagates in more of a curve, instead of linear, fashion. When the PVF is present, whether a NSDL is present or not, then the area propagations show trend lines similar to the other inhibitors with a steep linear line to start and a less steep linear line after a certain time.

AA6014 samples at 20°C without a NSDL, figure 6.3.1.3b, and shows that the PVF has some effect on reducing the corrosion area. When PVF is present the initial areas are approximately equal to that of the control with the difference in the corroded areas up to c.a. 100 hours being less than 5 mm^2. Between c.a. 100 hours to 250 hours, the area of corrosion for PVF 0.01 and 0.025 is larger than the area of the control sample, but again the difference in the area between PVF 0.01, 0.025 and the control is less than 5 mm^2. After c.a. 250 hours, the control sample produces the largest corrosion area, compared to all other samples. The corrosion areas for all samples at c.a 650 hours fall within a 25 mm^2 range. PVF of 0.1 is the most effective, producing the smallest corrosion area, followed by PVF 0.2. PVF 0.025 and 0.01 appear to have less

of an effect on corrosion inhibition, it is possible that there is insufficient pigment for effective or sustained ionic exchange.

AA6014 samples at 20 °C with a NSDL, figure 6.3.1.3c, all have a fairly linear trend. All PVF produce areas that are smaller than the control sample, for all measurements. Initially there is little difference in the areas measured, but as time passes the PVF spread out and the range of corrosion area is c.a. 43 mm^2. By c.a. 650 hours, PVF 0.1 has produced the smallest area of corrosion, followed by PVF 0.025. PVF 0.01 performs the least well, possible due to insufficient pigment for effective, or sustained ionic exchange, followed by PVF 0.2, potentially due to PVB saturation and restricted ionic exchange. There is no significant information from the figures to indicate whether the inhibitor, at any PVF, has an effect, whether good or bad, on the area of corrosion, except that PVF 0.1 does has some effect on reducing the area with or without a NSDL present. AA6022 samples at 140°C produced a similar trend to the results shown for 20°C.

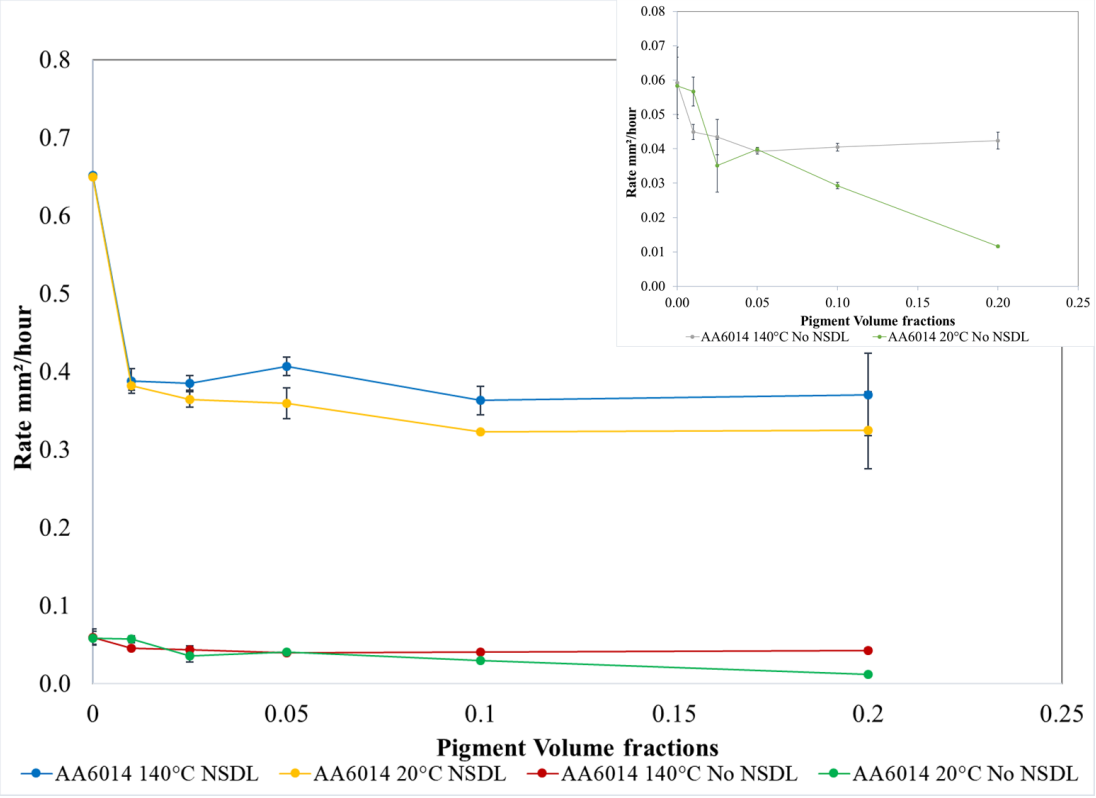

Figure 6.3.1.3d: Rate of FFC propagation for AA6014 samples, with and without a NSDL, with inhibitor hydrotalcite present across all pigment volume fractions at 20°C and 140°C. With the rate of FFC propagation for AA6014 samples without a NSDL shown in the top right-hand-corner. Y-error bars included.

Figure 6.3.1.3d shows the rate of FFC propagation for AA6014 samples, with and without a NSDL, with inhibitor hydrotalcite present across all pigment volume fractions at 20°C and 140°C. The standard deviation for each AA6014 sample is shown in table 25 below:

PVF of Hydrotalcite	Standard deviation mm²/hour			
	AA6014 20°C No NSDL	AA6014 20°C NSDL	AA6014 140°C No NSDL	AA6014 140°C NSDL
0.000	0.0083	0.0020	0.0104	0.0022
0.010	0.0042	0.0061	0.0022	0.0154
0.025	0.0077	0.0099	0.0051	0.0093
0.050	0.0006	0.0200	0.0007	0.0121
0.100	0.0009	0.0019	0.0011	0.0185
0.200	0.0004	0.0493	0.0024	0.0528

Table 25: Standard deviation at each PVF of Hydrotalcite for each AA6014 samples.

Figure 6.3.1.3d shows the rate of FFC propagation for AA6014 samples, with and without a NSDL, with inhibitor hydrotalcite present across all pigment volume fractions at 20°C and 140°C. This graph shows clearly that the rate of FFC propagation is greater when a NSDL is present. In the larger of the graphs, the rate of FFC propagation for AA6014 samples with a NSDL show an exponential decline as more PVF is added, with both temperatures showing a plateau at the PVF of 0.1 to 0.2 suggesting a PVF of between 0.1 and 0.2 would produce the most effective corrosion inhibition.

The smaller graph in figure 6.3.1.3d shows the rate of FFC propagation for AA6014 samples without a NSDL, with inhibitor hydrotalcite present across all pigment volume fractions at 20°C and 140°C. PVF at 20°C show a general trend that as the PVF increases, the rate of FFC propagation decrease, i.e. there is an increase in corrosion inhibition as the PVF increases, with the PVF of 0.2 having the slowest corrosion rate. PVF at 140°C also shows an increase in corrosion inhibition as the PVF increases, however the inhibition effect appears to reduce after PVF of 0.1 and increases further at PVF 0.2. A PVF of between 0.1 and 0.2 is likely to produce the most effective corrosion inhibition whether the surface has a NSDL present or not and at both temperatures, although the effect of the inhibitor is limited.

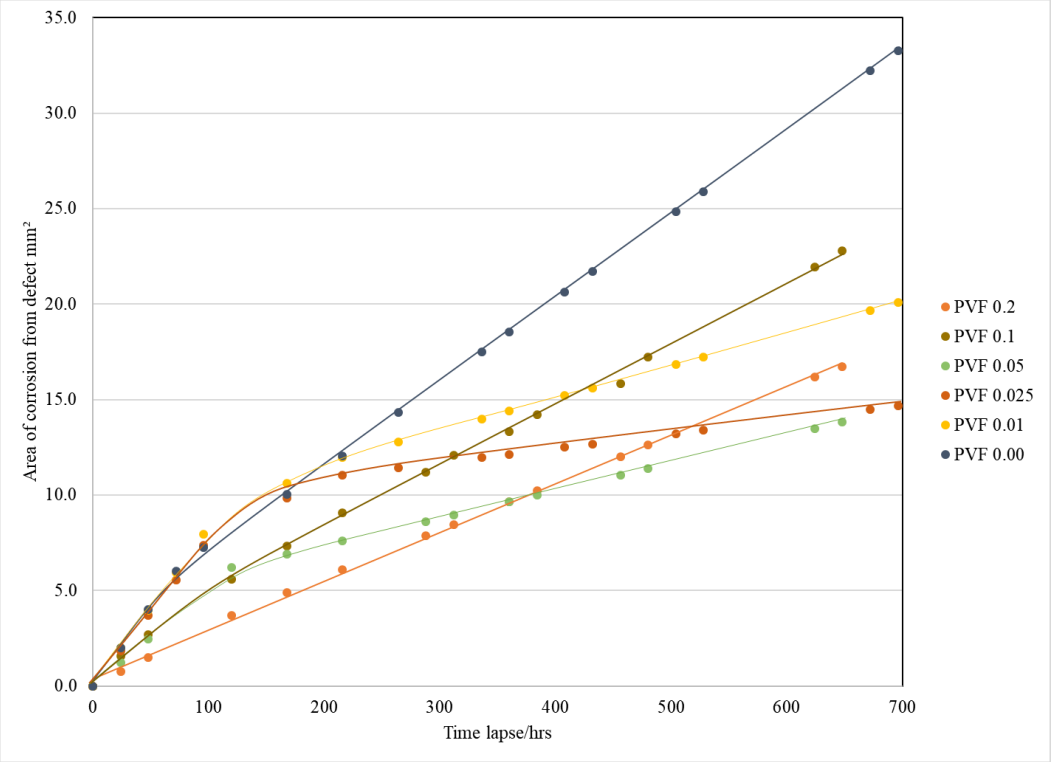

Figure 6.3.1.3e: Area of corrosion for AA6022 samples without a NSDL for each pigment volume fractions at 20°C. Samples were injected with 1µL of 2M and kept at 80% RH.

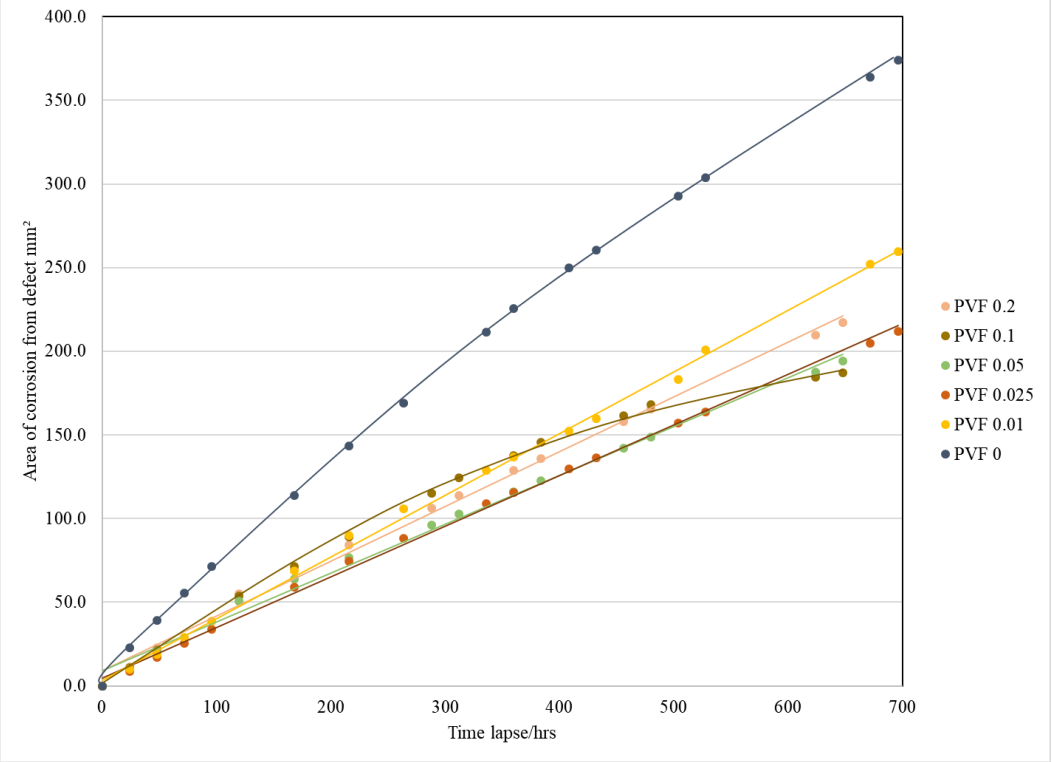

Figure 6.3.1.3f: Area of corrosion for AA6022 samples with a NSDL for each pigment volume fractions at 20°C. Samples were injected with 1µL of 2M and kept at 80% RH.

Error bars are not shown on the graphs to maintain clarity of the results. The standard deviations for the corrosion area for AA6022 with and without a NSDL can be seen in table 26 below:

PVF of Hydrotalcite	AA6022 No NSDL	AA6022 NSDL
	Mean SD area mm^2	Mean SD area mm^2
0	0.6761	4.8248
0.01	2.6082	7.1439
0.025	0.9011	3.7094
0.05	1.0053	0.1981
0.1	0.6572	4.1923
0.2	1.0363	1.6090

Table 26: Standard deviations of the corrosion area for all samples of AA6022 with different PVF of Hydrotalcite.

Figure 6.3.1.3a shows that the presence of a NSDL increases the corrosion area. It also shows that the type of FFC differs from having a NSDL present to it being absent with a NSDL showing both rapid S.A.FFC followed by, in some cases, a slower, more penetrative, SP-FFC. The graphs for AA6022 at 20 °C without a NSDL, figure 6.3.1.3e, and with a NSDL, figure 6.3.1.3f, show that when the pigment volume fraction (PVF) is zero, i.e., the control sample, then the area of corrosion propagates in a linear fashion, as found in previous chapters. However, when the PVF is present, on a sample without a NSDL, then the area propagations tend away from a linear relationship. Samples with a NSDL follow a more linear trend.

AA6022 samples at 20°C, without a NSDL, figure 6.3.1.3e, also have a similar result for PVF 0.01 between 100 and 300 hours. If the lines for PVF 0.1, 0.2 and 0.05 were extended towards 700 hours, then PVF 0.025 would also show the best corrosion inhibition, followed by PVF 0.05. PVF 0.1 has the weakest effect on corrosion inhibition out of the PVFs (Pigment Volume Fraction), followed by PVF 0.01 and 0.2, again the same results as AA6022 at 140°C. For AA6022 samples without a NSDL the PVF of 0.025 appears to inhibit the corrosion mechanism the most. However, the difference in corrosion area across the PVF samples is c.a. 13 mm^2, and a difference of 18 mm^2 with the control included. Again, it is possible that the PVF of 0.2 has

saturated the PVB and ionic exchange is restricted and the PVF of 0.01 has insufficient pigment for effective, and sustained, ionic exchange.

AA6022 samples at 20 °C with a NSDL, figure 6.3.1.3f, all PVF areas are smaller than the control sample and show a more linear trend. By c.a. 650 hours the control sample has produced the greatest corrosion area, followed by PVF 0.01 and PVF 0.2. The PVF that produced the smallest corroded area, at the end of the experiment was PVF 0.1, followed by PVF 0.05. It is possible that the PVF of 0.2 has saturated the PVB and ionic exchange is restricted and the PVF of 0.01 has insufficient pigment for effective, and sustained, ionic exchange. During the experiment, PVF 0.025 has the most consistent corrosion inhibition, showing a steady growth in the corrosion area. PVF 0.1 had been producing large area measurements, only surpassed by the control, until c.a. 400 hours. After 400 hours there is a sudden reduction in corrosion area growth and overall, it produces the smallest area. The difference in corrosion area across the PVF is c.a. 50 mm^2 with a difference of 160 mm^2 with the control included.

There is no significant information from the figures to indicate which PVF of the inhibitor would yield the best outcome. The inhibitor, in general has a marginal effect on the corrosion rate when a NSDL is present. It is possible that a PVF of 0.025 would produce some inhibition across the temperatures and surfaces. AA6022 samples at 140°C produced a similar trend to the results shown above, and the rates for both temperatures are shown below.

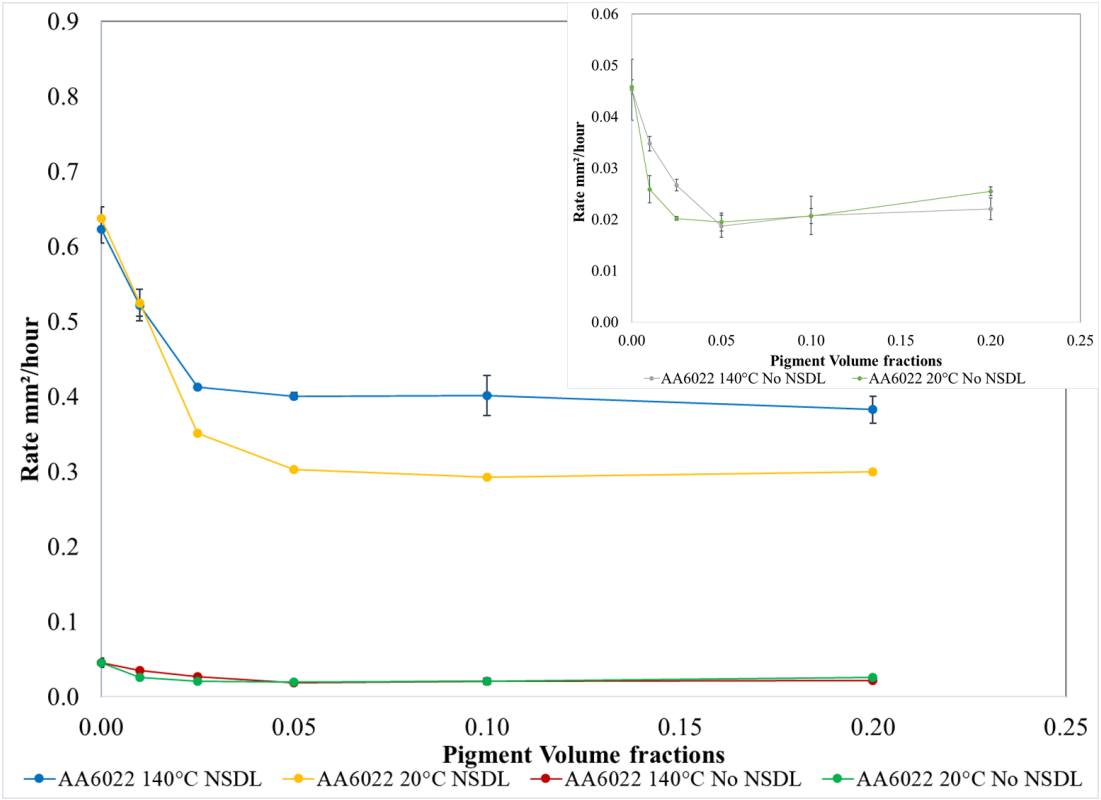

Figure 6.3.1.3g: Rate of FFC propagation for AA6022 samples, with and without a NSDL, with inhibitor hydrotalcite present across all pigment volume fractions at 20°C and 140°C. With the rate of FFC propagation for AA6014 samples without a NSDL shown in the top right-hand-corner. Y-error bars included.

Figure 6.3.1.3g shows the rate of FFC propagation for AA6022 samples, with and without a NSDL, with inhibitor hydrotalcite present across all pigment volume fractions at 20°C and 140°C. The standard deviation for each AA6022 sample is shown in table 27 below:

PVF of Hydrotalcite	Standard deviation mm²/hour			
	AA6022 20°C No NSDL	AA6022 20°C NSDL	AA6022 140°C No NSDL	AA6022 140°C NSDL
0.000	0.0014	0.0154	0.0059	0.0177
0.010	0.0027	0.0183	0.0014	0.0211
0.025	0.0004	0.0014	0.0011	0.0016
0.050	0.0018	0.0004	0.0021	0.0046
0.100	0.0015	0.0011	0.0038	0.0267
0.200	0.0009	0.0014	0.0021	0.0179

Table 27: Standard deviation at each PVF of Hydrotalcite for each AA6022 samples.

Figure 6.3.1.3g shows the rate of FFC propagation for AA6022 samples, with and without a NSDL, with inhibitor hydrotalcite present across all pigment volume fractions at 20°C and 140°C. This graph shows clearly that the rate of FFC propagation is greater when a NSDL is present. The larger graph shows the rate of FFC propagation for AA6022 samples with a NSDL have an exponential decline in rate as more PVF is added, with the PVF of 0.2 having the slowest rate at 140°C and PVF of 0.1 at 20°C and a plateau between the PVF of 0.1 to 0.2 at 20°C.

The smaller graph in figure 6.3.1.3g shows the rate of FFC propagation for AA6022 samples, without a NSDL, with inhibitor hydrotalcite present across all pigment volume fractions at 20°C and 140°C. The final areas seen in figure 6.3.1.3e show that the most effective PVF was 0.025 however the rates shown in the smaller graph in figure 6.3.1.3g show that the most effective PVF at 20°C was at 0.05. Although the PVF differs between the area and rate graphs, generally figure 6.3.1.3f does show that for the most part, as the PVF increases the rate decreases, exponentially to PVF 0.05, but an increase in rate is observed at both temperatures at PVF of 0.1 and 0.2. This suggests that the optimum PVF for AA6022, for either temperature, should be between PVF 0.025 to 0.05, which also agrees with the results from the area measurements. The PVF in this range should be enough to reduce the corrosion rate, without saturating the organic coating.

6.3.1.4 Comparison of inhibitors at 0.2 PVF for all samples of AA6014 and AA6022 at 140°C and 20°C with control samples at 0 PVF

Where inhibitor C is cationic benzotriazole (CBP), inhibitor D is diethyldithiocarbamate (DEDTC) and inhibitor H is hydrotalcite (HT).

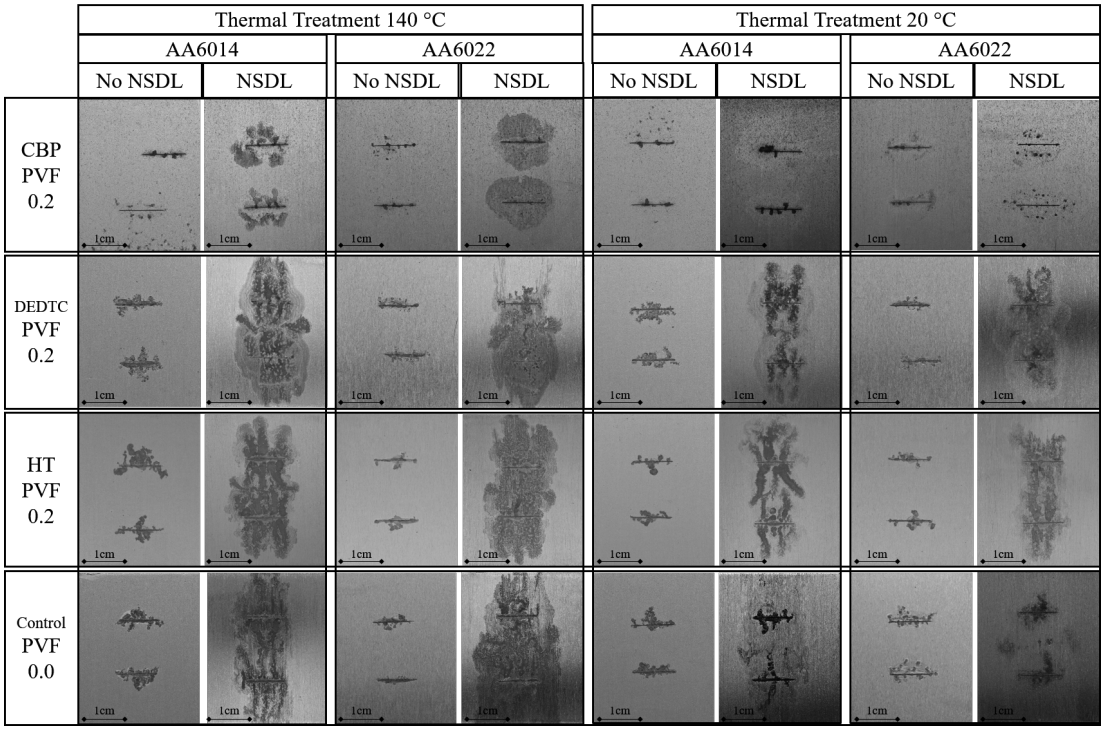

Figure 6.3.1.4a: Comparison of inhibitors at 0.2 PVF for all samples of AA6014 and AA6022 at 140°C and 20°C with control samples at 0 PVF at 80% RH and c.a. 700 hours.

Figure 6.3.1.4a shows the comparison of inhibitors at 0.2 PVF for all samples of AA6014 and AA6022 at 140°C and 20°C with control samples at 0 PVF. Images in the 1st, 3rd, 5th, and 7th columns show samples without a NSDL. Images in the 2nd, 4th, 6th, and 8th columns show samples with a NSDL present. It shows that the presence of a NSDL increases the corrosion area. It also shows that the type of FFC differs from having a NSDL present to it being absent with a NSDL showing both rapid S.A.FFC followed by, in some cases, a slower, more penetrative, SP-FFC. Figure 6.3.1.4a shows that the CBP reduces the area of corrosion on the samples and does not show a significant difference between DEDTC, HT and the control samples.

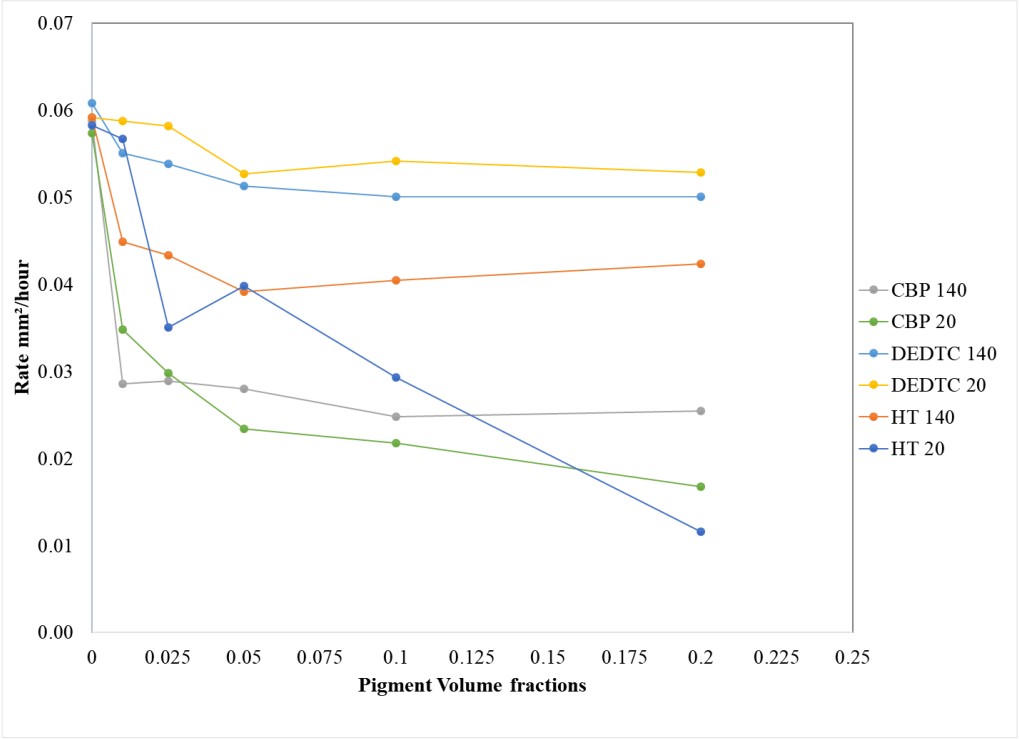

Figure 6.3.1.4b: Rate of FFC propagation for AA6014 samples, without a NSDL, for all inhibitors across all pigment volume fractions at 20°C and 140°C.

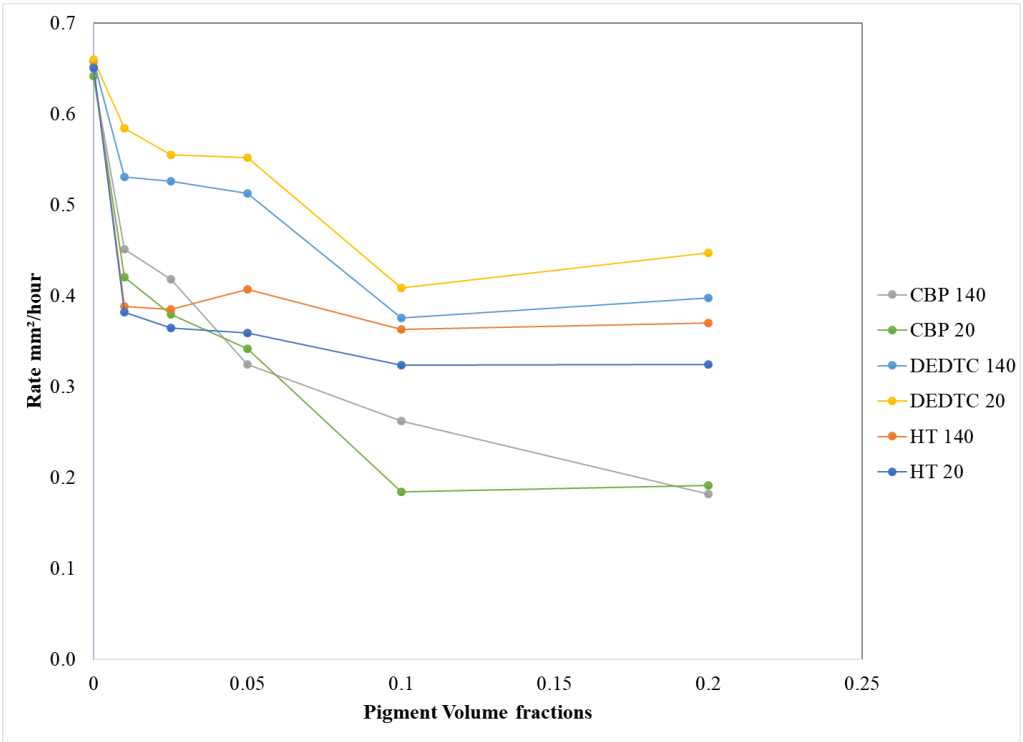

Figure 6.3.1.4c: Rate of FFC propagation for AA6014 samples, with a NSDL, for all inhibitors across all pigment volume fractions at 20°C and 140°C.

Figure 6.3.1.4b shows the rate of FFC propagation for AA6014 samples, without a NSDL, for all inhibitors across all pigment volume fractions at 20°C and 140°C. CBP at PVF 0.2 showed a significant reduction in corrosion rate at both 20°C and 140°C, going from c.a. 0.058 mm^2 to c.a. 0.018 mm^2 and c.a. 0.025 mm^2, respectively. HT showed the most significant reduction in corrosion but only for the 20°C, going from c.a. 0.059 mm^2 to c.a. 0.012 mm^2. DEDTC shows no significant reduction in corrosion rate, only going from c.a. 0.06 mm^2 to c.a.0.05 mm^2 across the PVF.

Figure 6.3.1.4c shows the rate of FFC propagation for AA6014 samples, with a NSDL, for all inhibitors across all pigment volume fractions at 20°C and 140°C. CBP at PVF of 0.1 to 0.2 showed a significant reduction in corrosion rate at both 20°C and 140°C, going from c.a. 0.65 mm^2 to c.a. 0.18 mm^2. HT and DEDTC produce a similar reduction in corrosion rate, c.a. 0.65 mm^2 to a range between c.a. 0.33 mm^2 to c.a. 0.45 mm^2, with the HT only performing slightly better. CBP of PVF of 0.1 to 0.2 appears to reduce the corrosion rate by the greatest amount on AA6014, whether a NSDL is present or not.

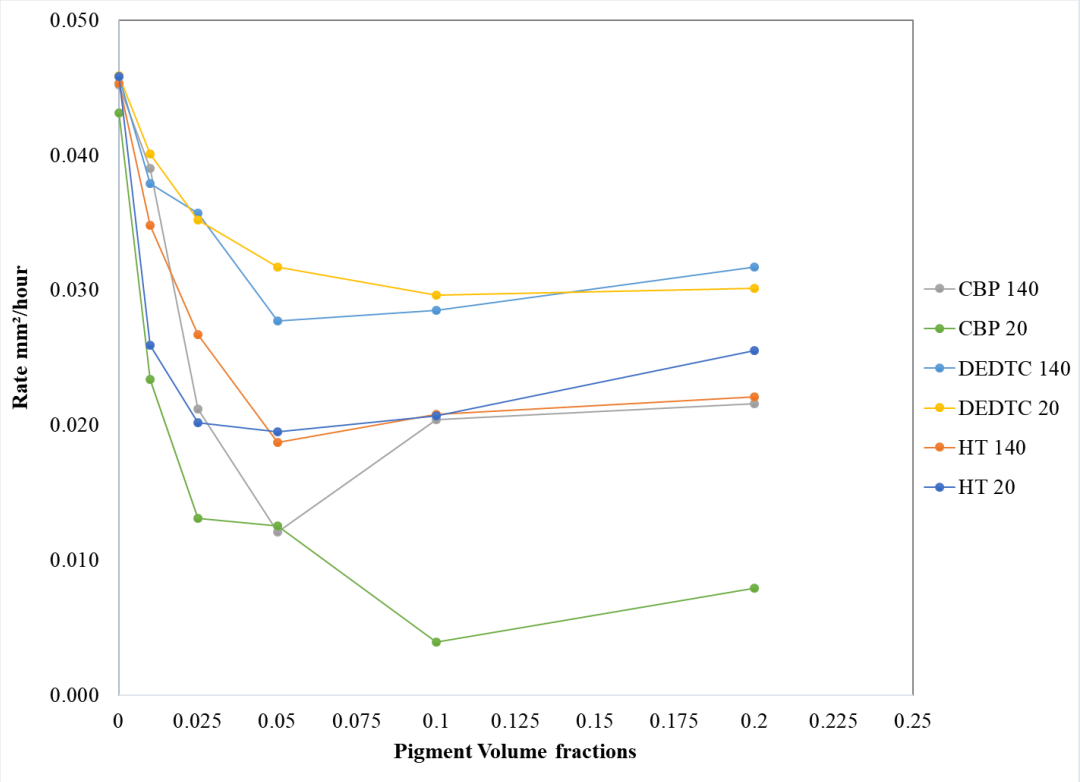

Figure 6.3.1.4d: Rate of FFC propagation for AA6022 samples, without a NSDL, for all inhibitors across all pigment volume fractions at 20°C and 140°C.

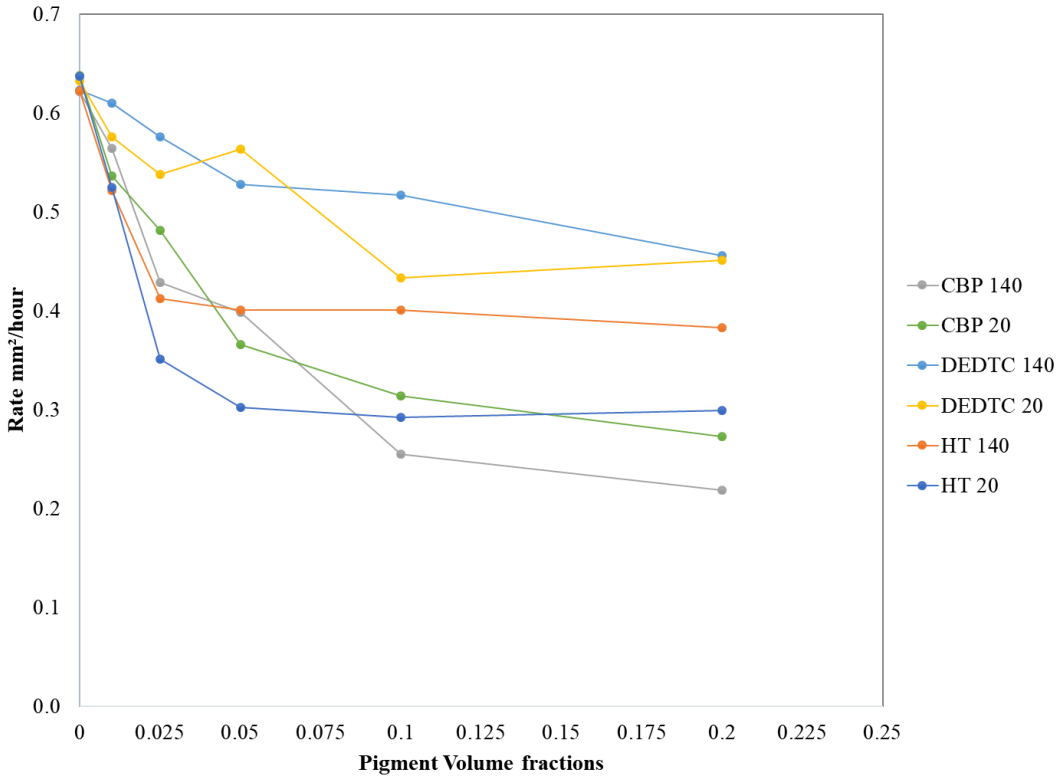

Figure 6.3.1.4e: Rate of FFC propagation for AA6022 samples, with a NSDL, for all inhibitors across all pigment volume fractions at 20°C and 140°C.

Figure 6.3.1.4d shows the rate of FFC propagation for AA6022 samples, without a NSDL, for all inhibitors across all pigment volume fractions at 20°C and 140°C. CBP with PVF of 0.1 has is the most effective corrosion inhibition at 20°C, reducing the rate from c.a. 0.043 mm^2 to c.a. 0.004mm^2. CBP with PVF of 0.05 has is the most effective corrosion inhibition at 140°C, reducing the rate from c.a. 0.043 mm^2 to c.a. 0.012mm^2. The HT showed some reduction in corrosion rate, but DEDTC showed the smallest effect on the reduction of corrosion rate. Within the different PVF of HT, the PVF of 0.05 was able to reduce the corrosion rate, the most effectively, from c.a. 0.045 mm^2 to c.a. 0.019mm^2, not too dissimilar to the results for CBP at 140°C. Within the different PVF of DEDTC, the PVF of between 0.05 and 0.1 was able to reduce the corrosion rate, the most effectively, from c.a. 0.045 mm^2 to c.a. 0.025mm^2 and 0.03mm^2, for 140°C and 20°C, respectively. Neither the HT or the DEDTC produce a noteworthy effect on the reduction of corrosion rate. CBP at PVF between 0.05 and 0.1 may need further investigating to find the optimum PVF that would show the largest reduction in corrosion rates for both temperatures.

Figure 6.3.1.4e shows the rate of FFC propagation for AA6022 samples, with a NSDL, for all inhibitors across all pigment volume fractions at 20°C and 140°C. CBP at PVF

0.2 showed a significant reduction in corrosion rate at both 20°C and 140°C, going from c.a. 0.63 mm^2 to c.a. 0.27 mm^2 and c.a. 0.22 mm^2, respectively. HT had some effect on both samples, reducing the rate from 0.63 mm^2 to c.a. 0.38 mm^2 and c.a. 0.29 mm^2, for 140°C and 20°C, respectively. DEDTC shows no significant reduction in corrosion rate, only going from c.a. 0.63 mm^2 to c.a. 0.43 to 0.45 mm^2 across the PVF. As with the investigation on AA6014, work on AA6022 has found that the use of CBP with a PVF of 0.1 to 0.2 appears to reduce the corrosion rate by the greatest amount, whether a NSDL is present or not.

DEDTC affects the breakdown potential and has an influence on the passive current by replacing the Cl^- with the inhibitor, however it is possible that the PVF used in this investigation were saturated with Cl^- as 1µL of 2M HCl was used and potentially the PVF was not high enough to see a clear effect.

Hydrotalcite has a positive layer charge due to the positions of Al^{3+} and Mg^{2+} with CO_3^{2-} located within the hydrated interlayer space, allowing for electroneutrality to be preserved. Hydrotalcite-like compounds are isomorphous with hydrotalcite having the general formula $[M^{2+}_{1-x}M^{3+}_x(OH)_2]^{x+}\left[A^{n-}_{x/n}\cdot yH_2O\right]$ where M^{2+} and M^{3+} are divalent and trivalent metal ions respectively, an^- is an anion and x falls in the range of c.a. 0.25-0.33. It has been proposed that the hydrotalcite and hydrotalcite-like pigments reduce the concentrations of H^- and Cl^- in the filament head and neutralising the acidic electrolyte thereby inhibiting the corrosion propagation due to their anion exchange properties[210,355]. Since hydrotalcite can neutralise the Cl^- in the electrolyte there were some positive results with HT but limited. Again, this could be a result of too little PVF to neutralise 1µL of 2M HCl fully. The results for AA6014 and AA6022 are similar to the results obtained by Coleman et al on aluminium alloys, AA6016 and AA6111[3,6,214]. They found that the presence of hydrotalcite, in its untreated form did reduce the amount of FFC but stated that it was insignificant as it only reduced the area of FFC by just over 50 mm^2. They also noted that the effect of the hydrotalcite may have been restricted due to the concentration of the electrolyte used, 2M HCl, and the exchange capacity reached very quickly allowing FFC to continue. The hydrotalcite-like compound showed a slight improvement to corrosion inhibition, but not noteworthy, the same being true for AA6014 and AA6022.

It is possible to use CBP as an effective inhibitor on AA6014 and AA6022 based on the results since the area of corrosion on the samples was reduced by c.a. 62.5% for AA6014 without a NSDL (140°C), 57.5% for AA6014 without a NSDL (20°C), c.a. 58.6% for AA6014 with a NSDL (140°C), c.a. 56.1% for AA6014 with a NSDL (20°C), c.a. 72.9% for AA6022 without a NSDL (140°C), c.a. 80.2% for AA6022 without a NSDL (20°C), c.a. 62.0% for AA6022 with a NSDL (140°C) and c.a. 70.3% for AA6022 with a NSDL (140°C). The rate of FFC propagation was also seen to drop considerably; AA6014 shows a reduction of c.a. 0.47 $mm^2\ hr^{-1}$ (72.3% reduction in rate), whereas AA6022 shows a reduction of c.a. 0.38 $mm^2\ hr^{-1}$ (60.3% reduction in rate). When no NSDL is present, AA6014 shows a reduction of c.a. 0.037 $mm^2\ hr^{-1}$ (63.8% reduction in rate), and AA6022 shows a reduction of c.a. 0.036 $mm^2\ hr^{-1}$ (81.8% reduction in rate).

Since CBP interacts with the surface, a greater effect should be observed with surfaces with a NSDL. CBP etches off the NSDL present, in doing so the surface now behaves as the bulk metal, and corrodes at a slower rate, i.e., CBP reduces the rate of FFC propagation. The BTA^- from the CBP dissolves into the electrolyte and removes the cations from the electrolyte, replacing them with benzotriazole. As shown in section 6.3.2 the BTA has little to no effect on the anodic regions but reduces current density in the cathodic region. This should therefore influence the trailing edge of the electrolytic head rather than the leading edge and why CBP showed a positive, but limited, inhibition effect in relation to area and rate. It is possible that the 1µL of 2M HCl contained an abundance of Cl^- and the CBP was eventually exhausted which is why there was still a large area of corrosion produced by the end of the investigation and why the rate was not reduced more significantly. CBP reduces the rate of FFC propagation in AA6014 more than in AA6022. This is easiest seen when a NSDL is present. AA6014 shows a reduction of c.a. 0.47 $mm^2\ hr^{-1}$, whereas AA6022 shows a reduction of c.a. 0.38 $mm^2\ hr^{-1}$. This is less significant when there is no NSDL with AA6014 showing a reduction of c.a. 0.037 $mm^2\ hr^{-1}$, and AA6022 showing a reduction of c.a. 0.036 $mm^2\ hr^{-1}$.

Other work[54,78, 85–92,105,106] identified the role that BTA^- has in the forming protective films with copper ions, formed from copper dissolution, from intermetallic particles and copper present at the surface as a result of an induced NSDL, providing anodic inhibition. BTA^- is also known to inhibit cathodic oxygen reduction on copper through

adsorption at the metal surface. Richards et al 369 found that when CBP was present in the organic PVB coating, an increase in the pigment volume fraction, resulted in reduced delamination rates; with the greatest inhibition and lowest rate when a PVF of 0.1 was used. AA6014 and AA6022 have showed a similar trend favouring PVF of values c.a. 0.1. Some samples showed a better corrosion inhibition at PVF of 0.05, and a slight increase in corrosion inhibition at 0.2, but the rate and areas did not change significantly between 0.1 and 0.2. When increasing PVF to 0.2 there is not a significant gain over the effect observed and measured for PVF of 0.1. Additionally, due to the high PVF at 0.2 the coating did not appear transparent, but more translucent and when corrosion products were formed a slight discolouration was observed. For effective results and a clear coating, then a PVF of 0.1 would be more favourable than a PVF of 0.2. It is also possible that CBP suppresses the corrosion rate on AA6014, more so than on the AA6022, due to a higher percentage of copper in its composition.

The general efficiency ranking order of the pigments used could be described as CBP > HT > HT-DEDTC. It is possible that due to the CBP being acidic in nature some of its efficiency may be related to the ability of the CBP to etch away some of the NSDL, in addition to providing a means of delivering an inhibitor into the underfilm region 369. The ability to etch away the NSDL to decrease rates of SA-FFC has been demonstrated previously on AA6111 using phenylphosphonic acid in PVB 354.

6.3.2 Effect of inhibitors – Potentiodynamic Experiments

Due to time constraints, the experimental work concentrated on the bulk alloy since the NSDL dissolves away so rapidly in 0.1 M NaCl. The "bulk" surface was used since it should provide the most realistic reflection of relative inhibitor efficiency. This section investigated the electrochemical behaviour of both uncoated AA6014 and AA6022 immersed in 0.1M NaCl solution in the presence and absence of dissolved BTA and DEDTC, to check inhibitive behaviour using conventional methodology and to gain some insight into their action on AA6014 and AA6022.

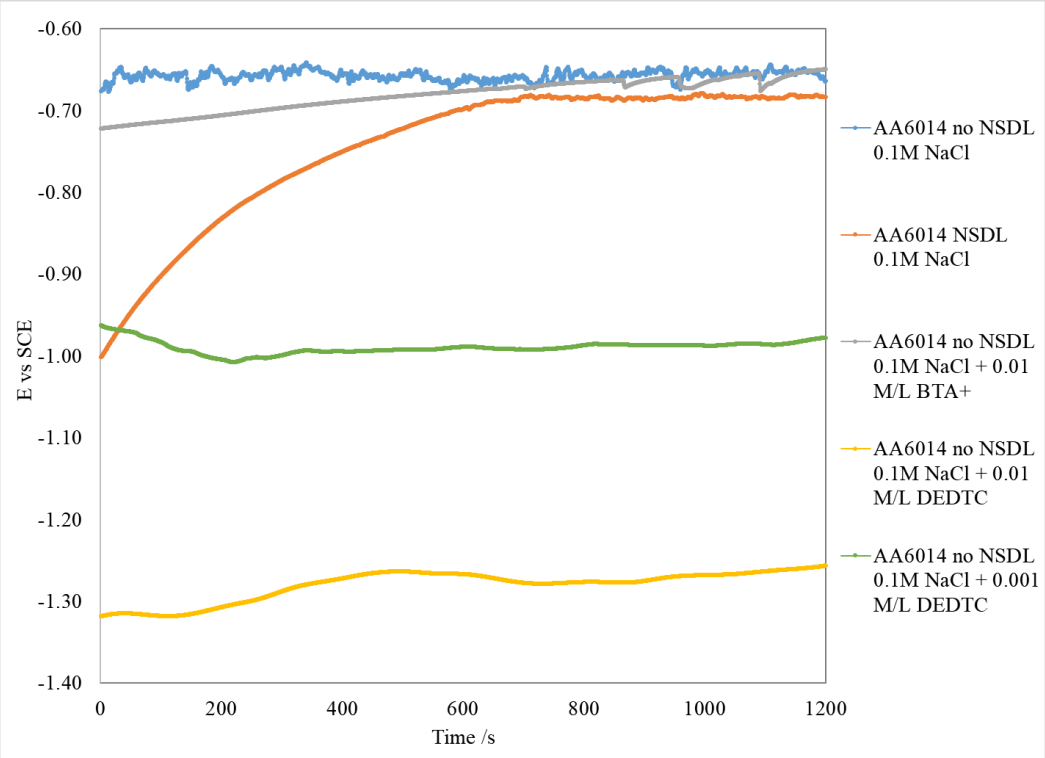

Figure 6.3.2a: open circuit potential, OCP, vs time plots for AA6014 samples with and without NSDL and with and without an inhibitor present.

Following the open circuit potential, OCP, scans the two alloys underwent cathodic potentiodynamic polarisation starting at -0.9V vs SCE (Standard Calomel Electrode), in 0.1 M NaCl (aq), in the presence and absence of dissolved BTA and DEDTC, at pH 6.5, sweeping the applied potential in a positive direction at a rate of 1 mV/s.

Figure 6.3.2a shows the open circuit potential, OCP, vs time plots for AA6014 samples with and without NSDL and with and without an inhibitor present. The open circuit potential, OCP, for AA6014 without a NSDL and without an inhibitor present (control sample) is c.a. -0.660V. Work shown in chapters 3, 4, 5 and previous sections in this

chapter, has shown that AA6014 samples with no NSDL present produce little corrosion, if any, at a RH up to 71%. Therefore, if the surface were to resemble samples without a NSDL, and have the same, or near to, surface potential then this could reduce the corrosion produced. Figure 6.3.2a shows that over time surfaces with a NSDL present age and eventually reach a potential similar to that of samples without a NSDL, as discussed in chapter 3. The inclusion of 0.01 ML^{-1}BTA decreased the initial potential to c.a. -0.720V, but at c.a. 700s the potential increased and overlapped the control sample. The presence of 0.01 ML^{-1} DEDTC and 0.001 ML^{-1} DEDTC both decreased the potential to c.a. -1.320V and -0.960V, respectively. The 0.01 ML^{-1} DEDTC appears to show an increase in potential over the 1200s, whereas the 0.001 ML^{-1} DEDTC appears to reduce in potential before a slight increase is observed. Due to the reduction in potential, it suggests that when the samples are run through the polarisation experiment then the current values will the lower in the cathodic branch, which is what was observed, figure 6.3.2b

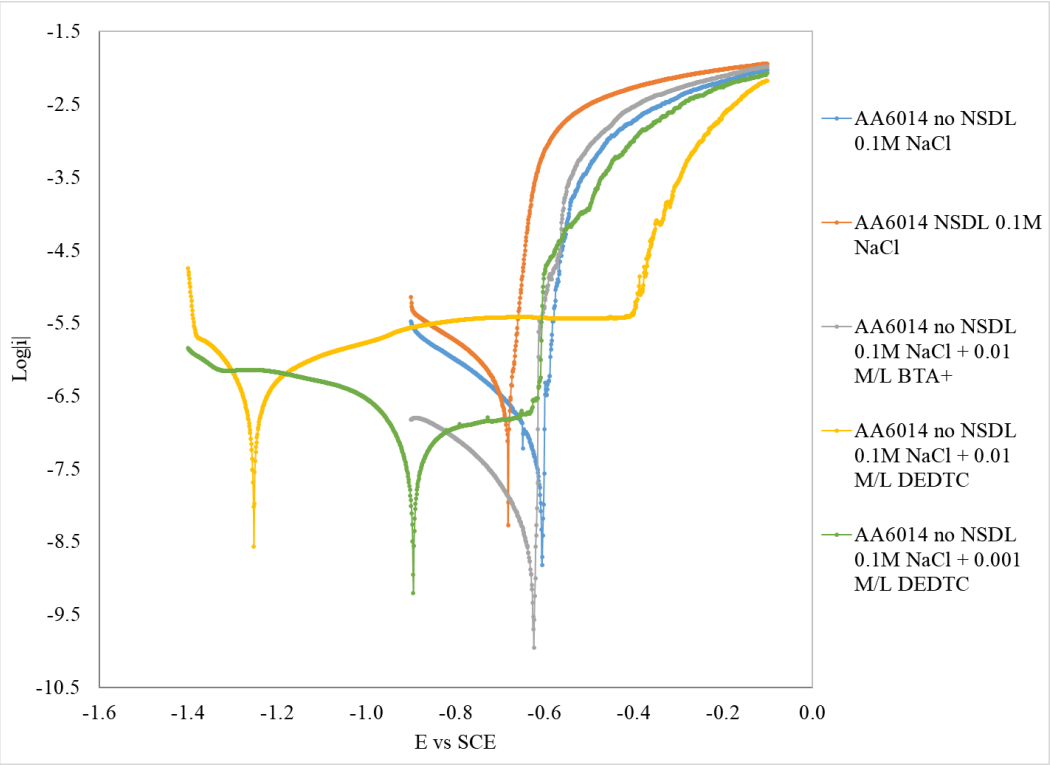

Figure 6.3.2b: polarisation curves for AA6014 samples with and without NSDL and with and without an inhibitor present. The samples were immersed in 0.1 M NaCl (aq), in the presence and absence of dissolved BTA and DEDTC, at pH 6.5, sweeping at a rate of 1 mV/s.

Figure 6.3.2b shows the polarisation curves for AA6014 samples with and without NSDL and with and without an inhibitor present. There is no evidence of a passive region in the anodic branch in the control electrolyte. It is possible that under these conditions this 6000 series alloy is not passive. It shows that the presence of a NSDL and inhibitors reduces the open circuit potential, OCP, with DEDTC has a very pronounced effect on both the open circuit potential, OCP, and Ecorr at both concentrations. 0.001 ML^{-1} DEDTC has a more negative Ecorr than the control and 0.01 ML^{-1} DEDTC, whereas 0.01 ML^{-1} DEDTC has a more negative open circuit potential, OCP, relative to 0.001 ML^{-1} DEDTC and the control. DEDTC appears to be a strong cathodic inhibitor, due to it reducing the E_{corr} down to a very negative potential, so much so that 0.01 ML^{-1} DEDTC does not appear to show any cathodic branch in the polarisation curves. BTA appears to have an effect, but mostly on the cathodic branch. The BTA has little to no effect on the anodic regions but reduces current density in the cathodic region. This should therefore influence the trailing edge of the electrolytic head rather than the leading edge and why CBP showed a positive inhibition effect in relation to area and rate in section 6.3.1 and possibly why its inhibiting effect is limited, even at large PVF.

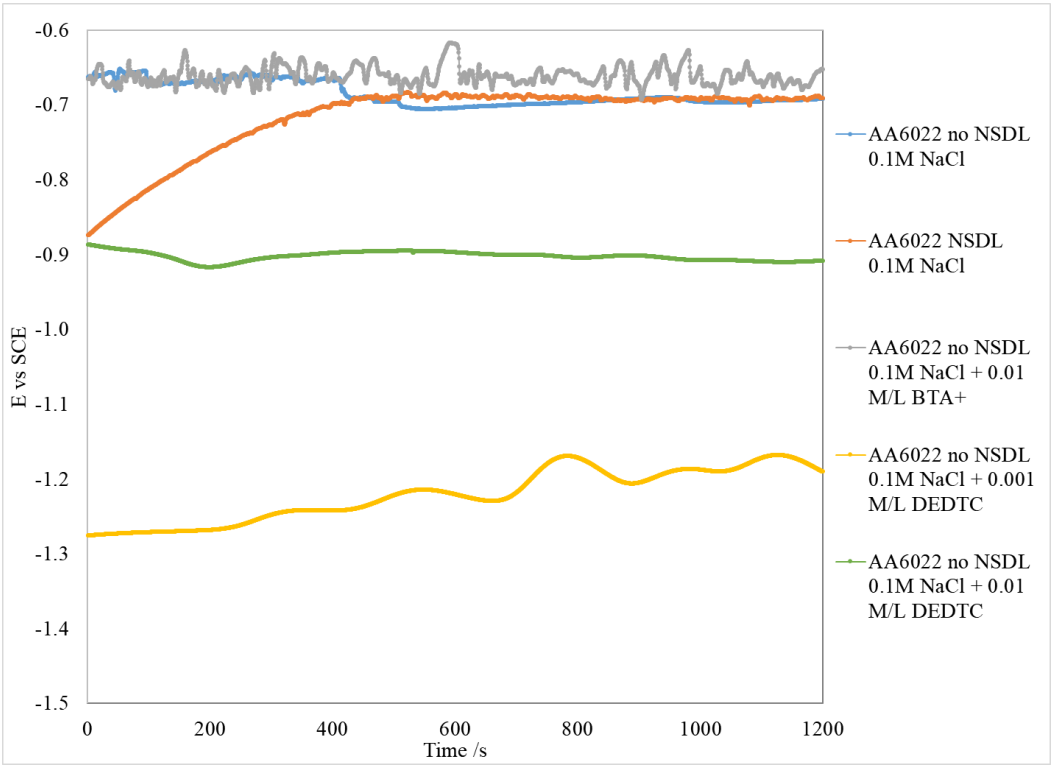

Figure 6.3.2c: open circuit potential, OCP, vs time plots for AA6022 samples with and without NSDL and with and without an inhibitor present.

Figure 6.3.2c shows open circuit potential, OCP, vs time plots for AA6022 samples with and without NSDL and with and without an inhibitor present. The open circuit potential, OCP, for AA6022 without a NSDL and without an inhibitor present (control sample) starts at c.a. -0.660V then reduces to c.a. -0.700V after c.a. 400s. Work shown in chapters 3, 4, 5 and previous sections in this chapter, has shown that AA6022 samples with no NSDL present produce very little corrosion, if any, at a RH up to 71%. Therefore, if the surface were to resemble samples without a NSDL, and have the same, or near to, surface potential then this could reduce the corrosion produced. Figure 6.3.2c shows that over time surfaces with a NSDL age and eventually reach a potential similar to that of samples without a NSDL, as discussed in chapter 3. The inclusion of 0.01 ML^{-1} BTA resulted in a fluctuating potential about c.a. -0.660V. At c.a. 400s when the control samples potential dropped to -0.700V, the potential of 0.01 ML^{-1} BTA stayed at c.a. -0.660V, c.a. 0.04V above the control sample. Williams et al 196, using SKP potentiometry, showed that BTA anions interact with the intact metal surface and depress the free corrosion potential, which could explain the less negative open circuit potential, OCP, for BTA here. The presence of 0.01 ML^{-1} DEDTC and 0.001 ML^{-1} DEDTC both decreased the potential to c.a. -1.280V and -0.880V, respectively. The 0.01 ML^{-1} DEDTC appears to show an increase in potential over the 1200s, to potentials of c.a. -1.190V to c.a. -1.170V, whereas the 0.001 ML^{-1} DEDTC appears to reduce in potential before a slight increase to c.a. -0.910V is observed. Due to the reduction in potential for DEDTC, it suggests that when the samples are run through the polarisation experiment then the current values will the lower in the cathodic branch, which is what was observed, figure 6.3.2d.

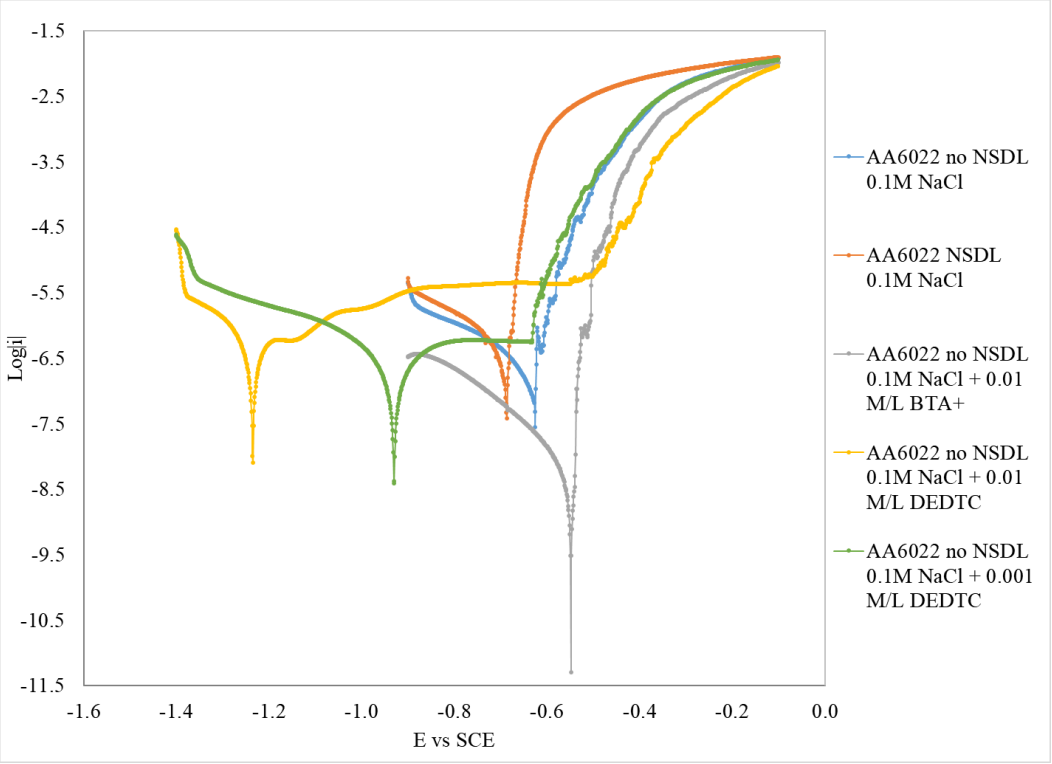

Figure 6.3.2d: polarisation curves for AA6022 samples with and without NSDL and with and without an inhibitor present. The samples were immersed in 0.1 M NaCl (aq), in the presence and absence of dissolved BTA and DEDTC, at pH 6.5, sweeping at a rate of 1 mV/s.

Figure 6.3.2d shows the polarisation curves for AA6022 samples with and without NSDL and with and without an inhibitor present. There is no evidence of a passive region in the anodic branch in the control electrolyte. It is possible that under these conditions this 6000 series alloy is not passive. It shows that the presence of a NSDL and inhibitors reduces the open circuit potential, OCP. DEDTC has a very pronounced effect on both the open circuit potential, OCP, and Ecorr at both concentrations. Increasing the DEDTC concentration produces a progressively more negative E_{corr} compared to the control. DEDTC appears to be a strong cathodic inhibitor, due to it reducing the Ecorr down to a very negative potential, so much so that 0.01 ML^{-1} DEDTC does not appear to show any cathodic branch in the polarisation curves. BTA appears to have a less negative open circuit potential, OCP, compared with the control. BTA has an effect, but mostly on the cathodic branch with little to no effect on the anodic regions, but significantly reduces current density in the cathodic region. This

should therefore influence the trailing edge of the electrolytic head rather than the leading edge and why CBP showed a positive inhibition effect in relation to area and rate in section 6.3.1 and possibly why its inhibiting effect is limited, even at large PVF.

The results in this section suggest that DEDTC should be a more effective inhibitor than BTA, because it seems to suppress cathodic kinetics more profoundly than BTA, as seen in figures 6.3.2b and 6.3.2d. The since DEDTC is far less effective and suggests that inhibition of oxygen reduction on copper rich phases is not the most important consideration in the design of an effective inhibitor of FFC on AA6014 and AA6022. The reason that BTA performs better may be related to results from previous studies on AA2024 FFC[192,196], where a similar trend in E_{corr} was observed (i.e. little change for BTA, but large negative shift in Ecorr for DEDTC), and went on to show that in-coating BTA adsorbs strongly on the oxide covered aluminium alloy surface and possibly restricts the adsorption of chloride, which is the precursor to anodic dissolution. This is possibly one of the reasons behind why the CBP is better performing. Previous work by Richards, C.A.J. et al.[377] identified the acidic nature of the CBP additive and its ability to partially etch away any NSDL present when the coating is first applied which would account for the reduction in cosmetic FFC rates when this inhibitor is used, whereas all others were ineffective. Previous work by Coleman et al 378. used PVB with additions of phenyl phosphonic acid to slow cosmetic FFC on AA6111. The efficiency of the inhibitor was linked to the etching away of the NSDL by the acidic nature of the coating.

6.4 Conclusions

Overall, the presence of a NSDL produces a greater area of FFC across its surface, as well as a quicker rate, when compared to the same sample setups where no NSDL is present. As with previous chapter, the FFC observed when a NSDL is present resembles rapid surface active FFC, followed by secondary and slower successive pitting FFC. Whereas the FFC produced on the samples with no NSDL present resembles the slower successive pitting FFC. As with previous chapters, AA6014 produces a greater area and quicker rate of FFC when compared to AA6022.

As expected from findings in chapter 5, most of the samples with a thermal treatment temperature of 140°C produce a slightly larger area of FFC when compared with the samples with a thermal treatment temperature of 20°C. The samples treated at 140°C have an inflated rate of FFC propagation compared to samples treated at 20°C for both AA6014 and AA6022.

DEDTC had a negligible effect on corrosion inhibition on both AA6014 and AA6022. HT had more of an effect on reducing the rate of FFC propagation, but overall, the corrosion area formed was still too similar to the control sample. Neither DEDTC nor HT provided samples where the corroded area was significantly different to the control sample or produced a corrosion rate significantly slower than the control sample to make them viable options.

CBP did produce some positive results. From the images and graphs in section 6.3.1 the area of corrosion on the samples was reduced by c.a. 60% for AA6014 without a NSDL, c.a. 58% for AA6014 with a NSDL, c.a. 77% for AA6022 without a NSDL, and c.a. 66% for AA6022 with a NSDL, (an average taken of both temperatures). The rate of FFC propagation dropped considerably; when a NSDL is present AA6014 shows a 72.3% reduction in corrosion rate, whereas AA6022 shows a 60.3% reduction in corrosion rate. When no NSDL is present, AA6014 shows a 63.8% reduction in corrosion rate and AA6022 shows an 81.8% reduction in corrosion rate. Overall, the PVF that had the greatest effect across the different surface and temperatures was 0.1 to 0.2 for AA6014, with 2 out of the 4 samples favouring 0.1 and with 2 out of the 4 samples favouring 0.2. The PVF that had the greatest effect across the different surface and temperatures AA6022 was not as clear. The PVF would fall within a PVF of 0.05

to 0.2. The samples with a NSDL reacted best to a PVF of 0.2, however the samples without a NSDL favoured 0.01 at 20°C and 0.05 at 140°C. Since the presence of a NSDL is unavoidable during the car manufacturing process and the existence of it increases susceptibility to cosmetic corrosion, then it would be more effective to use a PVF that will be most effective under these conditions. Therefore, a PVF of 0.2 is likely to produce the more favourable outcome for both AA6014 and AA6022.

Chapter 7 – The effect of mechanical deformation on FFC

7.1 Introduction

Due to environmental concerns relating to CO_2 emissions, in the 1980s there was a shift towards the use of aluminium sheet metals instead of steel. By replacing steel in doors, panels, and other areas, it was possible to reduce the weight of the vehicle, on average, by approximately 50%. Aluminium alloys, particularly from the AA6000 series, are an effective material to use due to it has fairly good formability and strength, although they tend to be lower that their steel counterparts 379. Compared to steel, aluminium is more corrosion resistant and able to produce clean, smooth finishes[383,384]. Aluminium alloys of the 6000 series have undergone many tests and manufacturing changes to produce a process and properties that have improved its formability and hemming performance. However, at room temperature the AA6000 series is less ductile than their steel counterparts. Due to the acute strains used in the hemming process, the aluminium alloys undergo localised deformations which result in splits/cracks on the surface of the outer bend radius[225,385,386]. This effect has a frost-like appearance and is commonly known as "orange peel." Over time these cracks propagate causing fractures along the apex of the hem. Although there have been studies regarding the bending of the AA6000 series, little is known about the surface deformation and performance[84,387,388]. This chapter investigates the deformation and its susceptibility to cosmetic corrosion.

During the car panelling process the sheet aluminium is cut, shaped and a folded hem is bent at each edge of the aluminium. Known as closure panels, the panels on cars are usually made up of several parts; the inner panel, providing structural integrity; smaller reinforcement sections, to add rigidity to the panel; the outer panel, mainly there for aesthetic purposes. Aluminium alloys provide "class-A" surface quality, meaning a freeform surface of high efficiency with ideal reflection quality[215].

Hemming is a mechanical joining process that uses plastic deformation to join the inner and outer panels together, whether on a door, bonnet, boot, roof, etc. These processes are cheaper than welding and have a high productivity relative to other processes[43,389]. Plastic deformation requires good ductility in order to form the join, it is a process that needs to be controlled to avoid the formation of defects. Hems are tight joins which are pressed together using great force. They produce clean seams

with increased stiffness and high strength. A hem is typically produced during the primary phases of manufacturing where the metal is subjected to plane strain. It uses a three-step process: flange bending, where the flange of the outer panel is bend 180° around the edge of the inner panel; pre-hemming and final hemming 383. However, since aluminium has limitations in relation to bendability (inter-crystalline crack formations on flat hemmed metal due to repeatedly bending the metal, or sharp bending), a different hem is produced, a rope hem. This hem has a larger radius to avoid crack formations that would be produced by traditional hems. Aluminium alloys of the 6000 series are not very ductile, due to the paint bake hardening process, therefore the hemmed edge is relatively large 385. Due to the need for a larger bend angle, to reduce defects, a two-stage flanging process is used to improve the outcome and reduce the radius. The first bend produces a relatively large bend angle, then the bend is compressed. Additional techniques have been utilised to improve the formability of the 6000 series 65. Further problems with the aluminium alloys are its relatively low Young's Modulus which results in low joint strength when compared to steel 390.

The highest quality hems, in the automotive sector, require the hem made by the outer metal to have a radius less than 1.5 mm. A quality inspection has typically been used to assess the surface quality, rather than a quantifiable method, even though several bending tests have been suggested[28,29,66,391,392]. Many of these tests evaluate the roughness along the bend by comparing images, which is inconsistent and difficult to standardise. There have been studies by Thuillier et al.[393–395] on the formability of aluminium sheet alloys, including AA6014-T4, which lead to them developing a ductile damage model based on critical void volume fraction centred on macroscopic tests. The work further investigated crack formation in the bent region. Other work 396 investigated other material and surface variable when subjected to hemming processes.

In 1998, Bottema et al 402 investigated Aluminium alloys of the 6000 series, AA6016, in relation to hemming and surface texture. They found AA6016 to have good formability, without compromising on strength. They concluded that using thermo-mechanical processing 1.2 mm AA6016-T4 sheets, with 10% pre-strain, were capable of flat hemming and could be used as a replacement for steel in vehicle panels.

Stoudt et al.[405] investigated hemming performance of automotive aluminium alloys in 2014. They used high resolution topographic imaging to evaluate the surfaces of aluminium alloys of the 6000 series which were bent 180° in a simulated hemming test. AA6451 was investigated due to it potentially having an improved paint bake response. A second, unnamed experimental AA6xxx was investigated due to it potentially having an improved hemming quality. It was suggested that due to the copper, magnesium and silicon content falling between that of AA6022 and AA6111, that the behaviour of the strengthen precipitates would be the same[112,406,407]. They followed the three-point bend test method, developed at General Motor[408], to evaluate and catergorise the hemming performace. Although steps were taken to reduce friction between the specimens and the rollers, graphite lubrication, there was still contact bewteen the surfaces. They also polished the specimens prior to testing, which is likely to have produced a NSDL. They reported that mechanically the alloys had similar properties, but showed differences in their surface morphology with one showing a greater distribution of intermetalic particles, with a wider range of particle size across the surface leading to poor particle cohesion, leading to large surface displacments that were disassociated with the underlying microsturcture. Although neither alloy showed visual signs of splits or cracks, the work proposed that the surface displacements could indicate the presence of short surface cracks. This could potentially lead to cosmetic corrosion of aluminium alloys of the 6000 series as these short surface cracks are deforming the surface.

The bending limit for AA6014-T4 was investigated in 2018 by Saxena et al.[409] They stated, as well as other work[398,410], that the forming limit curve, FLC, proposed by Goodwin[411] fails to predicte the fomability in hemming operations, due to a different failure mechanism and the exclusion of the effect of sheet bending. Saxena et al.[409] propose the need for bending limit curves as a replacement to FLC. Sarkar et al.[412,413] investigated AA6111 (and AA5754) and concluded that alloys with a high iron content have low bendability, and vice versa. The work conducted by Saxena et al.[409] focused on AA6014 (and DP600) and a punch radius of 0.4 mm and 2.0 mm. They found that initially, as the pre-strain process increases, the bending strain decreases as secondary particles are sheared away during pre-straining. However, as the pre-strain continued to increase, bending strain also increased. They noted that the lower radius produced higher strains on the the outer surface during bending, leading to brittle fracture due to

high tensile strain on the outer surface and and the inner surface experencing compressive strain. They noted that FLCs fail to evaluate bendability sufficiently and that bending limit curves are higher for smaller radii.

Gu et al.[414] investigated the fracture of flat-surface straight-edge hemmed 1 mm thick AA6014-T4. They stretched the sheet metal biaxially in order to create pre-strain prior to the hemming process. They observed and evaluated the effect of flange radius on the fracture produced and whether roller hemming or die hemming produced a different outcome. The found that the yield stress and ultimate tensile strength increased during the aging process, which is a desirable outcome. However, uniform elongation, plastic strain ratio and the strain hardening exponent decreased, which reduced the formability which is unfortunate outcome. During the die hemming process, they found that when the flange radius was ≤ 1 mm fracture (or potential fracture) was observed on the outer surface (convex surface), which deteriorated further during the hemming process. A flange of 1.2 mm only produced fractures during the hemming process, but a flange radius of 1.5 mm did not produce any signs of fracture. During the roller hemming process, they found that when the flange radius was <1.2 mm serious fracture occurred. In order for the roller hemming process to produce an acceptable hem a flange radius of at least 1.2 mm is required. At a flange radius of 1.2 mm the roller hemming process demonstrated a superior formability than the die hemming process. They concluded that overall die hemming has a better formability due to the linear increase in major strain and a fairly consistent value for minor strain.

The sponsoring company believed that this highly deforming hemming process could be responsible for generating an NSDL. This work is designed to test their hypothesis on whether it is possible that the hemming process could produce a surface deformed layer on the bend similar to the surfaces that are susceptible to *SA-FFC*. This chapter aimed to investigate the effect of the bending process and the type of FFC by ensuring no NSDL was produced on the surface.

Experimental

This section looks at FFC initiated on mechanically deformed samples at the same time as flat samples, used as a control measure. 2 flat samples were used for each alloy, one sample with a NSDL & the other sample without a NSDL. This should allow a direct comparison between the flat and bent samples. The flatter section of the bent section should behave the same way as the flat sample without a NSDL. The bent section of the bent sample could potentially behave in a comparable way to the flat sample with a NSDL.

All samples were prepared as described in Chapter 2.3 and 2.4; Alkali cleaning of the samples in NaOH (10% w/v), for c.a. 45s at 60°C, to dissolve any aluminium oxide and any NSDL on the surface. Samples were rinsed with distilled water and acetone before acid desmutting using concentrated HNO_3 (15.6 molar) for 30s at 25°C to remove impurities such as copper and iron from the surface, and to passivates the surface. The samples were again rinsed with distilled water and acetone. For the 35 x 40 mm^2 flat samples, when a NSDL was required, the surface was manually abraded using 180 grit silicon carbide paper for 5 mins. The abrasion direction was orientated in the same direction as the rolling direction. Samples were rinsed with distilled water and acetone prior to bar coating with 15.5% (w/w) ethanolic PVB (Polyvinyl butyral) solution to produce an air-dried PVB coating of thickness 30µm ± 5µm. 5mm defects were scribed through the PVB layer normal (90°) to the rolling/NSDL direction with a scalpel. Due to economy of samples, they were scribed with 3 defects c.a. 13mm apart and staggered, see figures 7.2a. The number of defects used, have been identified in each section. FFC was initiated by injecting the scribe with 0.5µL of 2M aqueous hydrochloric acid using a glass micro-capillary dispenser. The HCl injection method was intended to create greater reproducibility than methods involving full sample exposure either by salt fog, HCl vapour, or immersion in aqueous electrolyte [2,3].

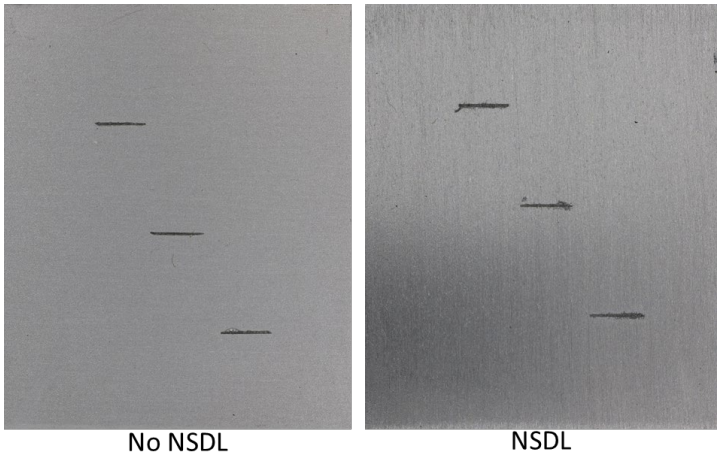

Figure 7.2a: flat sample with defect arrangement. Three 5 mm defects c.a. 13 mm apart staggered across the sample. The image on the left has a NSDL present, the figure on the right does not have a NSDL.

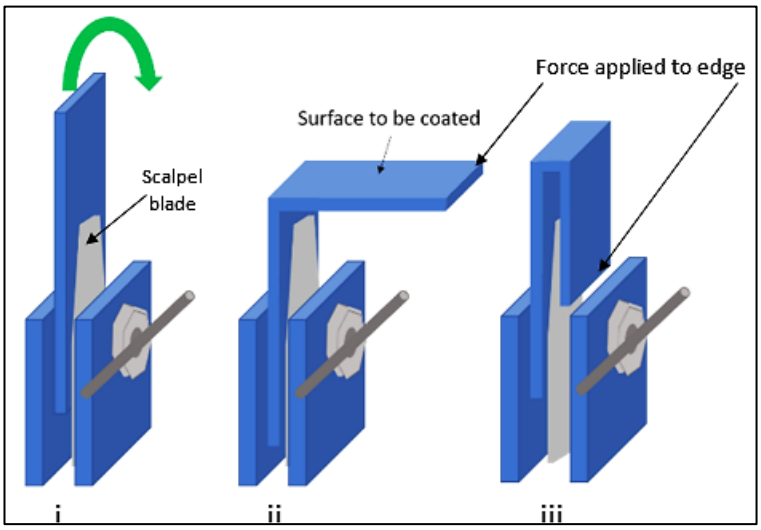

Figure 7.2b: a diagram of the bending technique used. i) Initial bending position in clamp with a scalpel blade on the inner surface. ii) Shows the flange being bent around the scalpel blade and iii) shows the flange in its final position.

Figure 7.2a shows flat sample defect arrangement, three 5 mm defects c.a. 13 mm apart staggered across the sample. The image on the left has a NSDL present, the figure on the right does not have a NSDL. Figure 7.2b shows how the mechanical deformation was achieved. The samples were cut so that part of the samples could be touched and manipulated into a bent sample, whilst the other part of the sample would remain untouched throughout to eliminate and shear forces on the surface. The samples were

50 x 15 mm^2. They were placed in a clamp with a lubricated pad to reduce friction and creating a NSDL (the section clamped was not used during the investigation, but precautions were still put in place), figure 7.2bi. Figure 7.2bii shows the inclusion of a 0.4 mm scalpel blade on the inner surface to bend the flange over. The flange was bent by applying a force to the top edge and pushing it over the blade. To create the shape shown in figure 7.2biii, the sample was removed from the vice and wrapped in paper, to reduce shear forces, and placed back into the vice where the 2 short edges were pressed together to close the bend. The edge will not be investigated during the investigation.

Figure 7.2c: i) Side profiles of the bent samples used. ii) Positions of the defects on the bend samples

Figure 7.2c shows the side profile of the samples, note that the bend radius is not consistent. This is due to this investigation being the preliminary work. If the investigation provides convincing evidence of the bend behaving similarly to samples with a NSDL then further investigations will follow using a die hemming process in order to maintain consistency in bend radius and reduce the radius in set increments. No NSDL was purposefully produced on any of the bent samples. The samples were also coated with 15.5% (w/w) ethanolic PVB solution to produce an air-dried PVB coating of thickness 30µm ± 5µm. However, they were coated using an 11 mm glue spatula with c.a 2 mm of electrical insulation tape on the edge of the samples to create the same coating thickness as the flat surfaces. Three 5 mm defects were scribed, with a scalpel, through the PVB layer normal (90°) to the rolling direction, on the bent samples and some of the flat samples, and 90° to the NSDL direction on the remaining flat samples. One was place at the apex of the bend, one was place where the bend

initiated and the final defect was on the flat section, see figure 7.2cii. FFC was initiated by injecting the defects with 0.5µL of 2M aqueous hydrochloric acid using a glass micro-capillary dispenser.

Figure 7.2d shows how the samples were stored. The samples were placed in sealed containers, with a specific saturated salt solution to obtain the desired % relative humidity, 93% RH (Sodium sulfate Decahydrate) & the other at 80% RH (Ammonium sulfate). A digital hygrometer and temperature sensor (Lascar's EasyLog EL-USB-2-LCD+) was placed in each container. The samples were periodically photographed as seen in figure 7.2e and observations noted.

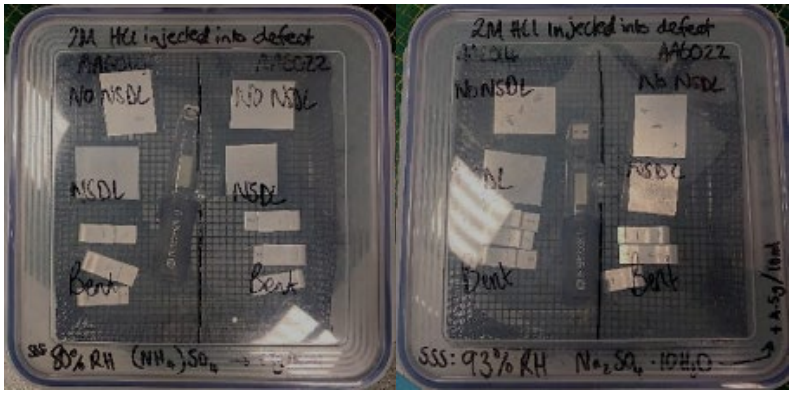

Figure 7.2d: Sealed boxes containing both flat and bent samples at 80% RH (Ammonium Sulfate) and 93% RH (Sodium sulfate Decahydrate)

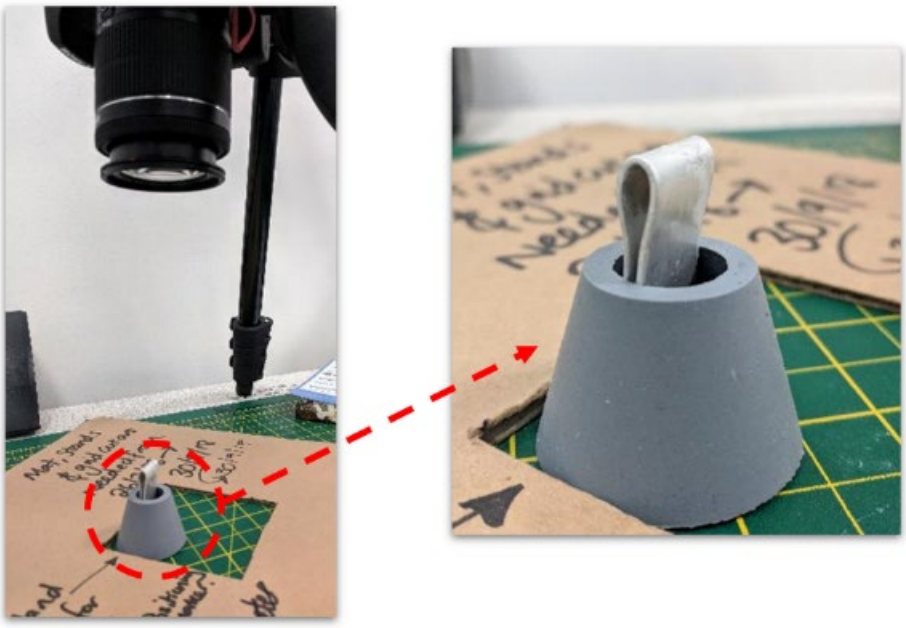

Figure 7.2e: How the images of the bent sample were taken

7.2 Results and Discussion

The images shown in this section show the Flat and Bent samples for AA6014 at 80% RH. The same experiments were also performed at a higher RH of 93% and produced the same outcome regarding the type of FFC and rates.

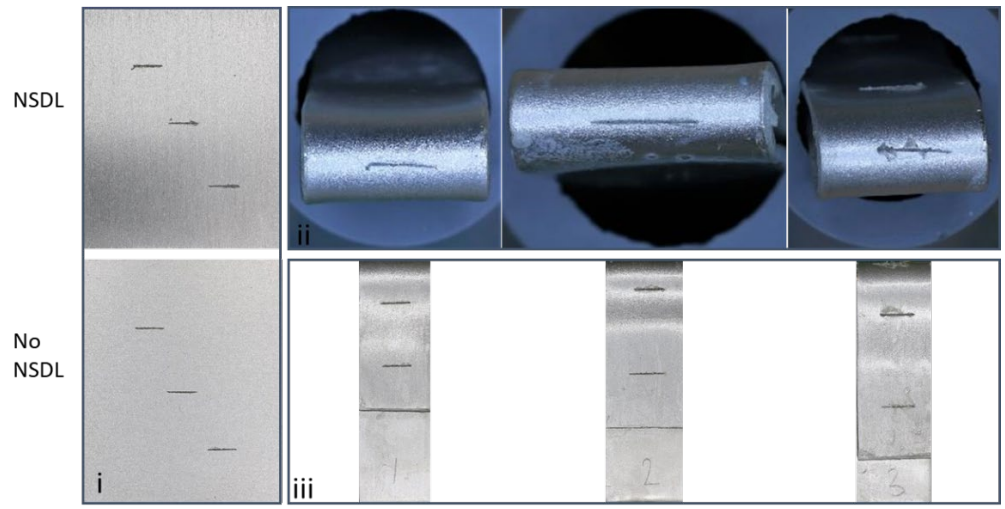

Figure 7.3a: flat and bent samples of AA6014 with three 5 mm defects each injected with 0.5µl of 2M HCl at 80% RH after 24 hours i) flat samples with and without a NSDL, ii) the apex of the bend with a defect, iii) two defects on the flatter region of the bent sample.

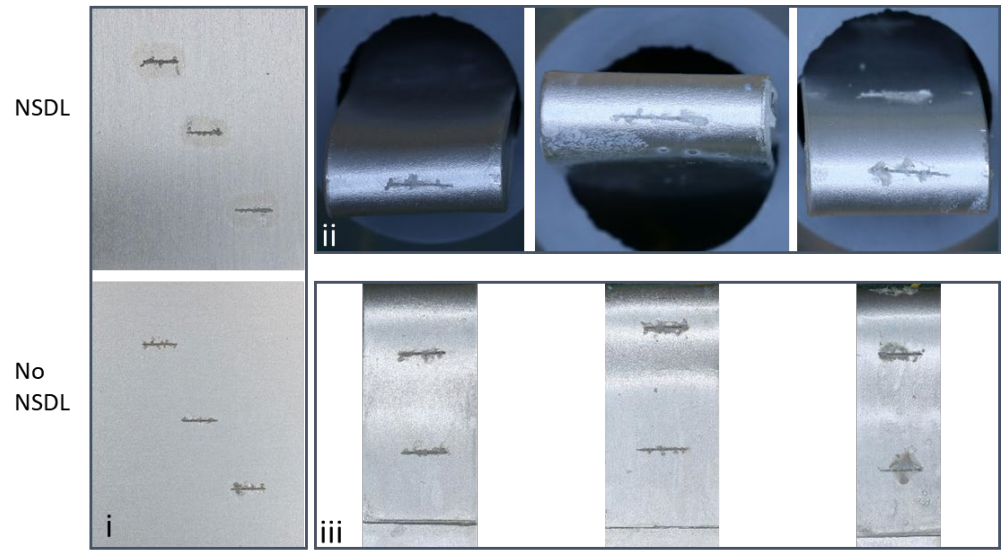

Figure 7.3b: flat and bent samples of AA6014 with three 5 mm defects each injected with 0.5µl of 2M HCl at 80% RH after 96 hours i) flat samples with and without a NSDL, ii) the apex of the bend with a defect, iii) two defects on the flatter region of the bent sample.

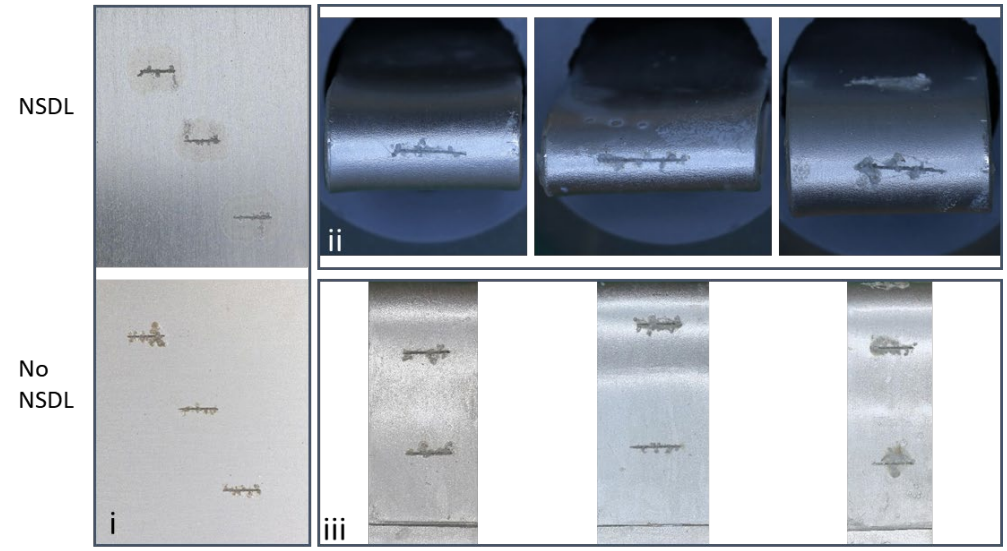

Figure 7.3c: flat and bent samples of AA6014 with three 5 mm defects each injected with 0.5µl of 2M HCl at 80% RH after 144 hours i) flat samples with and without a NSDL, ii) the apex of the bend with a defect, iii) two defects on the flatter region of the bent sample.

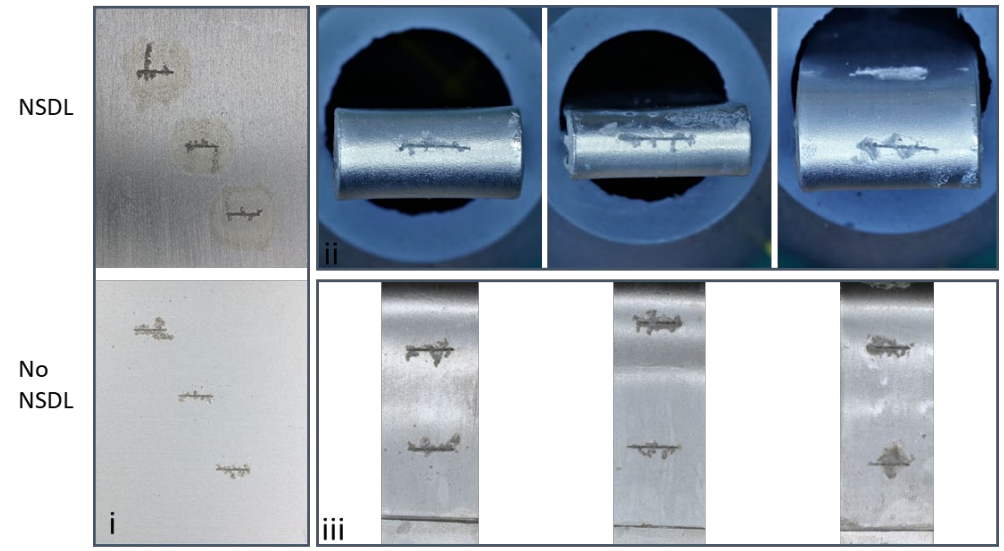

Figure 7.3d: flat and bent samples of AA6014 with three 5 mm defects each injected with 0.5µl of 2M HCl at 80% RH after 264 hours i) flat samples with and without a NSDL, ii) the apex of the bend with a defect, iii) two defects on the flatter region of the bent sample.

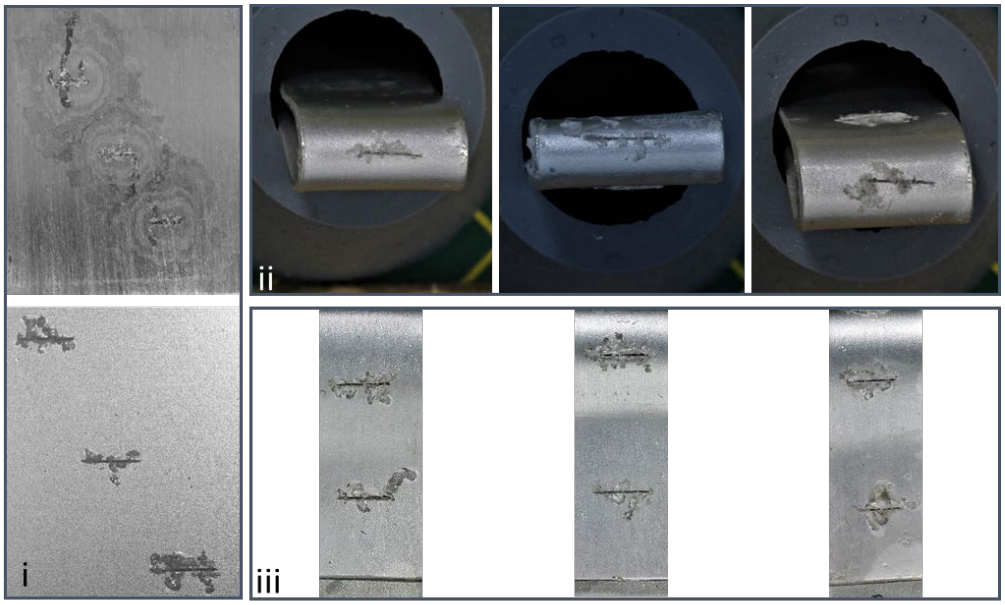

Figure 7.3e: flat and bent samples of AA6014 with three 5 mm defects each injected with 0.5µl of 2M HCl at 80% RH after 1104 hours i) flat samples with and without a NSDL, ii) the apex of the bend with a defect, iii) two defects on the flatter region of the bent sample.

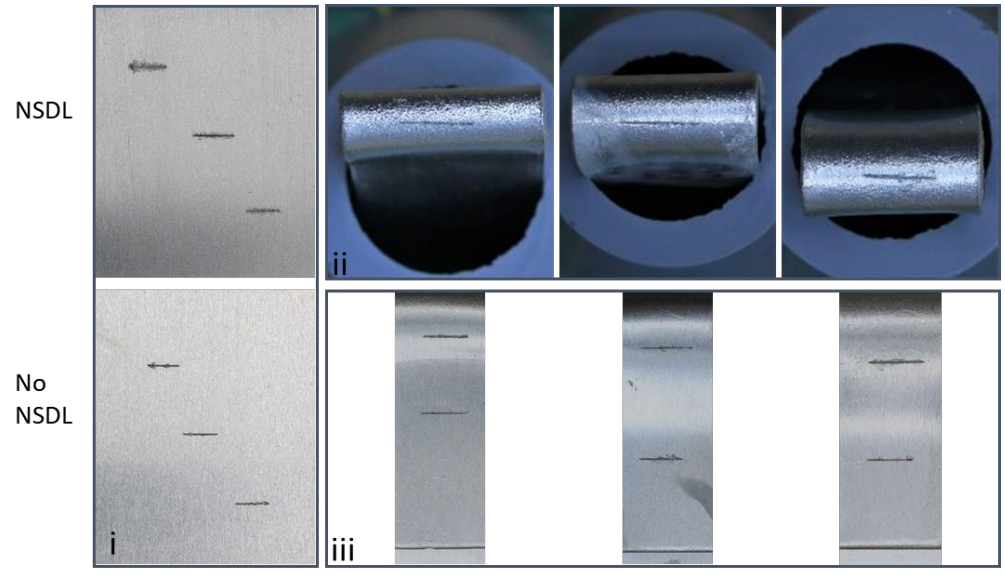

Figure 7.3f: flat and bent samples of AA6022 with three 5 mm defects each injected with 0.5µl of 2M HCl at 80% RH after 24 hours i) flat samples with and without a NSDL, ii) the apex of the bend with a defect, iii) two defects on the flatter region of the bent sample.

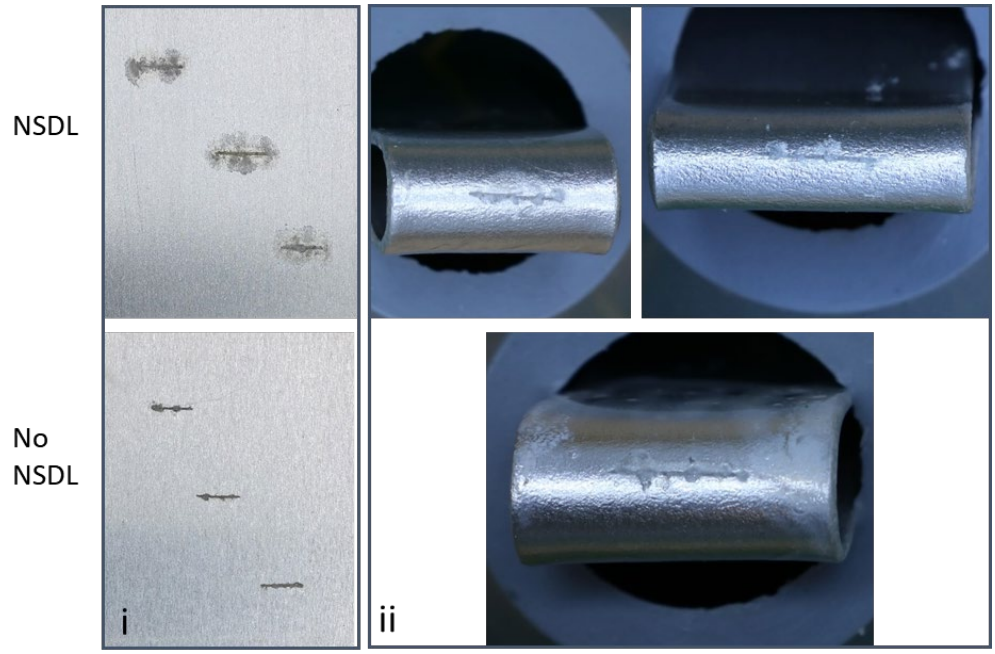

Figure 7.3g: flat and bent samples of AA6022 with three 5 mm defects each injected with 0.5µl of 2M HCl at 80% RH after 96 hours i) flat samples with and without a NSDL, ii) the apex of the bend with a defect.

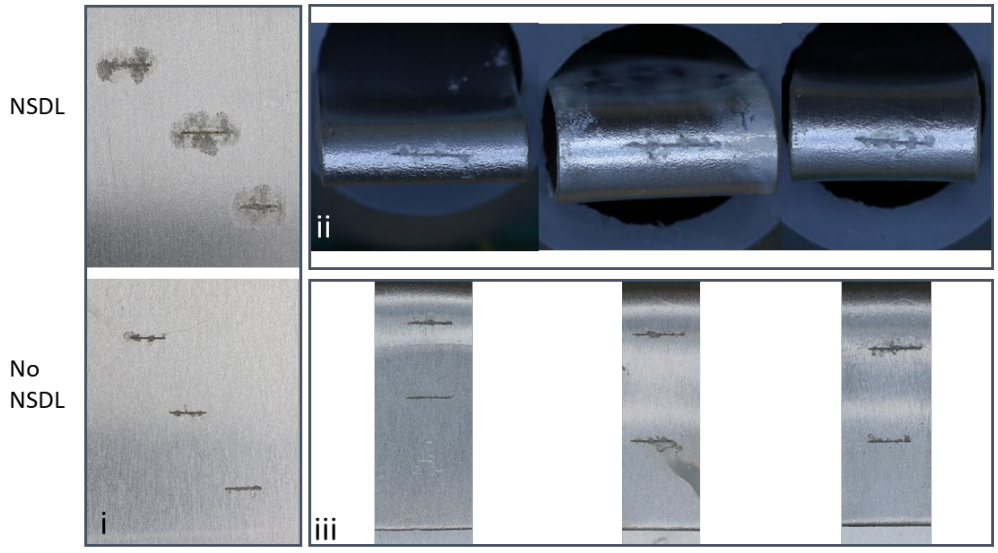

Figure 7.3h: flat and bent samples of AA6022 with three 5 mm defects each injected with 0.5µl of 2M HCl at 80% RH after 114 hours i) flat samples with and without a NSDL, ii) the apex of the bend with a defect, iii) two defects on the flatter region of the bent sample.

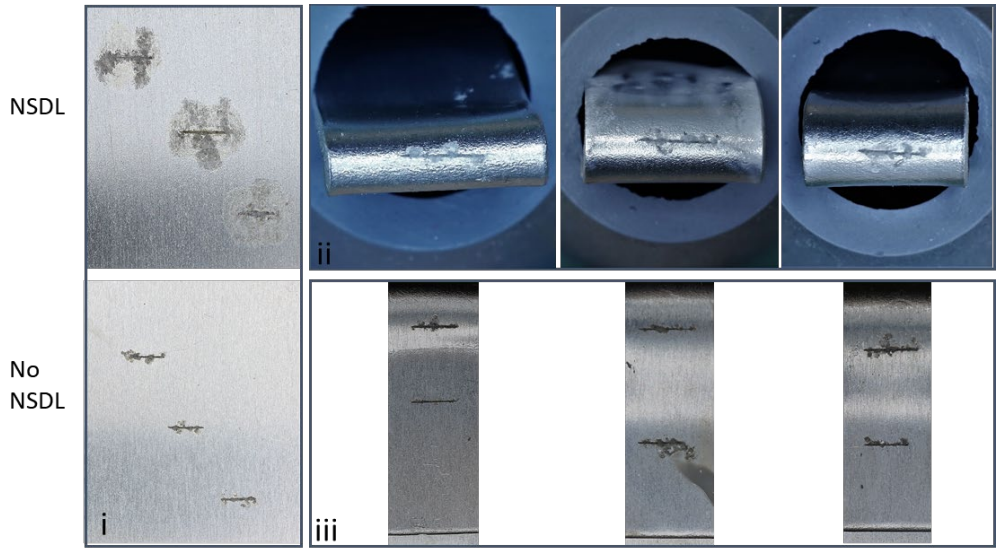

Figure 7.3i: flat and bent samples of AA6022 with three 5 mm defects each injected with 0.5µl of 2M HCl at 80% RH after 264 hours i) flat samples with and without a NSDL, ii) the apex of the bend with a defect, iii) two defects on the flatter region of the bent sample.

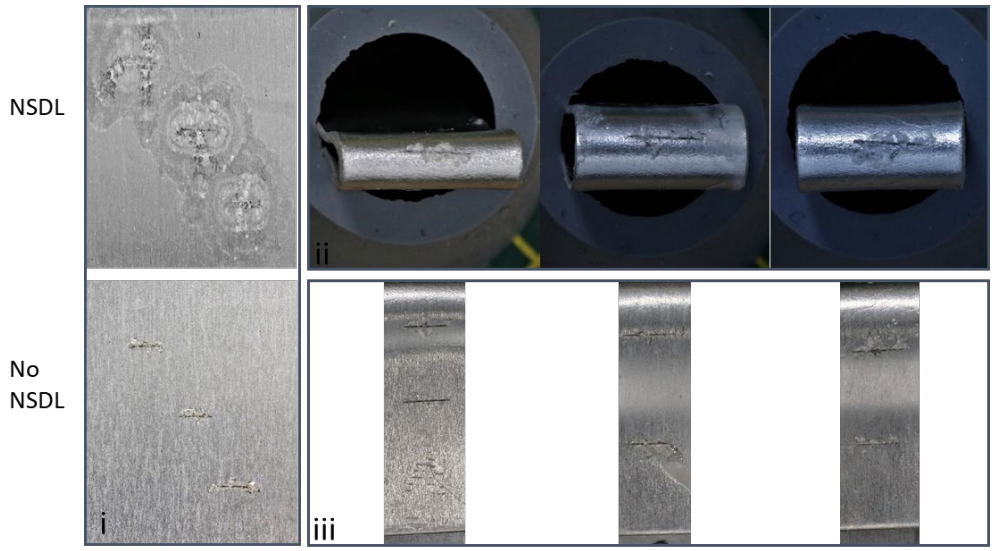

Figure 7.3j: flat and bent samples of AA6022 with three 5 mm defects each injected with 0.5µl of 2M HCl at 80% RH after 1104 hours i) flat samples with and without a NSDL, ii) the apex of the bend with a defect, iii) two defects on the flatter region of the bent sample.

The results shown in figures 7.3f to 7.3j for AA6022 at 80% RH, with 0.5µl of 2M HCl injected into the defect, show that across the 46 days the corrosion observed on the bent samples mirrors the flat sample without a NSDL, slow *SP-FFC*. There is no evidence of a corrosion pattern on the bent sample that mirrors the pattern observed on the flat sample when a NSDL is present, *SA-FFC*.

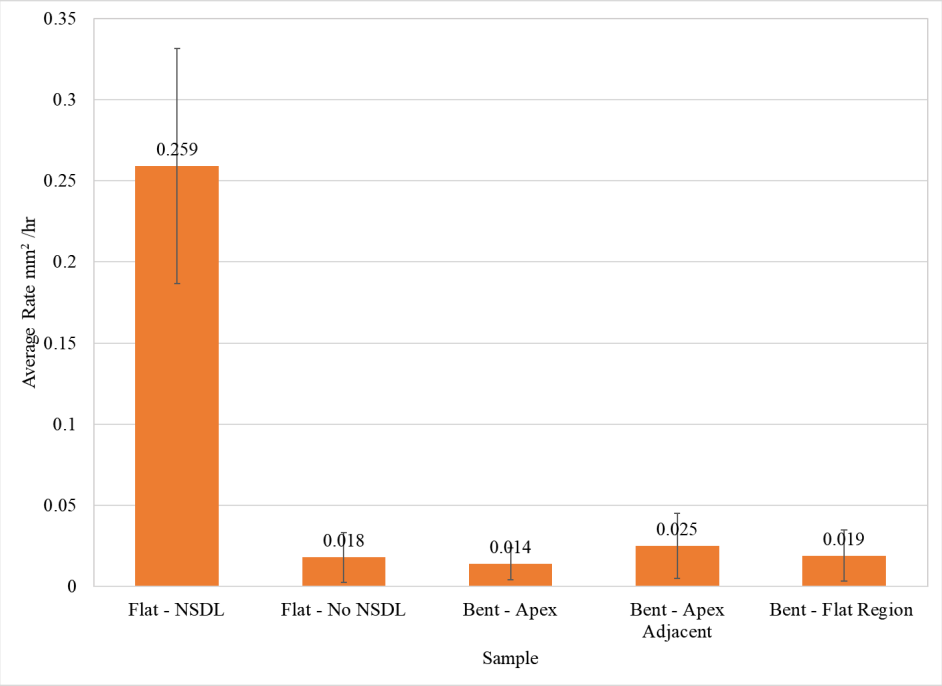

Figure 7.3k: Average rate of FFC propagation for all AA6014 samples.

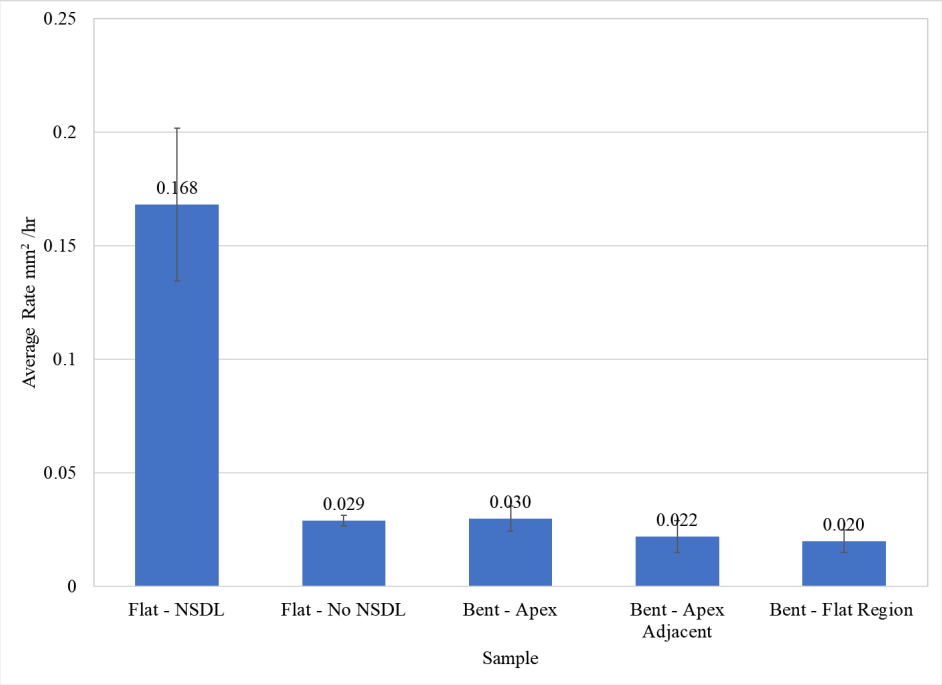

Figure 7.3l: Average rate of FFC propagation for all AA6022 samples.

Sample type	AA6014	AA6022
	SD mm^2/hr	
Flat - NSDL	0.0726	0.0336
Flat - No NSDL	0.0154	0.0022
Bent - Apex	0.0097	0.0056
Bent - Apex Adjacent	0.0202	0.0071
Bent - Flat Region	0.0157	0.0050

Table 28: Standard deviation for each region on AA6014 and AA6022 samples

Figures 7.3k and 7.3l show the rates of FFC propagation for samples AA6014 and AA6022, respectively. Table 28 show the standard deviation for each sample. The figures clearly show that the defect at the apex of the bend follows a similar rate and FFC progression as the flat sample without a NSDL. In fact, each defect on the bent samples have FFC propagation rates similar to the flat sample without a NSDL. There is no evidence that a defect on a bent sample alone will initiate SA-FFC, if an aggressive electrolyte is present and environmental conditions are favourable for FFC.

7.4 Conclusions

To achieve a prompt result, the samples used were not subjected to any pre-strain prior to the bend. As noted earlier in the chapter, pre-strain can reduce crack formation on the bend[409]. The desired outcome of a NSDL effect was more likely to be observed when a more deformed surface is produced, therefore pre-strain would have reduced this potential effect. However, the defects on the bent samples for AA6014 and AA6022, in both 80%RH and 93%RH, show similar corrosion to the flat samples when no NSDL is present, *SP-FFC,* across all the defect sites including the defects that were placed at the apex of the bend. The samples do not show any similarities with the flat samples that have NSDL. Since *SP-FFC* is only produced either on surfaces with no NSDL or on surfaces that have had the NSDL removed as a result of *SA-FFC* then it is likely that a NSDL has not been produced by bending the metal. These findings suggest that the bending alone does not produce a surface where a FFC pattern is produced similar to that produced by samples with NSDL. Due to the nature of the sample preparation and the care taken not to induce a NSDL, it is possible that on large scale panel hemming shear forces could be present and create a NSD-like layer which will produce FFC, based on the results of the preliminary investigation, it was decided that there would not be any secondary work conducted at this time.

The results shown in figures 7.3a to 7.3j for both AA6014 and AA6022, at 80% RH with 0.5µl of 2M HCl injected into the defect, show that across the 46 days the corrosion observed on the bent samples mirrors the flat sample without a NSDL, slow successive pitting FFC. There is no evidence of a corrosion pattern on the bent sample that mirrors the pattern observed on the flat sample when a NSDL is present, rapid surface active FFC. The extent of FFC observed on the bent surface correlates well with the “bulk” planar surface, but less so with a planar NSDL surface which supports a higher rate of FFC propagation.

Chapter 8 - Conclusions and Future Work

8.1 FFC and the Presence of a NSDL

The principal conclusions arising from the research described within this thesis are as follows:

- For uncoated samples, the presence of a NSDL produces a significantly more negative free corrosion potential compared to the bulk alloy. This has been observed through SKP and open circuit potential, OCP, scans. The SKP was done in humid air and open circuit potential, OCP, was monitored as a function of time in full immersion conditions using a NaCl (aq) electrolyte. Where FFC is not induced, (this was for a half-abraded specimen held in humid air) the potential difference observed between the NSDL and the Bulk for AA6014 and AA6022 has been measured. The open circuit potential, OCP, scans show that there is an average difference in the initial potentials of c.a 0.3V for AA6014 and c.a 0.4V AA6022. The SKP scans show that there is an average difference potential of c.a. 0.4V for AA6014 and c.a. 0.4V for AA6022.
- The SKP scanning and open circuit potential, OCP, measured in immersion conditions show that there is only a small difference in potentials between the two alloys. There is no clear information to suggest one having more corrosion resistance than the other, therefore it is difficult to comment on the rate of corrosion between the two.
- The potential difference between the two types of surfaces suggests that the samples with a NSDL are undergoing anodically activated driven corrosion, (when FFC is observed in the presence of a model PVB coating) whereas the absence of a NSDL are more likely to be driven by differential aeration. The SP-FFC closely resembles the features generated on previous studies on organically coated AA2024, where the main driving force, i.e. differential aeration, is assumed to be the same for SP-FFC on AA6000 series alloys.
- For PVB (Polyvinyl butyral) coated samples injected with 2M HCl (aq), FFC is observed for samples with and without a NSDL. The FFC observed differs depending on the surface. In the presence of a NSDL a fast form of superficial FFC is observed, known as surface active FFC. When a NSDL is not present, then a slower, more penetrating, form of FFC is observed, known as successive pitting FFC.

  All the work was initiated with HCl, if more work is to be conducted on AA6014 and AA6022 in relation to cosmetic corrosion then it may be useful to initiate corrosion

with NaCl due to the likelihood of it being in the environment. It would provide a real-life context, rather than an accelerated view, and potentially lead to further work.

8.2 FFC and Relative Humidity

The principal conclusions arising from the research described within this thesis are as follows:

- All AA6014 and AA6022 samples in environments where the relative humidity was greater than 12% exhibited corrosion. At relative humidities less than 33% RH the rate of corrosion was small but then increases after c.a. 33% RH up to 53% RH. This could be due to the sample boxes being opened briefly to monitor the %RH and to remove samples for images. Since FFC is seen to occur at RH levels below that of the deliquescence point of $AlCl_3$ (46%), then this could be an artefact produced by opening the chamber at regular intervals to extract specimens for imaging.
- For relative humidities between 53% and 80%, both AA6014 and AA6022 with a NSDL exhibited a mixture of rapid surface active FFC and a secondary, slower successive pitting FFC. After 80% both AA6014 and AA6022 show a reduction in successive pitting FFC with zero successive pitting FFC observed at 93% RH. The samples without a NSDL exhibit a mix of pitting and successive pitting FFC. Both AA6014 and AA6022 have similar trends with respect to relative humidity with a peak corrosion rate at c.a. 80% RH with a decrease in rate at c.a. 85%, but then an increase at c.a. 93%.
- The saturated salt solution of Aluminium Chloride hexahydrate produced a % RH of 46% at 20°C. This %RH saw an increase in corrosion rate, but also a difference in surface corrosion appearance.
- In all cases 80%RH has the largest rate of corrosion and showed most clearly the 2 types of FFC: surface active and successive pitting. At RH < 80% successive pitting is the more dominant FFC. At RH > 80% surface active FFC is more dominant. This investigation suggested that the optimum conditions required for FFC initiate and propagate is a RH of 80% and the presence of a NSDL. Although they were not measured, visually it is clear that the samples with a NSDL show the filament width increasing as %RH increases, up until 80% RH, after which the individual filaments are difficult to discern because they all merge into one unified feature.
- Both alloys show a significant increase in corrosion rate when the NSDL was present. This could be attributed to the potential difference measured using the SKP (Scanning Kelvin Probe), as seen in chapter 3. The surfaces comprising a NSDL show a clear increase of corrosion rate with the increase of humidity, with a peak corrosion at 80%

RH. The presence of a NSDL lowers the surface potentials significantly making them anodically activated compared to the bulk alloy, as seen in chapter 3. In this experiment, the lower potential has increased the rate of corrosion for these samples and can be considered the driving force for surface active FFC.

- Surfaces without a NSDL and with a NSDL exhibit a higher rate of corrosion for AA6014 than for AA6022 this result was not apparent in chapter 3 based on their surface potentials alone as there was not a significant difference between the surface potentials. This pattern could potentially be due to the composition of the alloys as seen in chapter 1 as a higher % of copper in the alloy can lead to a copper-rich surface after the sample has been prepared using caustic etching.

One saturated salt solution that could be investigated in future is NaCl due to the likelihood of it being present in the environment, especially in coastal areas. Other SSS to investigate would be those linked to industry as again they are likely to be present in the environment that the vehicles are in. This would produce results that could be of interest in a real-world context. Another route of inquiry would be to investigate the influence of wet-dry cycling on the FFC morphology. This type of process is more representative of real life, and it would be beneficial to gauge whether or not cyclic RH changes are more damaging in terms of FFC propagation compared to exposure to a fixed RH.

8.3 FFC and Thermal Treatment Temperature

The principal conclusions arising from the research described within this thesis are as follows:

- Whether a NSDL is present or not, AA6014 produced the greater extent of FFC affected areas relative to AA6022. The higher corrosion rate could be a result of AA6014 having a higher transition metal content, Cu and Fe, in its composition. The higher percentage of copper could potentially lead to a greater proportion of copper-rich intermetallic phases at the surface and grain boundaries as a result of thermal treatment. The presences of a NSDL lowers the surface potential, relative to the bulk alloy, by between 0.2V and 0.4V for AA6014 and between 0.1V to 0.3V for AA6022. The slightly larger potential difference in AA6014 could be another factor in the increase in corrosion rates.
- The effect of thermal treatment has negligible effect on surfaces without a NSDL with little change across the corroded areas and corrosion rates. AA6014 shows more of a trend for samples with and without a NSDL.
- The effect of thermal treatment is more clearly seen on surfaces with a NSDL with both AA6014 and AA6022 showing the greatest corrosion rates and greatest potential difference at 140°C. The thermal treatment temperatures of 210°C to 250°C showed the greatest corrosion resistance, with the slowest corrosion rates and smallest potential difference. This could be ascribed to the greater Cu and Fe content within the AA6014. It is possible that the 210°C to 250°C range produces a change in the precipitate distribution which may render the bulk a less active cathodic surface when coupled to the NSDL.
- Due to the vast difference in corrosion rate, further work could investigate temperatures between 200°C and 350°C at smaller increments to identify the temperature that produced the slowest corrosion rate. A similar investigation between 80°C to 180°C could be conducted to identify if there is a low enough temperature that produces a relative slow corrosion rate as lower temperatures produce better formability. This would hopefully produce a conclusive result as to what the ideal temperature is in order to keep FFC to a minimum even when a NSDL is present.

8.4 FFC and Inhibitors

The principal conclusions arising from the research described within this thesis are as follows:

- DEDTC, that is stored within the HT smart release pigment, had a negligible effect on corrosion inhibition on both AA6014 and AA6022.
- HT had some effect on reducing the rate of corrosion, but overall, the corrosion area formed remained rather similar to the control sample.
- Neither DEDTC nor HT provided samples where the corroded area was significantly different to the control sample or produced a corrosion rate significantly slower than the control sample to make them viable options for further investigation.
- CBP did produce some positive results: the area of corrosion on the samples reduced by c.a. 60% for AA6014 whether a NSDL was present or not; the area of corrosion on the samples reduced by c.a. 77% for AA6022 without a NSDL, and c.a. 66% for AA6022 with a NSDL. The rate of corrosion dropped considerably; when a NSDL is present AA6014 shows a 72% reduction in corrosion rate, whereas AA6022 shows a 60% reduction in corrosion rate. When no NSDL is present, AA6014 shows a 64% reduction in corrosion rate and AA6022 shows an 82% reduction in corrosion rate.

  Overall, the pigment volume fraction that had the greatest effect across the different surface and temperatures was 0.1 to 0.2 for AA6014, with 2 out of the 4 samples favouring 0.1 and with 2 out of the 4 samples favouring 0.2. The PVF (Pigment Volume Fraction) that had the greatest effect across the different surface and temperatures AA6022 was not as clear. The PVF would fall within a PVF of 0.05 to 0.2. The samples with a NSDL reacted best to a PVF of 0.2, however the samples without a NSDL favoured 0.01 at 20°C and 0.05 at 140°C.

  Since the presence of a NSDL is unavoidable during the car manufacturing process and the existence of it increases susceptibility to cosmetic corrosion, then it would be more effective to use a PVF that will be most effective under these conditions. Therefore, a PVF of 0.2 is likely to produce the more favourable outcome for both AA6014 and AA6022.

There is a plethora of alternative inhibitors that could be explored to reduce the corrosion on these alloys. Given that the CBP inhibitor has some effect, probably due

to its ability to each away some of the NSDL, then maybe other "etch primers" systems would be alternative promising candidates. For example, there are commercially available etch primers based on phosphoric acids which could be a "quick fix." Alternatively, other organic acids (e.g., phosphonic acids) which might form insoluble salts with Al^{3+} could be additives which might be incorporated into the model PVB system to gauge their relative efficiencies at slowing rates of SA-FFC.

8.5 FFC and Bending

The principal conclusions arising from the research described within this thesis are as follows:

- The defects on the bent samples for AA6014 and AA6022, in both at 80% RH and 93% RH with 0.5µl of 2M HCl injected into the defect, show that across the 46 days the corrosion observed on the bent samples mirrors the flat sample without a NSDL, slow successive pitting FFC (*SP-FFC),* across all the defect sites including the defects that were placed at the apex of the bend.
- There is no evidence of a corrosion pattern on the bent sample that mirrors the pattern observed on the flat sample when a NSDL is present, rapid surface active FFC *(SA-FFC)*. The samples do not show any similarities with the flat samples that have NSDL.
- These findings suggest that the bending alone does not produce a surface where a FFC pattern is produced similar to that produced by samples with NSDL. It is possible that on large scale panel hemming shear forces could be present and create a NSD-like layer which could produce FFC. However, it would be the presence of a NSDL that is producing the NSDL, not the hemming alone.

Due to time restraints and preliminary findings secondary work was not conducted. Future work could investigate the effect of using the two main types of hemming and see if they are producing a NSDL similar to that produced by abrasion. This would follow a similar process to that carried out in chapter 7, i.e., removing any NSDL during the sample preparation. If a NSDL is produced by hemming, then more investigations could follow by trying to improve the hemming process and techniques. If it does not produce a similar result to surfaces with a NSDL, then it is possible to assume that the corrosion observed at the hemming joints is a result of the sheets being polished or re-worked at a later stage and introducing a NSDL. Additionally, the microstructure of the NSDL produced on both alloys, either by abrasion or by bending, could be investigated to allow further insight into the two types for deformation.

Chapter 9 – References

(1) Williams, G.; Mcmurray, H. N.; Hayman, D.; Morgan, P. C. Physchemcomm 2001, 4 (6), 1–6.
(2) Mcmurray, H. N.; Coleman, A. J.; Williams, G.; Afseth, A.; Scamans, G. M. Mater. Sci. Forum 2006, 521 (2006), 679.
(3) Mcmurray, H. N.; Coleman, A. J.; Williams, G.; Afseth, A.; Scamans, G. M. J. Electrochem. Soc. 2007, 154 (7), 339.
(4) Williams, G.; Mcmurray, H. N. J. Electrochem. Soc. 2003, 150 (8), B380.
(5) Mcmurray, H. N.; Holder, A.; Williams, G.; Scamans, G. M.; Coleman, A. J. Electrochim. Acta 2010, 55 (27), 7843–7852.
(6) Coleman, A. J. J.; Mcmurray, H. N. N.; Williams, G.; Afseth, A.; Scamans, G. M. Alum. Alloy. 2006, Pts 1 2 2006, 519–521 (2006), 629–633.
(7) European Commission. Results Of The Review Of The Community Strategy To Reduce Co2 Emissions From Passenger Cars And Light-Commercial Vehicles; 2007.
(8) Seeland, A.; Oetken, M.; Kiss, A.; Fries, E.; Oehlmann, J. Environ. Sci. Pollut. Res. 2012, 19 (5), 1781–1790.
(9) European Commission. Accompanying The Adoption Of A Regulation On Co2/Cars; 2007.
(10) Www.Theicct.Org; International Council On Clean Transportation. 2014.
(11) Https://Drivealuminum.Org/. Drive Aluminum Http://Www.Drivealuminum.Org/ (Accessed Jun 7, 2018).
(12) Https://Inspectioneering.Com/News/2016-03-08/5202/Nace-Study-Estimates-Global-Cost-Of-Corrosion-At-25-Trillion-Ann. Nace Study Estimates Global Corrosion Cost At $2.5 Trillion Annually Https://Inspectioneering.Com/News/2016-03-08/5202/Nace-Study-Estimates-Global-Cost-Of-Corrosion-At-25-Trillion-Ann (Accessed Oct 12, 2017).
(13) Http://Insights.Globalspec.Com/Article/2340/Annual-Global-Cost-Of-Corrosion-2-5-Trillion. Annual Global Cost Of Corrosion: $2.5 Trillion | Engineering360 Http://Insights.Globalspec.Com/Article/2340/Annual-Global-Cost-Of-Corrosion-2-5-Trillion (Accessed Oct 12, 2017).
(14) Koch, G.; Thompson, N.; Moghissi, O.; Gould, M.; Payer, J.; Jacobson, G. 2016.
(15) Sheasby, P. G. (Peter G.; Pinner, R.; Wernick, S. (Simon). The Surface Treatment And Finishing Of Aluminium And Its Alloys.; Asm International, 2001.
(16) Sheasby, P. G. (Peter G.; Pinner, R.; Wernick, S. (Simon). The Surface Treatment And Finishing Of Aluminium And Its Alloys.; Asm International, 2001.
(17) Totten, G. E.; Mackenzie, D. S. Handbook Of Aluminum; 2003.
(18) Hind, A. R.; Bhargava, S. K.; Grocott, S. C. Colloids Surfaces A Physicochem. Eng. Asp. 1999, 146 (1–3), 359.
(19) Davis, J. R. 1999, 351.
(20) Hirsch, J.; Leroy, C.; Green, A. Mater. Sci. Forum 2006, 519, 1209.
(21) Meng, Q.; Frankel, G. S. Corrosion 2004, 60 (10), 897.
(22) El-Bedawy, M. E. M. 2010.
(23) Sukiman, N. L.; Zhou, X.; Birbilis, N.; Hughes, A. E.; Mol, J. M. C.; Garcia, S. J.; Zhou, X.; Thompson, G. E. In Intech : Aluminium Alloys - New Trends In Fabrication And Applications; Intech, 2012; Vol. 2, P 3.
(24) Shreir, L. .; Jarman, R. A.; Burstein, G. T. Corrosion - Metal/Environment

Reactions; 1994; Vol. 1.
(25) Birbilis, N.; Buchheit, R. G. J. Electrochem. Soc. 2005, 152 (4), B140.
(26) Graser, M.; Fröck, H.; Lechner, M.; Reich, M.; Kessler, O.; Merklein, M. Prod. Eng. 2016, 10 (4–5).
(27) Wang, B.; Chen, X.; Pan, F.; Mao, J.; Fang, Y. Trans. Nonferrous Met. Soc. China 2015, 25 (8), 2481–2489.
(28) Hui, W.; Ying-Bing, L.; Friedman, P.; Ming-He, C.; Lin, G. Trans. Nonferrous Met. Soc. China 2012, 22, 1.
(29) Quainoo, G. K.; Yannacopoulos, S. J. Mater. Sci. 2004 3915 2004, 39 (15), 4841.
(30) Alcoa. Alloy 6022 Sheet Higher Strength With Improved Formability Https://Www.Arconic.Com/Mill_Products/Catalog/Pdf/Alloy6022techsheet_Rev2.Pdf (Accessed Apr 11, 2017).
(31) Hirsch, J. Mater. Trans. 2011, 52 (5), 818.
(32) Muhammad, W.; Kang, J.; Brahme, A. P.; Ali, U.; Hirsch, J.; Brinkman, H. J.; Engler, O.; Mishra, R. K.; Inal, K. Mater. Sci. Eng. A 2019, 753, 179–191.
(33) Gu, Z.; Wang, G.; Yu, G. Metals (Basel). 2020, 10 (1), 81.
(34) Kahrimanidis, A.; Wortberg, D.; Merklein, M. Phys. Procedia 2014, 56 (C), 1410.
(35) Krajewski, P. E. The Effect Of Retrogression Heat Treatments On Aluminum Flanging And Trimming; 2006; Vol. 115.
(36) Butler,J.F.; Alcoa. Alcoa Micromill™ Breakthrough Technology for Next Generation Auto Sheet 2015 .
(37) Sarkar, J.; Kutty, T. R. G.; Wilkinson, D. S.; Embury, J. D.; Lloyd, D. J. Mater. Sci. Eng. A 2004, 369 (1–2), 258–266.
(38) Sarkar, J.; Kutty, T. R. G.; Conlon, K. T.; Wilkinson, D. S.; Embury, J. D.; Lloyd, D. J. Tensile And Bending Properties Of Aa5754 Aluminum Alloys; 2001.
(39) Scamans, G. M.; Birbilis, N.; Buchheit, R. G. 3.08 Corrosion Of Aluminum And Its Alloys.
(40) Thuillier, S.; Le Maoût, N.; Manach, P. Y. Int. J. Mater. Form. 2010, 3 (Suppl. 1), 223–226.
(41) Zecevic, M.; Roemer, T. J.; Knezevic, M.; Korkolis, Y. P.; Kinsey, B. L. Materials (Basel). 2016, 9 (3).
(42) Kleiner, M.; Geiger, M.; Klaus, A. Manufacturing Of Lightweight Components By Metal Forming.
(43) Mori, K. I.; Bay, N.; Fratini, L.; Micari, F.; Tekkaya, A. E. Cirp Ann. - Manuf. Technol. 2013, 62 (2), 673.
(44) Gracio, J. J.; Barlat, F.; Rauch, E. F.; Jones, P. T.; Neto, V. F.; Lopes, A. B. Int. J. Plast. 2004, 20 (3), 427–445.
(45) Prillhofer, R.; Rank, G.; Berneder, J.; Antrekowitsch, H.; Uggowitzer, P. J.; Pogatscher, S. Materials (Basel). 2014, 7 (7), 5047–5068.
(46) Lin, H. C.; Kuo, T. Y.; Lin, C. C. Metall. Mater. Trans. A Phys. Metall. Mater. Sci. 2009, 40 (11), 2578.
(47) Fishkis, M.; Lin, J. C. Z J. Wea Artic. 1997, 206 (96), 7480.
(48) Fridlyander, I. N.; Sister, V. G.; Grushko, O. E.; Berstenev, V. V.; Sheveleva, L. M.; Ivanova, L. A. Met. Sci. Heat Treat. 2002, 44 (9–10), 365.
(49) Miller, W. S.; Zhuang, L.; Bottema, J.; Wittebrood, A. J.; De Smet, P.; Haszler, A.; Vieregge, A. Mater. Sci. Eng. 2000, 280 (1), 37–49.
(50) Murtha, S. J. J. Mater. Manuf. 1995, 104, 657.

(51) Tao, G. H.; Liu, C. H.; Chen, J. H.; Lai, Y. X.; Ma, P. P.; Liu, L. M. Mater. Sci. Eng. A 2015, 642, 241–248.
(52) Sarkar, J.; Kutty, T. R. G.; Wilkinson, D. S.; Embury, J. D.; Lloyd, D. J. Mater. Sci. Eng. A 2004, 369 (1), 258.
(53) Mrówka-Nowotnik, G. .
(54) Krajewski, P. E. J. Mater. Manuf. 2006, 115, 754–761.
(55) Mukhopadhyay, P. Isrn Metall. 2012, 2012, 1–15.
(56) Zhou, J.; Wan, X.; Li, Y. Mater. Today Proc. 2015, 2 (10), 5015.
(57) Esmaeili, S.; Lloyd, D. J.; Jin, H. Mater. Lett. 2011, 65 (6), 1028.
(58) Bressan, J. D.; Bruschi, S.; Ghiotti, A. Int. J. Mech. Sci. 2016, 115–116, 702–710.
(59) Werinos, M.; Antrekowitsch, H.; Ebner, T.; Prillhofer, R.; Curtin, W. A.; Uggowitzer, P. J.; Pogatscher, S. Acta Mater. 2016, 118, 296–305.
(60) Yassar, R. S.; Field, D. P.; Weiland, H. .
(61) Chakrabarti, D. J.; Laughlin, D. E. Prog. Mater. Sci. 2004, 49 (3–4), 389–410.
(62) Golovashchenko, S. F. In Journal Of Materials Engineering And Performance; 2005; Vol. 14, Pp 508–515.
(63) Merklein, M.; Lechner, M.; Kuppert, A. Prod. Eng. 2012, 6 (6), 541–549.
(64) Zadpoor, A. A.; Campoli, G.; Sinke, J.; Benedictus, R. Mater. Des. 2011, 32 (3), 1229–1241.
(65) Kleeh, T.; Merklein, M.; Roll, K. Key Eng. Mater. 2011, 473, 501–508.
(66) Shreir, L. L.; Jarman, R. A.; Burstein, G. T. Corrosion - Corrosion Control; 1994; Vol. 2.
(67) Revie, R. W.; Uhlig, H. H. Corros. Corros. Control An Introd. To Corros. Sci. Eng. Fourth Ed. 2008, 1–490.
(68) Tisza, M.; Czinege, I. Int. J. Light. Mater. Manuf. 2018, 1 (4), 229–238.
(69) Aalco Metals Ltd. 2016, 1–6.
(70) Aalco. Temper Designations Non-Heat Treatable Alloy Designations Code; 2000.
(71) Buchheit, R. G.; Grant, R. P.; Hlava, P. F.; Mckenzie, B.; Zender, G. L. J. Electrochem. Soc. 1997, 144 (8), 2621.
(72) Vargel, C. Corros. Alum. 2020, 41–61.
(73) George, F. O. UK Univ. Manchester; 2011.
(74) Wloka, J.; Virtanen, S. J. Electrochem. Soc. 2007, 154 (8), 411.
(75) Polmear, I. J. Light Alloys: From Traditional Alloys To Nanocrystals; Elsevier/Butterworth-Heinemann, 2006.
(76) Mazurkiewicz, B.; Piotrowski, A. Corros. Sci. 1983, 23 (7), 697–707.
(77) Scully, J. R.; Knight, T. O.; Buchheit, R. G.; Peebles, D. E. Corros. Sci. 1993, 35 (1–4), 185–195.
(78) Birbilis, N.; Buchheit, R. G.; Ho, D. L.; Forsyth, M. Electrochem. Solid-State Lett. 2005, 8 (11), C180.
(79) Eckermann, F.; Suter, T.; Uggowitzer, P. J.; Afseth, A.; Schmutz, P. Electrochim. Acta 2008, 54 (2), 844–855.
(80) Goswami, R.; Spanos, G.; Pao, P. S.; Holtz, R. L. Mater. Sci. Eng. A 2010, 527 (4–5), 1089–1095.
(81) Boag, A.; Hughes, A. E.; Glenn, A. M.; Muster, T. H.; Mcculloch, D. Corros. Sci. 2011, 53 (1), 17–26.
(82) Hughes, A. E.; Boag, A.; Glenn, A. M.; Mcculloch, D.; Muster, T. H.; Ryan, C.; Luo, C.; Zhou, X.; Thompson, G. E. Corros. Sci. 2011, 53 (1), 27–39.
(83) Cavanaugh, M. K.; Buchheit, R. G.; Birbilis, N. Eng. Fract. Mech. 2009, 76

(5), 641–650.
(84) Mackenzie, S. D.; Totten, G. E. Analytical Characterization Of Aluminum, Steel, And Superalloys; Taylor & Francis, 2006; Vol. 8.
(85) Eigler, S. Ecs Meet. Abstr. 2015, Ma2015-01 (9), 882–882.
(86) British Standards Online Bsol. Bs En 1706:2010 Aluminium And Aluminium Alloys. Castings. Chemical Composition And Mechanical Properties Https://Bsol.Bsigroup.Com/Bibliographic/Bibliographicinfodata/000000000030183859 (Accessed Apr 11, 2017).
(87) Gov.Uk. Manufacture Or Adapt A Vehicle Https://Www.Gov.Uk/Browse/Driving/Manufacture-Adapt-Vehicle (Accessed Jun 30, 2017).
(88) Makeitfrom. 6014-T4 Aluminum Http://Www.Makeitfrom.Com/Material-Properties/6014-T4-Aluminum (Accessed Apr 11, 2017).
(89) Habibi, D. A. John Stuart Mill And The Ethic Of Human Growth; Springer Netherlands, 2001.
(90) Ambat, R.; Davenport, A. J.; Afseth, A.; Scamans, G. J. Electrochem. Soc. 2004, 151 (2), B53.
(91) Afseth, A.; Nordlien, J. H.; Scamans, G. M.; Nisancioglu, K. Corros. Sci. 2002, 44 (11), 2491–2506.
(92) Afseth, A.; Nordlien, J. H.; Scamans, G. M.; Nisancioglu, K. Corros. Sci. 2001, 43 (11), 2093–2109.
(93) Afseth, A.; Nordlien, J. H.; Scamans, G. M.; Nisancioglu, K. Corros. Sci. 2002, 44 (1), 145–162.
(94) Afseth, A.; Nordlien, J. H.; Scamans, G. M.; Nisancioglu, K. Corros. Sci. 2001, 43 (12), 2359–2377.
(95) Mol, J. M. C.; Hinton, B. R. W.; Van Der Weijde, D. H.; De Wit, J. H. W.; Van Der Zwaag, S. J. Mater. Sci. 2000, 35 (7), 1629–1639.
(96) Bryant, J. D. The Effects Of Preaging Treatments On Aging Kinetics And Mechanical Properties In Aa6111 Aluminum Autobody Sheet; Minerals, Metals And Materials Society, 1999; Vol. 30, Pp 1999–2006.
(97) He, Y.; Jia, Z.; Sanders, R. E.; Liu, Y.; Ding, L.; Xing, Y.; Liu, Q. J. Alloys Compd. 2017, 703, 272–279.
(98) Staley, P. A.; Metzger, J.; Griffo, D.; Simmons, E.; Griffo, C.; Bennahmias, M.; Kurtz, R.; Smith, D. K. Ecs Meet. Abstr. 2015, Ma2015-02 (12), 638–638.
(99) Scamans, G. M.; Frolish, M. F.; Rainforth, W. M.; Zhou, Z.; Liu, Y.; Zhouc, X.; Thompsonc, G. E.; Zhou, X.; Thompson, G. E. Surf. Interface Anal. 2010, 42 (4), 175–179.
(100) Bowden, F. P. Proc. R. Soc. London. Ser. A - Math. Phys. Sci. 1937, 160 (903), 575–587.
(101) Leth-Olsen, H.; Nordlien, J. H.; Nisancioglu, K. J. Electrochem. Soc. 1997, 144 (7), 196–197.
(102) Miao, W. F.; Laughlin, D. E. Metall. Mater. Trans. 2000, 31 (A), 361.
(103) Kovaćs, I.; Lendvai, J.; Nagy, E. Acta Metall. 1972, 20 (7), 975–983.
(104) Edwards, G. A.; Stiller, K.; Dunlop, G. L.; Couper, M. J. Acta Mater. 1998, 46 (11), 3893–3904.
(105) Andersen, S. J.; Zandbergen, H. W.; Jansen, J.; Tráholt, C.; Tundal, U.; Reiso, O. The Crystal Structure Of The B0 Phase In Al±Mg±Si Alloys.
(106) Edwards, G. A.; Dunlopl, G. L.; Couper2, M. J. .
(107) Thomas, G. 1961.
(108) Perovic, A.; Perovic, D. D.; Weatherly, G. C.; Lloyd, D. J. Scr. Mater. 1999,

41 (7), 703–708.
(109) Eskin, D. G. J. Mater. Sci. 2003, 38 (2), 279–290.
(110) Murayama, M.; Hono, K.; Miao, W. F.; Laughlin, D. E. Metall. Mater. Trans. A 2001, 32 (2), 239–246.
(111) Eskin, D. G. J. Mater. Sci. 2003, 38 (2), 279–290.
(112) Chakrabarti, D. J.; Laughlin, D. E. Prog. Mater. Sci. 2004, 49 (3–4), 389–410.
(113) Pickering, H. W. Corros. Sci. 1983, 23 (10), 1107–1120.
(114) Standard Guide For Development And Use Of A Galvanic Series For Predicting Galvanic Corrosion Performance 1 2. Referenced Documents 2.1 Astm Standards: G 3 Practice For Conventions Applicable To Electrochemical Measurements In Corrosion Testing 2 G 15 Terminology Relating To Corrosion And Corrosion Testing 2 G 16 Guide For Applying Statistics To Analysis Of Corrosion Data 2 G 71 Guide For Conducting And Evaluating Galvanic Cor-Rosion Tests In Electrolytes 2.
(115) Hack, H. P. 2.07 Galvanic Corrosion.
(116) Palmsens.Com; Knowledge Base. Tafel Plot Https://Www.Palmsens.Com/Knowledgebase-Article/Tafel-Plot-And-Evans-Diagram/ (Accessed Feb 22, 2023).
(117) Fousova, M.; Valesova, V.; Vojtech, D. Manuf. Technol. 2019, 19 (1), 29–36.
(118) Pourbaix, M. Atlas Of Electrochemical Equilibria In Aqueous Solutions, [1st Engli.; Pergamon Press: Oxford ;New York, 1966.
(119) Guillaumin, V.; Mankowski, G. Corros. Sci. 1998, 41 (3), 421–438.
(120) Iso:International Organization For Standardization. Iso 8044:2020(En), Corrosion Of Metals And Alloys Https://Www.Iso.Org/Obp/Ui/#Iso:Std:Iso:8044:Ed-5:V1:En (Accessed Jul 13, 2022).
(121) Mcmurray, H. N.; Williams, G. In Shreir's Corrosion; Elsevier, 2010; Pp 988–1004.
(122) Der, V.; Younis, A.; Holze Thomas Lampke, R. 2012.
(123) Mattsson, E. Br. Corros. J. 1978, 13 (1), 5–12.
(124) Roberge, P. R. Corrosion Inspection And Monitoring; Wiley-Interscience, 2007.
(125) Fontana, M. G. (Mars G. Corrosion Engineering; Mcgraw-Hill, 1987.
(126) Maaß, P.; Peißker, P. Corrosion And Corrosion Protection; Maaß, P., Peißker, P., Eds.; Wiley-Vch Verlag Gmbh & Co. Kgaa: Weinheim, 2011.
(127) De La Fuente, D. In Encyclopedia Of Materials: Metals And Alloys; Elsevier, 2022; Pp 160–169.
(128) Mccafferty, E. J. Electrochem. Soc. 1979, 126 (3), 385–390.
(129) Lu, Y. C.; Ives, M. B. Corros. Sci. 1995, 37 (1), 145–155.
(130) Popov, B. N. In Corrosion Engineering; Elsevier, 2015; Pp 289–325.
(131) Leblanc, P.; Frankel, G. S. J. Electrochem. Soc. 2002, 149 (6), B239.
(132) Wexler, S. B. De; Galvele, J. R. J. Electrochem. Soc. 1974, 121 (10), 1271.
(133) Mccafferty, E. Corros. Sci. 2003, 45 (7), 1421–1438.
(134) Shao, M.; Fu, Y.; Hu, R.; Lin, C. Mater. Sci. Eng. A 2003, 344 (1–2), 323–327.
(135) Szklarska-Smialowska, Z. Corros. Sci. 1999, 41 (9), 1743–1767.
(136) Obeyesekere, N. U. In Trends In Oil And Gas Corrosion Research And Technologies; Elsevier, 2017; Pp 215–248.
(137) Nguyen, T. H.; Foley, R. T. J. Electrochem. Soc. 1979, 126 (11), 1855–1860.
(138) Inhibition Of Pitting And Filiform Corrosion On Aa2024-T3 By Copper

Complexing Organic Compounds.
(139) Liao, C. M.; Wei, R. P. Electrochim. Acta 1999, 45 (6), 881–888.
(140) Mandel, M.; Krüger, L. Corros. Sci. 2013, 73.
(141) Liao, C.-M.; Olive, J. M.; Gao, M.; Wei, R. P. Corrosion 1998, 54 (6), 451–458.
(142) Muller, I. L.; Galvele, J. R. Corros. Sci. 1977, 17 (3), 179–193.
(143) Szklarska-Smialowska, Z. Corros. Sci. 1999, 41 (9), 1743–1767.
(144) Moore, K. L.; Sykes, J. M.; Grant, P. S. Corros. Sci. 2008, 50 (11), 3233–3240.
(145) Bocher, F.; Flower, H. M.; Ryan, M. P. J. Electrochem. Soc. 2006, 153 (12), B551.
(146) Galvele, J. R.; De De Micheli, S. M. Corros. Sci. 1970, 10 (11), 795–807.
(147) Pyun, S.; Lee, E. Electrochim. Acta 1995, 40 (12), 1963–1970.
(148) Dallek, S.; Foley, R. T. J. Electrochem. Soc. 1976, 123 (12), 1775–1779.
(149) Nguyen, T. H.; Foley, R. T. J. Electrochem. Soc. 1980, 127 (12), 2563–2566.
(150) Hœrlé, S.; Malki, B.; Baroux, B. J. Electrochem. Soc. 2006, 153 (12), B527.
(151) Barbucci, A.; Bruzzone, G.; Delucchi, M.; Panizza, M.; Cerisola, G. Intermetallics 2000, 8 (3), 305–312.
(152) Tomcsányi, L.; Varga, K.; Bartik, I.; Horányi, H.; Maleczki, E. Electrochim. Acta 1989, 34 (6), 855–859.
(153) Okada, T. Electrochim. Acta 1988, 33 (3), 389–395.
(154) Streicher, M. A. J. Electrochem. Soc. 1956, 103 (7), 375.
(155) Liao, M. Int. J. Fatigue 2003, 25 (9–11), 1059–1067.
(156) Serna, L. M.; Johnson, C. M.; Wall, F. D.; Barbour, J. C. J. Electrochem. Soc. 2005, 152 (7), B244.
(157) Atanasoska, L. D.; Dražić, D. M.; Despić, A. R.; Zalar, A. J. Electroanal. Chem. Interfacial Electrochem. 1985, 182 (1), 179–186.
(158) Sinyavskii, V. S.; Ulanova, V. V.; Kalinin, V. D. Prot. Met. 2004, 40 (5), 481–490.
(159) Scully, J. C. The Fundamentals Of Corrosion; Pergamon Press, 1990.
(160) Oldham, K. B.; Mansfeld, F. J. Appl. Electrochem. 1972, 2 (3), 183–191.
(161) Sharman, C. F. Nature 1944, 153 (3890), 621–622.
(162) University Of Manchester. Corrosion And Protection Centre.; International Corrosion Council. The Journal Of Corrosion Science And Engineering : Jcse.; Corrosion And Protection Centre, University Of Manchester Institute Of Science And Technology, 1995.
(163) Slabaugh, W. H.; Dejager, W.; Hoover, S. E.; Hutchinson, L. L. Ind. Eng. Chem. 1971, 76.
(164) Bautista, A. Prog. Org. Coatings 1996, 28 (1), 49–58.
(165) Ruggeri, R. T.; Beck, T. R. Corrosion 1983, 39 (11), 452–465.
(166) Van Loo, M.; Laiderman, D. D.; Bruhn, R. R. Corrosion 1953, 9 (8), 277–283.
(167) Funke, W. Prog. Org. Coatings 1981, 9 (1), 29–46.
(168) Leblanc, P. P.; Frankel, G. S. J. Electrochem. Soc. 2004, 151 (3), B105.
(169) Lebozec, N.; Persson, D.; Thierry, D.; Axelsen, S. B. Corrosion 2004, 60 (6), 584–593.
(170) Mcmurray, H. N.; Williams, G.; O'driscoll, S.; O?Driscoll, S.; O'driscoll, S. J. Electrochem. Soc. 2004, 151 (7), B406.
(171) Kayes, A. J.; Robinson, M. J.; Impey, S. J. Corros. Sci. Eng. 1999, 2, 3–9.
(172) Afseth, A.; Nordlien, J. H.; Scamans, G. M.; Nisancioglu, K. Corros. Sci. 2002, 44 (11), 2543–2559.

(173) Komisarov, V.; Talianker, M.; Cina, B. Mater. Sci. Eng. A 1996, 221 (1–2), 113–121.
(174) Sathiyakumar, M.; Gnanam, F. D. J. Mater. Process. Technol. 2003, 133 (3), 282–286.
(175) Saiz, E.; Tomsia, A. P.; Suganuma, K. J. Eur. Ceram. Soc. 2003, 23 (15), 2787–2796.
(176) Brown, G. M.; Shimizu, K.; Kobayashi, K.; Thompson, G. E.; Wood, G. C. Corros. Sci. 1993, 35 (1–4), 253–256.
(177) Moshier, W. C.; Davis, G. D.; Ahearn, J. S. Corros. Sci. 1987, 27 (8), 785–801.
(178) Ramesh, R.; Bhattacharya, R.; Williams, G. Mater. Sci. Eng. A 2012, 541, 128–134.
(179) Liu, Y.; Zhou, X.; Thompson, G. E. E.; Hashimoto, T.; Scamans, G. M. M.; Afseth, A. Acta Mater. 2007, 55 (1), 353–360.
(180) Hosking, N.; Nichols, M. Can. Inst. Mining, Metall. Pet. 2015, 54, 2–11.
(181) Mcmurray, H. N.; Holder, A.; Williams, G.; Scamans, G. Ecs Meet. Abstr. 2010, Ma2010-02 (17), 1285–1285.
(182) Liu, Y.; Zhou, X.; Thompson, G. E.; Hashimoto, T.; Scamans, G. M.; Afseth, A. J. Phys. Conf. Ser. 2006, 26 (1), 103–106.
(183) Zhou, X.; Liu, Y.; Thompson, G. E.; Scamans, G. M.; Skeldon, P.; Hunter, J. A. Metall. Mater. Trans. A 2011, 42 (5), 1373–1385.
(184) Le Bozec, N.; Persson, D.; Nazarov, A.; Thierry, D. J. Electrochem. Soc. 2002, 149 (9), B403.
(185) Ji, Y.; Guo, F.; Pan, Y. Trans. Nonferrous Met. Soc. China (English Ed. 2008, 18 (1), 126–131.
(186) Leng, A.; Streckel, H.; Hofmann, K.; Stratmann, M. Corros. Sci. 1998, 41 (3), 599–620.
(187) Leng, A.; Streckel, H.; Stratmann, M. Corros. Sci. 1998, 41 (3).
(188) Leng, A.; Streckel, H.; Stratmann, M. Corros. Sci. 1999, 41 (3), 579.
(189) Stratmann, M.; Leng, A.; Fürbeth, W.; Streckel, H.; Gehmecker, H.; Große-Brinkhaus, K. H.; Groβe-Brinkhaus, K.-H.; Große-Brinkhaus, K. H. Prog. Org. Coatings 1996, 27 (1–4), 261–267.
(190) Williams, G.; Mcmurray, H. N.; Loveridge, M. J. Electrochim. Acta 2010, 55 (5), 1740–1748.
(191) Watson, T. M.; Coleman, A. J.; Williams, G.; Mcmurray, H. N. Corros. Sci. 2014, 89 (C), 46–58.
(192) Williams, G.; Mcmurray, H. N. Electrochem. Solid-State Lett. 2004, 7 (5), B13.
(193) Williams, G.; Mcmurray, H. N. Prog. Org. Coatings 2017, 102, 18–28.
(194) Ho, D.; Brack, N.; Scully, J.; Markley, T.; Forsyth, M.; Hinton, B. J. Electrochem. Soc. 2006, 153 (9), B392.
(195) Williams, G.; Mcmurray, H. N.; Worsley, D. A. J. Electrochem. Soc. 2002, 149 (4), B154.
(196) Williams, G.; Mcmurray, H. N. N. Electrochim. Acta 2012, 69, 287–294.
(197) Williams, G. Ecs Trans. 2010, 24 (1), 67–76.
(198) Aldykiewicz, A. J.; Davenport, A. J.; Isaacs, H. S. 1996, 143 (1).
(199) Williams, G.; Coleman, A. J.; Mcmurray, H. N. Electrochim. Acta 2010, 55 (20), 5947–5958.
(200) Coelho, L. B.; Cossement, D.; Olivier, M. G. Corros. Sci. 2018, 130, 177–189.
(201) Mohammadi, I.; Shahrabi, T.; Mahdavian, M.; Izadi, M. J. Electrochem. Soc.

2020, 167 (13), 131506.
(202) Coelho, L. B.; Mouanga, M.; Druart, M. E.; Recloux, I.; Cossement, D.; Olivier, M. G. Corros. Sci. 2016, 110, 143–156.
(203) Williams, G.; Geary, S.; Mcmurray, H. N. Corros. Sci. 2012, 57, 139–147.
(204) 6016 (Alsi1.2mg0.4, A96016) Aluminum :: Makeitfrom.Com Http://Www.Makeitfrom.Com/Material-Properties/6016-Alsi1.2mg0.4-A96016-Aluminum (Accessed Jun 30, 2017).
(205) 6005a (Alsimg(A), 3.3210) Aluminum :: Makeitfrom.Com Http://Www.Makeitfrom.Com/Material-Properties/6005a-Alsimga-3.3210-Aluminum (Accessed Jun 30, 2017).
(206) 2024 (Alcu4mg1, 3.1355, 2l97, A92024) Aluminum :: Makeitfrom.Com Http://Www.Makeitfrom.Com/Material-Properties/2024-Alcu4mg1-3.1355-2l97-A92024-Aluminum (Accessed Jun 30, 2017).
(207) 7075 (Alzn5.5mgcu, 3.4365, 2l95, A97075) Aluminum :: Makeitfrom.Com Http://Www.Makeitfrom.Com/Material-Properties/7075-Alzn5.5mgcu-3.4365-2l95-A97075-Aluminum (Accessed Apr 11, 2017).
(208) Natishan, P. M.; O'grady, W. E. J. Electrochem. Soc. 2014, 161 (9).
(209) Schmidt, W.; Stratmann, M. Corros. Sci. 1998, 40 (8), 1441–1443.
(210) Williams, G.; Mcmurray, H. N. Electrochem. Solid-State Lett. 2003, 6 (3), B9.
(211) Williams, G.; Mcmurray, N. Forensic Sci. Int. 2007, 167 (2–3), 102–109.
(212) Frankel, G. S.; Stratmann, M.; Rohwerder, M.; Michalik, A.; Maier, B.; Dora, J.; Wicinski, M. Corros. Sci. 2007, 49 (4), 2021–2036.
(213) Holness, R. J.; Williams, G.; Worsley, D. A.; Mcmurray, H. N. J. Electrochem. Soc. 2005, 152 (2), B73.
(214) Coleman, A. J.; Mcmurray, H. N.; Williams, G.; Afseth, A.; Scamans, G. M. Scanning Kelvin Probe Studies Of Cosmetic (Filiform) Corrosion On Aa6016 And Aa6111; Vol. 863.
(215) Gulanová, J.; Lonek, S.; Gulan, L. Comput. Aided. Des. Appl. 2018, 15 (5), 757–763.
(216) Zhu, G.; Hu, X.; Kang, J.; Mishra, R.; Wilkinson, D. S. Mater. Sci. Eng. A 2011, 528 (12), 4187–4198.
(217) Massart, T. J.; Pardoen, T. Acta Mater. 2010, 58 (17), 5768–5781.
(218) Scheriau, S.; Pippan, R. Mater. Sci. Eng. A 2008, 493 (1–2), 48–52.
(219) Singh, R. .; Singh, A. . Scr. Mater. 1998, 38 (8), 1299–1306.
(220) Takeda, H.; Hibino, A.; Takata, K. Mater. Trans. 2010, 51 (4), 614–619.
(221) Sarvesha, R.; Alam, W.; Jain, J.; Singh, S. S. In Springer Proceedings In Materials; Springer Nature, 2021; Vol. 11, Pp 55–64.
(222) Asano, M.; Minoda, T.; Ozeki, Y.; Yoshida, H. Mater. Sci. Forum 2006, 519–521, 771–776.
(223) Bieler, T. R. In Minerals, Metals And Materials Society. Materials Processing And Manufacturing Division.; Tms, 2005; P 394.
(224) Lloyd, D. J.; Evans, D.; Pelow, C.; Nolan, P.; Jain, M. Mater. Sci. Technol. 2002, 18 (6), 621–628.
(225) Friedman, P.; Luckey, S. G. In Aluminum 2001: Proceedings Of The 2001 Tms Annual Meeting Automotive Alloys And Joining Aluminum Symposia; 2001; Pp 3–15.
(226) Steele, D.; Evans, D.; Nolan, P.; Lloyd, D. J. Mater. Charact. 2007, 58 (1), 40–45.
(227) Le Maoût, N.; Thuillier, S.; Manach, P. Y. Exp. Mech. 2010, 50 (7), 1087–1097.

(228) Lin, G.; Hu, S. J.; Cai, W. J. Manuf. Sci. Eng. 2009, 131 (5), 91–99.
(229) Mott, N. F. Proc. Phys. Soc. Sect. B 1951, 64 (9), 729–741.
(230) Pardoen, T.; Brechet, Y. Philos. Mag. 2004, 84 (3–5), 269–297.
(231) Hansen, N.; Jensen, D. J. Philos. Trans. R. Soc. London. Ser. A Math. Phys. Eng. Sci. 1999, 357 (1756), 1447–1469.
(232) Sarkar, J.; Kutty, T. R. G.; Wilkinson, D. S.; Embury, J. D.; Lloyd, D. J. Mater. Sci. Eng. A 2004, 369 (1–2), 258–266.
(233) Liu, Y.; Frolish, M. F.; Rainforth, W. M.; Zhou, X.; Thompson, G. E.; Scamans, G. M.; Hunter, J. A. Surf. Interface Anal. 2010, 42 (4), 180–184.
(234) Scamans, G. M.; Amor, M. P.; Ellard, B. R.; Hunter, J. A. In Aluminium Surface Science And Technology, Antwerp; 1997; P 229.
(235) Scamans, G. M.; Afseth, A.; Thompson, G. E.; Zhou, X. In Materials Science Forum; Trans Tech Publications Ltd, 2002; Vol. 396–402, Pp 1461–1466.
(236) Zhou, X.; Thompson, G. E.; Scamans, G. M. Corros. Sci. 2003, 45 (8), 1767–1777.
(237) Liu, Y.; Hashimoto, T.; Zhou, X.; Thompson, G. E.; Scamans, G. M.; Rainforth, W. M.; Hunter, J. A. Surf. Interface Anal. 2013, 45 (10), 1553–1557.
(238) De Wit, J. H. . Electrochim. Acta 2001, 46 (24–25), 3641–3650.
(239) Asami, K.; Oki, M.; Thompson, G. E.; Wood, G. C.; Ashworth, V. Electrochim. Acta 1987, 32 (2), 337–343.
(240) Dimitrov, N.; Mann, J. A.; Sieradzki, K. J. Electrochem. Soc. 1999, 146 (1), 98–102.
(241) Habazaki, H.; Paez, M. A.; Shimizu, K.; Skeldon, P.; Thompson, G. E.; Wood, G. C.; Zhou, X. Corros. Sci. 1996, 38 (7), 1033.
(242) Buchheit, R. G.; Grant, R. P.; Hlava, P. F.; Mckenzie, B.; Zender, G. L. J. Electrochem. Soc. 1997, 144 (8), 2621.
(243) Garcia-Vergara, S.; Skeldon, P.; Thompson, G. .; Bailey, P.; Noakes, T. C. .; Habazaki, H.; Shimizu, K. Appl. Surf. Sci. 2003, 205 (1–4), 121–127.
(244) Pires, I.; Quintino, L.; Rangel, C. M.; Thompson, G. E.; Sheldon, P.; Zhou, X. Trans. Imf 2000, 78 (5), 179–185.
(245) Garcia-Vergara, S. J.; Skeldon, P.; Thompson, G. E.; Williams, G.; Mcmurray, H. N. 2012, 159 (9), C428–C433.
(246) Caicedo-Martinez, C. E.; Koroleva, E.; Skeldon, P.; Thompson, G. E.; Hoellrigl, G.; Bailey, P.; Noakes, T. C. Q.; Habazaki, H.; Shimizu, K. J. Electrochem. Soc. 2002, 149 (4), B139.
(247) Zhou, X.; Thompson, G. E.; Habazaki, H.; Shimizu, K.; Skeldon, P.; Wood, G. C. Thin Solid Films 1997, 293 (1–2), 327.
(248) Iwata, M.; Nishikado, M.; Sato, E.; Itoi, Y. J. Japan Inst. Light Met. 1984, 34 (9), 531–536.
(249) Little, D. A.; Jakab, M. A.; Scully, J. R. Corrosion 2006, 62 (4), 300–315.
(250) Slabaugh, W. H.; Grotheer, M. Ind. Eng. Chem. 1954, 46 (5), 1014–1016.
(251) Lebozec, N.; Persson, D.; Thierry, D.; Axelsen, S. B. Corrosion 2004, 60 (6), 584–593.
(252) Leidheiser, H. Corrosion 1982, 38 (7), 374–383.
(253) Bierwagen, G. P. Prog. Org. Coatings 1996, 28 (1), 43–48.
(254) Koehler, E. L. Corrosion 1977, 33 (6), 209–217.
(255) Lebozec, N.; Persson, D.; Thierry, D.; Axelsen, S. B. Corrosion Engineering Section Effect Of Climatic Parameters On Filiform Corrosion Of Coated Aluminum Alloys; 2004.

(256) Scheck, K. Investigations On Filiform Corrosion On Organically Coated Aluminium And Parameters Affecting It, 1991.
(257) Broudy, H. An Attempt To Find Salts Which In Saturated Solution Yield Relative Humidities Not Yet Obtainable For Use In Biological Research, 1933.
(258) Williams, G.; Grace, R. Chloride-Induced Filiform Corrosion Of Organic-Coated Magnesium; 2011; Vol. 56, Pp 1894–1903.
(259) Kousis, C.; Keil, P.; Mcmurray, H. N.; Williams, G. Corros. Sci. 2022, 206.
(260) Liu, X. F. Corros. Sci. 2007, 49 (9), 3494–3513.
(261) Greenspan, L. J. Res. Natl. Bur. Stand. -A. Phys Ics Chem. 81 (1).
(262) O'brien, F. E. M. J. Sci. Instrum. 1948, 25 (3), 73–76.
(263) Engineering Toolbox. Saturated Salt Solutions And Air Humidity Https://Www.Engineeringtoolbox.Com/Salt-Humidity-D_1887.Html (Accessed Apr 3, 2018).
(264) Rockland, L. B. Anal. Chem. J. Am. Ceram. Soc. Powell. D. A., J. Set. Instr 1955, 27 (34), 1375.
(265) Carr, D. S.; Harris, B. L. .
(266) Hong, T. D.; Steve Edgington, S.; Ellis, R. H.; De Muro, M. A.; Moore, D. J. Invertebr. Pathol. 2005, No. 89, 136–143.
(267) Wan, Z.; Wang, H.-P.; Chen, N.; Wang, M.; Carlson, B. E. J. Mater. Process. Technol. 2017, 242, 12–23.
(268) Afseth, A.; Nordlien, J. .; Scamans, G. .; Nisancioglu, K. Corros. Sci. 2002, 44 (11), 2491–2506.
(269) Leth-Olsen, H.; Nisancioglu, K. Corros. 1997, 53 (9), 705.
(270) Schmidt, W.; Stratmann, M. Corros. Sci. 1998, 40 (8), 1441.
(271) Szklarska-Smialowska, Z. Corros. Sci. 1992, 33 (8), 1193–1202.
(272) Mazurkiewicz, B.; Piotrowski, A. Corros. Sci. 1983, 23 (7), 697.
(273) Garcia-Vergara, S.; Colin, F.; Skeldon, P.; Thompson, G. E.; Bailey, P.; Noakes, T. C. Q.; Habazaki, H.; Shimizu, K. J. Electrochem. Soc. 2004, 151 (1), B16.
(274) Pires, J.; Quiniino, L.; Rangel, C. M.; Thompson, G. E.; Skeldon, P.; Zhou, X. Trans. Inst. Met. Finish. 2000, 78 (5), 179.
(275) Buchheit, R. G. J. Electrochem. Soc. 1995, 142 (11), 3994.
(276) Ruggeri, R. T.; Beck, T. R. Corrosion 1983, 39 (11), 452–465.
(277) Ding, L.; He, Y.; Wen, Z.; Zhao, P.; Jia, Z.; Liu, Q. J. Alloys Compd. 2015, 647 (October), 238–244.
(278) Chang, C. S. T.; Banhart, J. Metall. Mater. Trans. A Phys. Metall. Mater. Sci. 2011, 42 (7), 1960–1964.
(279) Slabaugh, W. H. Filiform Corrosion Of Aluminum. Https://Apps.Dtic.Mil/Sti/Citations/Ad0726739 (Accessed Jan 9, 2023).
(280) Scheck, K. Univ. Stuttgart 1991.
(281) Bautista, A. Progress In Organic Coatings Elsevier Filiform Corrosion In Polymer-Coated Metals; 1996; Vol. 28.
(282) Leth-Olsen, H.; Nisancioglu, K. Corros. Sci. 1998, 40 (7), 1179–1194.
(283) Schneider, O.; Ilevbare, G. O.; Kelly, R. G.; Scully, J. R. J. Electrochem. Soc. 2007, 154 (8), C397.
(284) Leth-Olsen, H.; Nordlien, J. H.; Nisancioglu, K. Corros. Sci. 1998, 40 (12), 2051–2063.
(285) Leth-Olsen, H.; Afseth, A.; Nisancioglu, K. Corros. Sci. 1998, 40 (7), 1195–1214.

(286) Scamans, G. M.; Afseth, A.; Thompson, G. E.; Liu, Y.; Zhou, X. R. Mater. Sci. Forum 2006, 519–521 (Part 1), 647–654.
(287) Little, D. A.; Jakab, M. A.; Scully, J. R. Corrosion 2006, 62 (4), 300–315.
(288) Svenningsen, G.; Larsen, M. H.; Nordlien, J. H.; Nisancioglu, K. Corros. Sci. 2006, 48 (12), 3969–3987.
(289) Svenningsen, G.; Larsen, M. H.; Nordlien, J. H.; Nisancioglu, K. Corros. Sci. 2006, 48 (1), 258–272.
(290) Svenningsen, G.; Lein, J. E.; Bjørgum, A.; Nordlien, J. H.; Yu, Y.; Nisancioglu, K. Corros. Sci. 2006, 48 (1), 226–242.
(291) Svenningsen, G.; Larsen, M. H.; Walmsley, J. C.; Nordlien, J. H.; Nisancioglu, K. Corros. Sci. 2006, 48 (6), 1528–1543.
(292) 2004.
(293) Garcia-Vergara, S.; Colin, F.; Skeldon, P.; Thompson, G. E.; Bailey, P.; Noakes, T. C. Q.; Habazaki, H.; Shimizu, K. J. Electrochem. Soc. 2004, 151 (1), B16.
(294) Williams, G.; Mcmurray, H. N. Electrochem. Solid-State Lett. 2003, 6 (3), B9.
(295) Buchheit, R. G. J. Electrochem. Soc. 1995, 142 (11), 3994–3996.
(296) Buchheit, R. G.; Martinez, M. A.; Montes, L. P. J. Electrochem. Soc. 2000, 147 (1), 119–124.
(297) Ilevbare, G. O.; Scully, J. R. J. Electrochem. Soc. 2001, 148 (5), B196.
(298) Kendig, M.; Addison, R.; Jeanjaquet, S. J. Electrochem. Soc. 1999, 146 (12), 4419–4423.
(299) Kloet, J. Vander; Schmidt, W.; Hassel, A. W.; Stratmann, M. Electrochim. Acta 2003, 48.
(300) Buchheit, R. G.; Bode, M. D.; Stoner, G. E. Corrosion 1994, 50 (3), 205–214.
(301) Kolics, A.; Besing, A. S.; Baradlai, P.; Wieckowski, A. J. Electrochem. Soc. 2003, 150 (11), B512.
(302) Xia, L.; Akiyama, E.; Frankel, G.; Mccreery, R. J. Electrochem. Soc. 2000, 147 (7), 2556.
(303) Zhao, J.; Xia, L.; Sehgal, A.; Lu, D.; Mccreery, R. L.; Frankel, G. S. Surf. Coatings Technol. 2001, 140 (1), 51–57.
(304) Schmutz, P.; Frankel, G. S. J. Electrochem. Soc. 1999, 146 (12), 4461–4472.
(305) Zhao, J.; Frankel, G.; Mccreery, R. L. J. Electrochem. Soc. 1998, 145 (7), 2258–2264.
(306) Sehgal, A.; Lu, D.; Frankel, G. S. J. Electrochem. Soc. 1998, 145 (8), 2834–2840.
(307) Petrilli, F. L.; De Flora, S. Toxicity And Mutagenicity Of Hexavalent Chromium On Salmonella Typhimurium; 1977.
(308) Petrilli, F. L.; De Flora, S. Mutat. Res. Toxicol. 1978, 58 (2–3), 167–173.
(309) Epstein, S. S. Int. J. Heal. Serv. 2005, 35 (1), 1–38.
(310) Montemor, M. F. Surf. Coatings Technol. 2014, 258, 17–37.
(311) Aldykewicz, A. J.; Isaacs, H. S.; Davenport, A. J. 1995, 142 (10).
(312) Mansfeld, F.; Wang, V.; Shih, H. J. Electrochem. Soc. 1991, 138 (12), L74–L75.
(313) Arenas, M. A.; Bethencourt, M.; Botana, F. J.; De Damborenea, J.; Marcos, M. 2001, 43 (1).
(314) Bethencourt\, M. [; Botana\, J. [; Calvino\, J. [; Marcos, M. [; Rodri, A. [; Chaco Łn, ! Corros. Sci. 1998, 39 (11).
(315) Kendig, M. W.; Buchheit, R. G. Corrosion 2003, 59 (5), 379–400.
(316) Campestrini, P.; Terryn, H.; Hovestad, A.; De Wit, J. H. W. Surf. Coatings

Technol. 2004, 176 (3), 365–381.
(317) Decroly, A.; Petitjean, J. P. Surf. Coatings Technol. 2005, 194 (1), 1–9.
(318) Zheludkevich, M. L.; Yasakau, K. A.; Poznyak, S. K.; Ferreira, M. G. S. Corros. Sci. 2005, 47 (12), 3368–3383.
(319) Rosero-Navarro, N. C.; Pellice, S. A.; Durán, A.; Aparicio, M. Corros. Sci. 2008, 50 (5), 1283–1291.
(320) Moutarlier, V.; Neveu, B.; Gigandet, M. P. Surf. Coatings Technol. 2008, 202 (10), 2052–2058.
(321) Ouarga, A.; Lebaz, N.; Tarhini, M.; Noukrati, H.; Barroug, A.; Elaissari, A.; Ben Youcef, H. Towards Smart Self-Healing Coatings: Advances In Micro/Nano-Encapsulation Processes As Carriers For Anti-Corrosion Coatings Development; Elsevier B.V., 2022; Vol. 354.
(322) Wang, D.; Bierwagen, G. P. 2009, 64 (4).
(323) Bohm, S.; Mcmurray, H. N.; Worsley, D. A.; Powell, S. M. Mater. Corros. 2001, 52 (12), 896–903.
(324) Buchheit, R. G.; Guan, H.; Mahajanam, S.; Wong, F. Active Corrosion Protection And Corrosion Sensing In Chromate-Free Organic Coatings; 2003; Vol. 47.
(325) Karekar, S. E.; Bagale, U. D.; Sonawane, S. H.; Bhanvase, B. A.; Pinjari, D. V. Compos. Interfaces 2018, 25 (9), 785–808.
(326) Leal, D. A.; Kuznetsova, A.; Silva, G. M.; Tedim, J.; Wypych, F.; Marino, C. E. B. Appl. Clay Sci. 2022, 225, 106537.
(327) Cao, Y.; Zheng, D.; Zhang, F.; Pan, J.; Lin, C. 2022, 102, 232–263.
(328) Chen, S.; Huang, Z.; Yuan, M.; Huang, G.; Guo, H.; Meng, G.; Feng, Z.; Zhang, P. J. Mater. Sci. Technol. 2022, 125, 67–80.
(329) Arnott, D.; Ryan, N.; Hinton, B.; Sexton, B.; Hughes, A. 1985, No. Part 1.
(330) Arnott, D.; Hinton, B.; Ryan, N. Corrosion 1989, 45 (1), 12–18.
(331) Hinton, B. R. W. J. Alloys Compd. 1992, 180 (1–2), 15–25.
(332) Davenport, A. . J.; Isaacs, H. . S.; Kendig, M. . W. 1991, 32.
(333) Vieira, D. E. L.; Salak, A. N.; Ferreira, M. G. S.; Vieira, J. M.; Brett, C. M. A. Appl. Surf. Sci. 2022, 573, 151527.
(334) Pérez-Ramírez, J.; Abelló, S.; Van Der Pers, N. M. Chem. – A Eur. J. 2007, 13 (3), 870–878.
(335) Mills, S. J.; Christy, A. G.; Génin, J.-M. R.; Kameda, T.; Colombo, F. Mineral. Mag. 2012, 76 (5), 1289–1336.
(336) Miyata, S. Clays Clay Miner. 1983, 31 (4), 305–311.
(337) Nam, N. D. J. Electrochem. Soc. 2016, 163 (3), C76–C84.
(338) Granizo, N.; Vega, J. M.; Díaz, I.; Chico, B.; De La Fuente, D.; Morcillo, M. Prog. Org. Coatings 2011, 70 (4), 394–400.
(339) Mcmurray, H. N.; Williams, G. Corrosion 2004, 60 (3), 219–228.
(340) Kameda, T.; Miyano, Y.; Yoshioka, T.; Uchida, M.; Okuwaki, A. Chem. Lett. 2000, 29 (10), 1136–1137.
(341) Panitz, J. K. G.; Sharp, D. J. The Use Of Synthetic Hydrocalcite As A Chloride-Ion Getter For A Barrier Aluminum Anodization Process; Albuquerque, Nm, And Livermore, Ca (United States), 1995.
(342) Ralston, K. D.; Chrisanti, S.; Young, T. L.; Buchheit, R. G. J. Electrochem. Soc. 2008, 155 (7), C350.
(343) Isaacs, H. S.; Davenport, A. J.; Shipley, A. J. Electrochem. Soc. 1991, 138 (2), 390–393.
(344) Bethencourt, M.; Botana, F. J.; Cano, M. J.; Marcos, M. Appl. Surf. Sci. 2002,

189 (1–2), 162–173.
(345) Finšgar, M.; Milošev, I. Inhibition Of Copper Corrosion By 1,2,3-Benzotriazole: A Review; 2010; Vol. 52, Pp 2737–2749.
(346) Kovačević, N.; Kokalj, A. Mater. Chem. Phys. 2012, 137 (1), 331–339.
(347) Xhanari, K.; Finšgar, M. Arab. J. Chem. 2019, 12 (8), 4646–4663.
(348) Harvey, T. J.; Walsh, F. C.; Nahlé, A. H. J. Mol. Liq. 2018, 266, 160–175.
(349) Serdechnova, M.; Salak, A. N.; Barbosa, F. S.; Vieira, D. E. L.; Tedim, J.; Zheludkevich, M. L.; Ferreira, M. G. S. J. Solid State Chem. 2016, 233, 158–165.
(350) Zhang, W.; Buchheit, R. G. Corrosion 2002, 58 (7), 591–600.
(351) Mahajanam, S. P. V.; Buchheit, R. G. Corrosion 2008, 64 (3), 230–240.
(352) Li, J.; Hurley, B.; Buchheit, R. J. Electrochem. Soc. 2016, 163 (14), C845–C852.
(353) Buchheit, R. G.; Mamidipally, S. B.; Schmutz, P.; Guan, H. Corrosion 2002, 58 (1), 3–14.
(354) Coleman, A. J.; Mcmurray, H. N.; Williams, G.; Afseth, A.; Scamans, G. M. Electrochem. Solid-State Lett. 2007, 10 (5), C35.
(355) Vaccari, A. Appl. Clay Sci. 1999, 14 (4), 161–198.
(356) Dimitrov, N.; Mann, J. A.; Vukmirovic, M.; Sieradzki, K. J. Electrochem. Soc. 2000, 147 (9), 3283.
(357) Ilevbare, G. O.; Scully, J. R. Corrosion 2001, 57 (2), 134–152.
(358) Kolics, A.; Besing, A. S.; Wieckowski, A. J. Electrochem. Soc. 2001, 148 (8), B322.
(359) Dugdale, I.; Cotton, J. B. Corros. Sci. 1963, 3 (2), 69–74.
(360) Cotton, J. B.; Scholes, I. R. Br. Corros. J. 1967, 2 (1), 1–5.
(361) Poling, G. W. Corros. Sci. 1970, 10 (5), 359–370.
(362) Al-Hinai, A. T.; Osseo-Asare, K. Electrochem. Solid-State Lett. 2003, 6 (5), B23.
(363) Tromans, D.; Li, G. Electrochem. Solid-State Lett. 2002, 5 (2), B5.
(364) Tromans, D.; Sun, R. J. Electrochem. Soc. 1991, 138 (11), 3235–3244.
(365) Tromans, D. J. Electrochem. Soc. 1998, 145 (3), L42–L45.
(366) Cao, P. G.; Yao, J. L.; Zheng, J. W.; Gu, R. A.; Tian, Z. Q. Langmuir 2002, 18 (1), 100–104.
(367) Kendig, M.; Yan, C. J. Electrochem. Soc. 2004, 151 (12), B679.
(368) Sayed, S. Y.; El-Deab, M. S.; El-Anadouli, B. E.; Ateya, B. G. J. Phys. Chem. B 2003, 107 (23), 5575–5585.
(369) Richards, C. A. J.; Mcmurray, H. N.; Williams, G. Corros. Sci. 2019, 154, 101–110.
(370) Leidheiser, H.; Wang, W.; Igetoft, L. Prog. Org. Coatings 1983, 11 (1), 19–40.
(371) Ansell, P.; Berry, L.; Mcgettrick, J.; Searle, J.; Wint, N.; Mcmurray, N.; Williams, G. J. Electrochem. Soc. 2022.
(372) Williams, G.; Dodds, P. C.; Ansell, P.; Mcmurray, H. N. Ecs Meet. Abstr. 2016, Ma2016-02 (14), 1347–1347.
(373) Michailidou, E.; Mcmurray, H. N.; Williams, G. Ecs Meet. Abstr. 2017, Ma2017-02 (12), 774–774.
(374) Katz, S. A.; Salem, H. J. Appl. Toxicol. 1993, 13 (3), 217–224.
(375) Qafsaoui, W.; Blanc, C.; Pébère B, N.; Takenouti, H.; Srhiri, A.; Mankowski, G. Quantitative Characterization Of Protective Films Grown On Copper In The Presence Of Different Triazole Derivative Inhibitors.
(376) Xue, G.; Ding, J.; Cheng, P. Appl. Surf. Sci. 1995, 89 (1), 77–82.

(377) Richards, C. A. J.; Mcmurray, H. N.; Williams, G. Corros. Sci. 2019, 154, 101–110.
(378) Coleman, A. J.; Mcmurray, H. N.; Williams, G.; Afseth, A.; Scamans, G. M. Electrochem. Solid-State Lett. 2007, 10 (5), C35.
(379) Kleiner, M.; Geiger, M.; Klaus, A. Cirp Ann. - Manuf. Technol. 2003, 52 (2), 521.
(380) Lai, M.; Brun, R. In Key Engineering Materials; 2007; Vol. 344, Pp 1–8.
(381) Wang, X.; Embury, J. D.; Poole, W. J.; Esmaeili, S.; Lloyd, D. J. Metall. Mater. Trans. A 2003, 34 (12), 2913–2924.
(382) Cheng, L. M.; Poole, W. J.; Embury, J. D.; Lloyd, D. J. Metall. Mater. Trans. A 2003, 34 (A), 2481.
(383) Muderrisoglu, A.; Murata, M.; Ahmetoglu, M. A.; Kinzel, G.; Altan, T. J. Mater. Process. Technol. 1996, 59 (1–2), 10–17.
(384) Bloeck, M. Adv. Mater. Automot. Eng. 2012, 6, 85.
(385) Friedman, P. A.; Luckey, S. G. Pract. Fail. Anal. 2002, 2 (1), 33–42.
(386) Krajewski, P. E.; Carsley, J. E. In Aluminum 2003: Proceedings Of The 2003 Tms Annual Meeting; 2003; Pp 25–35.
(387) Sheasby, P. G.; Pinner, R.; Wernick, S. The Surface Treatment And Finishing Of Aluminium And Its Alloys.; Asm International, 2001; Vol. 7.
(388) Totten, G. E.; Mackenzie, S. . Handbook Of Aluminum; Dekker, 2003; Vol. 2.
(389) Mori, K. Adv. Mater. Res. 2014, 966–967, 29–47.
(390) Jimbert, P.; Eguia, I.; Perez, I.; Gutierrez, M. A.; Hurtado, I. J. Mater. Process. Technol. 2011, 211 (5), 916–924.
(391) Birbilis, N.; Buchheit, R. G. J. Electrochem. Soc. 2005, 152 (4), B140.
(392) Fröck, H.; Graser, M.; Reich, M.; Lechner, M.; Merklein, M.; Kessler, O. Prod. Eng. 2016, 10 (4), 383-.
(393) Le Maoût, N.; Thuillier, S.; Manach, P. Y. Mater. Des. 2010, 31 (6), 2725–2736.
(394) Thuillier, S.; Le Maoût, N.; Manach, P. Y. Int. J. Mater. Form. 2010, 3 (1), 223.
(395) Pradeau, A.; Thuillier, S.; Yoon, J. W. Int. J. Mech. Sci. 2016, 119, 23–35.
(396) Li, S.; Hu, X.; Zhao, Y.; Lin, Z.; Xu, N. Mater. Des. 2011, 32 (4), 2308–2316.
(397) Liewald, M.; Hönle, S.; Sindel, M. Int. J. Mater. Form. 2016, 9 (2), 203–213.
(398) Schleich, R.; Sindel, M.; Liewald, M. Int. J. Mater. Form. 2009, 2 (2), 69–74.
(399) Engler, O.; Marioara, C. D.; Aruga, Y.; Kozuka, M.; Myhr, O. R. Mater. Sci. Eng. A 2019, 759, 520–529.
(400) Engler, O.; Schäfer, C.; Myhr, O. R. Mater. Sci. Eng. A 2015, 639, 65–74.
(401) Muhammad, W.; Kang, J.; Brahme, A. P.; Ali, U.; Hirsch, J.; Brinkman, H.; Engler, O.; Mishra, R.; Inal, K. Mater. Sci. Eng. A 2019, 753, 179–191.
(402) Bottema, J.; Lahaye, C.; Baartman, R.; Zhuang, L.; De Smet, P.; Schoepen, F. In Journal Of Materials & Manufacturing; 1998; Vol. 107, Pp 900–907.
(403) Zhuang, L.; Bottema, J.; Kaasenbrood, P.; Miller, W. S.; De Smet, P. Mater. Sci. Forum 1996, 217–222 (Part 1), 487–492.
(404) Miller, W. .; Zhuang, L.; Bottema, J.; Wittebrood, A. .; De Smet, P.; Haszler, A.; Vieregge, A. Mater. Sci. Eng. A 2000, 280 (1), 37.
(405) Stoudt, M. R.; Hubbard, J. B.; Carsley, J. E.; Hartfield-Wünsch, S. E. J. Eng. Mater. Technol. 2014, 136 (3).
(406) Steele, D.; Evans, D.; Nolan, P.; Lloyd, D. J. Mater. Charact. 2007, 58 (1), 40–45.
(407) Gupta, A. K.; Bookbinder, J. B.; Sang, H. S.; Lloyd, D. J. Mater. Sci. Forum

2000, 331–337, 1297–1302.
(408) General Motors Corporation. Gmw15421 - Three-Point Bend Test For Hemming Performance Evaluation Https://Standards.Globalspec.Com/Std/13085682/Gmw15421 (Accessed Feb 23, 2023).
(409) Saxena, K. K.; Das, I. M.; Mukhopadhyay, J. Int. J. Mater. Form. 2017, 10 (2), 221–231.
(410) Denninger, R.; Liewald, M.; Held, C.; Sindel, M. In Aip Conference Proceedings; American Institute Of Physicsaip, 2011; Vol. 1353, Pp 1601–1605.
(411) Goodwin, G. M. Jstor - Sae Trans. 1968, 77, 380–387.
(412) Sarkar, J.; Kutty, T. R. G.; Wilkinson, D. S.; Embury, J. D.; Lloyd, D. J. Mater. Sci. Eng. A 2004, 369 (1–2), 258.
(413) Sarkar, J.; Kutty, T. R. G.; Conlon, K. T.; Wilkinson, D. S.; Embury, J. D.; Lloyd, D. J. Mater. Sci. Eng. A 2001, 316 (1–2), 52.
(414) Gu, Z.; Wang, G.; Yu, G. Metals (Basel). 2020, 10 (1), 81.